Durham E-Theses

Exploring Cosmology and Structure Formation via High-z Galaxies

NIKOLOUDAKIS, NIKOLAOS

How to cite:

Use policy

Exploring Cosmology and Structure Formation
via High-z Galaxies.

Nikolaos Nikoloudakis

Abstract

This thesis exploits the large-scale structure of the Universe via observations over a wide redshift range, with the aim of constraining the current cosmological models and galaxy formation physics. We present the eXtreme Multiplex Spectrograph (XMS), a proposed spectrograph that can map simultaneously 4000 Emission Line Galaxies (ELGs) and Luminous Red Galaxies (LRGs) in the range $0.4 \leq z \leq 0.8$, with a success rate of 88%. Figures of merit clearly indicate that XMS is better or even competitive compared to future surveys for measurements of the gravitational growth rate, Baryon Acoustic Oscillations (BAO) and dark-matter halo mass function. Next, by selecting a unique photometric sample of $130,000$ LRGs in the Sloan Digital Sky Survey (SDSS) Stripe 82, with an estimated average redshift $z \sim 1$, we perform a clustering analysis and compare the clustering evolution of the high-z Stripe 82 LRGs to lower-z LRGs. An immediate feature of the Stripe 82 LRGs clustering is a power excess at large scales. This behaviour is not expected within the ΛCDM model, making the conclusion of a slow clustering evolution as observed for the lower-z LRGs, non-trivial. Only Non-Gaussian models are able to describe the large scale clustering of the Stripe 82 LRGs. From follow up spectroscopic observations of a subsample of the Stripe 82 LRGs, we confirm that the average redshift of our sample is $z \sim 0.9$, while the slow clustering evolution of the LRGs is now slightly more favoured. However, Non-Gaussianity is still detected at a 2σ level. Finally, from the largest and deepest near-infrared field to present, the UltraVISTA survey, we select ≈ 4000 Distant Red Galaxies (DRGs) and study the largest galaxy separations ever probed with these massive galaxies. In agreement with previous results, UltraVISTA DRGs are strongly clustered objects. Furthermore, they show stronger clustering within their brighter K-limited samples, that could possibly imply luminosity segregation. Their connection to the local descendants cannot yet be established.

Exploring Cosmology
and Structure Formation
via High-z Galaxies

by Nikolaos Nikoloudakis

A thesis submitted to the University of Durham

in accordance with the regulations for

admittance to the Degree of Doctor of Philosophy.

Department of Physics

University of Durham

June 2013

Contents

List of Figures

List of Tables

Declaration

The work described in this thesis was undertaken between 2008 and 2013 while the author was a research student under the supervision of Prof. Tom Shanks in the Department of Physics at the University of Durham. This work has not been submitted for any other degree at the University of Durham or any other University.

Portions of Chapter 1 have been published as conference proceedings

- Content, R. and Barden, S. and Becerril, S. and Boehm, A. and Clark , P. and Costillo, P. and Dubbeldam, C. M. and Farrell, T. and Glazebrook, K. and Haynes , R. and Meisenheimer , K. and Miziarski , S. and Nikoloudakis , N. and Prada , L. F. and Rohloff, R.-R. and Shanks , T. and Sharples, R. M. and Wagner , K. **XMS and NG1dF: extreme multiplex spectrographs for wide-field multi-object spectroscopy**,
2010, Society of Photo-Optical Instrumentation Engineers Conference Series, 7735, 77351Q

Chapter 2 has been submitted in the form of a paper and accepted for publication

- Nikoloudakis, N., Shanks, T., Sawangwit, U., **Clustering analysis of high-redshift luminous red galaxies in Stripe 82**,
2013, MNRAS, 410, 241

Chapter 3 will be submitted in the form of a paper in MNRAS

- Nikoloudakis, N., Shanks, T., **Spectroscopy of high-z Stripe 82 LRGs**

Chapter 4 will be submitted in the form of a paper in MNRAS

- Nikoloudakis, N., Shanks, T., and the UltraVISTA Consortium, **Revealing the early Universe: counts and clustering of Distant Red Galaxies in UltraVISTA**

The major part of the work presented on this thesis is the author's own work except where specifically noted in the text, as summarised bellow :

- The halo model software featured in Chapters 2 and 3 is a adopted from the code provided by Dr. Utane Sawangwit

- The computer code used in the cross-correlation correction techinique of the observational parameters (Chapter 2) was adopted from the code originally written by Prof. Tom Shanks.

Acknowledgements

Chapter 1

Introduction

1.1   Understanding our Universe

Since the early days of Cosmology, various models that characterize our Universe have been proposed. The most prominent model of modern Cosmology, is the "Standard Cosmological Model" that describes an isotropic and homogeneous universe, that is in excess of 80 per cent of some exotic form of matter, the *dark matter* and the source of cosmic acceleration is best described by *dark energy*. All these characteristics of our Universe are enclosed within the flat Λ Cold Dark Matter $- \Lambda$CDM model paradigm. Observations of the cosmic structure over last 30 years, had a major influence in establishing the origin and the evolution of our Universe. There are two main probes, from where we can get insight for the current cosmological model; the Cosmic Microwave Background (CMB) radiation and the Large-Scale Structure (LSS) of the Universe.

The former has been studied first by the Cosmic Background Explorer (COBE) satellite, while later measurements from the Wilkinson Microwave Anisotropy Probe (WMAP) satellite (Spergel et al., 2003; Bennett et al., 2003), mapped with higher precision the temperature fluctuations of the CMB across the sky, while the third-generation mission dedicated to CMB measurements is the Planck mission (Planck Collaboration et al., 2013). The CMB at present has a thermal black body spectrum with $T = 2.7K$ and its temperature anisotropy varies as $\Delta T/T = 10^{-5}$ (Smoot et al., 1992) (neglecting the larger component due to our motion with respect to CMB).

In first place, the Cosmic Microwave Radiation (CMR) was in thermal equilibrium with the primordial quarks and elementary particles (hot plasma). Until its first 380,000 years, the Universe was not transparent to the electromagnetic radiation, due to the scattering of photons with the free electrons. Baryons and radiation were coupled and so

the gravitational collapse of the baryons was impeded by the radiation pressure creating acoustic waves. At the epoch of recombination, at $redshift \sim 1100$, the Universe had cooled to a temperature near $3000K$, sufficiently cool for photons to decouple from baryons, as protons captured free electrons and formed atomic hydrogen. At the same time, the sound speed is reduced, so the propagation of the acoustic waves is frozen. The modes of maxima or minima of these acoustic waves are imprinted in the angular power spectrum of the CMB (Peebles & Yu, 1970). The scale the acoustic waves travelled to prior recombination, is set by the sound horizon, hence can be accurately estimated and provide the basis for constraints on cosmological parameters (Peebles & Yu, 1970; Sunyaev & Zeldovich, 1970; Bond & Efstathiou, 1984, 1987; Holtzman, 1989; Hu & Sugiyama, 1996; Eisenstein et al., 1998; Hu & Dodelson, 2002).

The observed anisotropies in the CMB, provide crucial evidence that our Universe started from a hot and dense singularity after which it started expanding and cooling. The inflationary phase of the Universe has been proposed by Guth (1981). Evidence of the late time accelerated expansion by the cosmological constant Λ, are inferred through measurements of type Ia supernovae, where type Ia SNe act as *standard candles* to probe the luminosity-distance relationship (Riess et al., 1998; Perlmutter et al., 1999). The CMB radiation along with the light-elements abundance that we can observe today, argues even more that the Universe is the result of the Hot Big Bang.

On the other hand, the picture of the late Universe, the Large-Scale Structure, grows from the seeds of the primordial quantum fluctuations that we observe in the CMB background. With the term LSS, we refer to the *cosmic web* that consist of: galaxies, groups of galaxies, clusters, super-clusters, filaments, sheets and voids. While the initial fluctuations were small in amplitude, under gravitational instability, these Gaussian perturbations started to become denser and amplified to the gravitationally bound objects that we see today.

As galaxies are the (visible) building blocks for the rest, the most vital observations of Observational Cosmology have focused in mapping their three-dimensional positions in space and statistically interpreting their observables. From their spatial distribution, information for the properties of cosmic matter can be inferred, while their evolution with

time depends on the cosmological parameters. The gathering of the galaxy distribution information is achieved with galaxy surveys. It was since the time of Hubble when spatial distribution measurements had been introduced (i.e. Hubble, 1934; Carpenter, 1938), while later on, the first two-dimensional maps were the Palomar (Abell, 1959) and the Lick (Doughty et al., 1974) angular surveys. It goes back to those times, when the nature of the observed clumpy structure in the galaxy distribution could not be anticipated (Zwicky, 1952; de Vaucouleurs, 1958; Abell, 1961).

The modern state of the art complete surveys are the two degree Galaxy Redshift Survey (2dFGRS; Colless et al., 2001, 2003) with $\sim 10^5$ redshifts, $b_j < 19.5$ covering $1700\mathrm{deg}^2$ and the Sloan Digital Sky Survey (SDSS; York et al., 2000) with $\sim 10^6$ redshifts covering $10000\mathrm{deg}^2$. The large-scale clustering of galaxies based on data from these two surveys, were the first to measure the Baryon Acoustic Oscillations (BAO) features in the matter distribution, which have the same physical origin as the acoustic peaks in the CMB power spectrum. BAO appear as an single enhancement in the two-point correlation function or as wiggles in the power spectrum. The first clear BAO detection was in the correlation function of Luminous Red Galaxies in the SDSS survey at the comoving scale of $\sim 110 h^{-1}\mathrm{Mpc}$ (Eisenstein et al., 2005), which corresponds the sound horizon at that particular epoch (Eisenstein et al., 1998). The BAO in the matter power spectrum have different phases from the features in the CMB spectrum and a smaller amplitude, as baryons account only for approximately 20 per cent of the total mass in the Universe (Sugiyama, 1995; Eisenstein et al., 2005; Meiksin et al., 1999; Percival et al., 2010).

Measurements of the BAO scales at various epochs can be used as standard rulers to constrain the expansion history and the matter-energy content of the Universe (Blake & Glazebrook, 2003). The apparent size of the BAO depends on the equation of state of the dark energy and the curvature of the Universe, thus provides an estimate of the angular diameter distance at that particular epoch. BAO are key observations for ΛCDM model and we can obtain meaningful constraints if BAO measurements are combined with other probes. If BAO and SNe are combined with CMB data, to break the degeneracies by using CMB data alone (i.e. Bond et al., 1997; Efstathiou & Bond, 1999; Bridle et al., 2003), we can accurately determine the cosmological parameters and the content

of the Universe (Jungman et al., 1996; Riess et al., 1998; Perlmutter et al., 1999; Knox & Page, 2000; Hu & Dodelson, 2002; Percival et al., 2002; Bennett et al., 2003; Spergel et al., 2003; Riess et al., 2004; Tegmark et al., 2004b; Hinshaw et al., 2007; Wood-Vasey et al., 2007; Spergel et al., 2007; Dunkley et al., 2009; Komatsu et al., 2009, 2011).

The estimated contributions to the cosmic density, as derived from the 7-year WMAP data by Komatsu et al. (2011) in combination with clustering measurement data are $\Omega_{0,m} = 0.272$ for matter, $\Omega_{0,\Lambda} = 0.728$ for the cosmological constant and $\Omega_{0,b} = 0.044$ for baryons. Recent results from Planck mission measured $\Omega_{0,m} = 0.3175$, $\Omega_{0,\Lambda} = 0.6825$ and $\Omega_{0,b} = 0.048$, respectively (Planck Collaboration XVI et al., 2013a). The meaning of these quantities will be explained in the following discussion.

1.2 The Cosmological Principle and the Universe's Observables

The Cosmological Principle stands for the assumption that our Universe is homogeneous and isotropic; that has constant density and it looks the same in every direction. This hypothesis applies for the large scales, because if ones looks nearby objects like our solar system, our galaxy or even a galaxy cluster might lead to the conclusion that this approximation is wrong. In recent years, galaxy surveys have confirmed that homogeneity exists at large scales (Wu et al., 1999; Yadav et al., 2005).

1.2.1 The FRW metric

As an alternative description of the Cosmological Principle, we can have a fundamental observer at each location in space, to whom the Universe appears isotropic (Mo et al., 2010). In this way the observer defines a cosmological rest-frame, as the existence of two observers in the same point with a relative motion, would not allow them to observe the universe around them as isotropic. The isotropic and homogeneous Universe can be well described in Einstein's theory of general relativity using the Friedmann-Robertson-Walker[1] (FRW) metric of space-time:

$$ds^2 = c^2 dt^2 - \alpha^2(t) \left[\frac{dr^2}{1 - Kr^2} + r^2(d\theta^2 + sin^2\theta d\phi^2) \right], \tag{1.1}$$

---

[1]It has been developed independently from Friedmann (1922), Robertson (1935) and Walker (1937)

where c is the speed of light, $\alpha(t)$ is the scale factor, t is the proper-cosmic time of the fundamental observer, r, θ, ϕ are comoving coordinates and the constant K, the spatial curvature of the Universe. K can take values : 0, +1 or -1 by choosing an appropriate scaling of r. The proper distance between any two fundamental observers can be de written as :

$$l = \alpha(t) \int_0^{r_1} \frac{dr}{\sqrt{1 - Kr^2}} = \alpha(t)\chi(r_1), \tag{1.2}$$

where

$$\chi(r) = \begin{cases} sin^{-1}r & (K = +1, \ Closed \ Universe) \\ r & (K = 0, \ Flat \ Universe) \\ sinh^{-1}r & (K = -1, \ Open \ Universe). \end{cases} \tag{1.3}$$

1.2.2   Friedmann equations

For a universe that obeys the Cosmological Principle we can apply the Einstein field equation to the FRW metric and link $\alpha(t)$ and K to the matter/energy content of the Universe:

$$R_{\mu\nu} - \frac{R}{2}g_{\mu\nu} + g_{\mu\nu}\Lambda = \frac{8\pi G}{c^4}T_{\mu\nu}, \tag{1.4}$$

where $R_{\mu\nu}$ is the Ricci tensor (the contraction of curvature tensor), R the curvature scalar, $g_{\mu\nu}$ is given by the RW metric tensor , $T^{\mu\nu}$ the energy-momentum tensor of the matter field and Λ is the cosmological constant that Einstein defined for a static universe. The matter in the standard model of cosmology can be described as a perfect isotropic fluid with a matter-energy density ρ and a pressure P. The evolution of ρ is related with p through the equation of state, $p = w\rho c^2$, where w depends on the fluid nature as we will see later. Finally we obtain the solutions, which are usually referred to as Friedmann equations :

$$\frac{\ddot{\alpha}}{\alpha} = -\frac{4}{3}\pi G\left(\rho + \frac{3\rho}{c^2}\right) + \frac{\Lambda c^2}{3}, \tag{1.5}$$

$$\left(\frac{\dot{\alpha}}{\alpha}\right)^2 = \frac{8}{3}\pi G\rho - \frac{Kc^2}{\alpha^2} + \frac{\Lambda c^2}{3}. \tag{1.6}$$

The over-dot denotes the derivative with respect to t and G is the gravitational constant. The factor $\dot{\alpha}/\alpha$ is the expansion rate of the universe, otherwise the Hubble parameter H. Its value today is known as the Hubble constant $H_0 \equiv \dot{\alpha_0}/\alpha_0$. Hubble with his observations came across with one of the most revolutionary conclusions for modern Cosmology: that the galaxies are moving away from us with a recession velocity that is proportional to their distance from us[2]. This is the Hubble law (Hubble, 1929), a linear relation that is written as :

$$u = H_0 r. \tag{1.7}$$

Usually quantities that depend on the value of H_0 are conveniently expressed in terms of the parameter :

$$h \equiv \frac{H_0}{100 kms^{-1}Mpc^{-1}}, \tag{1.8}$$

as "a dimensionless number parametrizing our ignorance" (Hogg, 1999). The current value for Hubble's constant from WMAP data alone is $H_0 = 71.0 \pm 2.5 kms^{-1}Mpc^{-1}$ and $H_0 = 70.4^{+1.3}_{-1.4} kms^{-1}Mpc^{-1}$ when CMB data are incorporated with BAO and H_0 priors from Hubble Space Telescope (Jarosik et al., 2011). Hubble's constant can also be derived via calibrations of the magnitude-distance relationship from optical observations of "Standard Candles" such as type Ia SNe (i.e. Freedman et al., 2001) or Cepheid variables (i.e. Tanvir et al., 1999). The latest accurate measurement obtained from this kind of observations is with the HST of over 600 Cepheid variables is $H_0 = 73.9 \pm 2.4 kms^{-1}Mpc^{-1}$ (Riess et al., 2011).

Before continuing further, we need to introduce a basic phenomenon that has contributed significantly in the development of Observational Cosmology; the Doppler effect. This phenomenon takes place during change in the frequency of a wave for an observer moving relative to the source. The Doppler interpretation is also applied to the light that has been emitted from the receding galaxies, which has a fractional doppler shift due to their radial motion expressed via :

$$\frac{u}{c} = \frac{\lambda_{obs} - \lambda_{rest}}{\lambda_{rest}} \equiv z, \tag{1.9}$$

---

[2]Lemaitre two years before Hubble had already predicted that for an accelerating universe (Lemaître, 1927).

where c is the speed of light, u is the recession velocity, λ_{rest} is the wavelength of the photon in the rest frame of the galaxy, λ_{obs} is the observed wavelength and z is the *redshift*. This relationship holds for nearby galaxies where $u \ll c$ and we interpret their redshift as their recession velocity.

But as the emitted light form a galaxy is stretching trough the expanding space, we can relate the wavelength change to the scale factor through the FRW metric as :

$$\frac{\lambda_{obs}}{\lambda_{rest}} = \frac{\alpha_0}{\alpha_{em}}, \tag{1.10}$$

where t, em is the time that the light was emitted from the galaxy. From Eq. 1.9 and Eq. 1.10 we can directly relate z to α :

$$\alpha = \frac{1}{1+z}, \tag{1.11}$$

where the present value of the scale factor, a_0, has been normalized to unity. We will adopt the same normalization on the formalisms that follow next.

Differentiation of Eq. 1.5 with respect to proper time t we obtain (Dodelson, 2003):

$$\dot{\rho} = -3\frac{\dot{\alpha}}{\alpha}\left(\rho + \frac{p}{c^2}\right), \tag{1.12}$$

Introducing the equation of state at Eq. 1.12 by assuming for simplicity that w is independent of time, results to :

$$\rho \propto \alpha^{-3(1+w)} \tag{1.13}$$

w can be $0, 1/3$ and -1 if the universe contains non-relativistic matter/dust, ultra-relativistic matter/radiation and the cosmological constant/vacuum energy, respectively. In case where the universe is made up from different kind of fluids, the Friedmann equation still stands if the different components do not interact with each other. The total energy-density of the universe is given by :

$$\rho = \sum_{i=1}^{N} \frac{\rho_{i,0}}{\alpha^{3(1+w_i)}}, \tag{1.14}$$

where the $\rho_{i,0}$ is the present energy-density of the i-th component. Thus, for the present time the Friedmann equation can be expressed as:

$$H^2(t) = \frac{8\pi G}{3}\left[\rho_{m,o}\left(\frac{\alpha_0}{\alpha}\right)^2 + \rho_{r,o}\left(\frac{\alpha_0}{\alpha}\right)^4 + \rho_{\Lambda,o}\right] - \frac{Kc^2}{\alpha^2}, \tag{1.15}$$

where $\rho_\Lambda \equiv \Lambda c^2/8\pi G$. This relationship requires no transformation between the different components, otherwise the equation of state becomes time dependent.

1.2.3 Densities of the Universe

There is a critical density for the Universe, that corresponds to a spatially flat space ($K = 0$) at time t given by:

$$\rho_{crit,t} = \frac{3H(t)^2}{8\pi G}. \tag{1.16}$$

We can specify the density of the Universe by defining the density parameter for radiation, dust and cosmological parameter as:

$$\Omega_{m,t} \equiv \frac{\rho_{m,t}}{\rho_{crit,t}}, \Omega_{r,t} \equiv \frac{\rho_{r,t}}{\rho_{crit,t}}, \Omega_{\Lambda,t} \equiv \frac{\rho_{\Lambda,t}}{\rho_{crit,t}}. \tag{1.17}$$

Substituting Eqs. 1.17- 1.16 to Eq. 1.15, the Friedmann equation for the present time can be evaluated as:

$$\frac{8\pi G}{3}\rho_{\Lambda,0} = H_0^2 \left[1 - \Omega_{m,0} - \Omega_{r,0}\right] + \frac{Kc^2}{\alpha_0^2}. \tag{1.18}$$

Consequently, the curvature of the Universe is determined by the total matter density:

$$\Omega_{K,0} \equiv 1 - \Omega_0 = -\frac{Kc^2}{H_0^2}, \tag{1.19}$$

where $\Omega_0 = \Omega_{m,0} - \Omega_{r,0} - \Omega_{\Lambda,0}$.

Finally, if we know the present values for Ω_m, Ω_r, Ω_Λ and H, we can estimate their values at any redshift, via the Friedmann's equation as is re-expressed with the help of Eq. 1.12, Eq. 1.19:

$$H(z) \equiv \left(\frac{\dot{\alpha}}{\alpha}\right)(z) = H_0^2 \left[\Omega_{\Lambda,0} + (1 - \Omega_0)(1 + z)^2 + \Omega_{m,0}(1 + z)^3 + \Omega_{r,0}(1 + z)^4\right]^{1/2} \tag{1.20}$$

When the total matter density is equal to the critical density, $\Omega_0 = 1$, the universe is flat. In case where $\Omega_0 < 1$, that results to an open universe, with negative curvature and finally if the universe's density is $\Omega_0 > 1$ occurs to a positively curved closed universe.

By tracking down the expansion history of the Universe with Eq. 1.20, we can provide estimates of the cosmological parameters. Objects with known intrinsic luminosity or

proper size, can be used to measure directly their luminosity distance (D_L) or angular-diameter distance (D_A). D_L measurements involve objects such as "Standard Candles" i.e. type Ia SNe (Perlmutter et al., 1999; Riess et al., 1998), while the technique of D_A involves objects namely known as "Standard Rulers" i.e. BAO (Blake & Glazebrook, 2003; Eisenstein et al., 2005; Percival et al., 2010). The relationship that connects the measurements of the distance scales with $H(z)$ is given by:

$$D_A(z) = \frac{D_L(z)}{(1+z)^2} = \frac{r}{1+z} = \frac{c}{(1+z)H_0\sqrt{|\Omega_K|}} f_K \left[H_0\sqrt{|\Omega_K|} \int_0^z \frac{dz'}{H(z')} \right], \quad (1.21)$$

where

$$f_K(\chi) = r = \begin{cases} sin\chi & (K = +1) \\ \chi & (K = 0) \\ sinh\chi & (K = -1). \end{cases} \quad (1.22)$$

1.3 Quantifying Large-Scale Structure

1.3.1 Hierachical Structure Formation

Within the ΛCDM framework, the Large-Scale Structure that we observe in the local Universe, is the seed of the primordial fluctuations. In the early Universe, when perturbations are in the linear regime, their density contrast is $\delta = (\delta\rho)/\bar{\rho} = (\rho - \bar{\rho})/\bar{\rho} \ll 1$, where $\bar{\rho}$ is the mean density of the Universe. As these regions have initially higher density than the mean, they will attract more matter and become denser. The density perturbations grow up through gravitationally instability, and according to linear theory as $\delta(z) = D(z)\delta_0$, where $D(z)$ is the linear growth factor (Carroll et al., 1992).

Once the fluctuations reach the critical overdensity, (in ΛCDM model is $\delta_c \equiv 1.686$ for spherical collapse), the fluctuations stop growing and start collapsing until they form non-linear virialised dark structures, the dark matter haloes. When the baryons are concentrated in the potential wells of the newly formed dark matter haloes, the first stars and galaxies are formed, the galaxy formation progress has been triggered. These haloes following the theory of *hierarchical structure formation* will continue to grow in mass and

build up more massive galaxies, either by accretion of nearby material or via merging with other haloes (White & Rees, 1978; White & Frenk, 1991; Lacey & Cole, 1993).

1.3.2 Galaxy Surveys

Galaxy surveys are sophisticated probes for mapping the locations and properties of galaxies over a large volume, with ultimate aim to trace the matter distribution in the Universe (see Fig. 1.1). By combining observations and galaxy statistics we are in position to explain even more the Large-Scale Structure properties and further constrain the ΛCDM paradigm. Galaxy surveys are categorized into two types: redshift surveys and angular surveys. While angular surveys measure only the two-dimensional projection of the galaxies in the sky, redshift surveys on the other hand, also measure their third dimension, the galaxy distance in the valid direction via their redshift and Hubble's law.

The first wide-angle redshift survey was the Center for Astrophysics Redshift Survey (CfA; Davis et al., 1982). Following large galaxy surveys were the Automatic Plate-measuring Machine (APM; Maddox et al., 1990), the Southern Sky Redshift Survey (SSRS1; da Costa et al., 1991) and Las Campanas Redshift Survey (LCRS; Shectman et al., 1996). The latter survey, was a breakthrough for the progress in redshift surveys, as it combined wide-field optical imaging and multi-object spectrogragphs. The optical window of observations is limited to high galactic latitudes due to the zone of avoidance, hence one needs to extend even further the sky coverage with observations at the near-infrared (NIR) wavebands. Examples of the first large near-infrared surveys based on the Infrared Astronomy Satellite (IRAS; Strauss et al., 1992) were: the 1.2 Jy IRAS survey (Fisher et al., 1995), the QDOT survey (Saunders et al., 1990) and the PSCz survey (Saunders et al., 2000). Clustering measurements from those early surveys, when fitted with various cosmological models, were indicating a low matter density universe, $\Omega_m < 1$, providing evidence towards the standard model (Efstathiou et al., 1990; Saunders et al., 1991; Peacock & Dodds, 1994).

There are numerous other surveys, smaller, deeper, at various wavelengths, that have contributed dramatically to our understanding through observations of the visible Universe. The galaxy survey design each time, reflects the type of studies that needed to

carried out.

With improvements in technology, it is feasible to have large telescopes with high angular resolution, CCD cameras with Gigapixels of resolution and instruments in the optical and NIR ranges that can simultaneously target thousands of objects. There are a number of ongoing/upcoming ground-based, space-based surveys with multiwavelength coverage in the north or the south sky that will mark a new era in Cosmology: the Baryon Oscillation Spectroscopic Survey (BOSS; Schlegel et al., 2007) , the Dark Energy Survey (Flaugher, 2005), DESpec (Abdalla et al., 2012), the Visible and Infrared Survey Telescope for Astronomy (VISTA; McPherson et al., 2004), the VST-ATLAS[3], the Panoramic Survey Telescope and Rapid Response System (Pan-STARRS; Kaiser & Pan-STARRS Project Team, 2004), the Large Synoptic Survey Telescope (LSST; Tyson, 2002), the 4-metre Multi-Object Spectroscopic Telescope (4MOST; de Jong, 2011), the Subaru Measurement of Images and Redshifts (SuMIRe; Vivès et al., 2012), the Dark Energy Spectroscopic Instrument (DESI; Levi et al., 2013) and the EUCLID survey (Laureijs et al., 2011). All these spectroscopic and imaging surveys will cover tens to hundreds of square degrees at unique depths and by allowing us to extract as much cosmological information from them as possible, will advance our knowledge of galaxy formation and evolution.

1.3.3 Colour Selection Techniques

Measuring spectroscopic redshifts of distant faint galaxies ($z > 1$ with ∼25-26 magnitude), is a very time consuming task and even observations with the world largest 8-10m class telescopes (i.e. Very Large Telescope-VLT; Keck) are very non-trivial. Statistical studies of galaxy evolution require the minimum possible statistical uncertainty and need to sample large galaxy populations over large areas. There is clearly a need to isolate various types galaxies at different redshifts, using selection techniques based on the galaxy colours.

Efforts to estimate the galaxy redshift from photometry itself has been tried from early times (i.e. Baum, 1962). Consequently, redshift and angular surveys are linked,

---

[3]http://astro.dur.ac.uk/Cosmology/vstatlas/
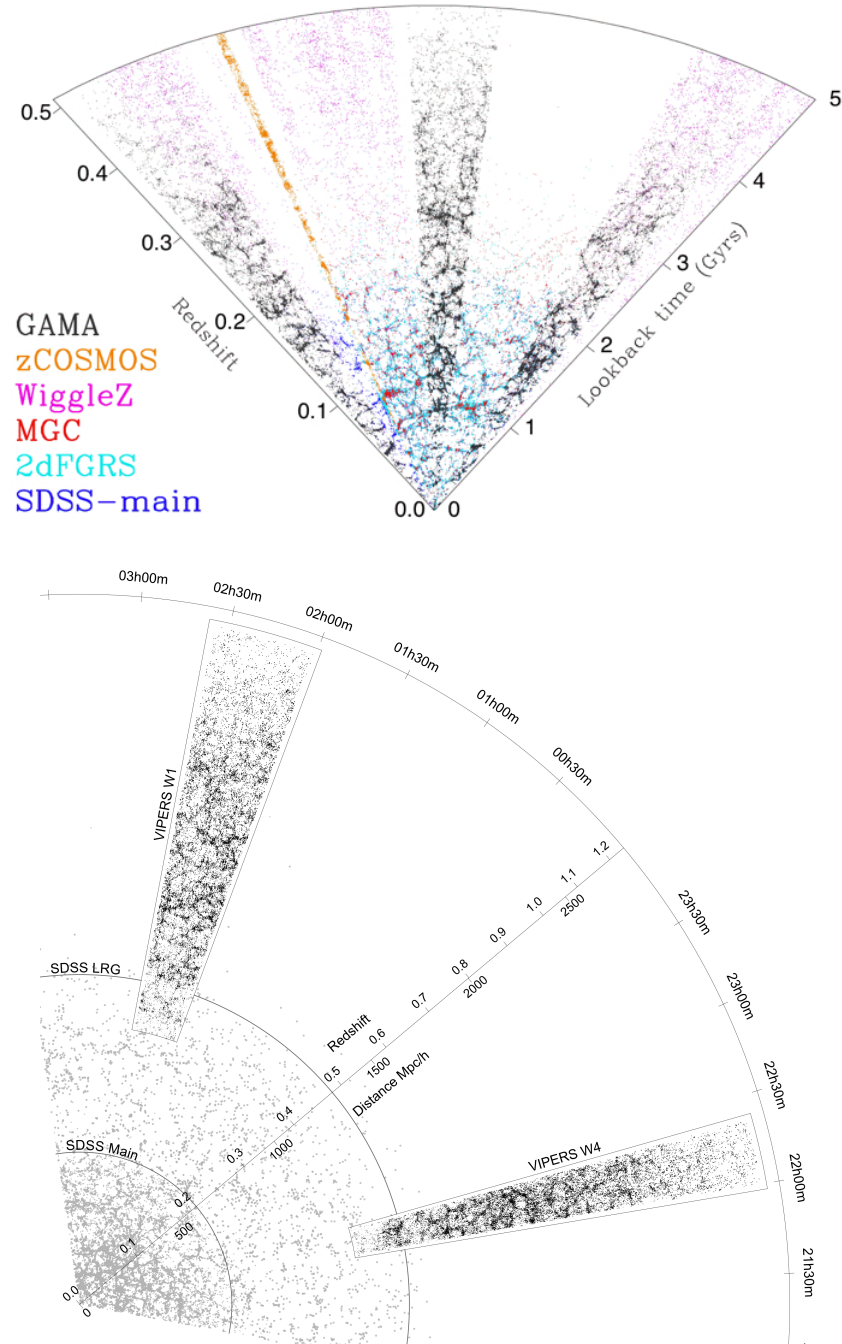
Figure 1.1: The Large-Scale Structure of the Universe footprint in a variety of galaxy surveys. (top) At $0.0 < z < 0.5$ we see a lookback time/redshift cone plot for a 2° wedge of sky ($1^o < \delta < +1^o$) showing data from the SDSS, 2dFGRS, Millenium Galaxy Catalogue (MGC; Liske et al., 2003), zCOSMOS (Lilly et al., 2007), WiggleZ and Galaxy and Mass Assembly (GAMA; Driver et al., 2011) surveys. Image credit: Driver et al. (2009). (bottom) Probing higher redshift regions $0.5 < z < 1.5$, we have again the SDSS main sample, the SDSS Luminous Red Galaxies (LRG; Eisenstein et al., 2001) samples (a 4° wedge is shown) and two deep fields from the VIMOS Public Extragalactic Survey (VIPERS; Fritz & Vipers Team, 2011). Image credit: Guzzo et al. (2013)

with what is nowadays referred to as *photometric redshift surveys*. Photometric redshift surveys measure galaxy fluxes in multiple wavebands, making possible to constrain the galaxy's spectral energy distribution (SED). Then, from comparison with galaxy templates, it is possible to identify spectral features on the SED, and finally to estimate the photometric redshifts (photo-z's). Galaxy templates are usually generated from spectral synthesis models (Bruzual & Charlot, 2003). SED template fitting and the photo-z's estimations are derived via photometric redshift codes (see Abdalla et al., 2011, for codes comparison).

The emitted light from galaxies depend on the stellar populations and more specifically on their age. Young stars, have higher temperatures and show strong UV emission compared to the old stellar populations (K-stars) which have low surface temperature and emit at longer wavelengths. The basic idea is to track down the broad features of the galaxy's SED such as: the 4000Å break or the Lyman limit discontinuity at 912Å as evolve with redshift on the colour-colour space. The Lyman break technique has been very successful colour selection method, to identify star-forming galaxies at $z > 3$ (Steidel et al., 1996). Similarly the 4000Å feature, is the key spectral feature for early-type passive galaxy and has prominently selected Luminous Red Galaxies (LRGs; Eisenstein et al., 2001; Padmanabhan et al., 2005; Blake et al., 2007; Cannon et al., 2006; Collister et al., 2007; Ross et al., 2008b) out to redshift $z \sim 0.8$. With analogous *drop-out* techniques certain classes of objects have been distinctively distinguished to: Emission-Line Galaxies (ELGs; Drinkwater et al., 2010), Distant Red Galaxies (DRGs; Franx et al., 2003) and Quassi-Stellar Objects (QSOs; Shanks et al., 2000).

Simple optical colours clearly set low redshift massive populations, i.e $g - r$ versus $r - i$ for LRGs (Eisenstein et al., 2001; Cannon et al., 2006; Ross et al., 2008b), whereas if detection at higher redshift is needed, a combination of optical and near-IR colours is essential as the emission from the old star populations is redshifted into the near-IR regime. A good example is the high redshift massive galaxies that can be selected through the $J - K > 1.3$ colour cut in AB magnitudes. This JK colour cut selects DRGs that occupy the redshift range $1 < z < 2$ (Franx et al., 2003). Other DRG studies though, have found that this population does not consist of early-types only, but from
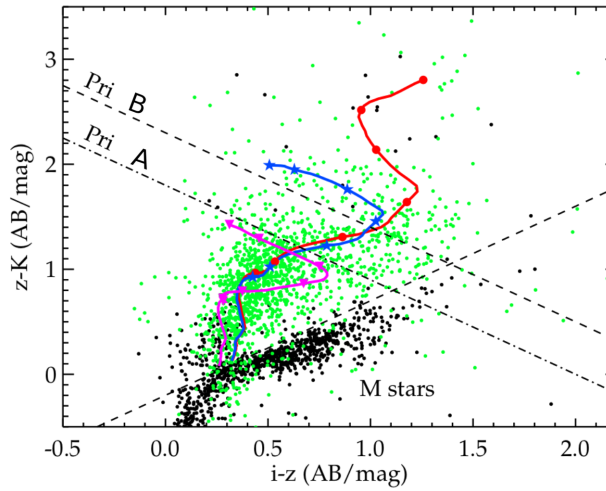
Figure 1.2: *iz* vs *zK* colour-colour plot that selects LRGs at $z \sim 1$ from Nikoloudakis et al. (2013). Evolutionary tracks for single burst (red line) and $\tau = 1\mathrm{Gyr}$ (blue line) are overplotted from $z = 0$ to 1.6 with symbols indicate z interval of 0.2. The evolutionary track of late type galaxies (magenta line) is also shown for comparison.

star forming galaxies too. Moreover, optical and near-IR colour cuts can be applied just to filter objects in redshift ranges.Daddi et al. (2004) used the $B - z$ versus $z - K$ cuts to distinguish galaxies at $z > 1.4$. Yet, this population can be furthermore divided into passive and star forming galaxies (pBzK and sBzK, respectively).

Colour selection is a key process that has been used in large surveys for cosmological applications. Eisenstein et al. (2005) used colour selections to spectroscopically follow up 40,000 LRGs in SDSS, and measured the Baryon Acoustic Oscillation features in galaxy clustering. In Chapter 2, for first time we introduce an optical and near-IR combination, izK, in SDSS Stripe 82 to effectively select $z \sim 1$ LRGs (see Fig. 1.2). In Chapter 3 we will present results from spectroscopic observations for a subsample of the Stripe 82 LRGs, which support even more that this colour selection characterizes efficiently this high-z population. Large cosmological surveys now favour of similar colour selections to select high-z LRGs, i.e. DES survey ($grizY$ filters) (Abdalla et al., 2012) and VST ATLAS ($ugriz$ filters) by taking advantage the overlap with VHS survey (JHK filters), will map thousands of high-z LRGS in order to probe dark energy.

1.3.4 Galaxy Clustering

Galaxy surveys provide us with catalogues of positions of galaxies, where these realizations can be considered either a homogeneous random point process (Neyman & Scott, 1952) or sets of points of an underlying continuous distribution (Rubin, 1954; Limber, 1954). The second approach is involving the correlation functions, which is the most common statistical tool in galaxy clustering studies. Totsuji & Kihara (1969) first introduced the correlation functions to describe the angular clustering of galaxies and its evolution with redshift and magnitude. The low order correlation functions, the two-point correlation function and its Fourier transform, the power spectrum, have been established in galaxy statistics with the pioneering studies of Yu & Peebles (1969), Peebles (1973) and Peebles & Hauser (1974).

Galaxy clustering depends on the internal properties of galaxies such as morphology (i.e. Hubble, 1936; Zwicky et al., 1968; Davis & Geller, 1976; Dressler, 1980; Postman & Geller, 1984; Guzzo et al., 1997; Willmer et al., 1998; Zehavi et al., 2002; Goto et al., 2003), luminosity (i.e. Davis et al., 1988; Hamilton, 1988; Park et al., 1994; Loveday et al., 1995; Benoist et al., 1996; Guzzo et al., 1997; Norberg et al., 2001; Zehavi et al., 2002, 2005b; Coil et al., 2006, 2008), colour (i.e. Willmer et al., 1998; Brown et al., 2000; Zehavi et al., 2002, 2005b; Coil et al., 2008), and spectral type (i.e. Norberg et al., 2002; Budavári et al., 2003; Madgwick et al., 2003).

To define the two-point correlation function, first one needs to consider two infinitesimal cells of volumes δV_1 and δV_2, separated by a vector $\mathbf{r}$. Then, the joint probability of finding one galaxy in each of these volumes is:

$$\delta P = n^2[1 + \xi(r)]\delta V_1 \delta V_2, \tag{1.23}$$

where n is the mean number density of galaxies and $\xi(r)$ is the *two-point spatial correlation function*. Under the assumption of homogeneity and isotropy of the density field/galaxy distribution, ξ depends only on the separation $\mathbf{r}$ alone. If the galaxy distribution is totally random (uniform random Poisson) that means that there is no correlation between the galaxies, $\xi = 0$, and the probability excess is given by the terms outside the brackets of Eq. 1.23. If galaxies are clustered then $\xi(r) > 0$ while $\xi < 0$ if galaxies are anti-correlated

at these scales.

The majority of the deep available galaxy catalogues have measured only the angular positions of galaxies in the sky. To perform clustering analysis in two dimensions (2-D), we require the equivalent of the spatial correlation function at two dimensions, that is the two-point angular correlation function, $w(\theta)$. In analogy to Eq. 1.23, in 2-D the probability of finding one galaxy in two small elements of solid angle $\delta\Omega_1$ and $\delta\Omega_2$, separated by an angle θ is given by:

$$\delta P = n^2[1 + w(\theta)]\delta\Omega_1\delta\Omega_2, \tag{1.24}$$

where n is the mean number of objects and $w(\theta)$ is the two-point angular correlation function.

For two-point correlation functions, either spatial or angular versions, various estimators have been introduced and applied to data. The fundamental one, is the natural estimator (Peebles & Hauser, 1974). The natural estimator employs a random catalogue of points/galaxies with the same geometry and selection function as the parent catalogue of the real data and is defined in the spatial case (3-D) as:

$$\xi(r) = \frac{N_{rd}}{N}\frac{DD(r)}{DR(r)} - 1, \tag{1.25}$$

where N_{rd} is the number of the random points, N is the number of the galaxies and $DD(r)$, $DR(r)$ is the number of galaxy and random-galaxy pairs in the interval $[r, r+dr]$, respectively. As the majority of the clustering studies presented in this thesis are referring to angular galaxy surveys, in Chapter 2 we will have a more extended discussion of the angular correlation function estimators and their variances.

The spatial and the angular two-point correlation function have a very simple relationship between them, hence making correlation functions even more fashionable tools to study the statistics of galaxies. Even if the redshift of individual galaxies is not available, the 3-D clustering information can yet be recovered using Limber's equation (Limber, 1953), which can relate the spatial correlation length, r_0, to the angular correlation length θ_0 of the $w(\theta)$ given the $n(z)$ and the selection function of the sample. The original scaling idea of Limber's, applies only for shallow samples where the curvature and evolution effects are not strong. Following Phillipps et al. (1978), we can define the rela-

tivistic generalization of Limber's equation as:

$$w(\theta) = \frac{\int_o^\infty dz_1 \chi(z_1)^2 (\frac{d\chi(z_1)}{dz_1})\phi(z_1)n(z_1) \int_0^\infty dz_2 \chi(z_2)^2 (\frac{d\chi(z_2)}{dz_2})\phi(z_2)n(z_2)\xi(r)}{\int_0^\infty \chi^2(\frac{d\chi}{dz})\phi(z)n(z)dz} \qquad (1.26)$$

where $\phi(z)$ is the galaxy selection function, $n(z)$ the comoving number density of the galaxies, χ is the radial comoving distance and the comoving distance between two galaxies, r, for a spatially flat cosmology is

$$r = \sqrt{\chi(z_1)^2 + \chi(z_2)^2 - 2\chi(z_1)\chi(z_2)cos\theta} \qquad (1.27)$$

Totsuji & Kihara (1969) were the first to adopt a power-law description for the spatial correlation function $\xi(r) = (r/r_0)^{-1.8}$ with $r_0 = 4.7h^{-1}\text{Mpc}$ by analyzing the angular catalogue Shane-Wirtanen from Lick survey and using Limber's equation. Other measurements have found that at scales $0.1 \leq r \leq 10h^{-1}Mpc$, the amplitude of the correlation function varies but the power-law slope γ, does not change and is $\gamma \simeq 1.8$ (Davis & Peebles, 1983; Shanks et al., 1989; Zehavi et al., 2002). At larger scales, $r > 30h^{-1}\text{Mpc}$ the $\xi(r)$ tends rapidly to zero, hence making it very difficult to make any measurements above the statistical noise. The equivalent power-law expression of the angular correlation function is: $w(\theta) = A\theta^{1-\gamma}$. The quantity r_0 for which ξ becomes unity, roughly defines the transition between the linear and the non-linear regimes.

Since the initial fluctuations are described by a Gaussian random field, it is more convenient to describe the flat comoving geometry of the Universe in the Fourier space. Due to isotropy and homogeneity, all the moments are invariant under translation and rotation and the density perturbation field can be Fourier transformed as:

$$\delta(\mathbf{k}) = \int \delta(\mathbf{x})e^{(i\mathbf{k}\cdot\mathbf{r})}d^3x, \qquad (1.28)$$

where $\mathbf{k}$ is the wave vector of the Fourier mode. The second moment, is very important as contains the power spectrum of the perturbation field, $P(k)$:

$$\langle \delta_\mathbf{k}\delta_{\mathbf{k'}} \rangle \equiv (2\pi)^3 \delta_D(\mathbf{k\text{-}k'})P(k), \qquad (1.29)$$

where δ_D is the Dirac function and $k = |\mathbf{k}|$. Another important moment is the expression of the two-point spatial correlation function :

$$\xi(\mathbf{r}) \equiv \langle \delta(\mathbf{x})\delta(\mathbf{x+r}) \rangle, \qquad (1.30)$$

where the angle brackets indicate an averaging over the normalization volume.

The power spectrum, $P(k)$, is the Fourier counterpart of the correlation function :

$$P(\mathbf{k}) = \int \xi(\mathbf{r}) e^{i\mathbf{k}\cdot\mathbf{r}} d^3 r, \tag{1.31}$$

where k is wavenumber related to r by $r = 2\pi/k$ and the inverse relation assuming isotropy in three dimensions is:

$$\xi(\mathbf{r}) = \int P(\mathbf{k}) e^{-i\mathbf{k}\cdot\mathbf{r}} \frac{d^3 k}{(2\pi)^3}. \tag{1.32}$$

The power spectrum is a more natural quantity as it directly measures the amplitude of density fluctuations at different length scales k and as it is also included in inflationary theories. The initial power spectrum is commonly assumed to be a power law:

$$P(k) \propto k^n, \tag{1.33}$$

where n is the spectral index and a popular choice is the scale-invariant spectrum of Zeldovich & Harrison with $n = 1$.

The power spectrum gives a more robust and direct measurement of the density field on large scales, whereas at those scales $\xi(r)$ is close to zero and the lack of precise knowledge of the mean density might increase the errors in the correlation function. In the power spectrum (as well as in the correlation function) is imprinted an important information that supports the ΛCDM model, the baryonic acoustic oscillations (BAO), which correspond to the the fingerprint of the size of the sound horizon, at the epoch of matter-radiation equivalence. In order to measure the power spectrum, we need large contiguous volumes and homogeneous samples. The two largest full completed key sky surveys, that started the era of precision cosmology are the 2dFGRS, SDSS. Both of these surveys had detected the BAO signal (Cole et al., 2005; Eisenstein et al., 2005), while recent measurements from WiggleZ and BOSS surveys have ascertained these features in their data (Blake et al., 2011; Anderson et al., 2012).

Observations have shown that different galaxies cluster differently (Dressler, 1980), where for instance early-type, red galaxies are more clustered compared to late-type, blue galaxies (Guzzo et al., 1997; Norberg et al., 2002; Madgwick et al., 2003; Conway

et al., 2005; Croton et al., 2007). Since galaxies are not exact tracers of the underlying mass distribution, the difference between the spatial distribution of galaxies and dark matter is characterized by :

$$\xi_g(r) = b^2 \xi_m(r), \tag{1.34}$$

where b is the scale-independent bias in the linear regime (Coles, 1993). As the galaxy formation process does not depend only on the local overdensities alone, Dekel & Lahav (1999) have developed a more general non-linear bias model. Observations in SDSS and 2dFGRS also found the luminosity dependent bias meaning that luminous galaxies are more strongly biased (Norberg et al., 2001, 2002; Tegmark et al., 2004a; Zehavi et al., 2005a) and the difference is more clear for galaxies with luminosity greater than the characteristic luminosity L_* of the Schechter luminosity function (Schechter, 1976).

Another approach for galaxy clustering statistics, is the Halo Occupation Distribution (HOD) model (see Cooray & Sheth, 2002, for a review), which actually has its roots in the approach of Neyman and Scott. The HOD model can be used to describe the galaxy distribution within the dark matter haloes, as N-body simulations or analytic methods can predict the formation and evolution of the dark matter haloes. The HOD model is a useful tool for interpreting the galaxy bias and non-linear clustering. The HOD model gives the probability $P(N|M)$, that N galaxies occupy a halo of mass M, given the halo mass function, halo density profile and halo bias. The HOD formalism as encodes the physics of galaxy formation, can be used to compare observations with semi-analytical galaxy formation models (Baugh, 2006)

In the HOD model, galaxies within a halo are separated into central and satellite galaxies. The galaxies pairs can either reside in the same halo (1-halo term) or distinct haloes (2-halo term). The former galaxy pairs dominate the correlation function at small scales while the latter pairs becomes dominant at larger scales. The HOD model power spectrum is then :

$$P(k) = P^{1h}(k) + P^{2h}(k) \tag{1.35}$$

It is obvious that the HOD model can tackle the non-linear regime at the level of virialised dark matter haloes, giving insight in the bias relation between galaxies and matter. The HOD model is used in Chapter 3 to fit the angular clustering measurements of

high redshift massive galaxies and there we will present a more analytic description of the HOD formalism.

1.3.5 Non-Gaussianity

Within the standard cosmological model, due to the single-field, slow-roll inflationary phase, it arises that the primordial density perturbations are nearly Gaussian (Guth, 1981). However, since the exact mechanisms driving inflation are not totally clear, recently it has been a surge in interest to study any departures from primordial Gaussianity (i.e. Bartolo et al., 2004a).

The common model to describe deviations from primordial Gaussianity is the so-called local model, which characterizes non-Gaussianity through the constant dimensionless parameter f_{NL} (Salopek & Bond, 1990; Verde et al., 2000; Komatsu & Spergel, 2001):

$$\Phi(x) = \phi_G(x) + f_{NL}(\phi_G(x)^2 - \langle \phi_G(x)^2 \rangle), \tag{1.36}$$

where Φ denotes the primordial curvature perturbation (Bardeen's gauge-invariant potential), $\phi_G(x)$ is a Gaussian random field and the degree of non-Gaussianity is parametrised by f_{NL}, that depends only on the local value of the potential.[4] Physically, a positive f_{NL} leads to a positive skewness in the density field (resulting to more rare objects) and negative skewness in the temperature field.

In order to study non-Gaussianity, we need explore higher order statistics such as bispectrum (the three-point function of the Fourier transform of eq. 1.36). For the standard slow roll inflation the typical value of f_{NL} is of the order of the slow roll parameter, 10^{-2} (Maldacena, 2003) but can become unity through the non-linear transformation of the observable (i.e. CMB temperature fluctuations) and the primordial field fluctuation (Bartolo et al., 2004b). Any detection of non-Gaussianity above unity will be a major finding, demanding further explanation of the inflationary paradigm. Current analyses of CMB measurements put tight constraints on the amount of allowed non-Gaussianity

---

[4]There are two conventions in the literature: the LSS convention where Φ is linearly extrapolated to $z = 0$ and the CMB convention that is it evaluated deep in the matter era. Here we use the CMB convention that is $f_{NL}^{LSS} \sim 1.3 f_{NL}^{CMB}$

with $f_{\mathrm{NL}}^{\mathrm{local}} = 32 \pm 21(1\sigma)$ (Komatsu, 2010), while the recent results from Planck measure $f_{\mathrm{NL}}^{\mathrm{local}} = 2.7 \pm 5.8(1\sigma)$ (Planck Collaboration XXIV et al., 2013).

Another direction for potential detection of Non-Gaussianity is with LSS observations (i.e. Matarrese et al., 2000; Scoccimarro et al., 2004; Dalal et al., 2008; Slosar et al., 2008; Xia et al., 2010a). Even if the initial fluctuations are Gaussian, the gravitational instability and the galaxy bias can produce non-linearities in the LSS, as if the primordial field is non-Gaussian. A small amount of non-Gaussianity can develop a detectable signature in LSS surveys, where then the clustering of dark matter haloes acquires a scale-dependent bias (Dalal et al., 2008):

$$b(k) = b_0 + \Delta b(k) = b_0 + f_{NL}(b_0 - 1)\delta_c \frac{3\Omega_m H_0^2}{\alpha g(\alpha)T(k)c^2 k^2}, \tag{1.37}$$

where b_0 is the Gaussian bias (constant on large scales), δ_c the collapse threshold, α the scale factor, Ω_m the matter density, H_0 the Hubble constant, $T(k)$ is the transfer function and $g(\alpha)$ is the growth suppression factor[5].

A positive f_{NL} results an imprint in the clustering pattern by enhancement of the overdensities as it is expected from a positively skewed distribution. The power spectrum of the distribution is modified at small wavenumbers due to the scale-dependent bias and offers a unique way of testing the nature of primordial fluctuations. Data from galaxies and quasars, where the scale-dependant bias has been applied, are compatible with strong limits from CMB measurements $f_{NL} = 53 \pm 25(1\sigma)$ and $f_{NL} = 58 \pm 24(1\sigma)$ from NVSS data and SDSS DR6 QSO data (Xia et al., 2010a). It is clear, that non-Gaussianity is emerging as a strong probe to distinguish between the various models describing the origins of the Universe.

1.4 This thesis

In this thesis, we present results regarding galaxy evolution and cosmology, with a main focus on massive galaxies at high redshift. As outlined above, our results are based on observations and the statistics of the LSS, using mainly the galaxy clustering. In Chapter

---

[5]The linear growth factor $D(\alpha)$, that is normalised to be α in the matter domination, is related to $g(\alpha)$ via $D(\alpha) = \alpha g(\alpha)/g(1)$, where $g(\alpha)$ is normalised to unity deep in the matter-dominated era.

2, we introduce eXtreme Multiplex Spectrograph (XMS), a proposed spectrograph that has been designed for classical 4-m wide field telescopes and multi-object observations. It is interesting to see, how competitive XMS' cosmological surveys are, which will be constituted by LRGs and ELGs at $z \sim 0.7$. We use the effective volume (Feldman et al., 1994) of the XMS surveys, as a figure of merit for our comparisons with the upcoming LSS surveys. We investigate XMS' exposure time and wavelength coverage success rate.

In Chapter 3, we perform a clustering analysis of ≈ 130000 uniquely izK selected LRGs in SDSS Stripe 82. The basic aim is to explore if the slow clustering evolution trend previously observed at lower redshifts (Wake et al., 2008; Sawangwit et al., 2011), continues at higher redshift. We adopt a cross-correlation technique to recover the redshift distribution of the LRG sample at $z \sim 1$ and infer the 3D clustering information by fitting various clustering models. By not be able to clearly explain the power excess in the clustering pattern at large scales as the clustering behaviour of the high-z LRGs is not in agreement with the standard model, we fit our data with non-Gaussian models.

In Chapter 4, we present the first spectroscopic observations of a LRG subsample from Chapter 3, that we have carried out using the VIMOS spectrograph on VLT. We find that the spectroscopic redshift distribution of the undertaken LRGs, nearly affirms the one that has been recovered through the cross-correlation technique in Chapter 3. This result is supporting even more the use of the cross-correlation technique as a mean to gain the redshift information, when planning large cosmological surveys consisted from photometric samples (i.e. VST ATLAS and VHS surveys). Taking into advantage the available spectroscopic $n(z)$, we accomplish a clustering study for the Stripe 82 LRGs, analogous to the one presented in Chapter 3.

In Chapter 5, we constrain the clustering evolution of the DRGs, by studying the largest up to date deep NIR field. We work on the UltraVISTA survey, where the clustering measurements are extended at even larger scales, from what has been examined in other studies. Using further galaxy statistics, we derive the number counts and compare the measured DRGs clustering with results from previous studies. Finally, in Chapter 6 we present the conclusions and summarise our results as well as how we can exploit further our findings in order to understand better the underlying physics of our Universe.

Chapter 2

eXtreme Multiplex Spectrograph and Future Cosmological Measurements

2.1 Introduction

For precise measurements of the cosmological parameters, the large-scale structure (LSS) of the Universe is the most promising aspect of modern Cosmology. Studies of the last decade suggest that we live in a Universe with an accelerating expansion. Today the Λ cold dark matter model-ΛCDM is the best explanation of our Universe. In the ΛCDM model, dark matter consists almost a third of the critical density for a spatially flat Universe and the remaining contribution to the energy density appears to be a form of dark energy. A description of dark energy is provided by the equation of state $w_{DE} = p_{DE}/\rho_{DE}$, where p_{DE} is the pressure in the dark energy and ρ_{DE} its density. In ΛCDM, an accelerating Universe is produced if $w < -\frac{1}{3}$ and the dark energy has the form of the cosmological constant Λ if $w = -1$ (vacuum energy). No current theory gives a clear explanation of why the dark energy density is the observed magnitude or why it happens to be close to the matter density today.

At present, there are four main observational probes of dark energy (Albrecht et al., 2006), which aim to measure distances as a function of redshift, the growth of structure, and possible fluctuations in dark energy at large scales. Type Ia supernovae measure

the luminosity distance versus redshift relation and provide a purely geometrical constraint. These measurements gave the first direct evidence for cosmic acceleration (Riess et al., 1998; Perlmutter et al., 1999). The next method is based on the evolution of the abundance of rich clusters, which depends on both geometry and the growth of perturbations. The same measurements can be done using weak gravitational lensing. The final way, also geometrical, uses baryon acoustic oscillations (BAO) as standard ruler to measure the angular diameter distance versus redshift (e.g. Blake & Glazebrook, 2003; Seo & Eisenstein, 2003). BAO are believed to be the method "least affected by systematic uncertainties, and for which we have the most reliable forecasts of resources required to accomplish a survey of chosen accuracy" (report of the Dark Energy Task Force; Albrecht et al., 2006). Many different kinds of surveys and experiments are being tried to determine the equation of state as function of redshift.

In this chapter we will investigate a proposed instrument that could be used in the upcoming generation of spectroscopic galaxy surveys. The eXtreme Multiplex Spectrograph (XMS), is designed for the prime focus of the 3.5m Calar Alto telescope, with the purpose of multi-object wide-field spectroscopic surveys. XMS will be consisted of four cloned spectrographs with $30' \times 25'$ field of view (FOV) each. The individual combination of the four spectrographs will offer a unique performance for the instrument, handing 4000 MOS slits simultaneously over a 1^0 field[1]. This supreme multiplex ability means that 25000-30000 galaxy redshifts can be measured in a single night, giving the opportunity to have large redshift surveys out to $z \sim 0.7$. XMS has the ability to measure simultaneously 4000 galaxy redshifts per 1.5h exposure for $i < 21$ absorption-line and $i < 22$ emission-line galaxies, so it could provide about 6×10^6 galaxy redshifts in a 200 night survey. The total survey could cover $1000 deg^2$ of sky offering the possibility for a better understanding of major questions in galaxy evolution and cosmology.

This instrument has never been built due to the lack of funding and the project has been abandoned. For this reason, this chapter today can be more useful as a historic reference. The study presented in this chapter refers to the XMS status and the available

---

[1]see Table 2.1 for summarised technical specifications of XMS. More details about XMS can be found at Content et al. (2010).

Table 2.1: Summary of XMS Instrument Specifications

Number of spectrographs	4
Image quality	$\sim$0.5″
Angular pixel size on sky	15 microns$<=>$ 0.44″
Field of view (FOV) of 1 spectrograph	30′ x 25′
Normal spectral resolution for 1.5″ slit	10 Å
Normal spectral resolution for 1.0″ slit	6.7 Å
High spectral resolution for 1.0″ slit	3.0 Å
λ pixel size normal resolution	2.9 Å
λ pixel size high resolution	1.3 Å
Total λ range available	4200-9200 Å
Grism 1 λ band (high priority)	5200-7200Å(OII $0.4< z <0.9$)
Grism 2 λ band (medium priority)	4200-5200Å(Lyα $2.5 < z < 3.5$)
Grism 3 λ band (low priority)	7200-9200Å

data/surveys until 2010;the end of XMS project. An instrument that could be introduced today as the alternative to XMS, is the 4-metre Multi-Object Spectroscopic Telescope (4MOST; de Jong, 2011).

2.2 XMS science case

The XMS project is a collaboration with Max Planck Institute für Astronomie, Instituto de Astrofisica de Andlalucia, Durham University, Edinburgh University and Portsmouth University, thus there are many powerful potential science cases for the XMS instrument. In the following, we outline the most important science drivers and further discuss their

physics background. [2]

- Observational Cosmology via galaxy redshift surveys at z∼0.7.

- Evolution of the Halo Mass function with Galaxy Evolution Survey-GES.

- Observational Cosmology via Lyman Break galaxy redshift surveys.

- Galactic Archaeology.

- Nearby and Distant Rich Clusters Survey.

- Calibrating Photo-z with spectroscopic redshifts.

2.2.1 Galaxy Redshift Surveys at $z \sim 0.7$ - CRS

The prime cosmological goals for XMS-Cosmology Redshift Survey (CRS) are the measurement of Gravitational Growth Rate and the measurement of the BAO, which are based on its ability to measure ∼4000 galaxy redshifts per 1.5hr exposure for i<21 absorption-line and i<22 emission- line galaxies at z∼0.5-0.7. 4000 emission/absorption redshifts an hour means ∼25000 redshifts a night or $\sim 5 \times 10^6$ galaxy redshifts in a 200 night survey. Such a survey could cover $\sim 1000 deg^2$ of sky and would give the opportunity for studies of galaxies clustering to be made over a wide range of scales (0.1-1000h^{-1}Mpc).

There are enough galaxies at the magnitude limits quoted above to fill ∼4000 XMS slits, since galaxy count data suggest that there are ∼4000 galaxies per square degree at i<21 and ∼9000 at i<22, 5000 of which will show emission lines. The wavelength coverage needed for these surveys is between 5200-7200Å, allowing the OII 3727Å to be observed in the range $0.4 < z < 0.9$ and the 4000Å break in the range $0.3 < z < 0.8$. The imaging base for XMS spectroscopy will come from Pan-STARRS, Physics of the accelerating Universe (PAU; Benítez et al., 2009) and ultimately LSST surveys.

---

[2]As the author has been involved mainly with the first two science cases, our discussion will be focused only on them.

Gravitational growth rate

Growth of structure in the Universe has been long recognised as one of the most powerful ways to learn about the nature of dark energy and other properties of our Universe. The relation between galaxy and dark matter clustering is however not straight forward (Kaiser, 1987). In the simplest model of linear bias, the galaxy overdensity δ_g is linearly biased by a constant factor, the linear bias factor b, relative to the underlying mass density δ_M, so :

$$\delta_g = b\delta_M,\tag{2.1}$$

or

$$b^2 = \frac{\sigma_8^2(galaxies)}{\sigma_8^2(mass)},\tag{2.2}$$

where σ_8^2 is the dimensionless variance in galaxy counts or mass in spheres of 8 $h^{-1}\mathrm{Mpc}$ radius. This choice is raised by the observational result that the variances of counts of galaxies in spheres of this size are of order unity so $b \approx 1/\sigma_8(mass)$.

We can measure the rate of the growth of structure using redshift-space distortions of galaxy clustering. If we use redshifts as a measure of distance through the Hubble relation, peculiar velocities distort the maps of galaxy distribution. Peculiar velocities are imprinted on the redshift-space clustering pattern by their two main contributions:

- At large scales, galaxies that fall into clusters look squashed along the line of sight in redshift space. This squashing effect leads to an increase in the clustering amplitude along the line of sight, known as the Kaiser effect (Kaiser, 1987):

$$P_s(\mathbf{k}) = (1 + \beta\mu_k^2)^2 P(\mathbf{k})\tag{2.3}$$

where $P(k)$ is the power spectrum of density fluctuations δ, the subscript s indicates redshift space, μ is the cosine of the angle between k and the line of sight and β is proportional to the velocity growth rate in linear theory.

- At small scales, compared with the size of the virialized clusters, the internal velocity dispersion elongates clusters along the line of sight, leading to the so-called Finger of God effect-FOG (Jackson, 1972).

Redshift space distortions thus provide a measure of the amount of dark matter which sources peculiar velocities. The observed distortions explain with important accuracy the motion of galaxies at large-scales, thus using their amplitudes, offering a measurement of the infall parameter β. The infall parameter is related to the cosmological density Ω_0, the present day ratio of the matter density of the Universe to the critical density required to close it, by:

$$\beta = \frac{f(\Omega_m)}{b} \approx \frac{\Omega_m^{0.6}}{b},$$

(2.4)

where b is the bias factor and Ω_m is given in a flat universe as:

$$\Omega_m(z) = \frac{\Omega_m^0 (1+z)^3}{\Omega_m^0 (1+z)^3 + \Omega_\Lambda^0}$$

(2.5)

The growth rate of density fluctuations at a given redshift is defined as:

$$f_g = \frac{dlnD}{dln\alpha}$$

(2.6)

where D is the linear growth factor, α the expansion factor. This is an excellent discriminator of dark energy parameters, so in principle, more powerful than standard classical tests of cosmology. Good estimations about f show that $f \sim \Omega_m(z)^{0.6}$ for a wide range of models (Peebles, 1980; Lahav et al., 1991) and by measuring β at a range of redshifts we can obtain the evolution of the gravitational growth rate.

Baryonic Acoustic Oscillations

A further aim would be to measure the scale-length of Baryon Acoustic Oscillations (BAO) as detected in galaxy clustering power spectra and correlation functions. These features are seen as an oscillation in the power spectrum and as a spike in the galaxy correlation function. BAO offer the opportunity to use them as a natural standard ruler

through the angular-diameter distance and the Hubble parameter relation (Blake & Glazebrook, 2003; Seo & Eisenstein, 2003) and allow tests of cosmological models. BAO received considerable attention the last years and have emerged as a key technique for exploring the nature of dark energy.

In particular, such observations will allow us to probe the equation of state of the vacuum energy, $p = w\rho$. Currently, the spike in the correlation function is tentatively detected in the 2dF Galaxy Redshift Survey of 250000 $z \sim 0.1$ galaxies (Cole et al., 2005). and also in the SDSS redshift survey of 75000 z 0.35 Luminous Red Galaxies (Eisenstein et al., 2005). In future bigger galaxy surveys will be needed to measure the BAO scale at higher redshifts and hence track any evolution in the vacuum energy equation of state with redshift. XMS BAO studies will identify systematics caused by non-linearity in galaxy power spectra that may result in different scale-lengths being measured for different types and luminosities of galaxy. The high multiplex of XMS will have a crucial role to play in the future of observational cosmology.

2.2.2   Evolution of halo mass function with galaxy evolution survey - GES

The main purpose of the XMS Galaxy Evolution Survey-XMS GES is to enable robust studies of halo masses, the evolution of galaxy luminosity, colours and spectral energy distribution. The aim of the XMS GES is to provide key constraints at $0.4 < z < 0.7$ in the kpc to Mpc range of halo scales, over which baryon physics become critical to our understanding of the structures we see. XMS GES will be equivalent to a SDSS redshift survey at a 3/5th of the age of the Universe. XMS GES will fill the gap between the up-coming large $z \sim 1$ galaxy redshift surveys (like SuMIRe and VIPERS; Guzzo et al., 2008) and the large multi-band photometric redshift surveys (like Pan-STARRS, DES and PAU).

XMS, with its $\sim 1^0$ field and extreme multiplexing capability, represents a unique facility capable of surveying these critical scales in a comprehensive manner over the proposed z range. The two key scientific goals that will be addressed by this survey are:

- A robust test of the CDM paradigm by measuring the predicted dark matter halo mass function from clusters to galaxy scales over a 6 Gyr baseline, a critical step

beyond SDSS and GAMA.

- A precise measurement of the galaxy formation efficiency in groups leading to fundamental constraints on galaxy formation models at $z \sim 0.5$, a pivotal connection between current results at $z \sim 0.1$ and future $z \sim 1$ redshift surveys.

Both these aims require the masses of groups to be measured with accurate velocities for many faint group members. The high multiplex ability of XMS will provide this information uniquely well at $z \sim 0.5$. Stellar masses for groups will also be needed and band photometry from UV to NIR. XMS by measuring redshift space distortions could give an estimate with the mass and then for the M/L of galaxy group haloes in CDM models. Such measurements could then allow new tests to affirm the process of galaxy formation as a function of halo mass environment. XMS-GES will thus trace the evolution of the halo mass function and the build up of stellar mass out to a look-back time when the Universe was 60% of its current age.

2.3   Effective volume of redshift surveys

Large volumes have to be surveyed in order to reach the statistical accuracy needed to obtain relevant constraints on dark-energy parameters via BAO or gravitational growth rate. Enough galaxies must be observed to reduce the shot noise below the irreducible component due to sampling variance. By shot noise, we mean the Poisson sampling noise, which is the dominant source noise in a survey. A typical galaxy survey does not contain all galaxies in a region of space but only those who are brighter than some flux limit. By combining different samples of galaxies, we hypothesise that the observed galaxies are drawn randomly from a hypothetical continuous existing population of galaxies. What characterises the survey is the radial selection function $\bar{n}(\mathbf{r})$ which is the expected mean number of galaxies at position $\mathbf{r}$ according with the selection criteria (i.e. the flux limit) of the survey.

Error estimation in the measurement of the power spectrum is given by:

$$\sigma_P \equiv \frac{\Delta P(k)}{P(k)} \simeq \sqrt{\frac{2}{N_m(k)} \left(1 + \frac{1}{\bar{n}P(k)}\right)} \approx 1/\sqrt{V_{eff}} \qquad (2.7)$$

which can be derived from Feldman et al. (1994), where the first term corresponds to the sampling error and is independent of redshift. The second term corresponds to Poisson shot-noise, and $\overline{n}$ indicates the number of observed galaxies in the survey. $N_m(k)$ is the number of Fourier modes present in a spherical shell extending from $k + \Delta k$ and is defined by

$$N_m(k) = V_{eff}(4\pi k^2 \Delta k)/(2\pi)^3 \tag{2.8}$$

where V_{eff} is the survey effective volume.

The effective volume for XMS surveys in our forecasting studies, is estimated via the integral (Feldman et al., 1994):

$$V_{eff}(k) = \int d^3r \left(\frac{n(\vec{r})P(k)}{1 + n(\vec{r})P(k)} \right)^2 \tag{2.9}$$

where $n(\vec{r})$ is the observed comoving number density of the sample at location $\vec{r}$ and $P(k)$ is the expected power spectrum amplitude.

2.4 XMS coherent survey programme effective volume comparisons

Eisenstein et al. (2005) used the SDSS LRG sample effective volume for comparison with other surveys (PSCz, MX, SDSS main and 2dFGRS). Following Eisenstein et al., we will present a comparison for galaxy surveys, using the effective volume as the figure of merit in checking XMS' survey competitiveness for cosmological measurements. We will consider the effective volumes of 3 XMS surveys in our comparisons:

- the XMS GES survey, with $3000deg^{-2}$ sky density at $i < 21$ for emission and absorption galaxies (ELGs and LRGs). The redshift range of this survey will be $0.4 < z < 0.7$ with high priority to measure halo masses and mass-to-light ratios

- the XMS CRS survey, with $1000deg^{-2}$ sky density for ELGs at $21 < i < 22$. The redshift range of this survey will be $0.5 \lesssim z \lesssim 0.9$, and the main aim is gravitational growth rate and BAO measurements.

- the XMS Galaxy Evolution + Cosmology Redshift Survey (XGECRS), a combination of XMS GES and XMS CRS surveys, is the final XMS survey that we will present in our comparisons[3]. The XGECRS will measure redshifts for a minimum of 4 million galaxies at $z < 1$ in $1000 deg^2$ of sky area during 250 clear nights of telescope time.

XMS high multiplex ability, means that there is no longer the need for a choice between ELGs or LRGs for cosmological measurements, since both types of galaxies can be observed simultaneously in the same volume, resulting overlapping in the science surveys. A comparison of the surveying abilities of the XMS component redshift surveys via the effective volume, is vital in order to understand the potentials of this instrument. For this reason, we select to compare future surveys with similar science drivers as XMS surveys; the Baryon Oscillation Spectroscopic Survey (BOSS; Schlegel et al., 2007), the WiggleZ Dark Energy Survey (Blake et al., 2009) and the Dark Energy Spectroscopic Instrument (DESI; Levi et al., 2013).

2.4.1   The Baryon Oscillation Spectroscopic Survey

Sloan Digital Sky Survey III, is a six year program that will use the wide-field 2.5m telescope at Apache Point Observatory to obtain four surveys, of which one of them will be the Baryon Oscillation Spectroscopic Survey (BOSS; Schlegel et al., 2007). BOSS survey will measure redshifts for 1.5×10^6 LRGs and 160000 high redshift quasars. BOSS will cover $10000 deg^2$ of high-latitude sky. Spectroscopic objects will be selected from SDSS imaging, and the galaxy sample will be pre-selected using colour cuts, thus galaxies of the sample will be at $0.4 < z < 0.7$. The galaxy sample will be deeper than the already existing SDSS sample, reaching $i \simeq 20$, with a space density $\overline{n} = 3 \times 10^{-4} h^3 Mpc^{-3}$ to $z \simeq 0.6$.

---

[3]The XGECRS survey parameters that used in our studies, are a combination of the XMS GES and CRS surveys.

2.4.2   The WiggleZ Dark Energy Survey

The WiggleZ Dark Energy Survey is a large-scale survey of intermediate-z UV-selected ELGs designed to provide 350000 spectra over $1000\mathrm{deg}^2$ in the redshift range $0.2 < z < 1$ during 165 nights of AAΩ multi-object spectrograph at 3.9m AAT. The primary aim of the survey is to measure precisely the scale of BAO in the galaxy cluster pattern over the proposed redshift range. The total volume that will be mapped after the completion of WiggleZ survey expected to be $V_{eff} \sim 1h^{-3}Gpc^3$ (Glazebrook et al., 2007).

Basic selection of the data made, concentrating to low signal-to-noise spectra of UV-selected ELGs in relatively short exposures (~ 1 hr). The primary goal is to obtain a total of 350000 spectra and 245000 of them to have reliable redshifts. The total survey area consists of seven equatorial regions, with a minimum angular dimension 10 deg each, corresponding to a spatial co-moving scale that exceeds at a factor of two the standard ruler preferred scale.

2.4.3   Dark Energy Spectroscopic Instrument

The Dark Energy Spectroscopic Instrument (DESI; Levi et al., 2013) is multi-fiber spectroscopic instrument that will be installed on the Mayall 4 meter telescope at Kitt Peak National Observatory, in order to map an area of $14000\mathrm{deg}^2$. DESI will fill the gap as a Stage-IV dark energy experiment (2018-2022), between the end of DES and the start of LSST. The goal of DESI will be to target 3 different types of objects: $\sim 4 \times 10^6$ LRGs at $0.5 < z < 1$, $\sim 18 \times 10^6$ ELGs at $0.5 < z < 1.7$ and $\sim 2.5 \times 10^6$ QSOs at $0.5 < z < 3.5$. The concept of DESI includes 5000 optical fibers, covering a wavelength range of $360-980\mathrm{nm}$. Spectral resolution is $R > 1500$ in blue, $R > 3000$ in red and $R > 4000$ in NIR.

The pre-imaging requirements over the $14000\mathrm{deg}^2$ area of DESI survey, for the different classes selection are: the completed Wide-Field Infrared Survey Explorer (WISE; Wright et al., 2010) satellite data along with $r \sim 23$ and $z \sim 2.15$ (at 5σ) for the LRGs, $g \sim 24$, $r \sim 23.5$, $z \sim 23$ (at 5σ) or $ug \sim 24$ and $r \sim 23.5$ for the ELGs. For the QSOs selection, $u, g, r, z \sim 23.5$ along with variability data are required.
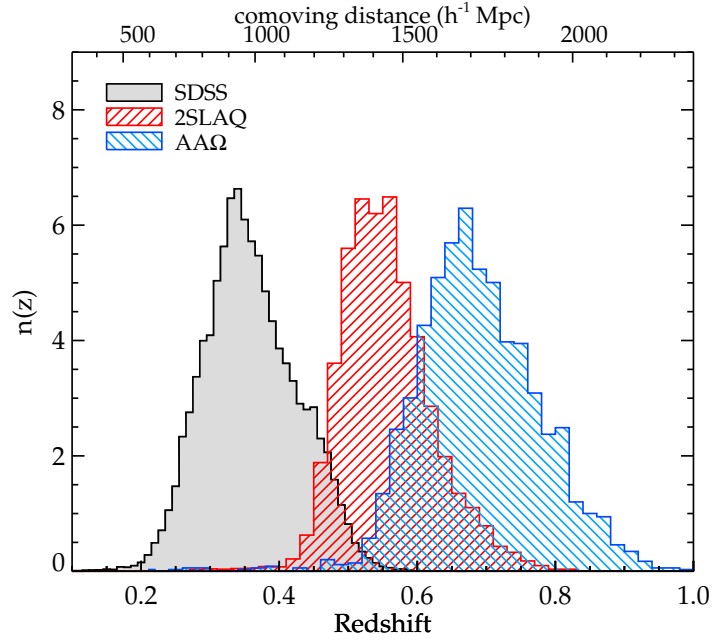
Figure 2.1: Top: Redshift distribution of SDSS, 2SLAQ and AAΩ LRG surveys that we adopt in the XMS studies. We apply the *n(z)* of 2SLAQ for the XMS GES case and the *n(z)* of AAΩ in the case of XMS CRS. Image credit: Sawangwit et al. (2011).

2.4.4   Results

Here we present the comparison we perform in terms of the effective volumes of the XMS surveys with BOSS, DESI and WiggleZ surveys. As the XMS surveys consist of emission and absorption galaxies, we include the estimations of the effective volumes for ELGs and LRGs also separately. The XMS CRS average redshift is at $z \sim 0.7$, hence we adopt as the model *n(z)* the AAΩ *n(z)* that peaks at $z = 0.68$ (Ross et al., 2008b) and is also similar to the proposed WiggleZ average redshift. For the XMS GES we use the 2SLAQ *n(z)* as model *n(z)*, which peaks at $z = 0.55$ (Cannon et al., 2006) (see Fig. 2.1).

   In Table 2.2 we present the parameters of each survey, as used in the calculations of their effective volumes. From Fig. 2.2, we see that the effective volume of DESI ELG, which will map galaxies at higher redshift and in a larger area, we see that this survey due to its high number density of the ELGs is unbeatable at almost all scales. For the XMS GES survey, as well as the rest XMS surveys, will be $\sim 10\times$ larger than the WiggleZ

Table 2.2: Parameters of compared surveys

survey	survey area	s_o	galaxy sky density	n(z)
	deg^2	$h^{-1}Mpc$	deg^{-2}	
XMS LRG	1000	10	350	AAΩ
XMS ELG	1000	5.3	1000	AAΩ
XMS GES	1000	6	3000	2SLAQ
XGECRS	1000	5.8	4000	model
BOSS LRG	10000	10	150	BOSS
WiggleZ ELG	1000	5.3	250	WiggleZ
DESI ELG	14000	5.3	2400	DESI
DESI LRG	14000	10	400	DESI

survey at scales $k > 0.1\mathrm{hMpc}^{-1}$. Individually the effective volume for the XMS ELG BAO measurements will be $3\times$ larger than the WiggleZ survey, indicating the great advent of the high space density of the XMS ELG survey design.

Moreover, compared to BOSS, we can see that the combination of high space density and survey area, will give the XMS GES and the XGECRS surveys the ability to measure the gravitational growth rate from redshift space distortions on scales $k > 1hMpc^{-1}$. Despite the fact that XMS will map a $10\times$ smaller area than BOSS, XMS GES and XGECRS will have a V_{eff} ~2-3$\times$ larger than BOSS on small scales. Furthermore, from our results is clear that the XMS ELG and XMS GES surveys have similar effective volumes at BAO scales, hence establishing the high-z ELGs also as potential tracers of the LSS.

At BAO scales, XMS GES volume is $\sim 5\times$ smaller than BOSS, when XGECRS is $\sim 2.5\times$ smaller. This makes XMS still competitive with BOSS at these scales, as XMS's error on the power spectrum estimation will only be $\sim 1.5\times$ larger than BOSS for XGECRS. In addition, XMS GES galaxy groups will have generally $20\times$ the membership of BOSS groups at the same scales, since the $3000\mathrm{deg}^{-2}$ sky density of XMS GES is $20\times$ higher than the $150\mathrm{deg}^{-2}$ sky density of BOSS. Thus, this means for XMS GES that it will provide correspondingly more accurate halo masses from velocity dispersions and
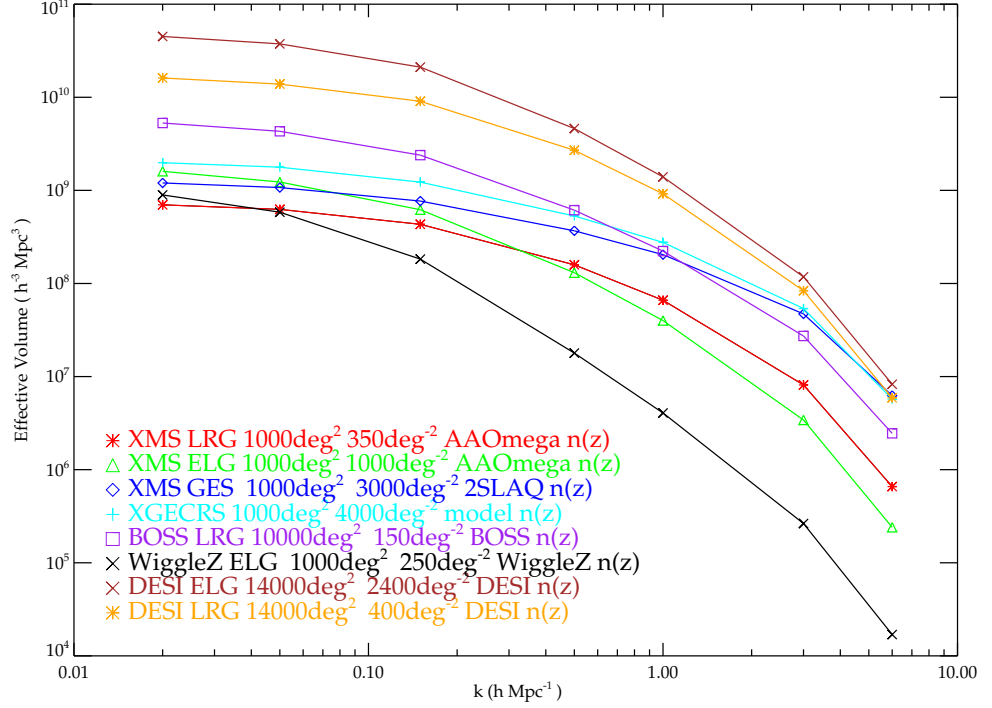
Figure 2.2: A comparison of the effective volumes of XMS surveys with WiggleZ, DESI and BOSS surveys. DESI's surveys effective volume are bigger at all scales, and can be only compared with XMS GES and XGECRS at small scales, as a result of these two XMS high number density surveys. XMS effective volumes will be $\sim10\times$ bigger than WiggleZ at scales $k > 0.1 hMpc^{-1}$. At small scales XMS GES has$\sim$2-3$\times$ larger effective volume than BOSS which means that at these scales redshift space distortions measurements for gravitational growth rate will be better with XMS. XMS GES galaxy groups will have 20$\times$ the membership of BOSS groups. At BAO scales XGECRS error on the power spectrum estimation will only be $\sim 1.5\times$ larger than BOSS.

for low mass groups where the BOSS membership is one (or less), the XMS mass will be much better.

We can understand that the ability to survey different types of galaxies in the same volume will also make XMS surveys sensitive to systematic differences related to galaxy colour/morphology in the BAO and gravitational growth rate results. We conclude that the XMS CRS is highly competitive for BAO and gravitational growth measurements. XGECRS allows a simultaneously galaxy evolution and cosmology, which is due its ability to map also the fainter $21 < i < 22$ ELGs along with the $i < 21$ LRGs at $z \sim 0.7$.

2.5 XMS efficiency tests

2.5.1 MOSCA data

We have used the MOSCA spectrograph on the 3.5m telescope in the Centro Astronómico Hispano Alemán-CAHA as an empirical test of XMS exposure time estimates. Despite the fact that MOSCA covers a 10′ field with only $\sim 3\%$ of the field-of-view of XMS, we choose MOSCA due to the fact that it has a variety of similar characteristics with XMS. These include throughput, spatial resolution and slit sizes. The effective focal ratio is $f/2.7$ and gives an image scale of 3 pixel per arcsec with a total FOV of $11' \times 11'$. 80% of the photons' energy on the CCD is contained within 15 micron radius, while the 100% is contained within 30 micron radius over the spectral range 3300 to 10000Å. The detector was a thinned CCD with 2048x4096 15 micron pixels.

MOSCA data were from William Herschel Deep Field that was observed on August 25 2008. These spectra were accomplished with the Green-250 grism with scale about 6Å/pixel and resolution ~ 25Å. On the WHDF field a selection of LRGs candidate to $i_{vega} < 21$ were observed along with a sample of ELGs candidate to $i_{vega} < 22$. These galaxies, were preselected by photo-z colour-cuts, in order to lie in the redshift range $0.4 < z < 0.8$. The riz colour selection of LRGs follows (Ross et al., 2008b) and the gri colour selection of ELGs follows (Bielby et al., 2010). Exposure times for WHDF were 2×1hr with the one mask and 1hr each for the other two. There was a problem with one of the latter 1hr exposure frame because a windowed read-out was used and this had as

a result to obtain only the half spectra. Observing conditions such as transparency and seeing ($1 - 1.5''$) were often poor.

In a try to improve our data sample from the WHDF field observations, we applied for more time in the CAHA. We looked the CFHTLS W4 field that overlaps with SDSS Stripe 82 field, which has also sufficiently deep photometry to create the colour-selected samples. Finally, we obtained another observing session on August 12 2009. This observation performed with the Red-500 grism, which had a resolution of 12Å closer to the 10Å expected from XMS. The selection of the LRGs was fainter at this field, with $i_{vega} < 21.5$. Exposure time was 3×0.5hr. Although this data sample has not been totally reduced, preliminary reduction shows that 5200-7200Å range to measure ELG and LRG redshifts in the range $0.4 < z < 0.9$ is the prime range for galaxy redshift surveys with XMS. Since the data from the CFHTLS W4 field have not been analysed yet, our analysis and results will be exclusively presented for WHDF field observations.

2.5.2   Data analysis

Data reduction has been performed using the following softwares:

- Image Reduction and Analysis Facility-IRAF[4]

- Graphical Astronomy and Image Analysis Tool-GAIA[5].

First, we used the *image region* option on GAIA to crop out single original spectra from the original raw frame. This was giving a stretch of 4300-8800Å usually for each spectrum, unless if the spectrum was on the edge of the field or either was contaminated from another spectrum.

The next step in our analysis was cosmic ray removal. At this point, we have to specify that for the 2hrs exposure mask, we had only one frame and as a consequence we could not use any pipeline for cosmic rays removal such as IRAF routine *imcombine* with *crreject*. Without having any other options, we had to clean each single spectrum by hand. To achieve this, we used GAIA which is a highly interactive image display tool.

---

[4]http://iraf.noao.edu/iraf/web/docs/prog.html
[5]http://star-www.dur.ac.uk/ pdraper/gaia/gaia.html
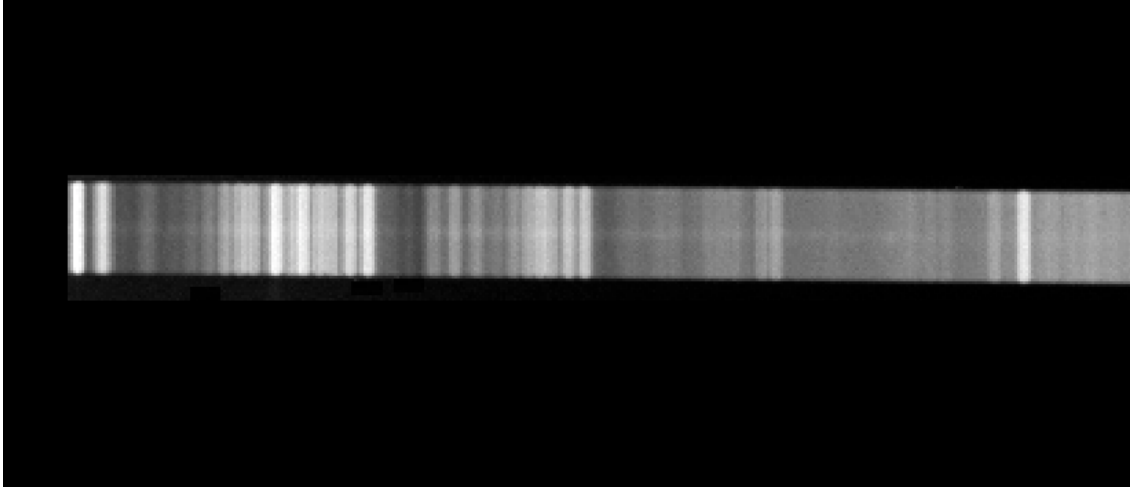
Figure 2.3: The final spectrum after being cropped from the original raw frame and being cleaned manually from cosmic rays.

By using *image region* and *image patch* options on GAIA, we patched the closest areas on features that we believed they look like cosmic rays on the spectrum. For this reason, we were working with a magnification of $10 - 15 \times$ while trying not to remove any useful data. For very faint ELGs this was a very difficult and time-consuming procedure because emission lines could be very easily confused with cosmic rays, due to the lack of a second frame that it could be used for comparison. A technique that was very useful for ELGs cases was obtained from Dr. Nigel Metcalfe, which we have to mention that his guidance offered us very important support for this analysis. Dr. Metcalfe created images of the emission lines by subtracting each CCD frame from copies of itself, shifted by +/-8 pixels in the spatial direction and then added the result. This removed the underlying sky very effectively. Finally, after completing cosmic ray removal, we had a cleaned 2-D spectra (see Fig. 2.3), ready to be used for further analysis with IRAF.

Following next, IRAF has been used for extraction and calibration procedures. Firstly we used *apall*, a routine that actually extracts the spectrum from the 2-D spectra. In some cases, the extraction parameters had to be changed according the type of the object. That was because, different type of galaxies, had also different continua and different S/N.

NOAO/IRAF V2.12.2a-EXPORT @nova.phyast.dur.ac.uk Wed 18:02:53 16-Sep-200
identify 14448t2 - Ap 1
WHDF_0022 (g-250)
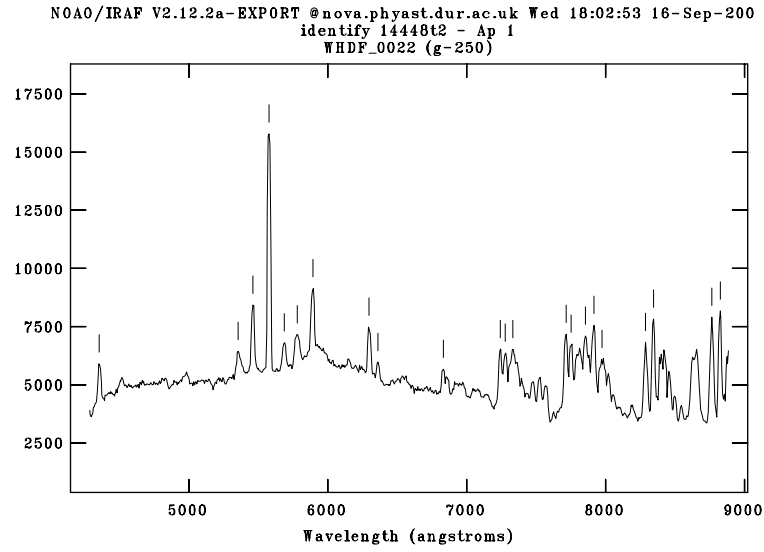
Figure 2.4: The night sky emission lines which where used to calibrate every spectrum.

Parameters that adjusted and affected the results were:

- The dispersion lines that were used for finding the centre of the spatial profile. Usually the middle of the dispersion axis was used, unless in the case of curved spectra.

- The number of dispersion lines that were summed to find a centre for the spatial profile (especially for ELGs since there was not necessary to use many lines along the spectrum as their signal to noise was different in comparison with LRGs).

Last, two groups of parameters that should be defined before analysis could proceed, were those referring to trace and background control. For trace controlling we adjusted :

- The number of the dispersion lines that were summed before searching for the peak at the spatial profile. This procedure was necessary in case of weak continua or curved spectra.

- The order of the polynomial fit, that was usually 2nd or 3rd order.

- The multispec format had to be set, in order to extract the object spectrum and the night sky spectrum from a single image.

Table 2.3: MOSCA field redshift completeness

Exposure	ELGs	LRGs	BGALs
2hrs	15/30	6/9	7/13
1hrs	6/23	3/4	2/21
1hrs	11/30	1/4	3/5

After completing *apall*, we had as an output the extracted sky background spectra as it mentioned previously. Using the *identify* routine on IRAF, we put the data on a linear wavelength scale and the calibration was based on the night sky emission lines (Figure 2.4). The last procedure of the data analysis was to match the calibrated sky spectrum with the object's spectrum, thus to be able to continue further with the galaxy redshift determination.

2.5.3   Redshift determination

After completing data reduction, we had to determine redshifts for our galaxy samples that consisted of ELGs and LRGs. ELGs have strong emission lines such as : OII 3727Å, OIII 4363Å, Hβ 4861Å, OIII 4959, 5007Å and LRGs can be easily identified from the Ca II H + K break. IRAF's routine *splot* offers many options for viewing and modifying the extracted spectra, making emission/absorption line measurement more feasible. The majority of redshifts were measured with *splot*, but some spectra did not present obvious features. Furthermore, in some cases there was the need for more precise redshift determination.

Redshift determination was obtained by templates cross-correlation using the interactive software 2dF RUNZ (private communication with S. Croom). RUNZ is a very useful tool and it offered the opportunity for faster cross-correlation of the galaxy spectra with template spectra. After completing redshift correlation with the use of RUNZ, we were convinced of the reliability of the measured redshifts.

In Fig. 2.5 we can see the redshift distribution per galaxy type and in Table 2.3 the redshift completeness overview. ELGs redshift success rate was 66% due to the fact
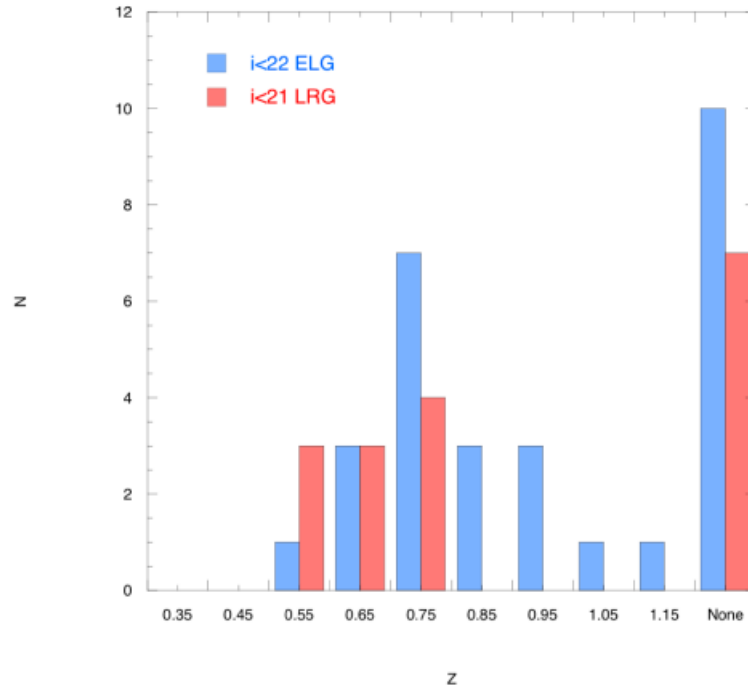
Figure 2.5: Redshift distribution from William Herschel Deep Field. Our sample redshifts determination performed by optical inspection using IRAF and 2dF RUNZ software. ELGs and LRGs redshift success rate are 66% and 58% respectively. Smaller success rate for LRGs caused by the fact that their sample was smaller in the MOSCA fields in comparison with ELGs.

that strong OII lines helped in their identification. The LRG sample was smaller in the MOSCA fields, with only 17 LRGs, resulting to their redshift success rate that was 58% (see Fig. 2.6, 2.7 for a sample of both galaxy types). These results showed that our assumptions for 1.5h exposure time for $i < 21$ absorption-line and $i < 22$ emission-line galaxies for XMS observations will offer accurate results.

2.5.4 Galaxy And Mass Assembly Spectra

In our try to test the reliability of XMS redshifts measurements in the 5200-7200Å passband, 267 spectra from the AAΩ Galaxy And Mass Assembly (GAMA; Driver et al., 2009) survey were used over a longer wavelength range and at a higher resolution. These spectra were artificially further redshifted by J.A. Peacock to ensure that their average

Figure 2.6: Top: ELG 2hrs i=19.94 z=0.95 OII. Bottom: ELG 2hrs i=21.59 z=0.63 OII, Hβ, OIIIx2.

NOAO/IRAF V2.12.2a-EXPORT pqct15@nova.phyast.dur.ac.uk Thu 20:23:45 26-Feb-
[8227f[*,1,1]]: WHDF_0021 (g-250) 3600. ap:1 beam:1
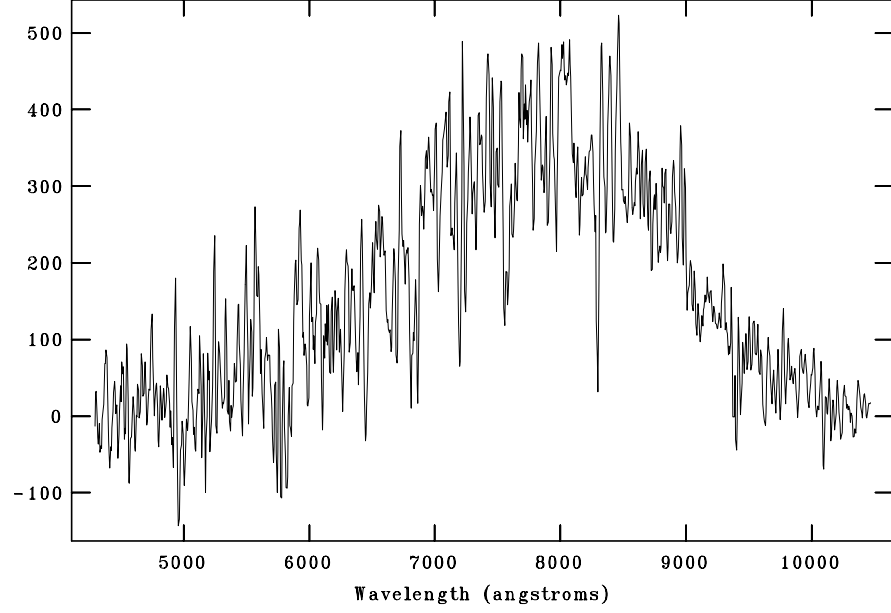
NOAO/IRAF V2.12.2a-EXPORT @xgpc42.phyast.dur.ac.uk Fri 16:24:11 16-Oct-20
[8488f[*,1,1]]: WHDF_0021 (g-250) 3600. ap:1 beam:1
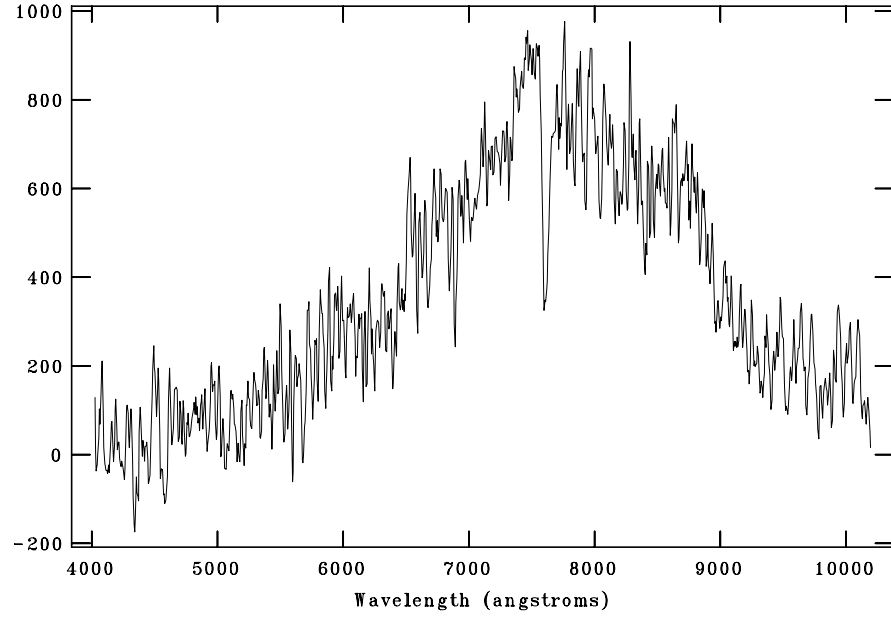
Figure 2.7: Top: LRG 2hrs i=20.35 z=0.74 CaII H+K break $\sim 6800\text{Å}$. Bottom: LRG 2hrs i=20.84 z=0.74 CaII H+K break $\sim 6800\text{Å}$.

redshift would be z$\sim$0.5. Moreover, all spectra were cut to the desirable wavelength range for XMS and smoothed to 10Å resolution of XMS. Finally, the spectra were then degraded to $S/N = 10$ per resolution element by adding random noise.

Redshifts were derived using 2dF RUNZ software by the author and his supervisor Prof. Tom Shanks. This was constructively a double-blind procedure because both of them were unaware of the actual AAΩ spectra redshifts (Fig. 2.8). To characterize redshifts qualities, we adopt a flag scheme in which each galaxy is assigned with a quality flag q. Flag value can be :

- $q = 3$: above 90% secure redshift, from strong spectral features.

- $q = 2$: 70-90% secure redshift measurement, based on several spectral features and continuum.

- $q = 1$: no reliable measurement possible.

The quality flags that we used for this estimation were $q = 3$ in red, $q = 2$ in blue and $q = 1$ in green. For $q = 2$ means that we were unable to determine the redshift because we could not identify any emission/absorption line in the wavelength range.

GAMA analysis results

- $\sim$56% of the redshift are within dz$\leq$0.01

- $\sim$70% of the redshift are within dz$\leq$0.05

Relative with quality flags we had the following statistical results :
q$\geq$3: $\sim$99% ($\sim$87%) to within $|z_{orig} - z_{TS}| \leq$0.05 (0.01)
q$\geq$2: $\sim$88% to within $|z_{orig} - z_{TS}| \leq$0.05
q$\leq$1: $\sim$30% to within $|z_{orig} - z_{TS}| \leq$0.05

Our results in comparison with the real redshifts are plotted in Figure 2.9 and z_{orig} representing the actual GAMA redshift while z_{TS} representing the measured "XMS" redshift. With a success rate of 88% we are convinced that our quality flags were reliable.
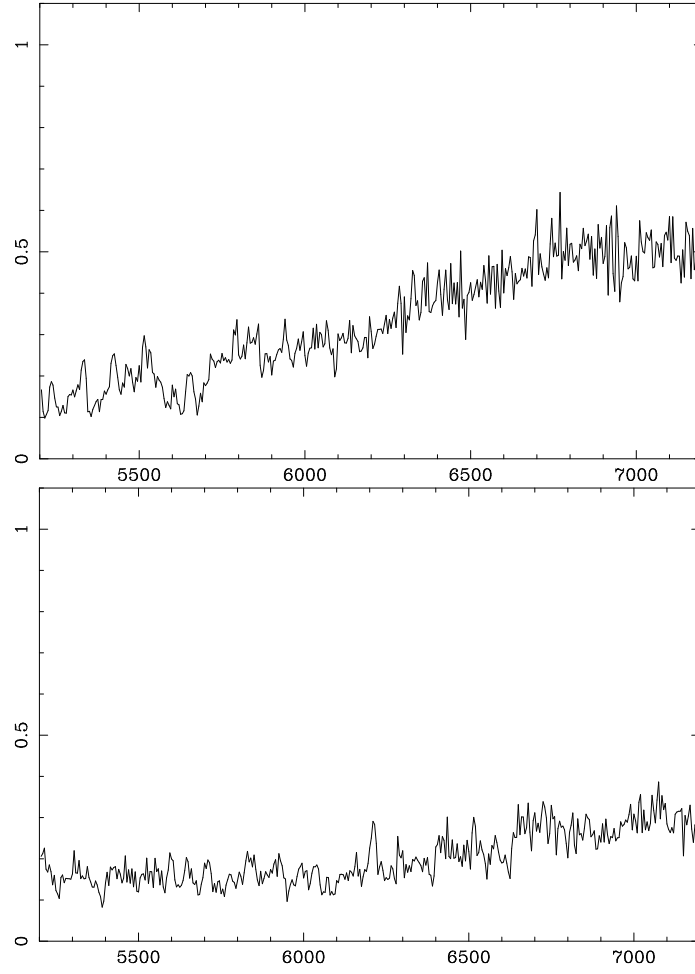
Figure 2.8: Two of the 267 AAOmega spectra at z=0.43 (top panel) and z=0.67 (bottom panel) that were edited to mimic XMS spectra. Redshifts determination performed using 2dF RUNZ software.
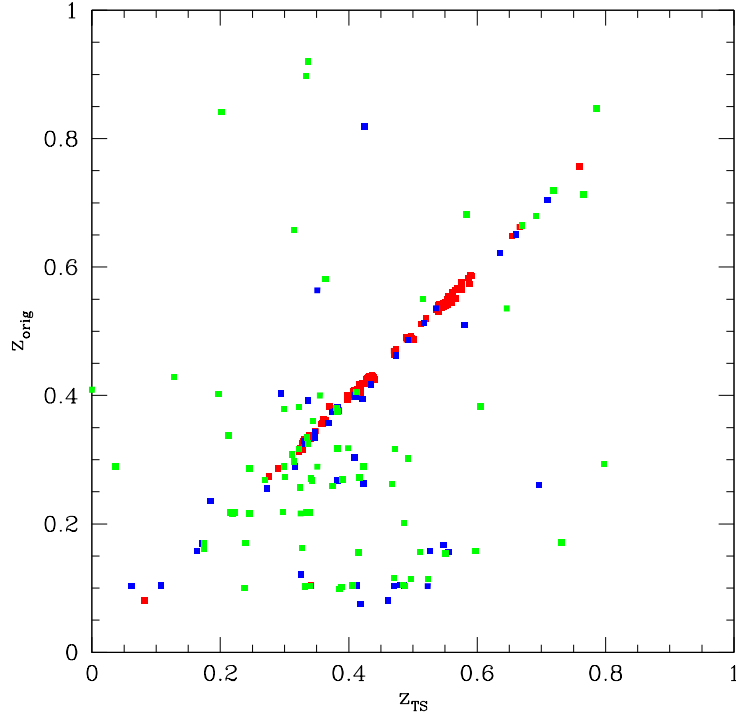
Figure 2.9: Comparison of 267 AAΩ galaxy redshifts-z_{orig} as originally measured for the GAMA project with fake XMS spectra-z_{TS}. The quality flags that we used are q=4 in red, q=3 in blue and q≤2 in green. In the $0.4 < z < 0.8$ redshift range that we are targeting with XMS, the success rate is 88%.

Furthermore, what we concluded for the wavelength range was not far from what it was expected, since in the original $z < 0.4$ range the OII and CaII H+K features fell below the 5200Å wavelength affecting negative XMS redshift definition. The same applies for z< 0.8 whenever these features lie beyond the 7200Å wavelength.

2.6   Conclusions

XMS a high multiplex ability of 4000 MOS slits over $1deg^2$ provides the opportunity to obtain large redshift surveys out to $z \sim 0.7$. Consequently, it could measure redshifts per 1.5h exposure for $i < 21$ absorption-line and $i < 22$ emission-line galaxies, providing about 6×10^6 galaxy redshifts in a 200 night survey.

We presented effective volume comparisons of the XMS surveys with WiggleZ, DESI

and BOSS. We understand that, by surveying different types of galaxies in the same volume, XMS will have the characteristic of being sensitive to systematic differences related to galaxy colour/morphology for cosmological measurements. DESI ELG and LRG surveys will probe larger area with high galaxy number density at higher redshift range, so these places them on the top of the rest of the surveys presented. Only XGECRS and XMS GES surveys will have similar effective volumes with DESI's surveys on smaller scales. This is indicating how accurate gravitational growth rate measurements we can obtain from those two XMS surveys, despite the fact that are designed in smaller areas with shallower samples.

We estimated that the effective volume of almost all the XMS surveys, will be larger than the WiggleZ at all scales. Moreover, we found that XMS GES will have an effective volume $\sim$2-3$\times$ larger than BOSS on scales $k > 1hMpc^{-1}$, making better XMS GES for gravitational growth rate measurements, despite its $10\times$ smaller area than BOSS. At BAO scales, XMS GES is still competitive for BAO measurements, while XGECRS will have only $\sim 1.5\times$ larger error than BOSS on the power spectrum estimation. It is clear from the above results, that high-z ELGs can be also play a pivotal role in LSS studies, as the XMS ELG survey for instance have a similar effective volume with the XMS GES at BAO scales. We also argued that the XMS GES galaxy groups will have generally $20\times$ the membership of BOSS groups at the same scales, due to the $20\times$ higher sky density of XMS GES. Hence, XMS GES will provide more accurate measurements of halo masses from velocity dispersions. In the case of low mass groups, where the BOSS membership is one (or less), the XMS mass will be much better.

Trying to test XMS exposure times estimates, we used data from the MOSCA spectrograph on the 3.5m telescope in the Calar Alto. MOSCA has similar characteristics to XMS such as throughput, spatial resolution and slit sizes. MOSCA targets consisted of ELGs and LRGs. After data reduction, we proceed to redshift determination which was based in the strong emission lines and the easily identified CaII H+K break. The success rate was 66% and 58% for ELGs and LRGs, respectively. These success rate percentages indicated that similar accurate observations can be obtained with XMS.

Furthermore, trying to test XMS observation capabilities in the 5200-7200$\mathring{A}$ pass-

band, we used 267 original spectra from the AAΩ GAMA survey. These spectra were edited to mimic XMS spectra. Redshift determination procedure was actually a blind test and redshifts derived without knowing their original values. The redshift success rate for XMS-GAMA spectra was 88%. As it was expected, features that lie outside the $0.4 \leq z \leq 0.8$ range gave poorer redshift estimates. This test indicated that XMS can accomplish observations in the 5200-7200Å passband and make reliable ELG and LRG redshift measurements in the range $0.4 \leq z \leq 0.8$.

Chapter 3

Clustering analysis of high-z LRGs in Stripe 82

3.1 Introduction

The statistical study of the clustering properties of massive galaxies provides important information about their formation and evolution which represent major questions for cosmology and astrophysics. The correlation function of galaxies remains a simple yet powerful tool for implementing such statistical clustering studies. (e.g. Peebles, 1980).

A lot of interest has been concentrated specifically on measuring the clustering correlation function of luminous red galaxies (LRGs) (Eisenstein et al., 2001) (see e.g Zehavi et al., 2005c; Blake et al., 2008; Ross et al., 2008b; Wake et al., 2008; Sawangwit et al., 2011). LRGs are predominantly red massive early-type galaxies, intrinsically luminous ($\geq 3L^*$) (Eisenstein et al., 2003; Loh & Strauss, 2006; Wake et al., 2006) and thought to lie in the most massive dark matter haloes. They are also strongly biased objects (Padmanabhan et al., 2007) and this coupled with their bright luminosity makes their clustering easy to detect out to high redshifts. For linear bias, the form of the LRG correlation function will trace that of the mass but even in this case the rate of correlation function evolution will depend on the bias model (e.g. Fry, 1996), which in turn depends on the galaxy formation process.

The passive evolution of the LRG LF and slow evolution of the LRG clustering (Wake et al., 2008; Sawangwit et al., 2011) seen in SDSS, 2SLAQ and $AA\Omega$ Surveys already presents a challenge for hierarchical models of galaxy formation as predicted for a cold dark matter (CDM) universe. Since the LRG clustering evolution with redshift has been

controversial, a major goal is to use the angular correlation function to test if the slow clustering evolution trend continues out to $z \approx 1$.

The uniformity of the LRG Spectral Energy Distributions (SEDs) with their 4000Å CaII H&K break, offer the ability to apply a colour-colour selection algorithm for our candidates. This technique has been successfully demonstrated primarily by Eisenstein et al. in SDSS in the analysis of LRG clustering at low redshift and then in 2SLAQ (Cannon et al., 2006) and $AA\Omega$ (Ross et al., 2008b) LRG surveys at higher redshifts.

In this chapter, the available deep optical-IR *ugrizJHK* imaging data from the SDSS + UKIDSS LAS/DXS surveys in Stripe 82 will be used. This combination of NIR and deep optical imaging data, on a moderate sample size of area $\sim 200 \deg^2$, results in a sample of $\approx 130\,000$ LRG candidates at redshift $z \approx 1$.

The main tool for our clustering analysis will be the two-point angular correlation function, $w(\theta)$, which has been frequently used in the past, usually in cases where detailed redshift information was not known. Hence, selecting Stripe 82 LRGs based on colour-magnitude criteria, correspond to a rough photometric redshift (photo-z) estimation based on the 4000Å break shifting through the passbands. We shall apply the cross-correlation technique which was introduced by Newman (2008) to measure the redshift distribution, $n(z)$, of our photometrically selected samples. One of the main advantages of $w(\theta)$ is that it only needs the $n(z)$ of the sample and then through Limber's formula (Limber, 1953) it can be related to the spatial two-point correlation function, $\xi(r)$.

In recent clustering studies, it was noted that the behaviour of $\xi(r)$, which has previously been successfully described by a single power-law of the form $\xi(r) = (r/r_0)^{-\gamma}$, significantly deviates from such a power-law at $\sim 1\ h^{-1}\mathrm{Mpc}$. The break in the power-law, can be interpreted in the framework of a halo model, as arising from the transition between small scales (1-halo term) to larger than a single halo scales (2-halo term). Currently, our theoretical understanding of how galaxy clustering relates to the underlying dark matter is provided by the halo occupation distribution model (HOD, see, e.g Jing et al. 1998; Ma & Fry 2000; Peacock & Smith 2000; Seljak 2000; Scoccimarro et al. 2001; Berlind & Weinberg 2002) via dark matter halo bias and halo mass function. Furthermore, the evolution of HOD can also give an insight into how certain galaxy populations

evolve over cosmic time (White et al., 2007; Seo et al., 2008; Wake et al., 2008; Sawangwit et al., 2011).

Throughout this chapter, we use a flat Λ-dominated cosmology with $\Omega_m = 0.27$, $H_0 = 100h$ $\mathrm{kms^{-1}Mpc^{-1}}$, h=0.7, $\sigma_8 = 0.8$ and magnitudes are given in the AB system unless otherwise stated.

3.2   Data

3.2.1   LRG sample selection

We perform a K-band selection of high redshift LRGs in Stripe 82 based on the combined optical and IR imaging data, *ugrizJHK*, from SDSS DR7 (Abazajian et al., 2009) and UKIDSS LAS surveys (Lawrence et al., 2007; Warren et al., 2007), respectively. In previous studies, *gri* and *riz* colours have been used to select low to medium redshift LRGs, such as SDSS (Eisenstein et al., 2001), 2SLAQ (Cannon et al., 2006) and AAΩ (Ross et al., 2008b) LRGs surveys up to $z \approx 0.7$. In this work we aim to study LRGs at $z \approx 1$, thus we use the *izK* colour magnitude limits for our selection in order to sample the 4000Å CaII H&K break of the LRGs' SED as it moves across the photometric filters (Fukugita et al., 1996; Smith et al., 2002) taking advantage of the NIR photometry coverage from UKIDSS LAS. Coupling the UKIDSS LAS to $K_{Vega} \leq 18$ with the SDSS ugriz imaging to $i_{AB} < 22.5$ in Stripe 82 produces an unrivaled combination of survey area and depth. Our selection criteria are :

$$
\begin{aligned}
&\text{SDSS Best Imaging} \\
&z - K + 0.9(i - z) \geq 1.8,\ Pri\ A \sim 700deg^{-2} \\
&z - K + 0.9(i - z) \geq 2.3,\ Pri\ B \sim 240deg^{-2} \\
&z - K - 0.9(i - z) \geq -0.2 \\
&-0.5 \leq i - z \leq 1.7 \\
&z - K \leq 4.0 \\
&17.0 \leq K \leq 18 \\
&z \leq 22.0.
\end{aligned}
\tag{3.1}
$$
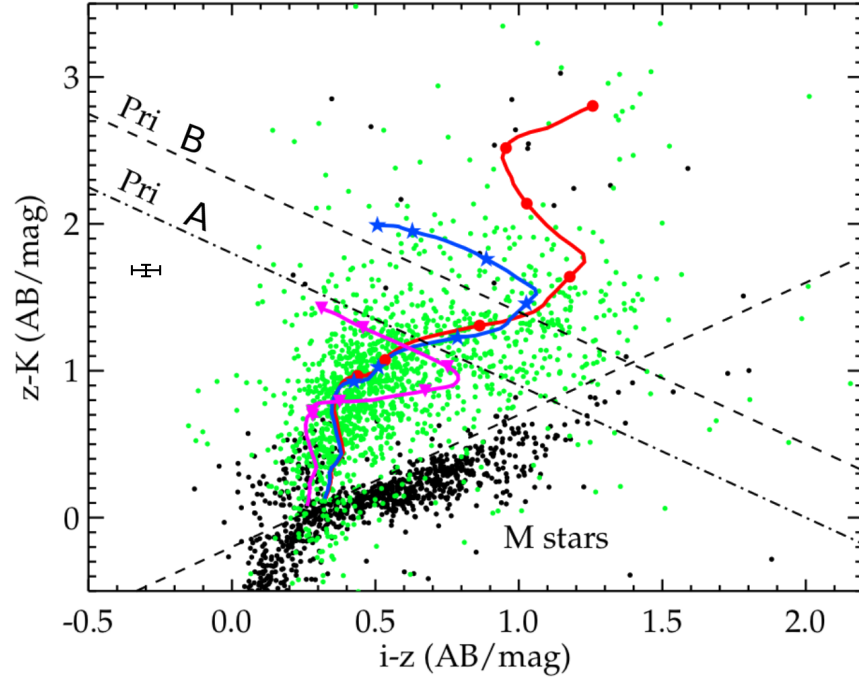
Figure 3.1: *iz* vs *zK* colour-colour plot. Priority A and B correspond to the $\sim 700 \deg^{-2}$ and $\sim 240 \deg^{-2}$ LRG samples, respectively. Objects with $J - K < 1.3$ which is typical for M stars are plotted as black circles where as those with $J - K \geq 1.3$ are plotted in green. Evolutionary tracks for single burst (red line) and $\tau = 1 \mathrm{Gyr}$ (blue line) are overplotted from $z = 0$ to 1.6 with symbols indicate z interval of 0.2. The evolutionary track of late type galaxies (magenta line) is also shown for comparison.

The photometric selection of LRGs at $z > 1$ requires a combination of optical and NIR photometry as the 4000Å band straddles the z band. The selection of high-redshift LRGs is done on the basis of SDSS iz photometric data and the LAS K band data (Fig. 3.1). LRG evolutionary models of Bruzual & Charlot (2003) are overplotted for single burst and $\tau = 1 \mathrm{Gyr}$ galaxy models indicating the *izk* plane area where we should apply our selections in order to study the high-z LRG candidates.

Late-type star contamination is a major problem in selecting a photometric sample of $z \approx 1$ LRGs. Here the $z - K$ colour also helps to distinguish the M stars colour locus from those of galaxies. From Fig.3.1, we see that most of the M stars lie at the bottom of the izK colour plane. We identify these M stars by assuming their typical NIR colour, $J - K < 1.3$. However, this means that our selection criteria must involve J band data

and would reduce the sky coverage due to the data availability. Therefore we choose to exclude these M stars by applying a cut in izK colour plane with the condition $z - K - 0.9(i - z) \geq -0.2$ in Eq. 3.1. The resulted stellar contamination of the LRG candidates is 4.5 per cent, much smaller than the 16 per cent of the $AA\Omega$ LRGs of Sawangwit et al. (2011) and similar to the 2SLAQ LRGs of Cannon et al. (2006).

All magnitudes and colours are given in SDSS AB system and are corrected for extinction using the Galactic dust map of Schlegel et al. (1998). All colours described below refer to the differences in 'model' magnitudes (see Lupton et al., 2001, for a review on model magnitudes) between SDSS model magnitudes and UKIDSS magnitudes, unless otherwise stated. The $3''$ aperture UKIDSS magnitudes will be close to total magnitudes at least for the fainter LRGs. The SDSS model magnitudes are close to total for bright and faint galaxies. So there will be some systematic error in the $z - K$ colour at bright magnitudes but the majority of our faint LRG sample will have colours that are accurate to within the random photometric error.

Applying the above selection criteria (Eq. 3.1) on the SDSS DR7, we have two main LRG samples with a total observed area (after masking) of $\approx 200\mathrm{deg}^2$. The first sample has 130819 LRGs candidates with a sky surface density of $\approx 700\mathrm{deg}^{-2}$ and the second one 44543 with a sky density of $\approx 240\mathrm{deg}^{-2}$. The $240\ \mathrm{deg}^{-2}$ LRG sample was selected in such a way to check if the redshift distribution implied by cross-correlations is higher than the $700\ \mathrm{deg}^{-2}$ LRG sample.

3.3 The 2-point angular correlation function measurements and errors

3.3.1 $w(\theta)$ estimators

The probability of finding a galaxy within a solid angle $\delta\Omega$ on the celestial plane of the sky at a distance θ from a randomly chosen object is given by (e.g. Peebles, 1980)

$$\delta P = n[1 + w(\theta)]\delta\Omega, \tag{3.2}$$

where n is the mean number of objects per unit solid angle. The angular two-point correlation function (2PCF) in our case, actually calculates the excess probability of finding a galaxy compared to a uniform random point process.

Different estimators can be used to calculate $w(\theta)$, so to start with we use the minimum variance estimator from Landy & Szalay (1993),

$$w_{LS}(\theta) = 1 + \left(\frac{N_{rd}(N_{rd} - 1)}{N(N - 1)} \right) \frac{DD(\theta)}{RR(\theta)} - 2 \left(\frac{N_{rd}}{N} \right) \frac{DR(\theta)}{RR(\theta)} \qquad (3.3)$$

where $DD(\theta)$ is the number of LRG-LRG pairs, $DR(\theta)$ and $RR(\theta)$ are the numbers of LRG-random and random-random pairs, respectively with angular separation θ summed over the entire survey area. N_{rd} is the total number of random points, N is the total number of LRGs and N_{rd}/N is the normalisation factor. For our calculation we used two LRG samples (as explained in § 3.2.1) with different sky density, thus the density of the random catalogue that we use is ~ 20 times and ~ 60 times the number of the real galaxies for the first and second LRG samples, respectively. Using a high number density random catalogue helps to ensure the extra shot noise is reduced as much as possible.

We also compute $w(\theta)$ by using the Hamilton (1993) estimator which does not depend on any normalisation and is given by,

$$w_{HM}(\theta) = \frac{DD(\theta) \cdot RR(\theta)}{DR(\theta)^2} - 1. \qquad (3.4)$$

The Landy-Szalay estimator when used with our samples gives negligibly different results to the Hamilton estimator. Note that the Landy-Szalay estimator is used throughout this work except in §3.6.1 where we used both estimators to test for any possible gradient in number density of our samples.

For the computation of the cross-correlations in §3.4 and §3.6 we use the estimator (Guo et al. (2012)) :

$$w_{cross}(\theta) = \frac{D_G D_S(\theta) - D_G R_S(\theta) - D_S RD(\theta) - R_G R_S(\theta)}{R_G R_S(\theta)} \qquad (3.5)$$

where the subscript G and S stands for the contribution in the pairs of the quantities that are cross-correlated in each case.

3.3.2   Error estimators

To determine statistical uncertainties in our methods, we used three different methods to estimate the errors on our measurements. Firstly, we calculated the error on $w(\theta)$ by using the Poisson estimate

$$\sigma_{Poi} = \frac{1 + w(\theta)}{\sqrt{DD(\theta)}}. \tag{3.6}$$

Secondly, we used the field-to-field error which is given by

$$\sigma_{FtF}^2(\theta) = \frac{1}{N-1} \sum_{i=1}^{N} \frac{DR_i(\theta)}{DR(\theta)} [w_i(\theta) - w(\theta)]^2, \tag{3.7}$$

where N is the total number of subfields, $w_i(\theta)$ is an angular correlation function estimated from the ith subfield and $w(\theta)$ is measured using the entire field. For this method we divide our main sample to 36 subfields of equal size $\sim 6\deg^2$. We also reduce the number of subfields down to 18 with sizes of $\sim 12deg^2$ as we want to test how the results could deviate by using different sets of subsamples. While Stripe 82 has only $\sim 2.5\deg$ height, our subfields with their $\sim 2.5\deg$ and $\sim 5\deg$ widths are a reasonable size for estimating the correlation function up to scales of $1 - 2\deg$.

Our final method is jackknife resampling, which is actually a bootstrap method. This technique has been widely used in clustering analysis studies with correlation functions (see, e.g Scranton et al. 2002; Zehavi et al. 2005a; Ross et al. 2007; Norberg et al. 2009; Sawangwit et al. 2011). The jackknife errors are computed using the deviation of the $w(\theta)$ measured from the combined 35 subfields out of the 36 subfields (or 17 out of 18 when 18 subfields are used). The subfields are the same as used for the estimation of the *field-to-field* error above. $w(\theta)$ is calculated repeatedly, each time leaving out a different subfield and hence results in a total 36 (or 18) measurements. The jackknife error is then

$$\sigma_{JK}^2(\theta) = \sum_{i'=1}^{N} \frac{DR_{i'}(\theta)}{DR(\theta)} [w_{i'}(\theta) - w(\theta)]^2, \tag{3.8}$$

where $w_{i'}(\theta)$ is a measurement using the whole sample except the ith subfield and $DR_{i'}(\theta)/DR(\theta)$ is approximately 35/36 (or 17/18) with slight variation depending on the size of resampling field. A comparison of the error estimators can be seen in Fig. 3.2. Poisson errors are found to be much smaller compared to jackknife errors particularly at larger scales.

Field-to-field errors give similar results as jackknife errors, except at $\theta \gtrsim 10'$ where the FtF errors underestimate the true error due to missing cross-field pairs. Since the jackknife errors are better at a scale of order $100'$ which are of prime interest here, these are the error estimators that will be used in this work unless otherwise stated.

When calculated in small survey areas, $w(\theta)$ can be affected be an 'integral constraint', ic. Normally $w(\theta)$ has a positive signal at small scales and if the surveyed area is sufficiently small, this will cause a negative bias in $w(\theta)$ at largest scales (Groth & Peebles, 1977), i.e. $w_{est}(\theta) = w(\theta) - ic$. The integral constraint can be calculated from (see e.g. Roche & Eales 1999):

$$ic = \frac{\sum RR(\theta)w_{model}(\theta)}{\sum RR(\theta)}, \tag{3.9}$$

where for the $w_{model}(\theta)$ we assume the standard ΛCDM model in the linear regime (§3.5.3). No integral constraint is initially applied to our full sample results as the expected magnitude of ic is smaller than the $w(\theta)$ amplitudes at scales analysed in this paper. This position will be reviewed when we move on to discuss models with excess power at large scales in §3.6.

To provide robust and accurate results from the correlation functions, we are also interested in model fitting to the observed $w(\theta)$ (see in §3.5.2, §3.5.4 and §3.5.3). Hence, for model fitting we will use the covariance matrix, which is calculated by:

$$\mathbf{C}_{ij} = \tfrac{N-1}{N} \sum_{i,j=1}^{N} [w(\theta_i) - \overline{w(\theta_i)}][w(\theta_j) - \overline{w(\theta_j)}] \tag{3.10}$$

where the $w_i(\theta_i)$ is the correlation function measurement value excluding the ith subsample and the factor $N - 1$ corrects from the fact that the realizations are not independent (Myers et al. 2007; Norberg et al. 2009; Ross et al. 2010; Crocce et al. 2011; Sawangwit et al. 2011). The jackknife errors are the square-root of the diagonal elements of the covariance matrix, so we can now calculate the correlation coefficient, which is defined in terms of the covariance,

$$\mathbf{r}_{ij} = \frac{\mathbf{C}_{ij}}{\sqrt{\mathbf{C}_{ii} \cdot \mathbf{C}_{jj}}} \tag{3.11}$$
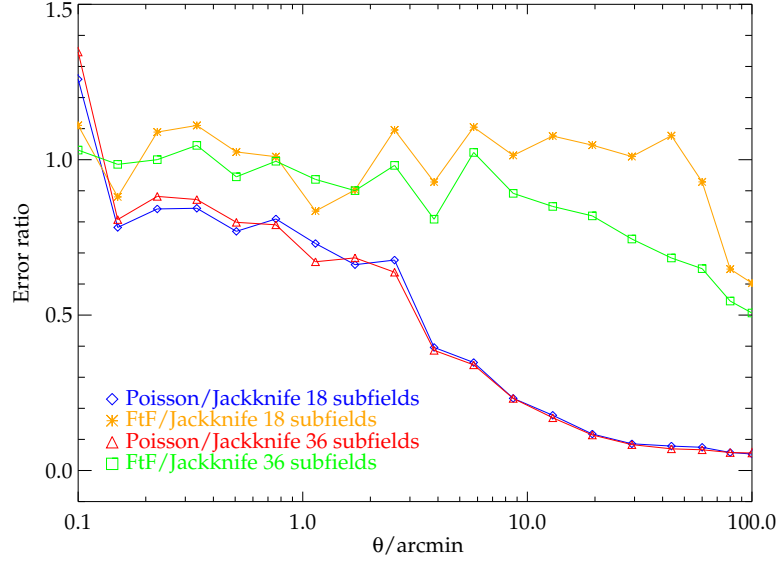
Figure 3.2: Comparison of the measured error ratios of the Jackknife, field-to-field and the Poisson errors for the $w(\theta)$ measurements of the 700 deg^{-2} Stripe 82 LRG sample. Two different resampling sets have been used for the Jackknife and field-to-field errors, the first one based on 36 subfields and the second from 18 subfields.

where $\sigma_i^2 = C_{ii}$ (see Fig. 3.3). We can see that the bins are strongly correlated at large scales. The covariance matrix is more stable when we use 36 Jackknife subfields instead of 18, so we will use only the covariance matrix for the case of 36 subfields.

3.3.3 Angular mask and random catalogue

To measure the observed angular correlation function we must compare the actual galaxy distribution with a catalogue of randomly distributed points. The random catalogue must follow the same geometry as the real galaxy catalogue, so for this reason we apply the same angular mask. The mask is constructed from 'BEST' DR7 imaging sky coverage[1]. Furthermore, regions excluded in the quality holes defined as 'BLEEDING', 'TRAIL ', 'BRIGHT_STAR ' and 'HOLE'. The majority of the holes in the angular mask is from the lack of *K* coverage in Stripe 82. The final mask is applied to both our data and

---

[1] http://www.sdss.org/dr7
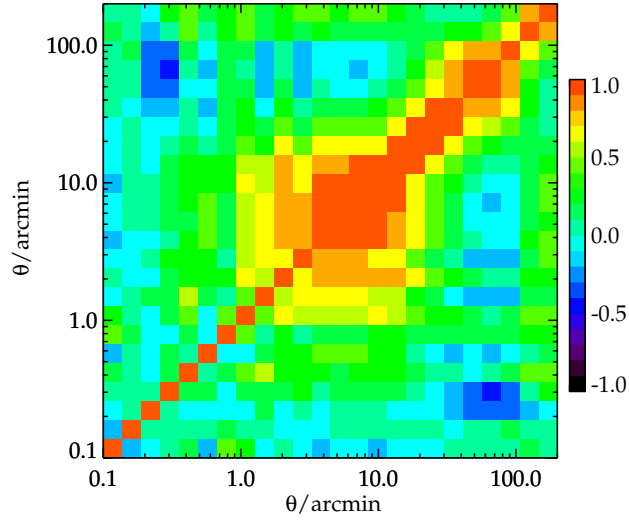
Figure 3.3: The correlation coefficients $\mathbf{r}_{ij}$, showing the level of correlation between each angular separation bin for the $700 \deg^{-2}$ Stripe 82 LRG sample as calculated by using 36 subfields.

random catalogue (see Fig. 3.4).

For generating the randomly distributed galaxies/points, we tried two different ways in order to modulate the surface density of the random points to follow the number density and the selection function of the real data. The selection function of the random catalogue mimics only the angular selection of the real data.

For the first method, we use a uniform density for the random points across the Stripe 82 area, so the normalization factor, N_{rd}/N, would be ~ 20 and ~ 60 for the $700 \deg^{-2}$ and the $240 \deg^{-2}$ LRG samples, respectively. A second random catalogue was created by dividing Stripe 82 into six smaller subfields ($15 \times 2.5 \deg^2$ each) and normalizing the density of random points to the density of galaxies within each subfield. The difference between the measured angular correlation function when we use the 'global' or the 'local' random catalogue is negligible. We will use the 'global' random catalogue for the clustering analysis. A kd-trees code (Moore et al., 2001) has been used to minimise the computation time required in the pair counting procedure.
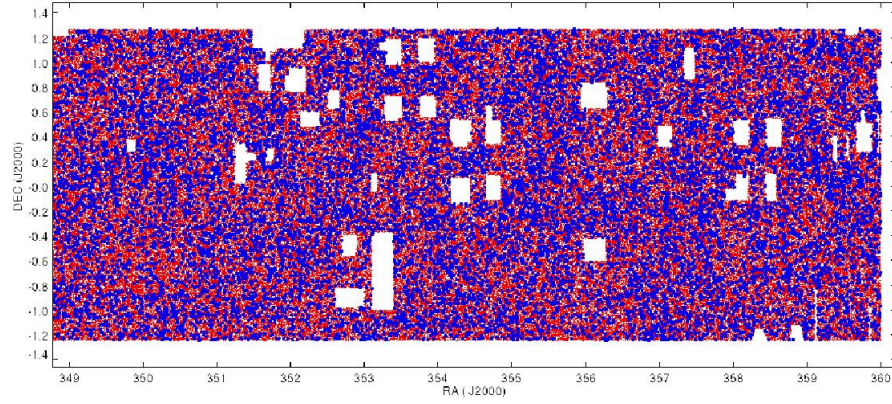
Figure 3.4: A fraction of the total $\sim 200 \deg^2$ observed area in Stripe 82. LRG candidates (red) and random objects (blue), follow the same angular selection. Empty sky patches resulting from the lack of K-band coverage in the combined optical-IR data.
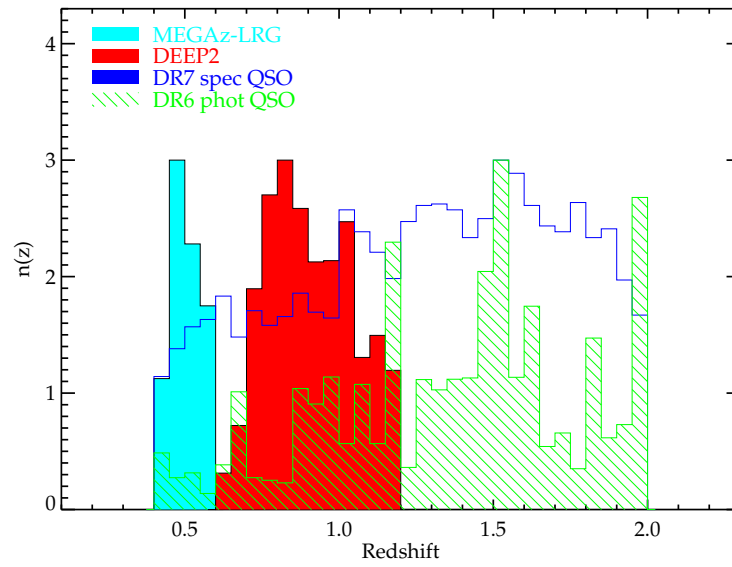
Figure 3.5: Normalised redshift distributions of MEGAz-LRGs, DEEP2 galaxies and SDSS QSOs in Stripe 82 that are used in the cross-correlations with the LRG samples.

3.4   LRG n(z) via cross-correlations

For our photometric selected LRG samples, only a very small fraction has a measured redshift, thus it is vital to estimate the *n(z)* of the Stripe 82 LRG samples.

One method for estimating the redshift distribution of the sample could be based on the various popular programs that derive photometric redshifts (photo-z's). Photo-z estimates are based on the deep multi-band photometry coverage, and work by tracing some specific spectral features across the combination of filters which are then compared with different type of SED templates. Indeed, our *izK* selection is a rough photo-z cut as we follow the movement of the 4000Å break across the selected bands. In order to use the angular correlation function and the information that is encoded we need the *n(z)* of our sample, hence we follow the technique of Newman (2008) for reconstructing the LRG redshift distribution from cross-correlations.

3.4.1   Redshift distribution reconstruction

We employ Newman's method, which is about determining the underlying redshift distribution of a sample of objects (LRGs in our case) through cross-correlation with a sample of known redshift distribution. By cross-correlating the sample (or samples) with known redshift and the sample under consideration, if both samples lie at the same distance, this will give a strong clustering signal. If the two samples that we are cross-correlating are separated and are at different z distances, no cross-correlation signal will result. Thus, through the cross-correlations we can infer our photometrically selected LRG sample z ranges.

Following Newman (2008) the probability distribution function of the redshift of the Stripe 82 LRG samples, $\phi_p(z)$, is:

$$\phi_p(z) = w(z)\frac{3-\gamma}{2\pi}\frac{d_A(z)^2 dl/dz}{H(\gamma)r_{0,sp}^{\gamma}r_{max}^{3-\gamma}} \tag{3.12}$$

where $w(z)$ is the integrated cross correlation function, $w_{sp}(\theta, z)$, of the LRG photometric samples with the samples of known spectroscopic redshift (see §3.4.2), $H(\gamma) =$

$\Gamma(1/2)\Gamma((\gamma-1)/2)/\Gamma(\gamma/2)$ where $\Gamma(\chi)$ is the Gamma function, d_A is the comoving angular distance and dl is the comoving distance at redshift z. The comoving distance r_{max} corresponds to the maximum angle at given redshift, which must be large enough to avoid nonlinear biasing effects.

To derive $\phi_p(z)$ via Eq. 3.12 we must estimate $w_{sp}(\theta, z) \sim \phi_p(z)\, r_{0,sp}^{\gamma_{sp}}$, since the angular size distance, $d_A(z)$ and the comoving distance $l(z)$ are given by the assumed cosmology. Thus we now require only knowledge of the γ_{sp} and $r_{0,sp}$ parameters as function of redshift. Fortunately under the assumption of linear biasing, the cross-correlation of the two samples under consideration is the result of the geometric mean of the autocorrelation functions of the samples, i.e. $\xi_{sp} = (\xi_{ss}\xi_{pp})^{\frac{1}{2}}$, hence we can use the information provided by autocorrelation measurements for each sample to break the degeneracy between correlation strength and redshift distribution.

Newman investigates the effect of systematics such as: different cosmologies, bias evolution, errors from the autocorrelation measurements and field-to-field zero points variations in the final redshift probability distribution result. These issues could be more important in the case of future photometric surveys aimed at placing constraints on the equation of dark energy.

3.4.2 Cross-Correlation data sets

Newman's angular cross-correlation technique requires the use of a data sample with known spectroscopic, or sufficiently accurate photometric, redshifts. For this reason we use a variety of samples with confirmed spectroscopic and photometric redshifts for the cross-correlations with Stripe 82 LRGs. The data samples that we use are: DEEP2 DR3 galaxies (Davis et al., 2003, 2007) , MegaZ-LRGs (Collister et al., 2007), SDSS DR6 QSOs (Richards et al., 2009) and SDSS DR7 QSOs (Schneider et al., 2010). In Fig. 5.3 we show the normalised redshift distributions of all the samples and in Table 3.1 we present the number of objects in each redshift bin.

By using the above data sets for cross-correlation we satisfy the principal requirements of Newman's method, with the most important being that the sky coverage of the data sets must overlap the Stripe 82 LRGs. It must be mentioned though that not all

Table 3.1: Number of objects in each separate redshift-bin used for the cross-correlations with Stripe 82 LRGs

| | sample | | | |
| | DEEP2 | MegaZ-LRGs | DR6 Photometric Sample | DR7 Spectroscopic sample |
redshift				
0.4 - 0.6	-	30503	436	456
0.6 - 0.8	3152	-	695	526
0.8 - 1.0	5512	-	1199	547
1.0 - 1.2	3620	-	1630	729
1.2 - 1.4	-	-	1312	820
1.4 - 1.6	-	-	2646	854
1.6 - 1.8	-	-	1193	803
1.8 - 2.0	-	-	1990	668

the redshift surveys have the same sky coverage as Stripe 82 LRGs, so we reconstruct two redshift distributions via the cross-correlations providing us with the opportunity to check how much the *n(z)* cross-correlation technique is affected by area selection. One $n(z)$ is reconstructed by using all the data sets, the other $n(z)$ by using only SDSS QSOs in the cross-correlations.

SDSS DR6 & DR7 QSOs

QSO surveys are the main samples that we used for our cross-correlation measurements and they span the redshift range $0.4 \leq z \leq 2.0$. When we refer to QSO data sets, we separate them into spectroscopic and photometric samples.

For the spectroscopic QSO sample we use the fifth edition of the SDSS Quasar Catalog, which is based on the SDSS DR7 (Schneider et al., 2010). The original data set contains 105,783 spectroscopically confirmed QSOs, from which only 5,403 in Stripe 82 have been used at $0.4 \leq z \leq 2.0$ for cross-correlations (Table 3.1) with $i < 22$ ($\sim 28\%$ of QSOs at $i > 20$).

The photometric QSO sample comes from the photometric imaging data of the SDSS DR6 (Richards et al., 2009). The parent catalogue contains $\sim 1,000,000$ QSOs candidates from which we use 11,101 with $i < 21.3$ in Stripe 82 and in the same redshift range as the spectroscopic QSOs.

In Fig. 3.6 we plot the cross-correlations between the Stripe 82 LRGs and the SDSS QSOs. We show only the case for cross-correlations of the $700 \ \mathrm{deg}^{-2}$ Stripe 82 LRG sample with the spectroscopic and photometric SDSS QSOs. Cross-correlation with the $240 \ \mathrm{deg}^{-2}$ LRG sample does not differ much. Errors shown here and for the other cross-correlation cases are jackknife errors.

DEEP2 Sample

The next sample of galaxies that we use is DEEP2 DR3 galaxies (Davis et al., 2003, 2007). The survey coverage in Stripe 82 is $\sim 1.7 \ \mathrm{deg}^2$ with $i < 24$. Galaxies in DEEP2 are split in three redshift bins with 0.2 step in the redshift range $0.6 \leq z \leq 1.2$. The redshift distribution of the DEEP2 DR3 sample is shown in Fig. 5.3, with 12,284 galaxies in total. In Fig. 3.7 we show the results of the cross-correlations of the $700 \ \mathrm{deg}^{-2}$ and $240 \ \mathrm{deg}^{-2}$ LRG samples with the DEEP2 galaxies in the three aforementioned redshift bins.

MegaZ-LRG sample

The last sample that we use are LRGs from the MegaZ-LRG photometric catalogue (Collister et al., 2007). MegaZ-LRGs are used only in the redshift range of $0.4 \leq z \leq 0.6$ with $i < 20$. This sample offers us the ability to check the clustering properties of our high-redshift LRG candidates with another sample of LRGs. The total number of MegaZ-LRGs that we use for cross-correlations is 30,503. In Fig. 3.8 are shown the cross-correlations between the Stripe 82 LRGs and the MegaZ-LRGs.
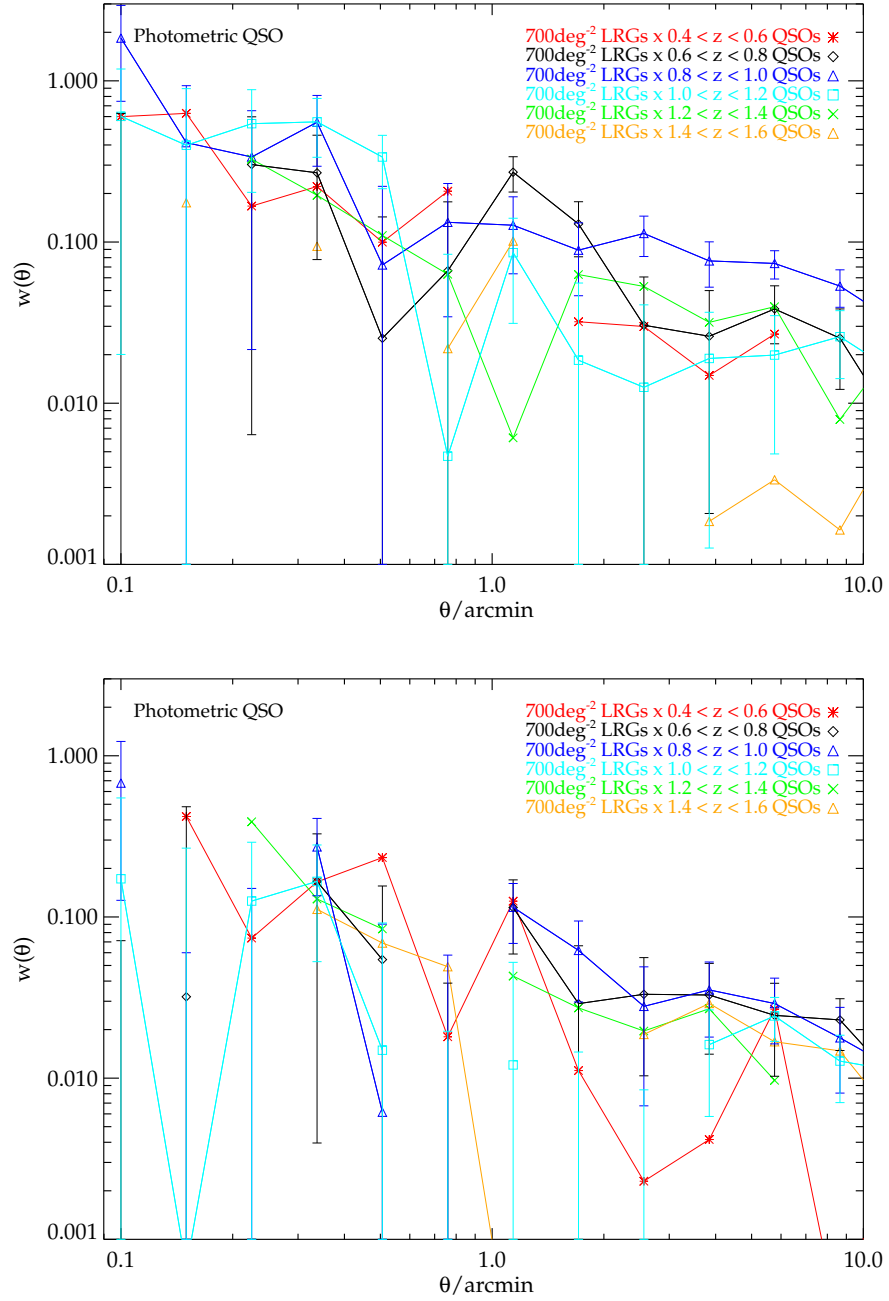
Figure 3.6: (a): Cross-correlation measurements of the $700 \, \mathrm{deg}^{-2}$ Stripe 82 LRG sample with spectroscopic SDSS QSOs. (b): Same as (a) but now photometric SDSS QSOs are involved in the cross-correlations. Measurement uncertainties are 1σ jackknife errors.
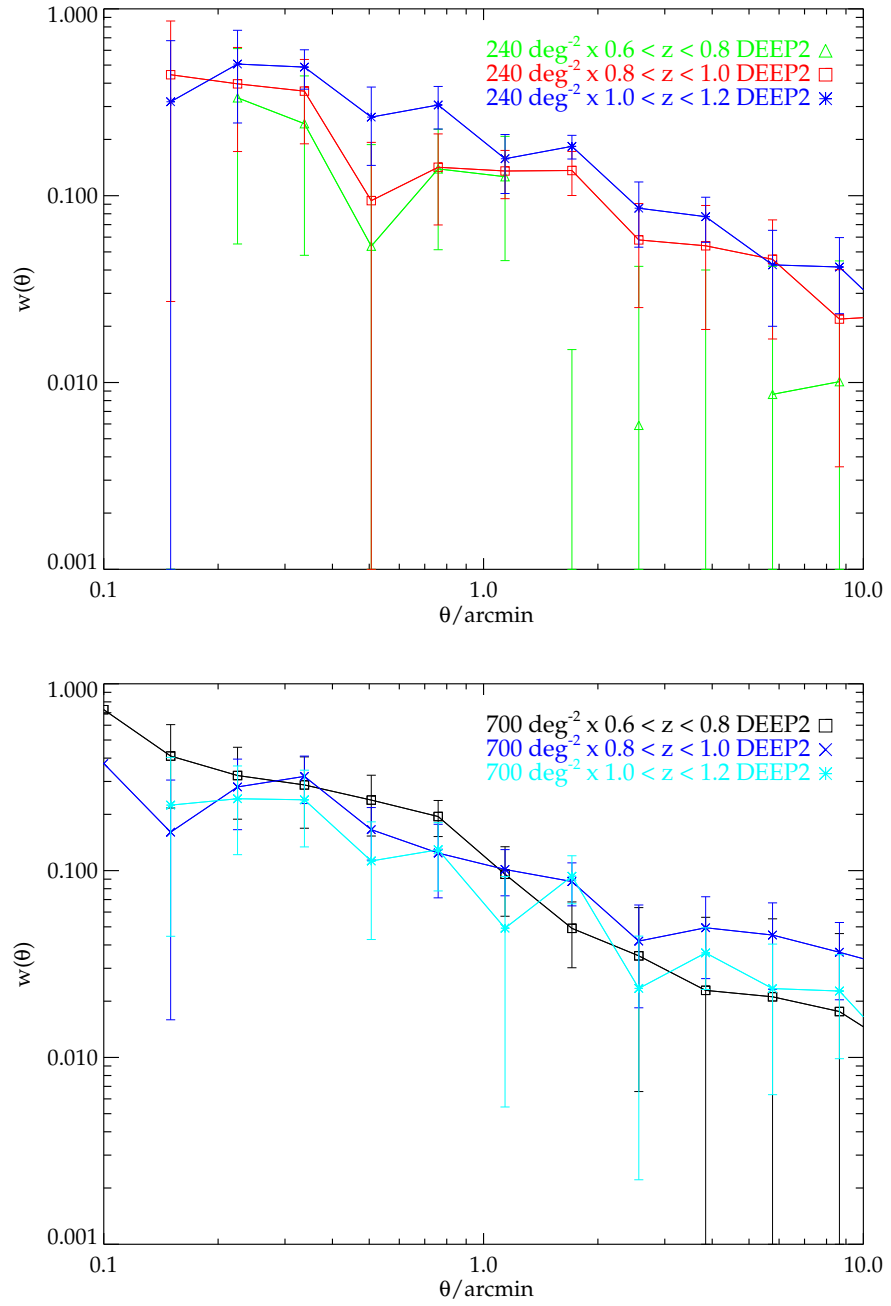
Figure 3.7: Cross-correlation measurements of the $240 \ \mathrm{deg}^{-2}$ and $700 \ \mathrm{deg}^{-2}$ Stripe 82 LRG samples with DEEP2 galaxies in (a) and (b), respectively. Uncertainties are 1σ jackknife errors.
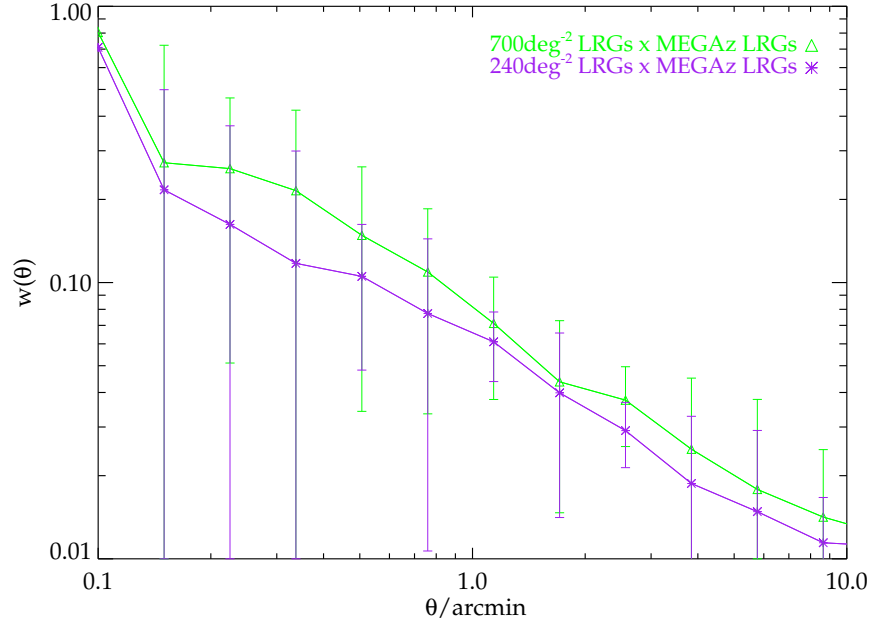
Figure 3.8: Cross-correlation measurements of the $700\ \mathrm{deg}^{-2}$ (green diamond) and $240\ \mathrm{deg}^{-2}$ (purple star) Stripe 82 LRGs with MegaZ-LRGs, along with 1σ jackknife errors.

3.4.3 Cross-Correlation results for *n(z)*

Having estimated the clustering signal from the cross-correlations of the above samples, we proceed to the reconstruction of the redshift distribution of the photometrically selected Stripe 82 LRG candidates. To estimate the probability distribution function of the redshift, $\phi_p(z)$, for the high-z LRG candidates we use equation (3.12). The pair-weighted clustering signal of the cross-correlations has been integrated up to $\approx 6'$ for each redshift bin.

In Fig. 3.9 we can see the two cases of the estimated probability distribution function of the redshift for the high-z LRG candidates. For the first case, $\phi_p(z)$ has been estimated by using the spectroscopic SDSS QSOs whereas in the other case, $\phi_p(z)$ is estimated using only the photometric SDSS QSOs (DEEP2 galaxies and MEGAz-LRGs are also always used). For both cases we plot the errors estimated for each point in the redshift bin from the contributed cross-correlated sample.
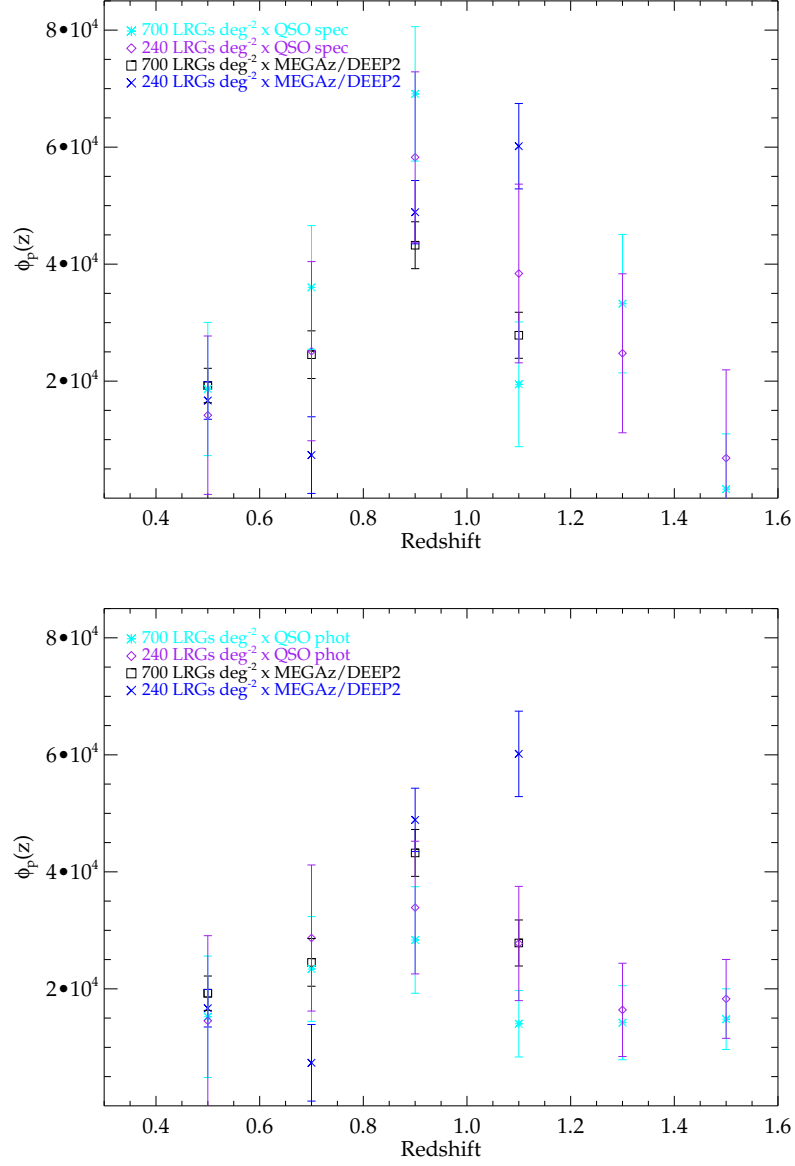
Figure 3.9: (a) The probability distribution function of the redshift, $\phi_p(z)$, of the 700 $\deg^{-2}$ and 240 $\deg^{-2}$ Stripe 82 LRGs as estimated through cross-correlations with MEGAz-LRGs, DEEP2 galaxies and spectroscopic SDSS QSOs. (b) Same as in (a) but now using photometric SDSS QSOs instead of spectroscopic in the cross-correlations. Error bars shown in both cases are 1σ jackknife summed up to $6'$.

To estimate the redshift distribution, *n(z)*, we use the weighted mean for the $\phi_p(z)$ in each redshift bin, calculated through :

$$n(z) = \frac{\sum\limits_{i=1}^{k}(\phi_p(i)/\sigma_i^2)}{\sum\limits_{i=1}^{k}(1/\sigma_i^2)}, \qquad (3.13)$$

where *k* is the total number of bins at that redshift, $\phi_p(i)$ is the measured probability distribution function of each cross-correlation data set in the *i*th bin and σ_i the error on that measurement.

The spectroscopic QSO $\phi_p(z)$ in Fig. 3.9a compared to the photo-z case in Fig. 3.9b, gives increased probability at $z \sim 1$. This may be explained by the SDSS QSO spectroscopic redshifts being more precise. For this reason, in our analysis and in fitting models to our $w(\theta)$ results, we will use only the spectroscopic *n(z)* for higher accuracy.

In Fig. 3.10 we plot the normalized redshift distribution of the $240 \deg^{-2}$ and $700 \deg^{-2}$ LRGs samples as calculated from Eq. 3.12 - 3.13. When we selected the two LRG samples from the izK colour-plane, we applied a redder selection for the $240 \deg^{-2}$ sample (see Eq. 3.1), aiming for a sample with a slightly higher redshift peak in the distribution as predicted from the evolutionary tracks in Fig. 3.1. This small difference may be seen between the spectroscopic *n(z)* of the $700 \deg^{-2}$ and $240 \deg^{-2}$ samples where the bluer cut has an average of $z \sim 1$ where for the redder sample the average is $z \sim 1.1$. But since the $700 \deg^{-2}$ LRG sample has higher statistical accuracy in the *n(z)* determination, the majority of our analysis will be focused in this sample.

3.5 Results

3.5.1 Measured $w(\theta)$ and comparisons

In Fig. 3.11 we compare the observed angular correlation function of the $700 \deg^{-2}$ LRG in Stripe 82 with Sawangwit et al. (2011) results. The $w(\theta)$ measurements are presented with 1σ Jackknife errors.

The work of Sawangwit et al. involved three LRG data sets at $z \leq 1$:
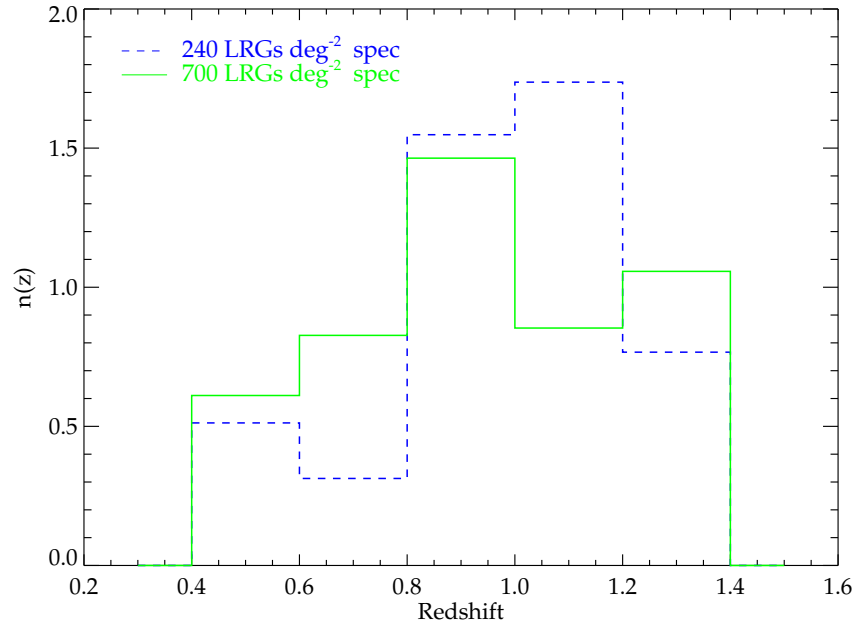
Figure 3.10: Weighted normalised redshift distribution of the Stripe 82 LRGs candidate samples when we use the spectroscopic SDSS QSOs along with the DEEP2 and MEGAz-LRG data sets. As expected the $700 \deg^{-2}$ sample (solid green line) n(z) peak is lower when compared with the $240 \deg^{-2}$ sample (dashed blue line).

1. SDSS LRGs at $z \sim 0.35$

2. 2SLAQ LRGs $z \sim 0.55$

3. AAΩ LRGs $z \sim 0.68$

From Fig. 3.11 we can see that at small scales, $\theta \lesssim 1'$, the clustering trend for all the samples is similar but with decreasing amplitude for increasing redshift. At larger scales, we note that the $w(\theta)$ of the Stripe 82 LRGs seems to have a flatter slope than the other samples, departing from the expected behaviour for the correlation function.

Further comparisons below with the LRG clustering results of Sawangwit et al. will focus on the slope and amplitude of the $w(\theta)$ results, with an initial view to interpret any changes in terms of evolution. It is therefore of interest to see how the Stripe 82 sample match to the LRG samples used in previous studies in terms of luminosity and comoving
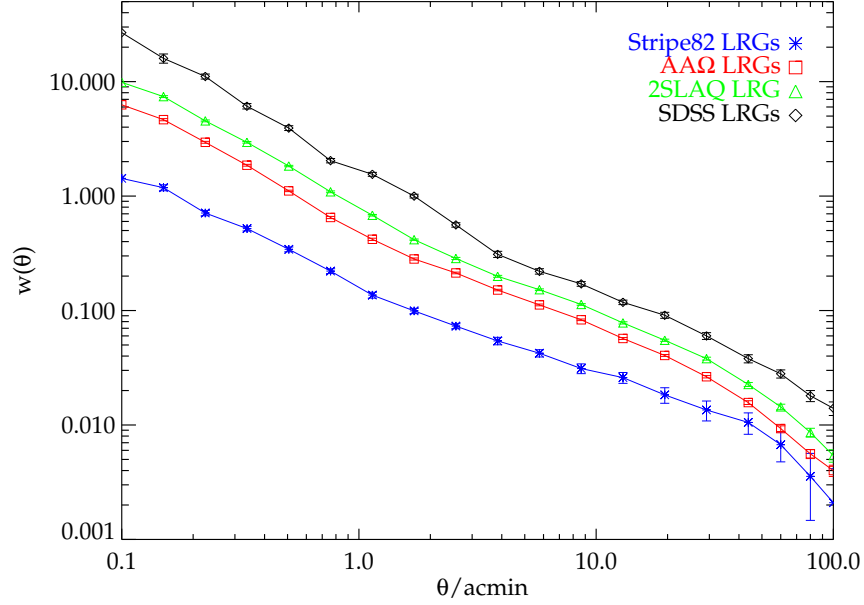
Figure 3.11: The angular correlation function, $w(\theta)$, from the 700 deg^{-2} Stripe 82 LRGs (star), AAΩ LRGs (square), 2SLAQ LRGs (triangle) and SDSS LRGs (diamond). At small scales all of the measurements show similar clustering behaviour, but at large scales the Stripe 82 clustering slope appears to be flatter than the lower z samples.

space density.

A pair-weighted galaxy number density is given by (see e.g. Ross et al., 2008a) :

$$n_g = \int dz \frac{H(z)n(z)}{\Omega_{obs} \, c \, l^2(z)} \times n^2(z) \Big/ \int dz n^2(z) \qquad (3.14)$$

where Ω_{obs} is the observed area of the sky, $l(z)$ is the comoving distance to redshift z and c is the speed of light. The observed space density for the 700 deg^{-2} Stripe 82 sample is found to be $\approx 3.20 \pm 0.16 \times 10^{-4} \mathrm{h}^3 \mathrm{Mpc}^{-3}$. The quoted 1σ error has been estimated from the difference of the number density as calculated through Eq. 3.14 and by converting Fig. 3.10 into a plot of number density as a function of z (by dividing its bin by its corresponding volume).

Within the uncertainties of our $n(z)$, the 700 deg^{-2} sample appears to have similar space density to that of the AAΩ LRG sample (see Table 3.2 in §3.5.2). However, in this study we do not yet have redshift information for individual LRGs, not even for a subset

of the sample. Hence it is more uncertain if our sample has similar luminosity as the LRG samples used by Sawangwit et al. (2011). We therefore take the fact that the samples are number-density matched to imply that they are also approximately luminosity matched which may turn out to be a reasonable assumption (see e.g. Sawangwit et al. 2011). This then should enable us to compare the clustering slopes and amplitudes of the AAΩ and Stripe 82 and infer any evolution independently of luminosity dependence.

3.5.2 $w(\theta)$ **and power-law fits**

Our first aim here is to fit power-laws to the Stripe 82 $w(\theta)$ to provide a simple parameterisation of the results. Our second aim is to make comparisons of the 3-D correlation amplitudes and slopes to measure evolution. Both aims will require application of Limber's formula to relate the 2-D and 3-D correlation functions.

We begin by noting that the simplest function fitted to correlation functions is a single power-law with amplitude r_0 and slope γ. In previous studies, the spatial correlation function has been frequently described by a power-law of the form:

$$\xi(r) = \left(\frac{r}{r_0}\right)^{-\gamma}. \tag{3.15}$$

The angular correlation function as a projection of $\xi(r)$ can be written as $w(\theta) = \alpha\theta^{1-\gamma}$, commonly with a slope fixed at $\gamma = 1.8$. The amplitude of the angular correlation function, α, can be related with the correlation length r_0 through Limber's formula (Eq. 1.26) using the equation (Blake et al., 2008):

$$\alpha = C_\gamma \, r_0^\gamma \int dz \, n(z)^2 \left(\frac{dx}{dz}\right)^{-1} x(z)^{1-\gamma}, \tag{3.16}$$

where $n(z)$ is the redshift distribution, $x(z)$ is the comoving radial coordinate at redshift z and the numerical factor $C_\gamma = \Gamma\left(\frac{1}{2}\right)\Gamma\left(\frac{\gamma}{2} - \frac{1}{2}\right)/\Gamma\left(\frac{\gamma}{2}\right)$.

A deviation from a single power law at $\sim 1\mathrm{h}^{-1}\mathrm{Mpc}$ has been measured in previous studies (Shanks et al., 1983; Blake et al., 2008; Ross et al., 2008b; Kim et al., 2011; Sawangwit et al., 2011) and can be explained by the the 1-halo and 2-halo terms imprinted in the clustering signal under the assumption of the halo model (see §3.5.4). To parameterise

the clustering characteristics of our sample, we fit a single-power law and a double-power law to our measured angular correlation function. The double power-law form is given as:

$$w_1(\theta) = \left(\frac{\theta}{\theta_{0,1}}\right)^{1-\gamma_1} \quad (\theta < \theta_b) \tag{3.17}$$

$$w_2(\theta) = \left(\frac{\theta}{\theta_{0,2}}\right)^{1-\gamma_2} \quad (\theta \geq \theta_b) \tag{3.18}$$

with θ_b to be the break point at $\approx 1.2'$ where the power-law slope changes from being steeper at small scales ($< 1.2'$), to flatter at large scales.

Table 3.2: Best fit parameters for the single and double power-law fits to the angular correlation function.

Sample	$\bar{z}$	n_{g} $(h^3 Mpc^{-3})$	Single power-law				Double power-law			
			γ	$r_0(h^{-1}\,\mathrm{Mpc})$	χ^2_{red}		$\gamma_{1,2}$	$r_{0,1,2}(h^{-1}\,\mathrm{Mpc})$	$r_b(h^{-1}\,\mathrm{Mpc})$	χ^2_{red}
AAΩ LRGs	0.68	2.7×10^{-4}	1.96 ± 0.01	7.56 ± 0.03	42.8		2.14 ± 0.01	5.96 ± 0.03	1.3	3.4
$(110 deg^{-2})$							1.81 ± 0.02	7.84 ± 0.04		
Stripe82 LRGs	1.0	$3.20 \pm 0.16 \times 10^{-4}$	2.01 ± 0.01	7.54 ± 0.16	5.89		2.01 ± 0.02	7.63 ± 0.27	2.38	3.65
$(700\ deg^{-2})$							1.64 ± 0.04	9.92 ± 0.40		

Figure 3.12: The best-fit single power law (diamond) and double power law (triangle), for the $700 \deg^{-2}$ LRGs candidates overplotted on the angular correlation function (square) with the 1σ Jackknife error. Lower panel shows the fitting residuals.

The power-laws are fitted in the range $0.1' < \theta < 30'$ using the χ^2-minimization with the full covariance matrix constructed from the jackknife resampling (see §3.3.2):

$$\chi^2 = \sum_{i,j=1}^{N} \Delta w(\theta_i) \mathbf{C}_{ij}^{-1} \Delta w(\theta_j) \tag{3.19}$$

where N is the number of angular bins, $\Delta w(\theta_i)$ is the difference between the measured angular correlation function and the model for the ith bin, and $\mathbf{C}_{ij}^{-1}$ is the inverse of the covariance matrix.

For the single power-law, our best-fit spatial clustering length and clustering slope pair from Limber's formula are measured to be $r_0 = 7.54 \pm 0.16 \mathrm{h}^{-1}\mathrm{Mpc}$ and $\gamma = 2.01 \pm 0.01$ with associated reduced $\chi^2_{red} = 5.89$. The $r_0 - \gamma$ pairs for the double power-law are $r_{0,1} = 7.63 \pm 0.27 \mathrm{h}^{-1}\mathrm{Mpc}$ and $\gamma_1 = 2.01 \pm 0.02$ at small scales and $r_{0,2} = 9.92 \pm 0.40 \mathrm{h}^{-1}\mathrm{Mpc}$ and $\gamma_2 = 1.64 \pm 0.04$ at large scales with a reduced $\chi^2_{red} = 3.65$. From the intersection of the 2 power law for $\xi(r)$, we have calculated the break scale, $r_b = 2.38 \mathrm{h}^{-1}\mathrm{Mpc}$. This is higher than the $r_b = 1.3 - 2.2 \mathrm{h}^{-1}\mathrm{Mpc}$ estimated from the SDSS, 2SLAQ and AAΩ LRG

surveys (Sawangwit et al., 2011).

In Fig. 3.12 we show the data points including the 1σ Jackknife errors with the best-fitting power laws where the largest scale considered in the fitting was $\theta < 30'$, which corresponds to $r \lesssim 20h^{-1}Mpc$ at $z \sim 1$ for the 700 deg^{-2} LRG sample. Fig. 3.12 confirms that the double power-law clearly gives a better fit to the data than the single power-law. Note that in the case of the single power-law and the double power-law at small scales, our results give $r_0 - \gamma$ values consistent with outcomes from previous studies. However, at large scales the Stripe 82 slope ($\gamma_2 = 1.64 \pm 0.04$) is significantly flatter than the AAΩ result ($\gamma_2 = 1.81 \pm 0.02$).

Fig. 3.13 shows the double power-law fits for AAΩ (dashed red lines) taken from Sawangwit et al. and then evolved (black and green dot-dashed lines) to the Stripe 82 depth using Eq. 3.16 under the assumptions of comoving and virialised clustering, respectively. We shall interpret the amplitude scaling in the discussion of evolution in §3.7.1 later. At this point we again note that the biggest discrepancy seems to be at large scales where the Stripe 82 slope is increasingly too flat relative to the AAΩ result. Fitted parameters are given in Table 3.2, where the best-fit power-law parameters for the AAΩ LRG sample (Sawangwit et al., 2011) are also presented for comparison.

We note here that Kim et al. (2011) studied the clustering of extreme red objects (EROs) at $1 < z < 2$ in the SA22 field and they report a similar change of the large scale slope. Gonzalez-Perez et al. (2011) tried to fit clustering predictions from semi-analytic simulations to the Kim et al. ERO $w(\theta)$ but found that the model underpredicts the clustering at large scales.

3.5.3 ΛCDM model fitting in the linear regime

Since the standard ΛCDM model was found to give a good fit to the lower redshift LRG samples of Sawangwit et al. (2011), we now check to see whether the flatter large-scale slope of the Stripe 82 LRG $w(\theta)$ leads to a statistically significant discrepancy with the ΛCDM model at $z \approx 1$. We generate matter power spectra using the 'CAMB' software (Lewis, Challinor, & Lasenby, 2000), including the case of non-linear growth of structure correction. For this reason we use the 'HALOFIT' routine (Smith et al., 2003) in 'CAMB'.
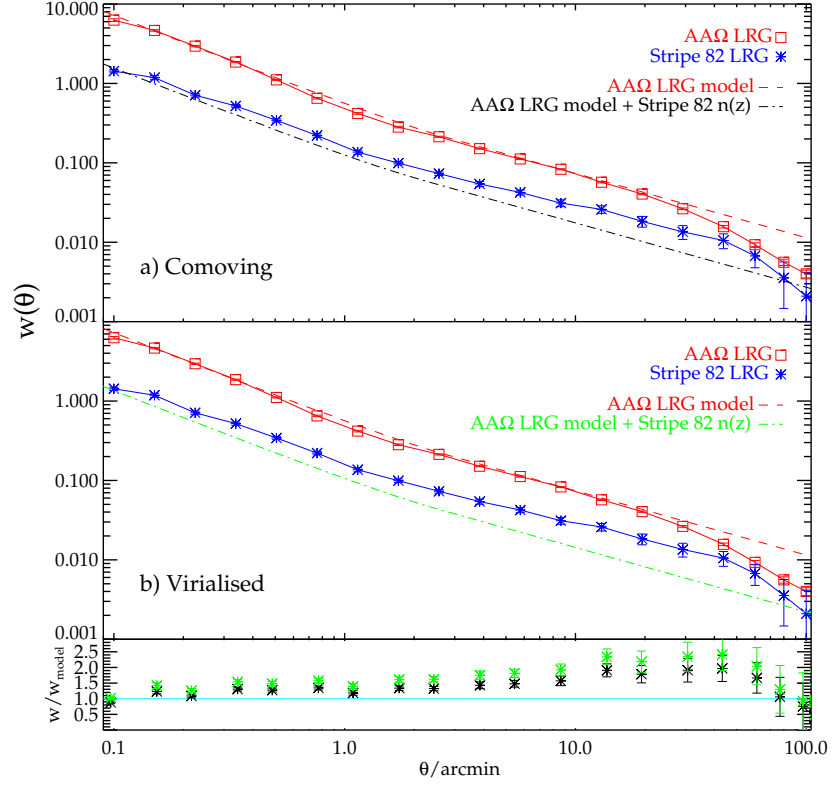
Figure 3.13: **a)** The AAΩ LRG raw $w(\theta)$ measurements (red square) with predictions from comoving evolution model (dashed red line), using the best-fit double power-law $r_0 - \gamma$ values with Limber's formula as Sawangwit et al. (2011) calculated. We then evolve the AAΩ best-fits utilising the estimated $700 \deg^{-2}$ Stripe 82 LRG *n(z)* under the assumption of comoving evolution (dashed-dot black line) clustering. The observed Stripe 82 LRG $w(\theta)$ is shown as well (blue star). **b)** Same raw measurements as above, but now compared to the virialised evolution clustering model. Stripe 82 LRG $w(\theta)$ measurements are described more accurate with comoving evolution at small and large scales compared to virialised evolution as it can been seen from the lower panel, where are plotted the residuals of the observed Stripe 82 $w(\theta)$ versus the comoving evolution (black star) and virialised evolution (green star) models, respectively.
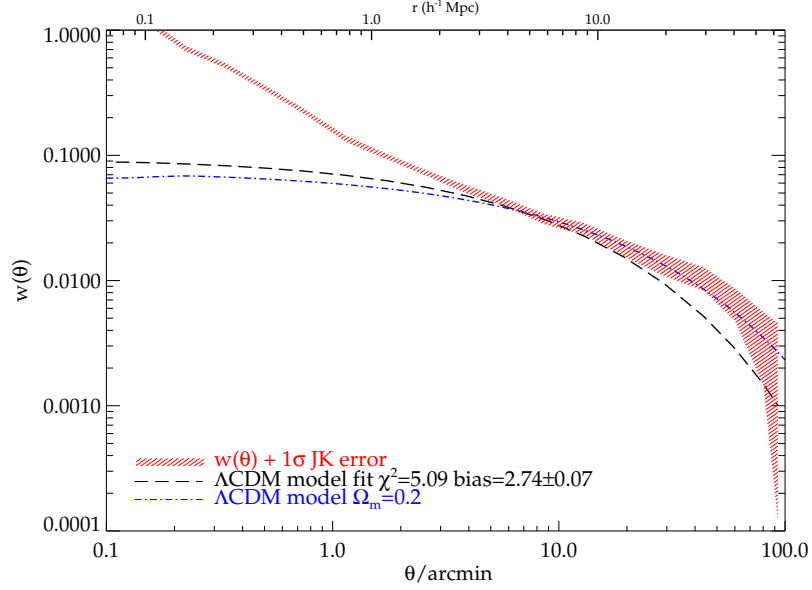
Figure 3.14: The best-fit spatially flat, ΛCDM model assuming $\Omega_m = 0.27$ compared to the observed $w(\theta)$ of Stripe 82 700 $\deg^{-2}$ LRGs in the linear regime. The standard model cannot explain the large scale power excess in the angular correlation function of the Stripe 82 LRGs. The shaded area corresponds to $\pm 1\sigma$ jackknife error. Also shown is a spatially flat ΛCDM model with the same parameters as before except for a lower value of $\Omega_m = 0.2$ and an arbitrary normalisation. The $\Omega_m = 0.2$ model appears to give a better fit than the standard $\Omega_m = 0.27$ model.

Our models assume a ΛCDM Universe with $\Omega_\Lambda = 0.73$, $\Omega_m = 0.27$, $f_{baryon} = 0.167$, $\sigma_8 = 0.8$, $h = 0.7$ and $n_s = 0.95$. Then we transform the matter power spectra to obtain the matter correlation function, $\xi_{\mathrm{m}}(r)$, using:

$$\xi_{\mathrm{m}}(r) = \frac{1}{2\pi^2} \int_0^\infty P_m(k) k^2 \frac{\sin kr}{kr} dk. \tag{3.20}$$

The relationship between the galaxy clustering and the underlying dark-matter clustering is given by the bias, b_g :

$$b_{\mathrm{g}}^2(r) = \frac{\xi_{\mathrm{g}}(r)}{\xi_{\mathrm{m}}(r)}. \tag{3.21}$$

As we are interested in the linear regime, we fit the projected $\xi_{\mathrm{m}}(r)$ to the Stripe 82 LRG $w(\theta)$ in the range $4' \lesssim \theta \lesssim 45'$, corresponding to comoving separations $3 \lesssim r \lesssim 30 \mathrm{h}^{-1}$Mpc. By fitting the model predictions to the measured $w(\theta)$ it will result with the best linear bias factor, the only free parameter in this case. For our fitting, the χ^2-

minimization with the full covariance matrix constructed from the jackknife resampling (see §3.3.2) has been used.

The best-fit linear bias parameter is estimated to be $b = 2.74 \pm 0.07$ with $\chi^2_{red} = 5.09$. The upper limit of our fitted range in θ was varied, while the lower limit stayed constant to avoid any contribution from the non-linear regime. Thus, for the range $\sim 4' - 30'$ the best-fit bias is $b = 2.8 \pm 0.08$ with $\chi^2_{red} = 4.72$ and at $\sim 4' - 60'$ is $b = 2.69 \pm 0.07$ with $\chi^2_{red} = 5.18$. In Fig. 3.14 we plot the LRG $w(\theta)$ with the 1σ error and the ΛCDM model with the best-fit bias. For low values of the upper limit of the fitting range, the measured biases are in approximate agreement with other results in the literature. But in terms of the flat slope of $w(\theta)$ at large scales, the standard ΛCDM linear model is inconsistent with the data at the $2 - 3\sigma$ level. One of the aims of the next section will be to see if a HOD model can explain the flat large-scale slope of the $z \approx 1$ Stripe 82 LRGs.

3.5.4 Halo model analysis

We are going to use the approach of the halo model (see Cooray & Sheth, 2002, for a review) of galaxy clustering to finally fit our angular correlation function results. Under the halo-model framework we can examine the way the dark matter haloes are populated by galaxies through the Halo Occupation Distribution (HOD). Various studies have used this model to fit their results (e.g. Masjedi et al., 2006; White et al., 2007; Blake et al., 2008; Wake et al., 2008; Brown et al., 2008; Ross et al., 2008a; Zheng et al., 2009; Sawangwit et al., 2011; Gonzalez-Perez et al., 2011) as a way to explain the galaxy correlation function and gain insight into their evolution. Specifically, we shall investigate whether the HOD model may be able to explain the flatter slope of the correlation function observed here.

In the halo model, the clustering of galaxies is expressed by the contribution of number of pairs of galaxies within the same dark matter halo (one-halo term, $\xi 1$) and to pairs of galaxies in two separate haloes (two-halo term) :

$$\xi(r) = \xi_{1h}(r) + \xi_{2h}(r). \tag{3.22}$$

The 1-halo term dominates on small scales $\lesssim 1Mpc$.

The fundamental ingredient in the HOD formalism of galaxy bias is the probability distribution $P(N|M)$, for the number of galaxies N to hosted by a dark matter halo as a function of its mass M.

We use the so-called centre-satellite three-parameter HOD model (e.g. Seo et al., 2008; Wake et al., 2008; Sawangwit et al., 2011) which distinguishes between the central galaxy and the satellites in a halo. This separation has been shown in simulatations (Kravtsov et al., 2004) and has been commonly used in semi-analytic galaxy formation models in the last years (Baugh, 2006).

Different HODs are applied for the central and satellite galaxies. We assume that only haloes which host a central galaxy are able to host satellite galaxies. The fraction of haloes of mass M with centrals is modelled as:

$$\langle N_{\rm c}|M\rangle = \exp\left(\frac{-M_{\rm min}}{M}\right). \tag{3.23}$$

In such haloes, the number of satellite galaxies follows a Poisson distribution (Kravtsov et al., 2004) with mean:

$$\langle N_{\rm s}(M)\rangle = \left(\frac{M}{M_1}\right)^{\alpha}. \tag{3.24}$$

To describe the distribution of the satellite galaxies around the halo centre we use the NFW profile (Navarro et al., 1997). So, the mean number of galaxies residing in a halo of mass M is:

$$\langle N|M\rangle = \langle N_{\rm c}|M\rangle \times (1 + \langle N_{\rm s}|M\rangle. \tag{3.25}$$

and the predicted galaxy number density from the HOD is then:

$$n_{\rm g} = \int {\rm d}M\, n(M)\, \langle N|M\rangle \tag{3.26}$$

where $n(M)$ is the halo mass function, where in our case we use the model of Sheth & Lemson (1999).

From the HOD we can derive useful quantities which are the central fraction :

$$F_{\rm cen} = \frac{\int {\rm d}M\, n(M)\, \langle N_{\rm c}(M)\rangle}{{\rm d}M\, n(M)\, \langle N_{\rm c}(M)\rangle\, [1 + \langle N_{\rm s}(M)\rangle]}, \tag{3.27}$$

and the satellite fraction of the galaxy population:

$$F_{\rm sat} = \frac{1}{n_{\rm g}} \int {\rm d}M\, n(M)\, \langle N_{\rm c}(M)\rangle\, \langle N_{\rm s}|M\rangle, \tag{3.28}$$

as $F_{sat} = 1 - F_{cen}$. We can also determine the effective mass, M_{eff}, of the HOD:

$$M_{\text{eff}} = \frac{1}{n_{\text{g}}} \int dM \, n(M) M \, \langle N|M \rangle, \tag{3.29}$$

and the effective large-scale bias:

$$b_g = \frac{1}{n_{\text{g}}} \int dM \, n(M) b(M) \, \langle N|M \rangle, \tag{3.30}$$

where $b(M)$ is the halo bias, for which we use the ellipsoidal collapse model of Sheth et al. (2001) and the improved parameters of Tinker et al. (2005).

As the galaxy correlation function is the Fourier transform of the power spectrum, the 1-halo term and the 2-halo term of the clustering functions can be written as:

$$P(k) = P_{1\text{h}}(k) + P_{2\text{h}}(k). \tag{3.31}$$

Moreover the 1-halo term can be distinguished from the contribution of the central-satellite pairs, $P_{\text{cs}}(k)$, and satellite-satellite pairs, $P_{\text{ss}}(k)$, (see e.g. Skibba & Sheth, 2009):

$$P_{\text{cs}}(k) = \frac{1}{n_{\text{g}}^2} \int dM \, n(M) 2 \, \langle N_{\text{c}}|M \rangle \, \langle N_{\text{s}}|M \rangle \, u \, \langle k|M \rangle, \tag{3.32}$$

and

$$P_{\text{ss}}(k) = \frac{1}{n_{\text{g}}^2} \int dM \, n(M) \, \langle N_{\text{c}}|M \rangle \, \langle N_{\text{s}}|M \rangle^2 \, u \, \langle k|M \rangle^2, \tag{3.33}$$

where $u \, \langle k|M \rangle$ is the NFW density profile in Fourier space and we have simplified the number of satellite-satellite pairs $\langle N_{\text{s}}(N_{\text{s}} - 1)|M \rangle$ to $\langle N_{\text{s}}|M \rangle^2$ since the satellites are Poisson-distributed.

The 2-halo term is evaluated as:

$$\begin{aligned}
P_{2\text{h}}(k, r) &= P_{\text{m}}(k) \times \frac{1}{n_{\text{g}}'^2} \\
&\times \left[\int_0^{M_{\text{lim}}(r)} dM \, n(M) b(M, r) \, \langle N(M) \rangle \, u(k, M) \right]^2,
\end{aligned} \tag{3.34}$$

where $P_{\text{m}}(k)$ is a non-linear matter power spectrum. We derive the mass limit, $M_{\text{lim}}(r)$, using the 'n_{g}'-matched' approximation of (Tinker et al., 2005), which accounts the effect of halo exclusion: different haloes cannot overlap. n_{g}' is the restricted galaxy number density (Eq. B13 of Tinker et al. (2005)).

Table 3.3: Best-fit HOD parameters for the AAΩ LRGs and the 700 deg^{-2} Stripe 82 LRGs

Sample	$\bar{z}$	$M_{\min}$ $(10^{13}h^{-1}M_{\odot})$	M_1 $(10^{13}h^{-1}M_{\odot})$	α	n_{g} $(10^{-4}h^3Mpc^{-3})$	M_{eff} $(10^{13}h^{-1}M_{\odot})$	F_{sat} (per cent)	b_{lin}	χ^2_{red}
AAΩ	0.68	1.02 ± 0.03	12.6 ± 1.0	1.50 ± 0.03	3.1 ± 0.4	3.0 ± 0.1	9.0 ± 0.09	2.08 ± 0.03	13.6
S82 (10′)	1.0	3.09 ± 0.75	30.2 ± 6.7	2.38 ± 0.12	0.5 ± 0.3	4.0 ± 0.6	2.13 ± 1.0	3.01 ± 0.21	2.4
S82 (30′)	1.0	2.57 ± 0.31	25.7 ± 3.1	2.28 ± 0.04	0.6 ± 0.2	3.6 ± 0.5	2.62 ± 0.07	2.90 ± 0.15	2.3
S82 (45′)	1.0	2.19 ± 0.63	21.9 ± 5.6	2.24 ± 0.12	0.8 ± 0.3	3.3 ± 0.6	3.17 ± 0.10	2.81 ± 0.18	3.1
S82 (60′)	1.0	2.19 ± 0.21	21.9 ± 2.1	2.25 ± 0.05	0.8 ± 0.2	3.3 ± 0.3	3.17 ± 0.08	2.81 ± 0.10	3.6

For the scale-dependent halo bias, $b(M, r)$, we use the model given by Tinker et al. (2005):

$$b^2(M, r) = b^2(M) \frac{[1 + 1.17\xi_{\mathrm{m}}(r)]^{1.49}}{[1 + 0.69\xi_{\mathrm{m}}(r)]^{2.09}}, \qquad (3.35)$$

where $\xi_{\mathrm{m}}(r)$ is the non-linear matter correlation function. For the 2-halo term, we need to correct the galaxy pairs from the restricted galaxy density to the entire galaxy population.

By using Limber's formula to project the predicted spatial galaxy correlation function $\xi(r)$ to the angular correlation function $w(\theta)$ and we fit for a variety of the three-parameter halo model (M_{min}, M_1, α).

The best-fit model for each of our sample is then determined from the minimum value of the χ^2-statistic using the full covariance matrix. We use the full covariance matrix over the range $0.25' < \theta < 60'$ in our fitting. Smaller scales are excluded in the fitting because any uncertainty in the $\xi(r)$ model can have a strong effect on $w(\theta)$ due to the projection. To determine the 1σ error on the fits, the region of parameter space from the best fits with $\delta\chi^2 \leq 1$ (1σ for 1 degree of freedom) is considered. For b_{lin}, M_{eff}, F_{sat} and n_{g} which depend on all the three main parameters, the considered region of the parameter space becomes $\delta\chi^2 \leq 3.53$.

Fig. 3.15a shows the resulting best-fit HOD of the mean number of LRGs per halo along with the central and satellite contributions. The best-fitting values for M_{min}, M_1 and α where $M_{min} = 2.19 \pm 0.63 \times 10^{13}\mathrm{h}^{-1}\mathrm{M}_\odot$, $M_1 = 21.9 \pm 5.6 \times 10^{13}\mathrm{h}^{-1}\mathrm{M}_\odot$ and $\alpha = 2.24 \pm 0.12$, respectively. The associated values for b_{lin}, M_{eff}, F_{sat} and n_{g} are given in Table 3.3.

We see that the $\langle N|M \rangle$ of the LRGs flatten at unity, as expected from the assumption satellite galaxies are hosted by halos with central galaxies. The LRGs as expected populate massive dark matter haloes with the masses $\approx 10^{13} - 10^{14}\mathrm{h}^{-1}\mathrm{M}_\odot$. With the fraction of LRGs that are satellites being less than 5%, we therefore find that $> 95\%$ of LRGs are central galaxies in their dark matter haloes. The best fit linear bias, $b_{\mathrm{lin}} \approx 2.8$, agrees with the prediction from Sawangwit et al. (2011) in the case of a long lived model for the LRGs and indicates that the LRGs are highly biased tracers of the clustering pattern. The effective mass, $M_{\mathrm{eff}} \approx 3 \times 10^{13}\mathrm{h}^{-1}\mathrm{M}_\odot$, confirms that LRGs are hosted by the most massive dark matter haloes. Despite the fact that we use a higher redshift LRG sample, our
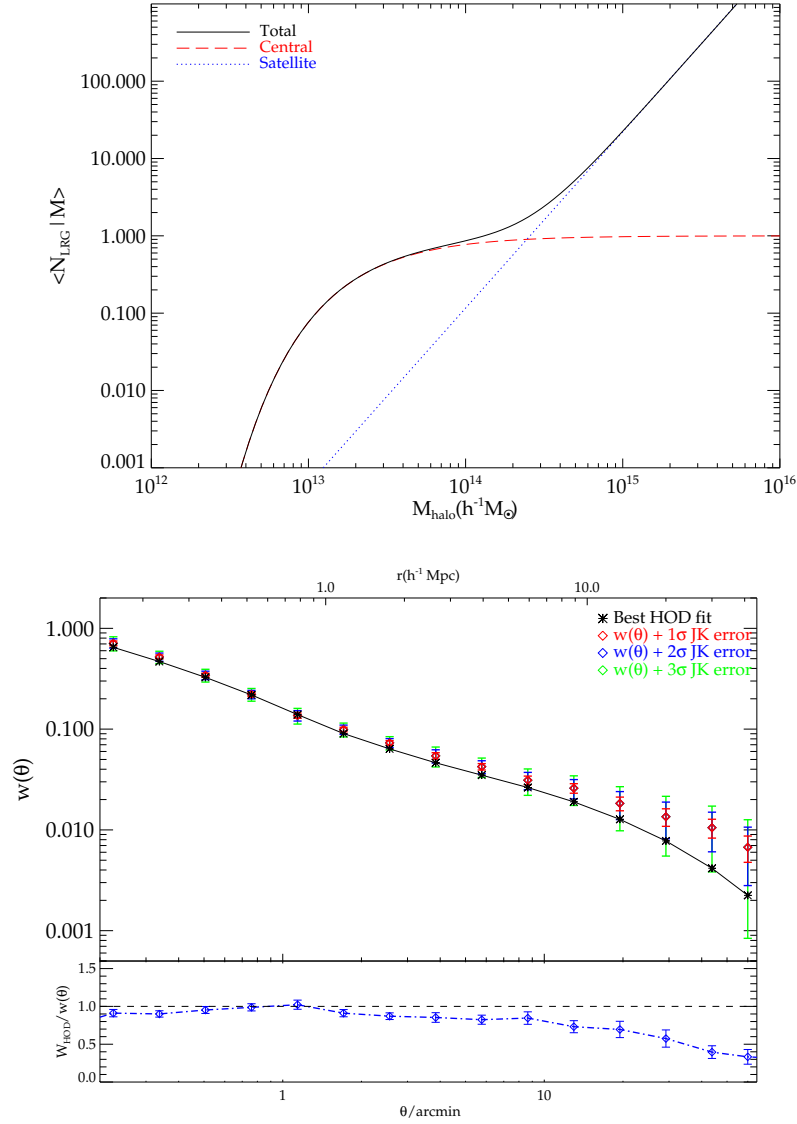
Figure 3.15: (a) The mean number of LRGs per halo as a function of halo mass at $z = 1$. The total, central and satellite contributions are shown by the solid, dashed and dotted lines, respectively. (b) The measured angular correlation function $w(\theta)$ for the 700 $\deg^{-2}$ LRG sample with the best HOD fit (black star). The 1, 2 and 3σ Jackknife errors are shown in red, blue and green, respectively.

best-fit HOD parameters are statistically not too dissimilar to those found in previous LRG studies (see Table 3.3).

In Fig. 3.15b we show the best-fit model for $w(\theta)$, compared to the data. The first thing we notice is that while at small scales the best-fit HOD are in good agreement with the $w(\theta)$ measurements, at large scales the model fits only at $2 - 3\sigma$. The flatter slope at large scales is responsible for that and we still are not able to say if this can be explained by evolution in the linear regime or any kind of systematic effect. In §3.6 we will check systematic errors that could affect our results.

Moreover, due to the high value of the best-fit reduced $\chi^2 = 3.1$, we also try to fit the HOD models at different scales by using 4 different maximum θ bins of the covariance matrix in our fits, which we present in Table 3.3. The fits at large scales did not improve and above $45'$ there was not any change in the best-fit HOD measurements.

Considering the two-halo term in the HOD model, one can see that the bias in this regime is mostly scale-independent and the correction factor is in fact having the opposite effect on the slope. The scale-independent bias is simply the average of the halo bias, $b(M)$, weighted by the halo mass function and the mean number of galaxies hosted by the corresponding halo. One way to boost the large-scale amplitude is to increase M_{min} and therefore increase the mass range of the halo where most galaxies occupy and hence linear bias and amplitude of the two-halo term. However, to compensate for the increase numbers of satellite galaxies (and consequently small-scale clustering amplitude) one must also increase M_1, the mass at which a halo hosts one satellite galaxy on average. And in order to produce the overall flatter slope one needs to increase M_1/M_{min}. However, this would still overpredict the clustering amplitude in the intermediate scales, $r \sim 5 - 10 \text{ h}^{-1}\text{Mpc}$. Note that our best-fit HOD gives $M_1/M_{\mathrm{min}} \approx 10$, consistent with previous results for lower redshift LRGs of (Sawangwit et al., 2011) and (Wake et al., 2008). However, as noted earlier including $w(\theta)$ bins at larger and larger scales does not change the best-fit parameters which means that M_1/M_{min} also remains unchanged due to the reason discussed above. We therefore conclude that the HOD prescription in the framework of standard ΛCDM cannot explain the observed large-scale slope in $w(\theta)$ of the $z \approx 1$ LRG sample.

3.6 Tests for systematic errors

In this section we will present an extended series of checks for systematic errors that might have affected our clustering analysis, with the major issue being the flatter slope at large scales as estimated in §3.5.2, §3.5.3 and §3.5.4. Tests for possible systematics that will be discussed here are:

- data gradient artefacts,

- $w(\theta)$ estimators bias,

- survey completeness,

- observational parameters ; such as star density, galactic extinction, seeing etc.

3.6.1 Data gradients and $w(\theta)$ estimator bias

A false clustering signal at large scales can arise from artificial gradients in the data, as the correlation function is very sensitive to such factors. In attempting to explain the behaviour of the observed $w(\theta)$ at large scales, first we divide the LRG sample area in 6 equal subfields in RA. Then the angular correlation function of each subfield has been calculated using the Landy & Szalay, Hamilton and the Peebles estimator - the standard estimator. Furthermore, we average the $w(\theta)$ results of the 6 subfields as measured by each estimator and we compare them with $700 \ \mathrm{deg}^{-2}$ LRG $w(\theta)$ full sample results (see Fig. 3.16).

From these comparisons, it is clear that when we use the Landy & Szalay and Hamilton estimators, we do not find any significant difference in the amplitude of the measured $w(\theta)$ between the averaged subfields' or between the full samples' measurements. When the averaged $w(\theta)$ measurements are compared with those from the full sample, only a very slightly smaller clustering signal in the averaged $w(\theta)$'s is seen, barely visible in Fig. 3.16. Furthermore, this is only the amount expected from the integral constraint (see §3.3.2) on $w(\theta)$, if the above Landy & Szalay estimate is assumed to apply in a single sub-field area. The standard estimator is known to be subject to larger statistical errors at
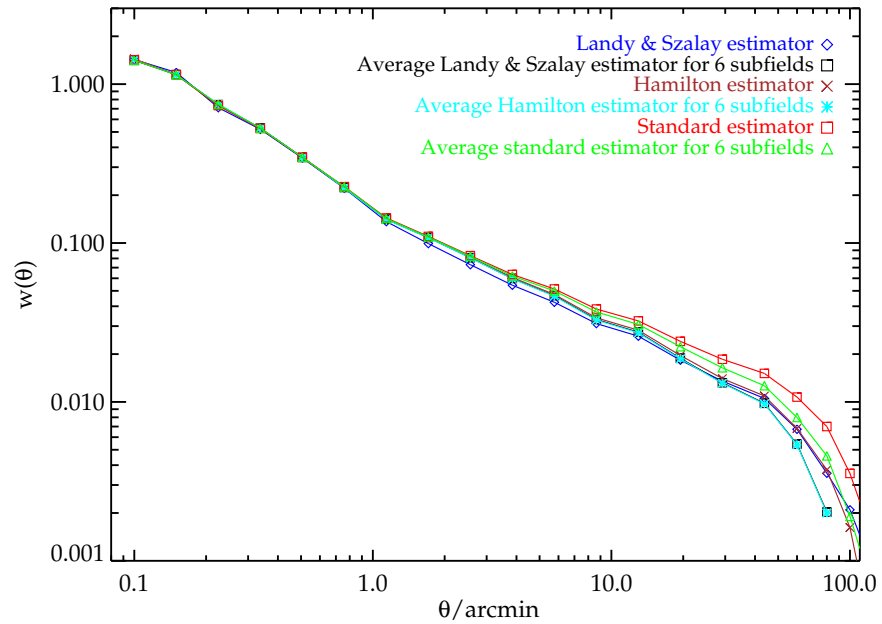
Figure 3.16: $w(\theta)$'s from Landy Szalay, Hamilton and standard estimator of the $700 \deg^{-2}$ LRG sample. For comparison, the averaged $w(\theta)$'s from the 6 subfields (see text for more detail), are overplotted as measured from each estimator. Landy & Szalay and Hamilton estimators, give similar results for the average subfields and the full sample measurements, respectively. The standard estimator is more biased, at larger scales.

large scales and here the signal is actually stronger when compared with the other two estimators.

Moreover, in Fig. 3.17 we display the results of the $w(\theta)$ measurements from the 6 subfields individually against the full sample measurements as estimated with the Landy & Szalay estimator in all cases. Even now we cannot see any major trend through the subfields' correlation function measurements, except possibly for the $15^0 \leq RA \leq 30^0$ subfield which has a steeper slope at larger scales.

3.6.2 Magnitude incompleteness

Another issue that we want to address is how the clustering signal can be affected by magnitude incompleteness. The izK colour selection used for the LRGs is applied up to the faintest limits of the SDSS-UKIDSS LAS surveys (see §3.2.1). To account for this, first
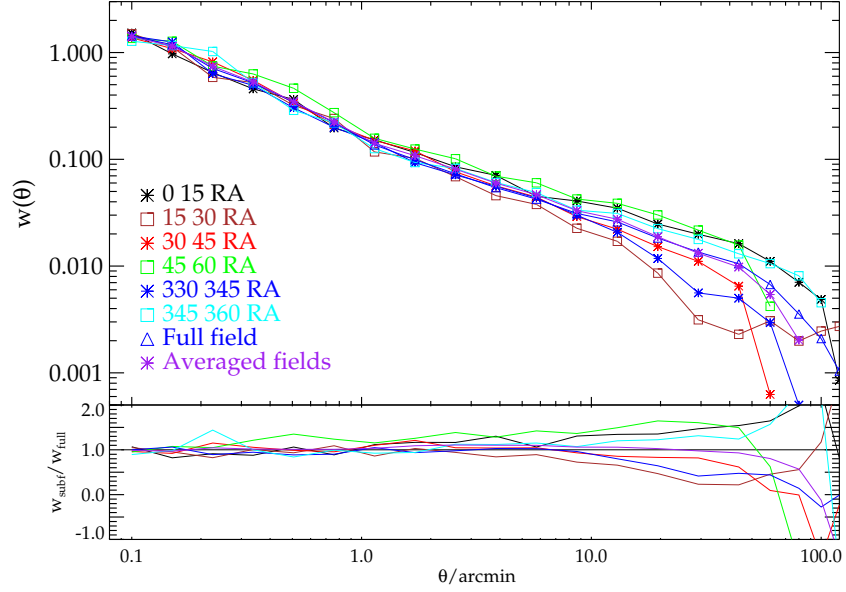
Figure 3.17: $w(\theta)$ results of the 6 equal size subfields ($15 \times 2.5\mathrm{deg}^2$ each) across Stripe 82, the total area as estimated by using the Landy Szalay estimator and the averaged clustering signal from the 6 subfields. In the bottom panel are displayed the ratios of the $w(\theta)$ of each subfield compared to the total area.

K	LRGs 700 deg^{-2}
17.0-17.2	4894
17.2-17.4	11096
17.4-17.6	22490
17.6-17.8	38659
17.8-18.0	53680

Table 3.4: K-limited sub-samples used for auto-correlations in Fig. 20.

we divide the 700 deg^{-2} LRG sample in 5 K magnitude bins in the range $17 < K < 18$. The number of LRGs in each magnitude bin is shown in Table 3.4.

Measurements of the angular correlation function from each K-bin are shown in Fig. 3.18, where measurement uncertainties are not shown as we are mostly interested in the shape of the $w(\theta)$ in the linear regime. The clustering signal from the K-magnitude
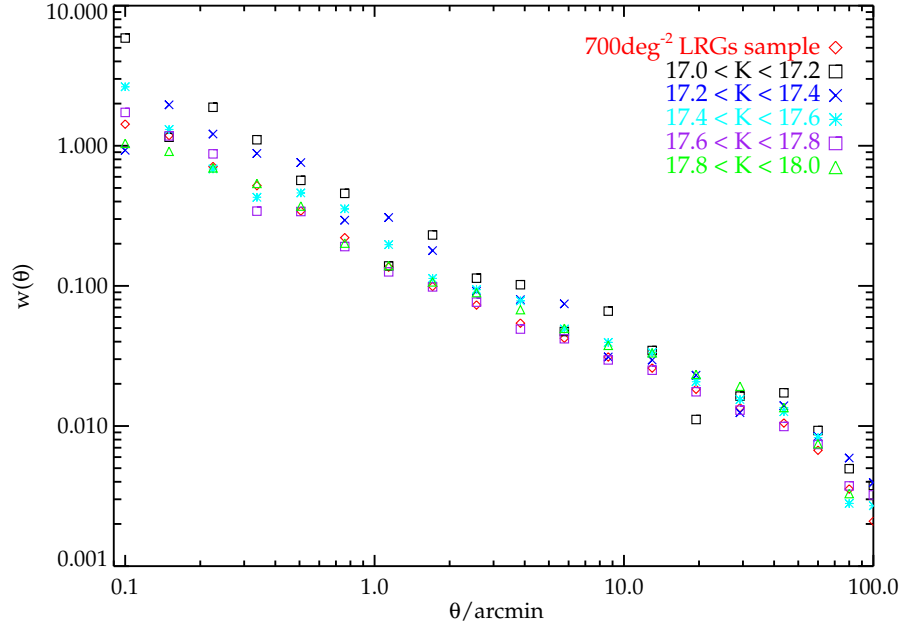
Figure 3.18: Auto-correlation functions from Landy-Szalay estimator for the 700 deg^{-2} LRG K-limited sub-samples from Table 4. Total sample is overplotted for comparison.

bins compared to the full sample do not show any significant difference at large scales and follow the full sample $w(\theta)$ shape. At smaller scales we see that the clustering from the brighter samples is higher than for the fainter samples, as expected.

The final tests of the magnitude incompleteness check are via the use of brighter colours in the zK selection. We therefore selected on the basis of brighter magnitudes down to $z \leq 21.2$ and $K \leq 17.2$, in various combinations and re-measured the angular correlation function. Even with these bright cuts, we did not see any change in the excess at large scales.

3.6.3 Observational parameters

The final test to identify a potential observational systematic effect follows the approach described by Ross et al. (2011), referring primarily to the area effectively masked by stars with magnitudes similar to the galaxies in the field. We cross-correlated the 700 deg^{-2} LRG sample with the Stripe 82 star catalogue from Ivezić et al. (2007), in 4 magnitude

bins, $i < 19.5, 20, 20.5, 21$. From the measured autocorrelation function of stars and the cross-correlation function of stars with LRGs we computed the effect of stellar masking on the LRG correlation function using their equations (28) and (29). We show these results in Fig. 3.19a.

The cross correlation results show a very small anticorrelation between LRGs and stars for the $i = 19.5$ and 20.5 bins. A possible explanation for this anticorrelation might be related to the fact that we see an increase in the star number density between $330 \leq RA \leq 340$ deg (see Fig. 3.19b). Next, we calculate the expected $w(\theta)$, as defined in Eq. 29 of Ross et al. (2011). In all cases, there was little difference in the expected and observed $w(\theta)$ of the $700 \deg^{-2}$ LRG sample. We conclude that the effect of stellar masking is essentially negligible, less than 1% of the clustering signal at $\theta \approx 90'$.

Stellar contamination could be another source of that could result extra power at larger scales. In Sawangwit et al. (2011), as emphasised earlier by Ross et al. (2008b), the *riz* selected AAΩ LRGs are expected to have 16 per cent stellar contamination. Sawangwit et al. after correcting their observed $w(\theta)$ upwards by the factor $1/(1 - f)^2$, where f is the contamination fraction (Blake et al., 2008), their results where in good agreement with the original measurements. For our case, the $z - K$ colour of the LRGs, reduces even more the stellar contamination down to 4.5 per cent. We need to correct the angular clustering signal by 9.5 percent. This correction affects only the amplitude and not the shape of the $w(\theta)$, so the origin of the power excess at large scales is still unknown.

Ross et al. (2011) also checked observational parameters such as: galactic extinction, sky background, seeing and airmass using the cross-correlation technique. The Stripe 82 LRG sample is K-limited. Hence, we explore if the above observed parameters from the UKIDSS LAS K-band could be sources of systematic errors at large scales. Fig. 3.20 displays the number density of Stripe 82 LRGs and how it is related with each potential observational systematic (stars are from Ivezić et al. 2007). From Fig. 3.20 we see a sharp decrease in the number of LRGs with high galactic extinction and poor seeing. The airmass fluctuations are also large compared to the error bars. The majority of the LRGs lie within the first few bins of galactic extinction, seeing and airmass in Fig. 3.20, but the LRGs in the rest of the bins with higher values could introduce systematics in the
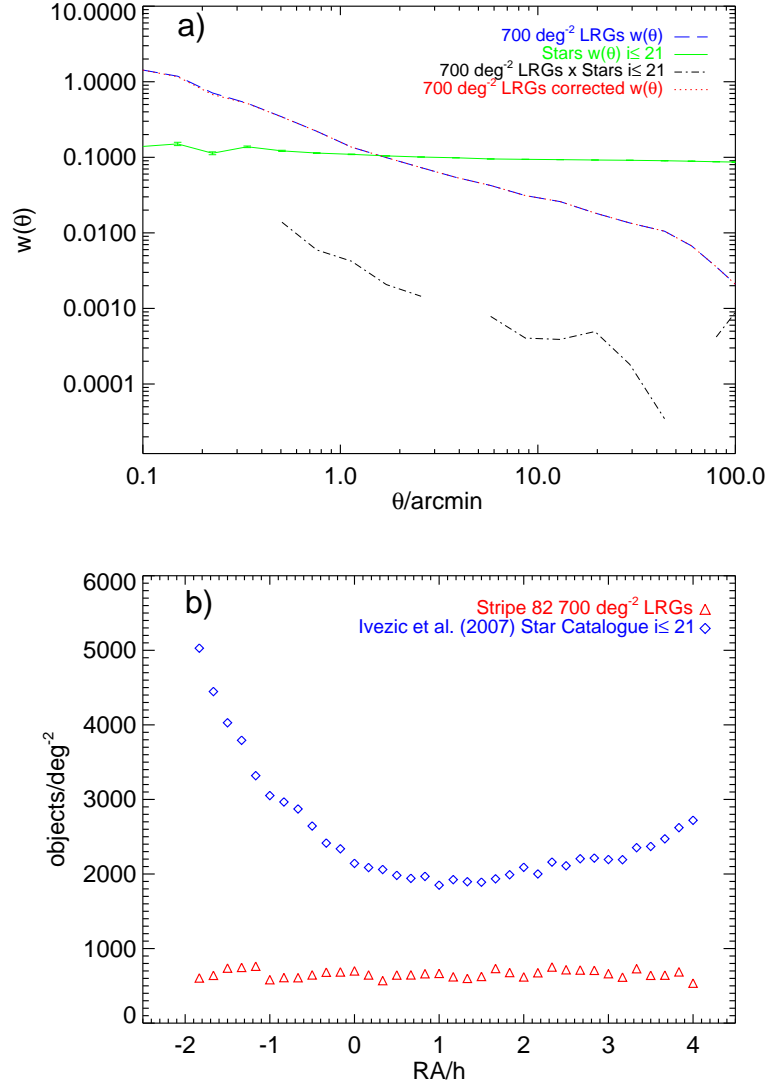
Figure 3.19: **a)** The observed $w(\theta)$ of Stripe 82 LRGs (blue dashed line), Stripe 82 star catalague of Ivezic et al. (2007) autocorrelation (green line) for $i \leq 21$, cross-correlations of the aforementioned LRGs-stars (black dashed-dot line) and the resulted corrected observed autocorrelation function following Ross et al. (2011). We see that there is no difference between the observed LRGs and the corrected $w(\theta)$'s, respectively. **b)** The number density of the stars up to $i = 21$ from Ivezic et al. (2007) catalogue (blue diamonds) and the $700 \deg^{-2}$ LRG sample (red triangles) across the Stripe 82. There is a strong gradient in the star distribution towards one end of the Stripe 82 at $330 \lesssim RA \lesssim 340$deg or $-2 \lesssim RA \lesssim -1$hr in the abscissa notation. But when we excluded this area from the star-LRG cross-correlation, there was no change in the large-scale $w(\theta)$ signal.
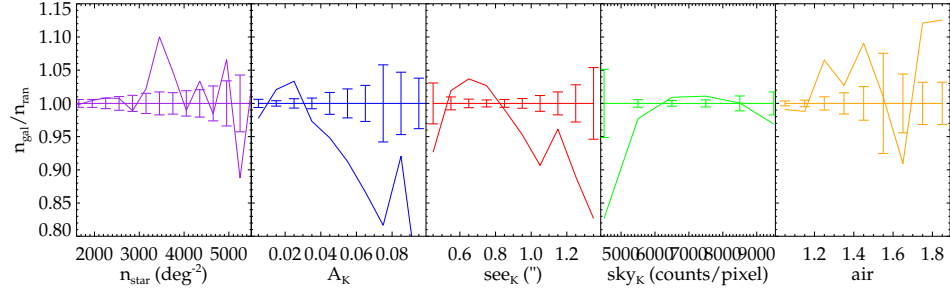
Figure 3.20: The projected number density of Stripe 82 LRGs as a function of the potential observable systematics: stellar density (n_{star}), Galactic extinction (A_k) in the K-band, the K-band seeing (see_K), K-band background median sky flux in counts per pixel and the airmass (air). The errors are the standard deviation of the measurements within each bin.

clustering signal.

Ho et al. (2012) present a method to identify which combination of the observed parameters could have the biggest effect on the clustering measurements. The authors in this work expressed the linear relationship between the potential observational systematic and its effect on the observed overdensity of galaxies, through the ϵ factor. In Fig. 3.21a we show the ϵ_i parameters for each of the the observational parameters. The Ross et al. (2011) cross-correlation correction technique requires that ϵ be constant, so we use the best-fitting constant value of ϵ as calculated with the lowest chi-square fits from field-to-field errors. We find that the biggest correction in the angular correlation function is for the combined seeing, airmass and galactic extinction observational parameters (see Eq. 29 of Ross et al.). Also, a slightly smaller correction has been found for stars, sky background and galactic extinction. In Fig. 3.21b we show the original uncorrected $w(\theta)$ for the Stripe 82 LRGs, the $w(\theta)$ after applying the combined correction for the seeing, airmass and galactic extinction. In the same figure, for comparison we plot the best-fit ΛCDM model as displayed in Fig. 3.14. So far this correction in our $w(\theta)$ results is the most important. But still as we can see from Fig. 3.21b, at the range $20-80'$, the amplitude of the angular correlation function does not show the expected behaviour of the standard model. We have checked for the most common sources of systematics
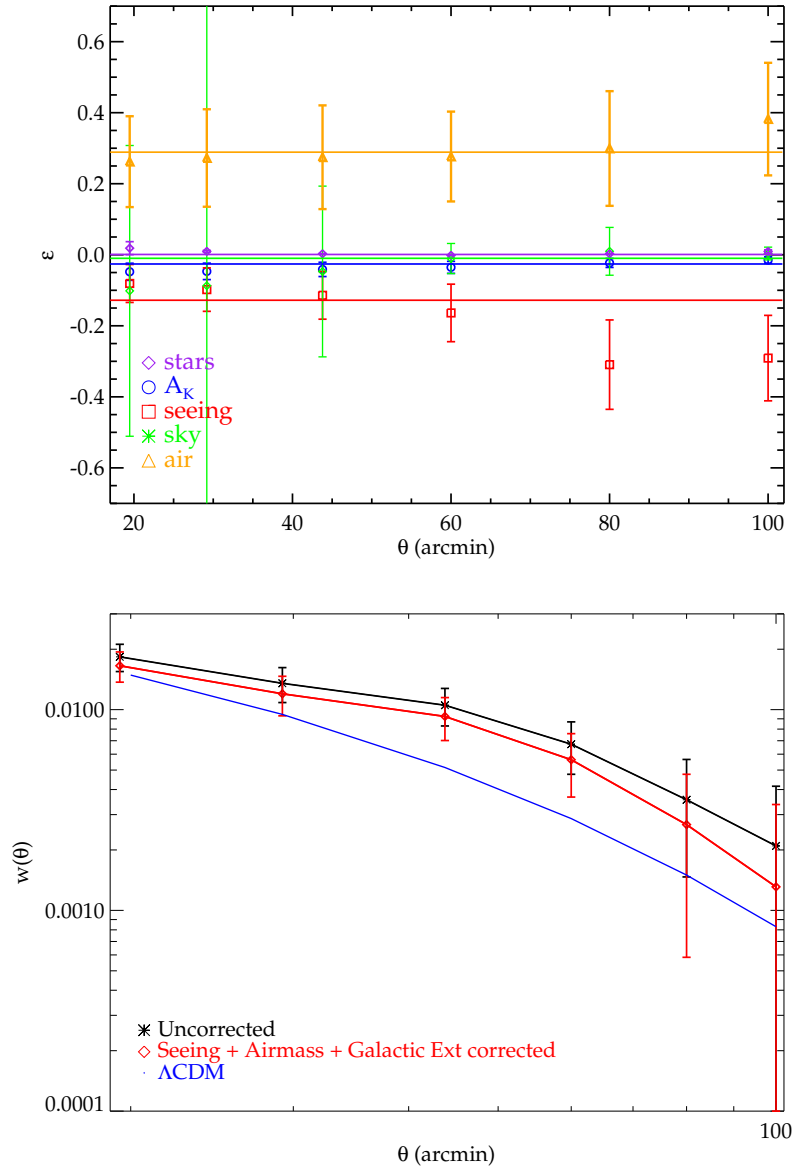
Figure 3.21: **a)** (upper) Similar to Ross et al. 2011 we plot ϵ, the linear factor between the potential observational systematic and its effect on the observed overdensity of galaxies for stars (purple diamond), galactic extinction (blue diamond), seeing (red squares), sky background (green diamond) and airmass (orange triangle). The solid lines are the best-fitting constant value of ϵ for each systematic. **b)** (lower) The $w(\theta)$ measurement of the Stripe 82 LRGs without any cross-correlation correction (black star) and $w(\theta)$ corrected for seeing, airmass and galactic extinction combined (red diamond). The best-fit ΛCDM model to the uncorrected measurement is plotted (blue line).

in the literature. Our data could still be affected by hidden artefacts, a case that future studies might be able to identify, but for the moment we will take the corrected result in Fig. 3.21b as our best estimate. Note that the HOD fits of §3.5.4 were only done up to $\theta \leq 60'$ where there is little change in the form of our $w(\theta)$ result.

3.7 Clustering evolution

3.7.1 Intermediate scales

First, we compare the clustering of the $z \approx 1$ Stripe 82 LRG sample to the lower redshift $z \approx 0.68$ $AA\Omega$ LRG sample. We recall that these LRG samples have approximately the same space density and so should be approximately comparable. We follow Sawangwit et al. (2011) and by using our best-fit r_0 and γ we make comparison with their data and models via the integrated correlation function in a 20 h^{-1}Mpc sphere, ξ_{20}.

$AA\Omega$ LRG results are described better with the long-lived model of Fry (1996). Fry's model assumes no merging in the clustering evolution of the galaxies while they move within the gravitational potential, hence the comoving number density is kept constant. The bias evolution in such a model is given by:

$$b(z) = 1 + \frac{b(0) - 1}{D(z)} \tag{3.36}$$

where D(z) is the linear growth factor.

However, the flat slope beyond 1h^{-1}Mpc causes a highly significant, $\approx 50\%$, rise in ξ_{20} above the $AA\Omega$ ξ_{20} as we can see in Fig. 3.22 (see also Figs. 3.13a,b). If we assume that the 2 samples are matched then we would conclude that all of the models discussed by Sawangwit et al. (2011) were rejected.

One possibility is that the 700 deg^{-2} LRG sample is closer to the SDSS and $AA\Omega^*$ LRG space density of 1.1×10^{-4} h^{-3}Mpc^{-3} because the LRG ξ_{20} fits the extrapolated models better there. If so, then this would imply that the Stripe 82 LRG $n(z)$ width was underestimated in the cross-correlation procedure and this would then increase the de-projected amplitude of $\xi(r)$, suggesting that this explanation may not work. Similarly a larger correction for stellar contamination would also produce a higher Stripe 82 clus-
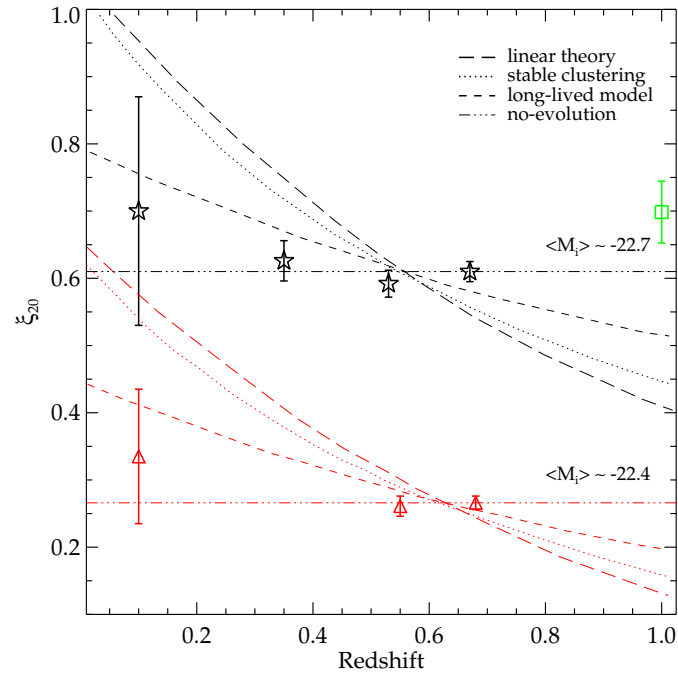
Figure 3.22: The LRG ξ_{20} measurements as a function of redshift and luminosity from Sawangwit et al. (2011). Lowest redshift data are early-type galaxies from 2dFGRS (Norberg et al., 2002). Stars represent the brighter samples (SDSS, 2SLAQ* and $AA\Omega^*$-LRG), where the lower luminosity samples, triangles, have been lowered by 0.2 for clarity. The *i*-band absolute magnitude LRGs have been corrected using the dust map of Schlegel et al. (1998) and $K + e$ corrected to $z = 0$ using the Early-type galaxy templates from Bruzual & Charlot (2003). The 700 deg^{-2} Stripe 82 LRGs ξ_{20} measurement is at $z = 1$ (square).

tering amplitude. We do not believe that looking further into the evolution of the bias (Papageorgiou et al., 2012) and DMH is warranted until we understand the flat slope of the Stripe 82 $w(\theta)$ at large scales.

3.7.2 Small scales

At smaller scales ($r < 1\ \mathrm{h}^{-1}\mathrm{Mpc}$) the situation is less complicated by the flat large-scale slope. Here Sawangwit et al. found that a virialised model gave a better fit to the slightly faster evolution needed to fit the small-scale correlation function amplitudes than a comoving model. But in the present case, the scaling between the AAΩ and Stripe 82 LRGs in Fig. 3.13a,b, shows that here the comoving model is preferred at small scales over the faster virialised evolution. This fits with the more general picture of the Stripe 82 LRGs presenting a higher amplitude than expected all the way down to the smallest scales. Unfortunately the remaining uncertainty in the Stripe 82 LRG luminosity class is still too large to make definitive conclusions on this evolution possible.

HOD evolution

Given the uncertainty in ξ_{20} caused by the flat $w(\theta)$ slope on intermediate - large scales, we will extend further the studies at small-scales, using the HOD model to interpret the small-scale clustering signal of the LRGs. Based on the HOD fit at $z \approx 1$, we again follow Sawangwit et al. (2011), (and references therein) and test long-lived and merging models by comparing the predictions of these models to the SDSS HOD fit from Sawangwit et al. These authors and also Wake et al. (2008) found that long-lived models were more strongly rejected at small scales ($r < 1\ \mathrm{h}^{-1}\mathrm{Mpc}$) than at intermediate-large scales.

Again we follow the approach of Wake et al. (2008) and Sawangwit et al. (2011) who assumed a form for the conditional halo mass function Sheth & Tormen (2002) and a sub-Poisson distribution for the number of central galaxies in low-redshift haloes of mass M such that

$$\langle N_{\mathrm{c}}(M) \rangle = 1 - \left[1 - \frac{C(M)}{N_{\max}} \right]^{N_{\max}}, \tag{3.37}$$

where $N_{\max} = \mathrm{int}(M/M_{\min})$,

$$C(M) = \int_0^M \mathrm{d}m\, N(m, M)\, \langle N_{\mathrm{c}}(m) \rangle \tag{3.38}$$

and $N(m, M)$ is the expression of Sheth & Tormen (2002) for the conditional halo mass function which generalizes that of Lacey & Cole (1993). The mean number of satellite galaxies in the low-redshift haloes is then given by

$$\langle N_{\mathrm{c}}(M) \rangle \langle N_{\mathrm{s}}(M) \rangle = S(M) + f_{\mathrm{no-merge}}\left[C(M) - \langle N_{\mathrm{c}}(M) \rangle \right], \tag{3.39}$$

where

$$S(M) = \int_0^M \mathrm{d}m\, N(m, M)\, \langle N_{\mathrm{c}}(m) \rangle \langle N_{\mathrm{s}}(m) \rangle. \tag{3.40}$$

and the main parameter is $f_{\mathrm{no-merge}}$ which is the fraction of un-merged low-z satellite galaxies which were high-z central galaxies.

This model is called 'central-central mergers' in Wake et al. (2008). More massive high-z central galaxies are more likely to merge with one another or the new central galaxy rather than satellite-satellite mergers.

Setting $f_{\mathrm{no-merge}} = 1$ means that there is no merging of initial central galaxies in subsequently merged haloes, so it is similar to the passive/long-lived model. $f_{\mathrm{no-merge}}$ equals to 0 means that all the central galaxies in haloes at high redshift merge to form new central and/or satellite galaxies in the low redshift haloes. In the analysis below, we use the best-fit HOD model values as estimated for scales up to $45'$ (see Table 3.3).

The $f_{\mathrm{no-merge}} = 1$ case is shown as the $w(\theta)$ passive model in Fig. 3.23 and is clearly rejected by the data at $\theta \lesssim 10'$ (see lower panel). Best-fit HOD predictions of the satellite fraction in the case of the passively evolved LRGs from $z_{earlier} = 1$ to $z_{later} = 0.35$ is $F_{sat} = 18.6 \pm 2.5\%$ whereas Sawangwit et al. measured $F_{sat} = 18 \pm 1\%$ for a brighter selection of LRGs at $z_{earlier} = 0.68$. We see that both these results, for the long-lived model, are significantly higher compared to the best-fit SDSS HOD, $F_{sat} = 8.1 \pm 1.8\%$. The difference in the number of the satellite galaxies is explained as the predicted clustering amplitude at small scales (1-halo term) for the passive model, is higher compared to the SDSS HOD fit as it is clearly shown in Fig. 3.23. Higher clustering signal at small scales indicates the presence of too many satellite galaxies in the low-redshift haloes.
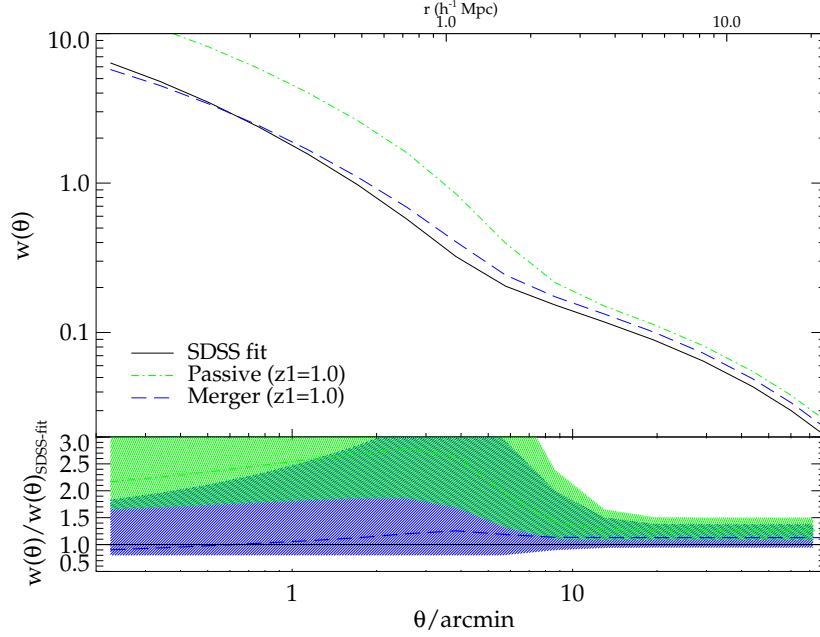
Figure 3.23: The predicted SDSS LRG $w(\theta)$'s at $z_{later} = 0.35$ for the case of passively ($f_{\mathrm{no-merge}} = 1$) evolving the best-fit HOD of Stripe 82 LRGs sample from $z_{earlier} = 1$ and the case where central galaxies merging is allowed from $z_{earlier} = 1$ ($f_{\mathrm{no-merge}} = 0.21$), in green dot-dashed line and blue long-dashed line, respectively. The bottom panel shows the ratios of the evolved $w(\theta)$'s to the SDSS best-fit, the shaded regions signify the 1σ uncertainties.

The $w(\theta)$ merger model is described by $f_{\mathrm{no-merge}} = 0.21$ as presented in Fig. 3.23 and clearly fits the data well. For this model the satellite fraction at $z = 0.35$ estimated to be $F_{sat} = 7.29 \pm 4.5\%$ and is in a good agreement with Sawangwit et al. Moreover, the best-fit HOD model values for the evolved $z_{earlier} = 1$ LRGs to $z_{later} = 0.35$ for bias and galaxy number density are $b = 2.24 \pm 0.24$ and $n_g = 0.67 \pm 0.41 \ 10^{-4}\mathrm{h}^3\mathrm{Mpc}^{-3}$, respectively. When the Stripe 82 best-fitting HOD model is compaerd to the SDSS best-fitting model, with $b = 2.08 \pm 0.05$ and $n_g = 1.3 \pm 0.4 \ 10^{-4}\mathrm{h}^3\mathrm{Mpc}^{-3}$, the number of galaxies at $z = 0.35$ have been decreased by almost 50% due to central-central merging. The evolved linear bias and galaxy number density are consistent with the $z = 0.35$ best-fit HOD of Sawangwit et al. at $1 - 1.5 \ \sigma$ level.

Note that the agreement at large scales in Fig. 3.23 is somewhat artificial given the underestimation of $w(\theta)$ by the HOD model in Fig. 3.15b which remains unexplained

in the HOD formalism. But at these smaller scales the result that the merging model fits better than the long-lived or indeed the virialised clustering model of Fig. 3.13b may be more robust, given the reasonable fit of the HOD model at small scales ($\theta < 3'$) in Fig. 3.15b.

3.8   Test for Non-Gaussianity

One possible explanation for the flat slope seen at large scales is scale-dependent bias, although this is usually discussed more in the context of small-scale clustering. However, scale dependent bias at large scales has previously been invoked to explain the discrepancy between the APM $w(\theta)$ results and $\Omega_m = 1$ CDM models (Bower et al., 1993); in this case the scale dependence was caused by 'cooperative galaxy formation'.

Another possibility is that the LRG power spectrum may be closer to the primordial power spectrum at higher redshifts. But we have seen that the Stripe 82 clustering result are not in line with the standard ΛCDM model. These correlation function results are better fitted by a model with $\Omega_m = 0.2$ rather than $\Omega_m = 0.27$ (see Fig. 3.14), useful at least as an illustration of the size of the LRG clustering excess.

The third possibility is that the $z \approx 1$ LRG power spectrum may be better explained by scale-dependent bias at large scales due to primordial non-Gaussianity in the density fluctuations. The primordial non-Gaussianity of the local type is parameterised by $f_{\rm NL}^{\rm local}$ (see Bartolo et al., 2004a, for a review) and is expected to contribute a $1/k^2$ term to the power spectrum and evolves as $\approx 1 + z$ (see Eq. 3.41). It is therefore best seen at large-scales and high redshifts. Fig. 1 of Xia et al. (2010b) shows the potential effect of non-Gaussianity on the biased clustering of radio sources with a similar redshift to the LRGs discussed here. It can be seen that the non-Gaussianity causes a strong positive tail to the correlation function for $\theta >$ a few degrees.

Xia et al. (2010b), following Blake & Wall (2002), found that the NRAO VLA Sky Survey (NVSS) survey angular correlation function showed a strong positive tail suggesting that $f_{NL}^{\rm local} = 62\pm27$. Xia et al. (2011) also inspected the angular correlation function of the DR6 QSO sample and found similar results to the radio sources with again an extended

correlation function being seen implying similar values of f_{NL} (hereafter we shall use just f_{NL} to denote $f_{\mathrm{NL}}^{\mathrm{local}}$) as for the radio sources. This led to only slightly weaker constraints than for the radio sources in terms of the value of f_{NL}.

Sawangwit et al. (2011) measured the combined angular correlation function of LRGs at $z \approx 0.35, 0.55, 0.68$ and found that although the results were in agreement with ΛCDM at scales $< 100\mathrm{h}^{-1}\mathrm{Mpc}$, at larger scales there was a possible excess, although this could still be due to systematics.

We then proceeded to follow Xia et al. and fit f_{NL} models. We use their relation between the non-Gaussian and Gaussian biases (b_{NG} and b_G)

$$b_{\mathrm{NG}}(z) - b_{\mathrm{G}}(z) \simeq 2(b_{\mathrm{G}}(z) - 1)f_{\mathrm{NL}}\delta_{\mathrm{ec}}(z)\alpha_{\mathrm{M}}(k) \,. \tag{3.41}$$

Here $\delta_{\mathrm{ec}}(z)$ is the critical density for ellipsoidal collapse and $\alpha_{\mathrm{M}}(k) \propto 1/k^2$ contains the scale and halo mass dependence (see Xia et al. for more details.)

We first applied this relation to the case of the NVSS radio sources at $z \approx 0.7$. We found that adding the $1/k^2$ term to the standard cosmology $P(k)$ caused it to diverge and so we had to apply a large-scale cut-off, so that for $k < k_0$ then $P(k) = 0$. This is clearly a source of uncertainty in fitting for f_{NL}. Nevertheless, we found that for $k_0 = 10^{-6}$, we could reproduce the results of Xia et al. (2010b).

We then applied the same technique and cut-off to the combined $AA\Omega$ LRG and the Stripe 82 LRG $w(\theta)$'s (after applying the combined correction for seeing, airmass and galactic extinction as estimated in § 3.6.3). We first took the value of $b_G = 2.08$ from the halo model fits of Sawangwit et al. (2011) and fitted for f_{NL}. The result is shown in Fig. 3.24a. We find that for $AA\Omega$ LRGs, the results for f_{NL} are reasonably compatible with those from the NVSS catalogue with values of $f_{\mathrm{NL}} = 60 - 80$ giving a better fit to the data in the range $1.5 < \theta < 6.5\mathrm{deg}$.

The prediction from non-Gaussianity is that the large scale slope will further flatten with redshift. We therefore compared the Stripe 82 LRGs to models with the same f_{NL} values and find no inconsistency (see Fig. 3.24b). Clearly the errors at the largest scales are more significant for the Stripe 82 data than for the $AA\Omega$ LRGs or the NVSS radio sources. However, the predicted flattening of the Stripe 82 correlation function at
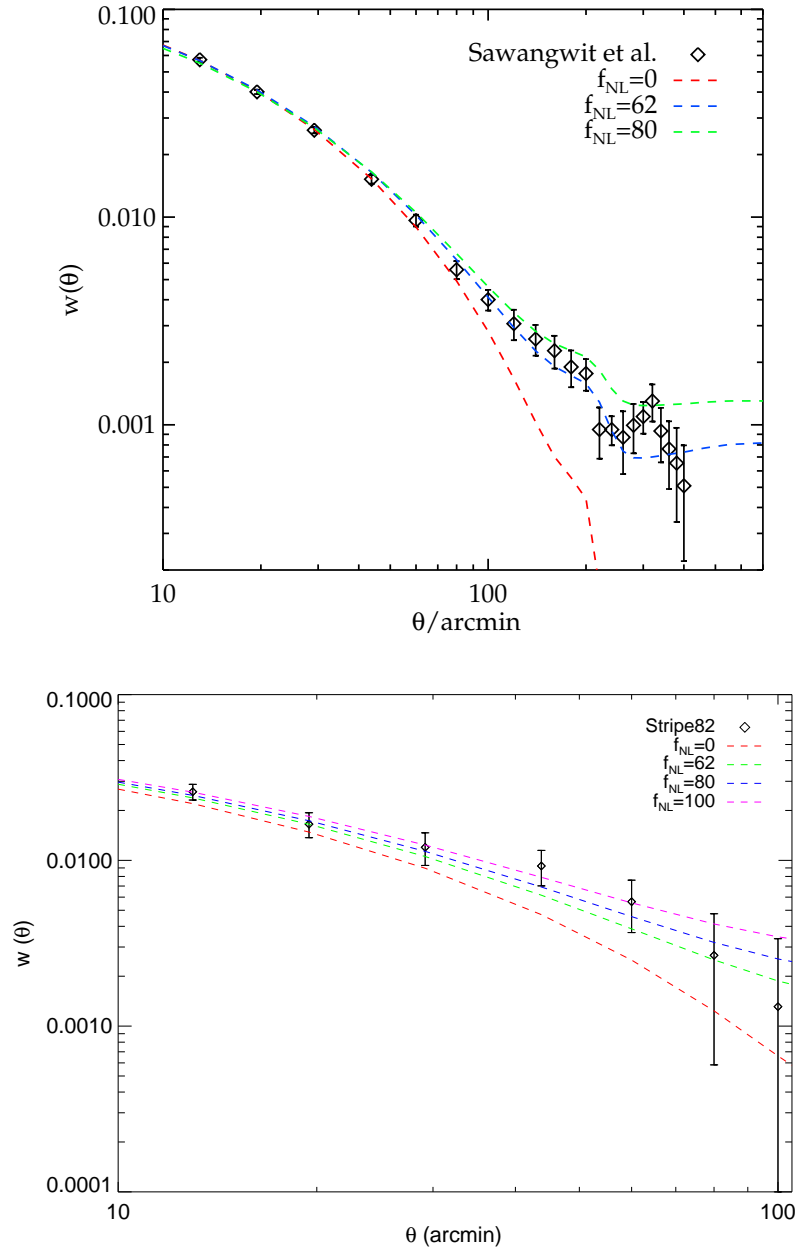
Figure 3.24: **a)** (upper) The combined correlation function of Sawangwit et al (2011) for the $z = 0.35$, $z = 0.55$ and $z = 0.68$ LRG samples, compared to a standard ΛCDM model ($f_{NL} = 0$) and models with increasing degrees of primordial non-Gaussianity ($f_{NL} = 62, 80$). **b)** (lower) The Stripe-82 $z \approx 1$ LRG correlation function compared to a standard ΛCDM model ($f_{nl} = 0$) and models with increasing degrees of primordial non-Gaussianity ($f_{NL} = 62, 80, 100$).
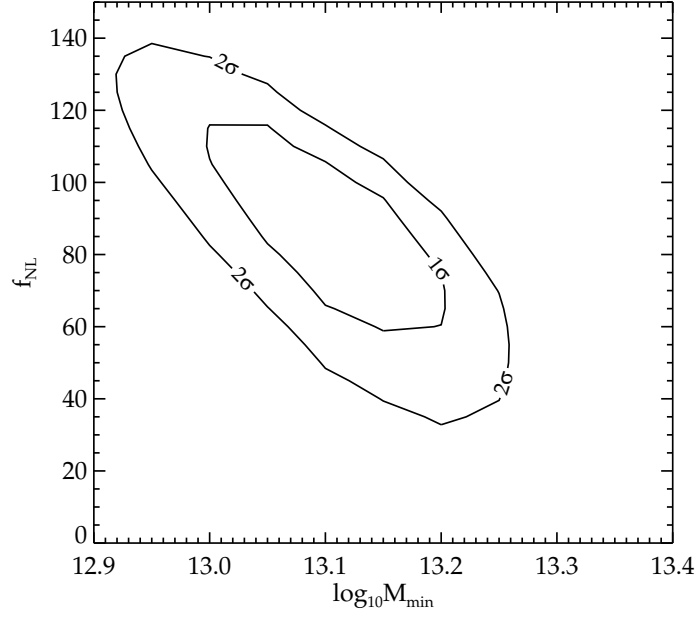
Figure 3.25: The minimum χ^2 is 5.5 over 11 d.o.f and the best-fit parameters are $f_{\mathrm{NL}} = 90 \pm 30$ (1σ) and $M_{min} = 1.26 \pm 0.22 \times 10^{13}\mathrm{h}^{-1}\mathrm{M}_\odot$. The best-fit M_{min} here is lower than the full HOD fit assuming $f_{NL} = 0$ at $2.2 \times 10^{13}\mathrm{h}^{-1}\mathrm{M}_\odot$.

$\theta \approx 1\mathrm{deg}$ makes the non-Gaussian models more consistent with the data in this smaller angular range than the $f_{\mathrm{NL}} = 0$ model. At larger scales the errors are larger and the data is therefore more in agreement with the standard model.

Fig. 3.25 shows the effect of jointly fitting f_{NL} on the minimum halo mass, M_{min}, in the HOD model. The best fit model now gives $M_{min} = (1.26 \pm 0.22) \times 10^{13}h^{-1}M_\odot$ and $f_{NL} = 90 \pm 30$, lower than then the $M_{min} = 2.2 \times 10^{13}h^{-1}M_\odot$ value when $f_{nl} = 0$ is assumed in the full HOD fit.

We should say that rather than detections of non-Gaussianity, the present $AA\Omega$ and Stripe 82 LRG results should be more regarded as upper limits on non-Gaussianity. Large-scale angular correlation function results are still susceptible to large-scale gradients and even though there is no direct evidence for these in the $AA\Omega$ or Stripe 82 samples, there is still the possibility that these exist in the data. On the other hand, the classic test for the reality of a correlation function feature is that it scales correctly with

depth and at least the SDSS and Stripe 82 LRG correlation functions in Figs. 3.24a,b look like they do so. It will be interesting to see if as QSO surveys (Sawangwit et al., 2012) and $z \approx 3$ LBG surveys (Bielby et al., 2013) grow, whether the correlation functions at higher redshift also show an increased slope flattening as predicted for the non-Gaussian models.

The other uncertainty that has arisen is in the non-Gaussian model itself where we have found that there is a rather strong dependence on a small-scale cut-off, k_0. Other authors have made some reference to this problem but only implicitly. It will be interesting to see if more accurate models for non-Gaussianity can numerically predict this cut-off from first principles.

3.9   Summary and conclusions

We have measured $w(\theta)$ for $\approx 130\,000$ colour selected galaxies in Stripe 82 exploiting SDSS DR7 $i + z$ bands and UKIDSS LAS K photometry. We used the cross-correlation technique of Newman (2008) to establish that the average redshift of the LRGs is $z \approx 1$. This sample therefore probes higher redshifts than the previous SDSS LRG samples of Sawangwit et al. (2011). We have established that a sample with sky density $\approx 700\mathrm{deg}^{-2}$ has a comparable space density to the $z \approx 0.68$ $AA\Omega$ LRG sample of Sawangwit et al. (2011). However, this is only an approximate correspondence which makes evolutionary comparisons between the redshifts more tricky. What is clear is that the $z \approx 1$ LRGs generally have a relatively high clustering amplitude. Compared to the $AA\Omega$ LRG $w(\theta)$ scaled to the depth of the Stripe 82 LRGs, the Stripe 82 $w(\theta)$ is higher at all scales, even those below $< 1\ \mathrm{h}^{-1}\mathrm{Mpc}$. Thus at intermediate scales, the $z \approx 1$ LRGs are not only more clustered than predicted by the long-lived evolutionary model, they are also more clustered than the comoving model. At small separations ($\lesssim 1\ \mathrm{h}^{-1}\mathrm{Mpc}$) the correlation function amplitude is again somewhat higher than the $AA\Omega$ results scaled by the previously preferred stable clustering model. The Stripe 82 $w(\theta)$ also shows a very flat slope at large scales which means that the ΛCDM linear model has become a poorer fit than at lower redshift.

Partly to look for an explanation for the flat large-scale slope, we then fitted a HOD model to the Stripe 82 $w(\theta)$. The best fit parameters were $M_{min} = 2.19 \pm 0.63 \times 10^{13} \text{ h}^{-1}\text{M}_\odot$, $M_1 = 21.9 \pm 5.6 \times 10^{13} \text{ h}^{-1}\text{M}_\odot$, $b_{\text{lin}} = 2.81 \pm 0.18$, $M_{\text{eff}} = 3.3 \pm 0.6 \times 10^{13} \text{ h}^{-1}\text{M}_\odot$, $F_{\text{sat}} = 3.17 \pm 0.08\%$ and $n_{\text{g}} = 0.8 \pm 0.3 \times 10^{-4} \text{ h}^3\text{Mpc}^{-3}$. The high amplitude of the correlation function clearly pushes the halo masses up and the space densities down. The lowest chi-square fits were found when large scales were excluded but the reduced chi-squares were still in the range 2.3-3.6. This is actually an improvement over the lower redshift samples but this is certainly due to the larger errors on the Stripe 82 data. We conclude that it is not possible to find an explanation for the flat slope in the Stripe 82 $w(\theta)$ on the basis of the HOD model.

We also then studied the evolution of the HOD between $z = 1$ and $z = 0.35$. Similar to Sawangwit et al. (2011), we concluded that a pure passive model with a low merger rate might produce too steep a $w(\theta)$ slope at small scales ($< 1 \text{ h}^{-1}\text{Mpc}$). In this case, we have already noted that the small scale amplitude may also be too high for a passive model with stable clustering.

We have looked for an explanation of the flat slope in terms of systematics by cross correlating the Stripe 82 LRG sample with stellar density, airmass, seeing, sky background and galactic extinction and used the method of Ross et al. (2011) to correct our $w(\theta)$. Even the combined correction for seeing, airmass and galactic extinction only produced a small change in $w(\theta)$ at large scales.

We conclude that the high amplitude and flat slope of the Stripe 82 LRGs $w(\theta)$ may have a significant contributions from the uncertainty in the comparison between $AA\Omega$ and Stripe 82 LRG luminosities. However, this leaves a similar contribution from a new and unknown source. We have discussed large-scale, primordial, non-Gaussianity as one possibility for the source of this large-scale excess. We have suggested that the evidence from the $AA\Omega$ sample itself for an excess at even larger scales may fit in with the behaviour expected from non-Gaussianity over this redshift range. In this case we returned to the fitting of halo masses including the non-Gaussian component and found that the best fit M_{min} decreased from $2.2 \times 10^{13}\text{M}_\odot$ to $1.3 \times 10^{13}\text{M}_\odot$. More importantly, if the Stripe 82 large-scale $w(\theta)$ excess proves reliable and not due to systematics, then

we have made a significant detection of non-Gaussianity in the $z \approx 1$ LRG distribution with an estimated local non-Gaussianity parameter estimate of $f_{\mathrm{NL}}^{\mathrm{local}} = 90 \pm 30$. This represents a 3σ detection at a level comparable to the present upper limit from WMAP CMB measurements of $f_{\mathrm{NL}}^{\mathrm{local}} = 32 \pm 21$ (Komatsu, 2010), while our results are rejected if we take into consideration the recent results from Planck with $f_{\mathrm{NL}}^{\mathrm{local}} = 2.7 \pm 5.8(1\sigma)$ (Planck Collaboration XXIV et al., 2013)[2].

---

[2](Planck Collaboration XVI et al., 2013b) found that the low-l spectrum of the Planck data deviates 2.7 from the best-fit CDM model, while (Planck Collaboration XXIII et al., 2013) found positive kurtosis of the wavelet coefficients. These findings were also detected in WMAP data, indicating that this cannot be a systematic. Extra studies are needed before Planck data can place tight constraints on f_{NL}

Chapter 4

Spectroscopy of high-z Stripe 82 LRGs

4.1 Introduction

The growth of the most massive red galaxies represents a fundamental test for CDM models of galaxy formation and evolution. For example, (De Lucia et al., 2006) use the latest semi-analytical ΛCDM models of structure formation (with AGN feedback) to trace the formation history of such galaxies and find that 80% of the stars in present-day massive ellipticals formed at high redshift (a median of $z \sim 2$). However, these stars are not assembled into a massive galaxy (through "dry mergers" in which no additional star-formation is triggered) until much later, e.g., $z \sim$0.5. In such models, the most massive galaxies generally double their masses between $z \approx 1$ and $z \approx 0$.

These predictions are already being challenged. A number of recent spectroscopic i.e. SDSS and 2SLAQ and photo-z i.e. Classifying Objects by Medium-Band Observations in 17 filters- COMBO-17[1] and NOAO Deep Wide-Field Survey-NDWFS[2] surveys, have suggested that more than 80% of the stellar mass in low redshift LRGs (>4L*), is in place by $z < 0.9$ (Bundy et al., 2006; Borch et al., 2006; Cimatti et al., 2006; Wake et al., 2006; Brown et al., 2007) (see Fig. 4.1). Furthermore, recent analyses of the stacked spectral indices of 2SLAQ and AUS LRG spectra have shown that a bulk of the stellar populations in these galaxies was formed between $1.3 < z < 1.9$. There remains a gap in the observations of the most luminous LRGs at $z \gtrsim 1$ which cannot be efficiently addressed with current spectroscopic surveys such as DEEP2 and the VIMOS VLT DEEP

---

[1]http://www.mpia-hd.mpg.de/COMBO/
[2]http://www.noao.edu/noao/noaodeep/
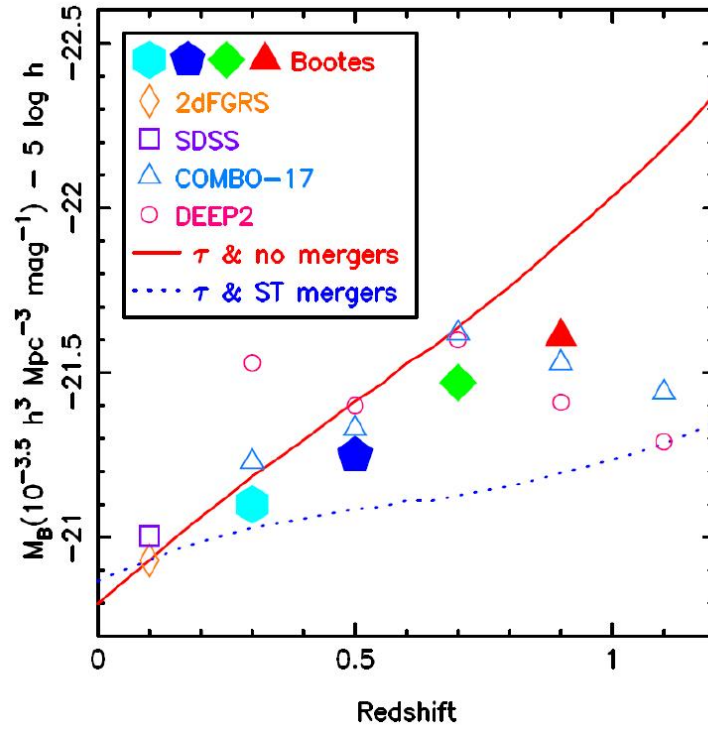
Figure 4.1: The luminosity of $\sim 4L^*$ red galaxies (Brown et al., 2007) suggests that $\approx 80\%$ of stellar mass contained within these luminous red galaxies was already in place at $z \sim 0.7$ and is consistent with no mergers at $z < 0.7$.

Survey (VVDS; Le Fèvre et al., 2005b), because their respective r and i band selections make them highly incomplete in this redshift range; yet this is the redshift range in which the models diverge most significantly.

In this chapter we present the spectroscopic results for LRGs at $z \gtrsim 1$ on Stripe 82 from observations that have been carried out with VIsible Multi Object Spectrograph (VIMOS; Le Fèvre et al., 2003) at the ESO Very Large Telescope (UT3) during Period 86A[3]. The spectroscopic LRGs have the same colour selection as with those used in clustering analysis in Chapter 2 (see Eq. 3.1, Priority A, 700 $\deg^{-2}$). This allows us to use the resulting spectroscopic *n(z)* of the Stripe 82 LRGs, in order to study evidence of their clustering evolution and discuss their impact on the results based on the photometric *n(z)* of Chapter 2.

---

[3](086.A-0806)

Field of View	$7' \times 8'$ with a 0.205″ pixel size
EEV CCD	4k× 2k
MR grism/ GG475	480-1000nm

Table 4.1: Basic VIMOS characteristics (per channel)

4.2 Spectroscopic Observations

In Period 86A we proposed to observe a 5deg×0.25deg area or 20 VIMOS fields of ≈ 750 $0.4 < z < 1.4$ LRGs. In this redshift regime, the wide field of VIMOS and its wavelength coverage, makes this instrument suitable for studying the Stripe 82 LRGs. From previous LRG LFs, we calculated that we should be able to detect ≈ 33 LRGs per VIMOS field assuming passive evolution. This is efficient in that the way to survey bigger volumes is by covering larger areas of sky in the minimum reasonable exposure time. In Table 4.1 we give a summary of VIMOS characteristics.

4.2.1 Spectroscopy

We used the VIMOS Exposure Time Calculator (ETC)[4], that simulates imaging and spectroscopic observations, in order to plan our LRG Stripe 82 VIMOS observations. The ETC results are based on the simulation of four main components : the telescope, the instrument, the atmosphere and the source. The $z = 1.4$ LRGs brighter than our $M_r < -22.5$ ($> 4L^*$) limit, are expected to have $i_{AB} < 22.4$ or $i_{vega} < 22.0$, assuming the luminosity distance for the standard cosmology and the appropriate (passive) K+E correction.

The VIMOS MOS ETC gives S/N=2.0 per 2.73Å pixel at the 4000Å CaII H+K break redshifted to 9600A in a 60 min exposure for an $i_{vega} = 22$ GALEV elliptical at z=1.4. This assumes an observation at 10 days from New Moon at airmass 1.2 and 1.2″ seeing. The quoted R=580 (with 1″ slits) for the Medium-Red grism with GG475 filter, implies the resolution at 9600Å is 16.6Å. Over the 16.6Å or ~ 6.1 pixel resolution elements this gives S/N~5.0. The same assumptions at redshift $z = 1.1$ (expected average redshift) give S/N=5.8 per resolution element at the H+K break redshifted to 8400Å. To observe

---

[4]http://www.eso.org/observing/etc/doc/ut3/vimos/vimos-etc-um.html

Target	α (J2000)	δ (J2000)	Magnitude
Stripe 82e (10 fields)	01 00 00	+00 00 00	I=22.0
Stripe 82f (10 fields)	01 40 00	+00 00 00	I=22.0

Table 4.2: LRG observed targets

20 fields (see Table 4.2) means that we need 30hrs of VIMOS MOS spectroscopy time. All the following discussion, is based on spectroscopic data from 7 out of 20 VIMOS fields (total amount of time granted).

4.3 Data reduction

Here, we detail the data reduction procedures we apply on the VIMOS LRG spectroscopic data. The main tool for data reduction is the *ESO Recipe Execution Tool (ESOREX)*, ESO's VIMOS official pipeline[5]. Reduction steps involve different recipes, so we mention each recipe's parameters that included within each step. It is important to note, that observations of Period 86 were made with the upgraded CCDs of VIMOS, that improve the throughput and suppose to reduce fringing problem in the red end of the spectrographs which allow finer sky subtraction.

Data reduction steps and the VIMOS pipeline recipes involved within step each are structured as :

- Creation of general calibration data - *vmbias recipe*.

- Creation of MOS calibration data - *vmmoscalib recipe*.

- MOS data reduction - *vmmosscience recipe*.

4.3.1 Vmbias

`Vmbias` pipeline recipe creates a MASTER BIAS image from an input of 5 raw bias frames. *Vmbias* parameters that we use are :

---

[5]http://www.eso.org/sci/software/cpl/esorex.html

1. **Stack Method** : Frame combination method for the raw bias input frames, median.

2. **Remove Overscan** : Remove overscan regions from the MASTER BIAS image, true.

3. **Clean Cosmic** : Cosmic ray (CR) removal from each raw bias frame, true. We need to determine what is a CR event and what is not. This algorithm is the same applied by the MIDAS command *FILTER/COSMIC*[6], where all pixels which have an abnormal excess with respect to the local noise are flagged as potentially belonging to a CR. Once all the pixels characterised as CRs events have been located, they are listed an a CR events table. CR pixel values then, are interpolated by using the bad cleaning pixel algorithm, which consists of replacing bad pixel value with an estimate based on a set of surrounding *good* pixels. The bad pixel cleaning can be used with combination of the CR pixels positions and the bad pixel table provided for each quadrant by ESO.

4. **Clean Bad Pixels** : Interpolate bad pixels on MASTER BIAS image, true. To perform the bad pixel correction, a bad pixel table (*CCD TABLE*) for each VIMOS arm is provided within *ESOREX*.

The default parameters in *vmbias* give us satisfactory results. In the description of the *vmmoscalib* and *vmmosscience* recipes, we will mention the default parameters of the recipes, which are providing acceptable solutions for the vast data majority.

4.3.2 Vmmoscalib

`Vmmoscalib` recipe identifies the reference lines on MOS arc lamp exposures and traces the spectral edges on the associated flat field exposures. Input files for this recipe are : CONFIGURATION TABLE, LINE CATALOG, MASTER BIAS image (from *vmbias*), MOS ARC SPECTRUM image and three MOS SCREEN FLAT images. The CONFIGURATION TABLE defines a set of configuration parameters which control the way spectra are extracted for any particular grism. The LINE CATALOG contains the reference wavelengths for the arc lamp that we use.

---

[6]http://www.eso.org/sci/software/esomidas/midas-overview.html
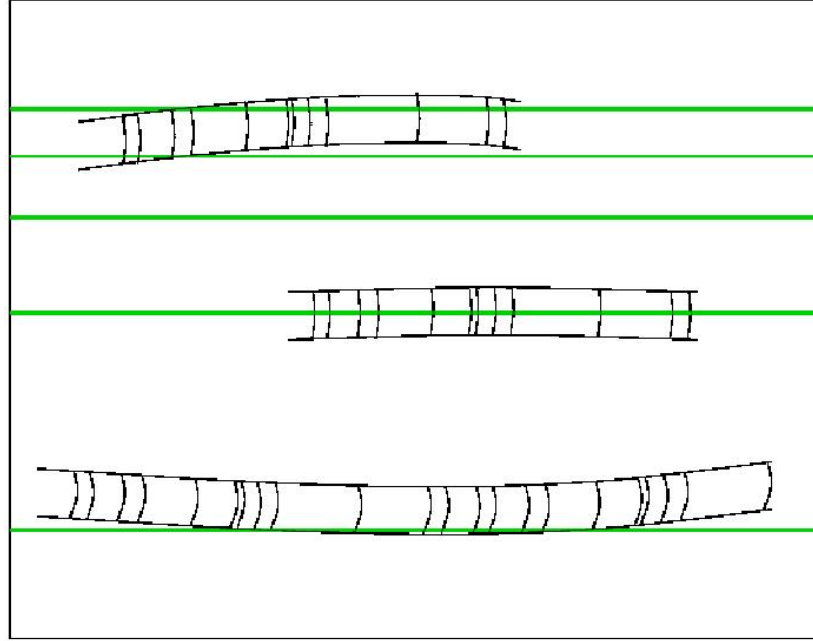
Figure 4.2: CCD columns (green lines) may not cut the whole range of the raw arc lamp spectra, as spectra are not read along their curvature. Image credit: ESO VIMOS pipeline Team.

More specific, *vmmoscalib* retrieves the line pattern to be searched on arc lamp exposures from the reference arc lamp line pattern. To evaluate the sky background (in ADU/s), the central 1600×1800 region of the CCD is dividing into 10×10 equal sized regions and the median level of each region is computed, thus, the sky background level is defined by the mean of the 10 lowest values. After bias and background subtraction, the MOS ARC SPECTRUM exposure is examined. For each CCD column, the peak-detection task runs and produces a list of reference arc lamp lines candidates. From the candidates' list, alone with the pattern-recognition task, *vmmoscalib* selects the identified lines. Note though, that not all the arc lines are expected to be identified, because spectra could be distorted and some CCD rows may cross a spectrum partially or entirely (see Fig. 4.2).

Vmmoscalib's parameters can be divided into three main categories : wavelength calibration [1-9], spatial curvature calibration [10-12], flat field normalization [13-14]. Each of these parameters have been set as indicated in Appendix B:

After *vmmoscalib*'s completion, it is necessary to check that the chosen input parameters work properly. According *ESOREX's* instructions, we need first to check if all the spectra have been detected and traced correctly. The way to do this, is by blinking and ensuring perfect alignment of the MOS MASTER SCREEN FLAT and the MOS COMBINED SCREEN FLAT images. The first image shows the spectra position, while the second works as a map that shows where the spectra are found. From the MOS CURVATURE TRACES table, we can obtain more details of the tracing accuracy. As wee can see in Fig. 4.3, with the selected parameters (*cdegree=2*), the residuals are oscillating from positive to negative values, within the accepted range of 0.2-0.3 pixels

Next, we must check the spectra calibration, where for this purpose we need to examine the MOS ARC SPECTRUM EXTRACTED image. This image contains the arc lamp spectra of each slit, after removing all the optical and spectral distortions (see *GAIA*'s screen shot in Fig. 4.4). As the spectral lines appear perfectly aligned and vertical, we understand that the computed extracted mask has been correctly applied.

The last detailed check of the solution, is by examining the MOS DISPLAY RESIDUAL image, from where we can see the residuals of the wavelength solution of each row of each extracted slit spectrum. MOS DISPLAY RESIDUAL image pixels are filled with zeroes, except the pixels where a reference line has been detected and identified. In Fig. 4.5, we have a screen-shot of the MOS DISPLAY RESIDUAL image, that displays the measured corresponding residuals (in pixels). By setting the default value of *wreject =0.7*, the observed residuals do not present any systematic trend and are within the acceptable range of 0.2 pixels. Systematics trends, along the dispersion direction, can appear as lines of all-positive (white) followed by negative (blacks) residuals, in a wavy repeated way.

4.3.3   Vmmosscience

`Vmmosscience` recipe reduces the MOS scientific spectra by applying the extraction mask and the normalised flat field created by the recipe *vmmoscalib*. Input files needed for this recipe are : CONFIGURATION TABLE (same as in *vmmoscalib*), MASTER BIAS image (from *vmbias*), MOS CURVATURE COEFFICIENT table, MOS DISPLAY COEFFI-
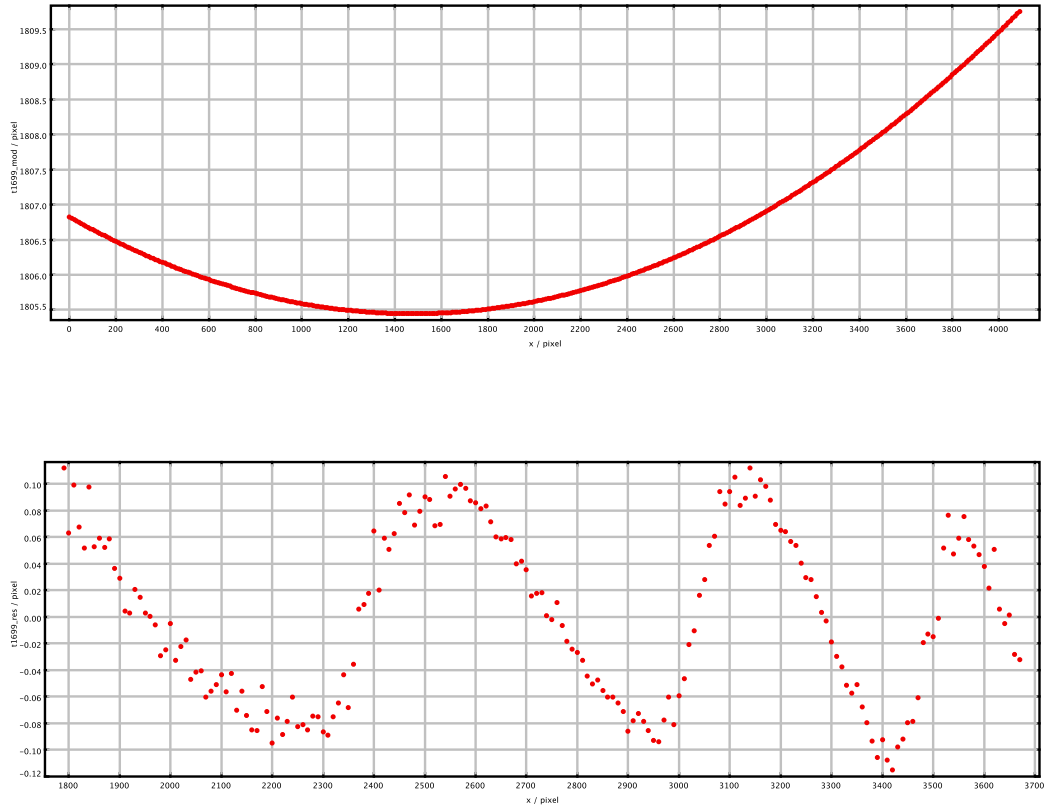
Figure 4.3: The MOS CURVATURE TRACES table contains details about the tracing of each detected arc spectrum. Top: Tracing and modelling of one spectral edge tracing. Bottom : Systematic residuals of spectral edge tracing of top figure.
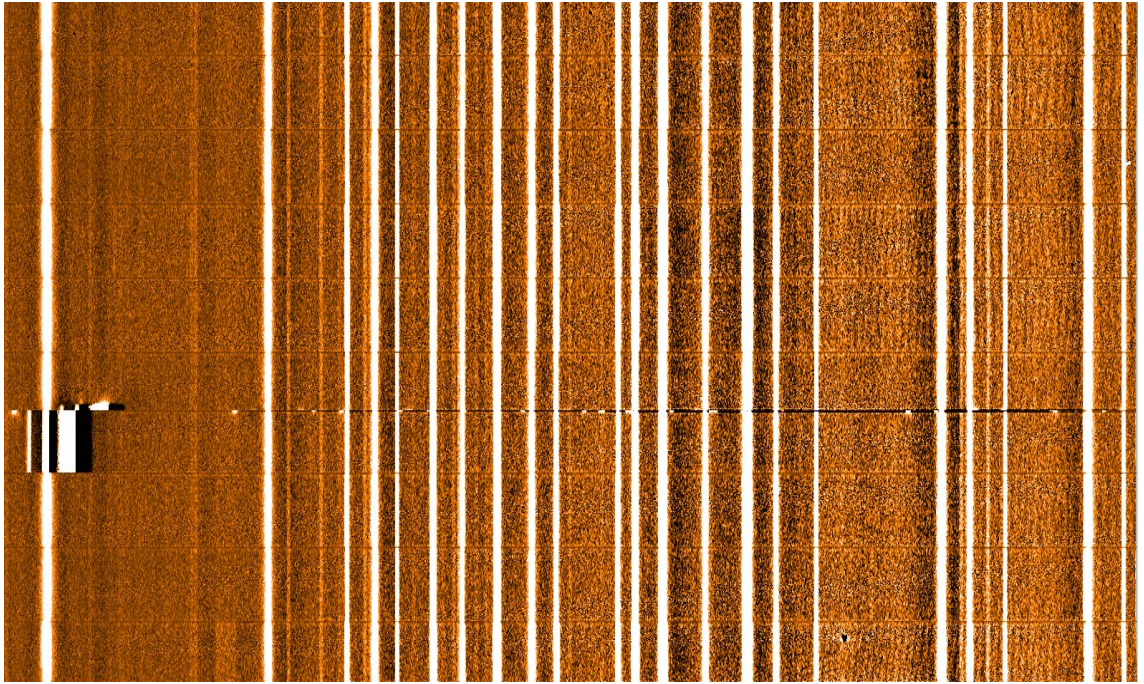
Figure 4.4: MOS ARC SPECTRUM EXTRACTED from VIMOS Argon arc lamp exposure. The calibrated slit spectra are vertically ordered as in the original CCD frame. Contaminations from 0_{th} order spectra are presented at the blue end of the slits.
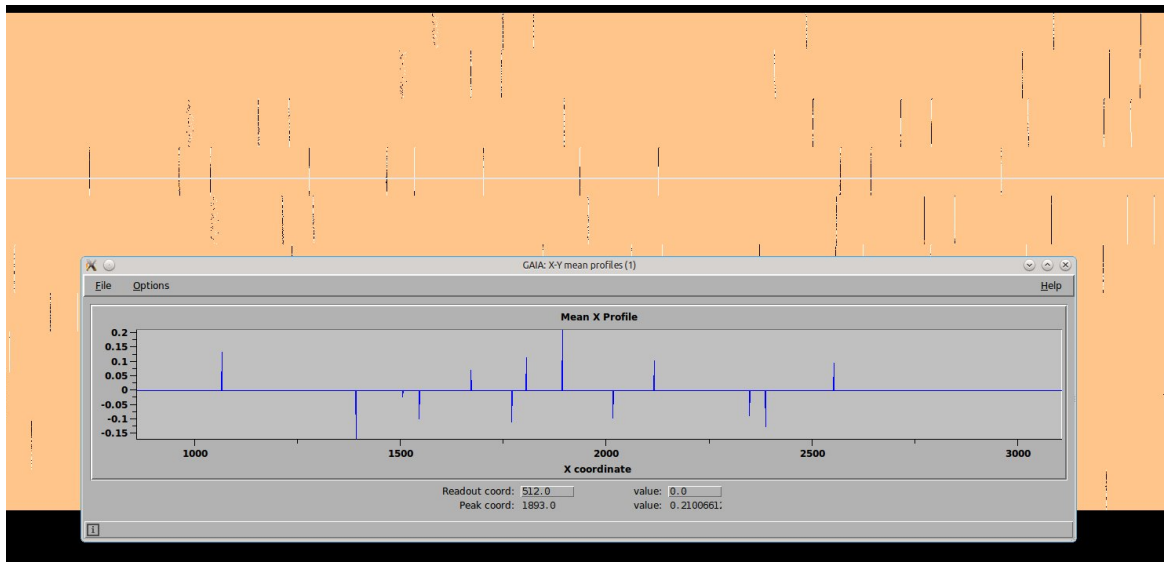
Figure 4.5: MOS DISPLAY RESIDUAL from an arc calibration. In the front panel is a plot of the residuals from one image row within the shown pixel range.

CIENT table, MOS MASTER SCREEN FLAT image, MOS SCIENCE image, MOS SLIT LOCATION table, SKY LINE CATALOG table, EXTINCTION table and STANDARD FLUX table. MOS SCIENCE images ($3\times$) are the scientific raw exposures, which contain the spectra of the objects and of the three guide stars used per pointing (see Fig. spectrum). The SKY LINE CATALOG contains the reference wavelengths of the sky lines used for adjusting the input wavelength solution to the observed scientific spectra.

Vmmosscience first subtracts the bias and flat field corrects the input scientific exposures. Next, the sky lines are used to align the wavelength solution. For every single slit spectrum, the wavelength solutions that estimated earlier from the calibration data, are used to locate reference sky lines around their expected position.

Vmmosscience then extracts the slit spectra, as are read from the pre-processed input image, following the shapes of the modelled spectral distortions (from MOS DISPLAY COEFFICIENT and MOS CURVATURE COEFFICIENT tables). The reasampling of the slit spectra along the spatial direction is according the MOS ARC SPECTRUM EXTRACTED entry, and along the dispersion direction at the wavelength step defined by *dispersion* parameter. By having all the slit spectra extracted and rectified, *vmmosscience* runs a detection algorithm to locate the emission of any possible objects. This is achieved by computing the mean spatial profile of each spectrum and looking for signal significantly higher than the background noise and if it is accepted with the expected seeing.

The last step of *vmmosscience* is the the object extraction. Two methods are available for object extraction : the simple aperture extraction and the the optimal extraction of Horne (1986), where in our case the latter method is used. Horne's algorithm uses an average of the signal optimally weighted by a function of the signal noise. CR and possible effects of a residual spatial curvature are also taken care by this extraction method.

Vmmosscience's parameters can be divided into 6 main categories : wavelength calibration [1-2], flat field correction [3], sky subtraction[4-5], stacking[6] and finally, object detection and extraction[7-12]. Each of these parameters have been set as indicated in Appendix C.

After vmmosscience's completion, we need to run some basic checks to ensure that
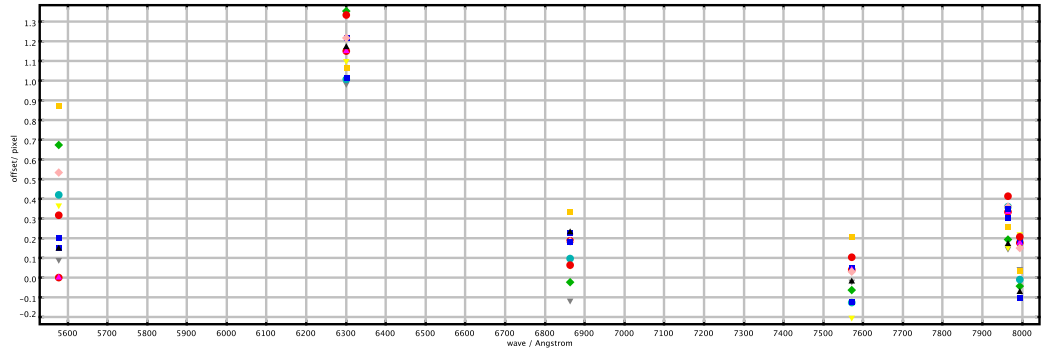
Figure 4.6: Systematic sky line offsets from day-calibration expectation. As we observe a systematic offset for all slits, it means that the sky alignment of the wavelength solution has been applied (*sky align=0*), hence there is no need to reprocess the data.

the recipe worked properly with the chosen input parameters. The first check is related to the wavelength calibration, that is performed with calibrations lamps at day time. Due to the nature of this calibration, systematics can be arise from instrumental effects such as: flexures or change in temperature. For these reasons, wavelength calibration needs to be tested against the observed positions of the sky lines in the scientific slit spectra. In Fig. 4.6 we plot, for the identified slits, the median offset in pixels for each sky line from its expected position. The appearance of systematic offsets in Fig. 4.6, confirms that an alignment of the distortion model to the true sky lines has been applied, so there is no need to reprocess the data.

From the MOS SCIENCE SKY EXTRACTED image we can have an overall quality optimization of the calibration, as this image contains the scientific spectra from each slit after removing the optical and spectral distortions. All the visible sky lines appear perfectly aligned and vertical, as we can see from Fig. 4.7, indicating that the calibration has worked properly. Following next, a check on the quality of the calibration solution can be made by examining the MOS SCIENCE DISPLAY COEFFICIENT SKY table, that contains the mean uncertainty of the wavelength calibration solution for each slit spectrum row. The model uncertainty is computed as the rms of the input model accuracy
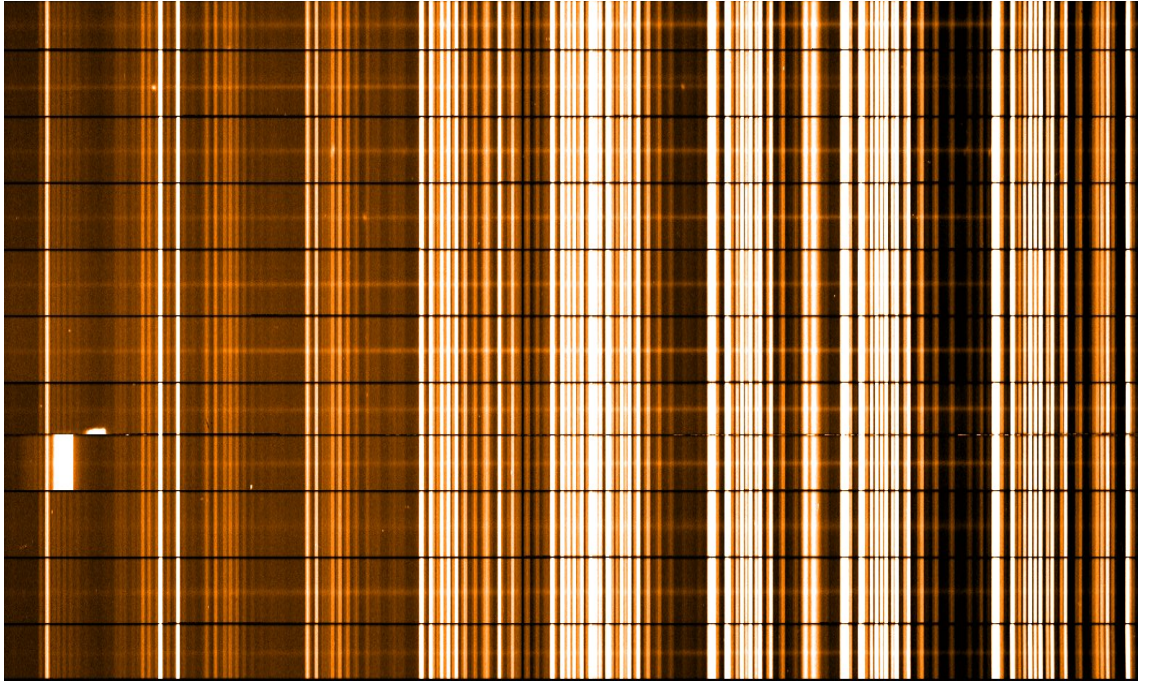
Figure 4.7: MOS SCIENCE SKY EXTRACTED image where the visible sky lines are aligned and vertically, implying that our calibration is very good.

and the sky line correction accuracy. Given at a 1σ limit, an acceptable uncertainty is of the order of 0.1 pixel (much smaller than the rms residual of the lamp calibration and of the sky line correction).

Having secured that the spectra have been properly wavelength calibrated, the sky background subtraction needs to be checked by viewing the sky subtracted spectra in MOS SCIENCE EXTRACTED image. From Fig. 4.8, we see that the spectra have a smooth look, except at the regions where bright lines have been subtracted. The final and more robust check, is to confirm that the residual noise is compatible with the statistical error associated to the extracted object spectra. The extracted spectra are contained in the MOS SCIENCE REDUCED image and the regions corresponding to sky lines include a few noisier points, whose deviation from the spectral continua are almost never higher than the 3σ deviation. Whenever the above condition is fulfilled, we are sure that the sky subtraction is completed correctly.
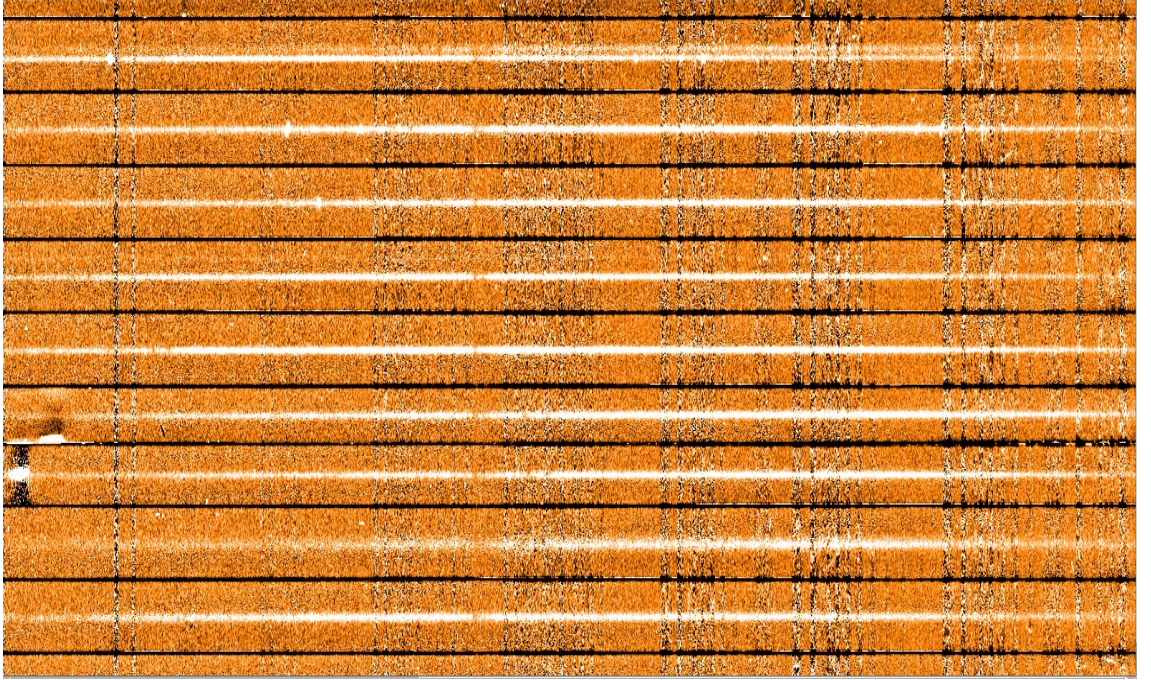
Figure 4.8: From the MOS SCIENCE EXTRACTED image we can have a quick optimization of the sky subtraction. The spectra should have generally a smooth look and will appear noisier at the regions where bright sky lines have been subtracted.

4.4 Spectroscopic results

In the previous section, we described the reduction steps of the raw LRG VIMOS data from Period 86, along with the resulting outputs. Having ensured that our products have been created with best possible quality, here we will present the spectroscopic redshift measurements of the Stripe 82 LRGs. Based on the lower LRGs LFs, we estimated what we should be able to detect ≈ 33 LRGs per VIMOS pointing. For our 7 VIMOS pointings, we should expect ≈ 231 LRGs, when as we will see later, there have been selected 280 LRG candidates in total.

4.4.1 Redshift determination

In Chapter 1, for MOSCA data, we used the 2dF RUNZ software for redshift determinations with templates cross-correlation. As our LRG sample from VLT is bigger, and

specifically is divided in quadrants, we find particularly useful to use $SpecPro$ (Masters & Capak, 2011) software. $SpecPro$ is an interactive IDL program for viewing and analyzing spectra. One of its key functions, that makes $SpecPro$ favourable for our analysis, is that it has been designed to examine spectra from multislit spectrographs. This makes $SpecPro$ ideal for the VIMOS data, as the data are stored per slit mask per quadrant, thus to run the program we only have to insert the slit number of the 1-D spectrum from the desired quadrant.

The 1-D spectrum structure, contains three fields : $flux$, $ivar$ and $lambda$. The $flux$ field is the spectrum, the $ivar$ is the inverse variance of the $flux$, and $lambda$ is the wavelength at each pixel. $SpecPro$ allows the user to handle the data through a variety of available tasks, hence, we take advantage of the following ones: adjustment of redshift guess, binning and smoothing the 1-D spectrum, overplot galaxy templates and plotting of the redshifted emission/absorption features. In Fig. 4.9, we show how the 1-D spectra of 4 random VIMOS LRGs as are displayed on $SpecPro's$ interface. Furthermore, we can also see the galaxy templates, with overlays of emission and absorption lines, redshifted to the selected redshift. Moreover, the atmospheric absorption regions are also shown. The information of position of the telluric lines, has been proved to be very useful in redshift determination, for cases where the Ca II H + K break was coinciding in these regions.

$SpecPro$'s templates span a broad range of galaxy types. For the early type galaxies which we are dealing with, redshifts have been derived by cross-correlating mainly the following galaxy templates: red galaxy, green galaxy, VVDS elliptical and VVDS early spiral (Le Fèvre et al., 2005a) template. The red galaxy template is for a passive galaxy template from $PEGASE$ spectral evolution model (Fioc & Rocca-Volmerange, 1997). The green galaxy template refers to an early spiral/spiral template from $PEGASE$. VVDS elliptical template is from a passive galaxy template, with strong absorption and no emission while the VVDS early spiral has stronger emission and less absorption. One would expect, that the elliptical galaxies templates would be able to match the majority of the LRGs, but we also came across cases where even a VVDS starburst template could fit the observed spectrum. In Fig. 4.10 we show the reduced spectra with mea-
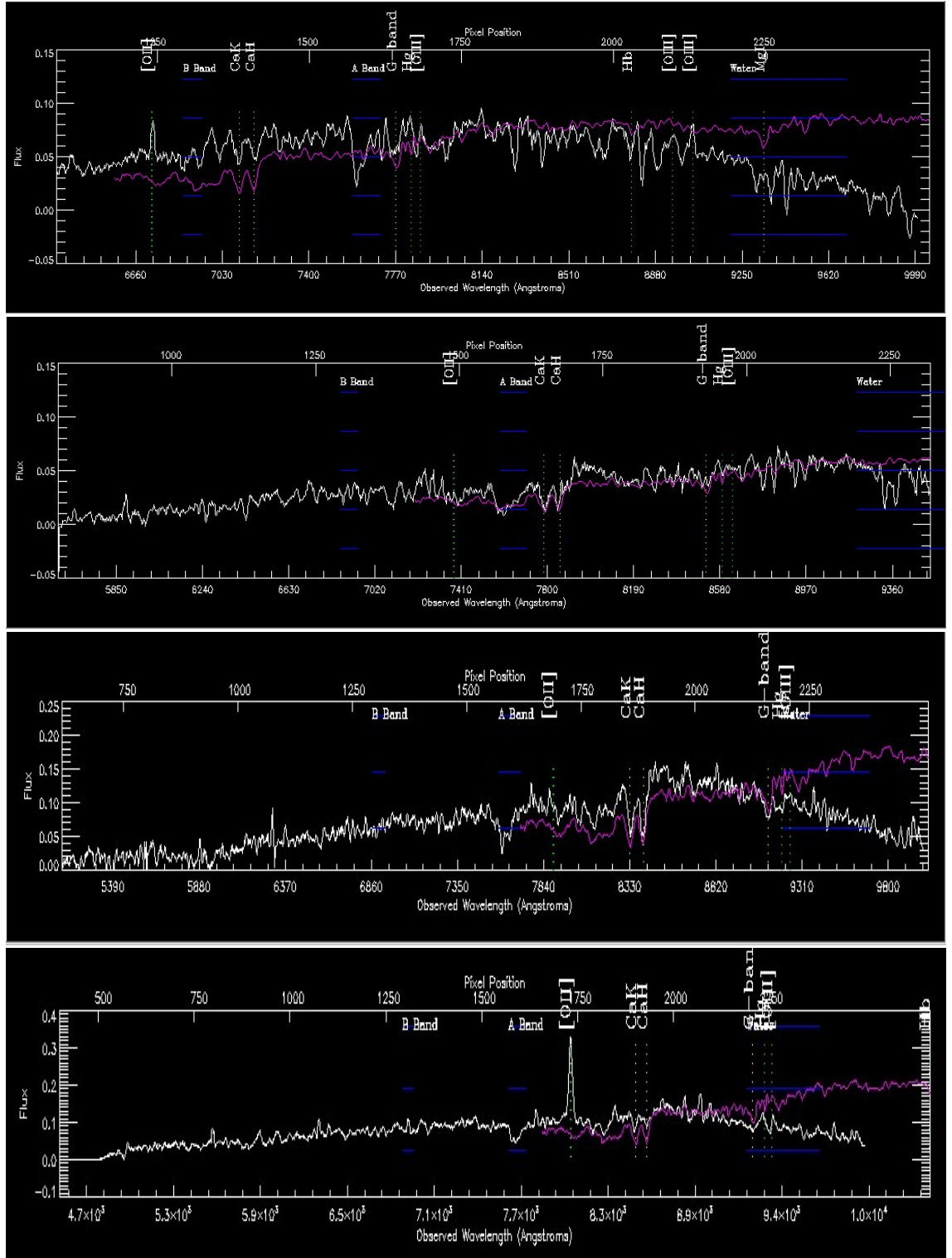
Figure 4.9: *SpecPro* output for a sample of 4 LRGs spectra with measured redshfits (flags=*q*3): 0.805, 0.979, 1.118 and 1.147 starting from the top to bottom. For each spectra we can also see the emission and absorption lines from the redshifted templates (green and white, respectively). Also, the telluric absorption regions are shown (blue ranges). The flux is arbitrarily.
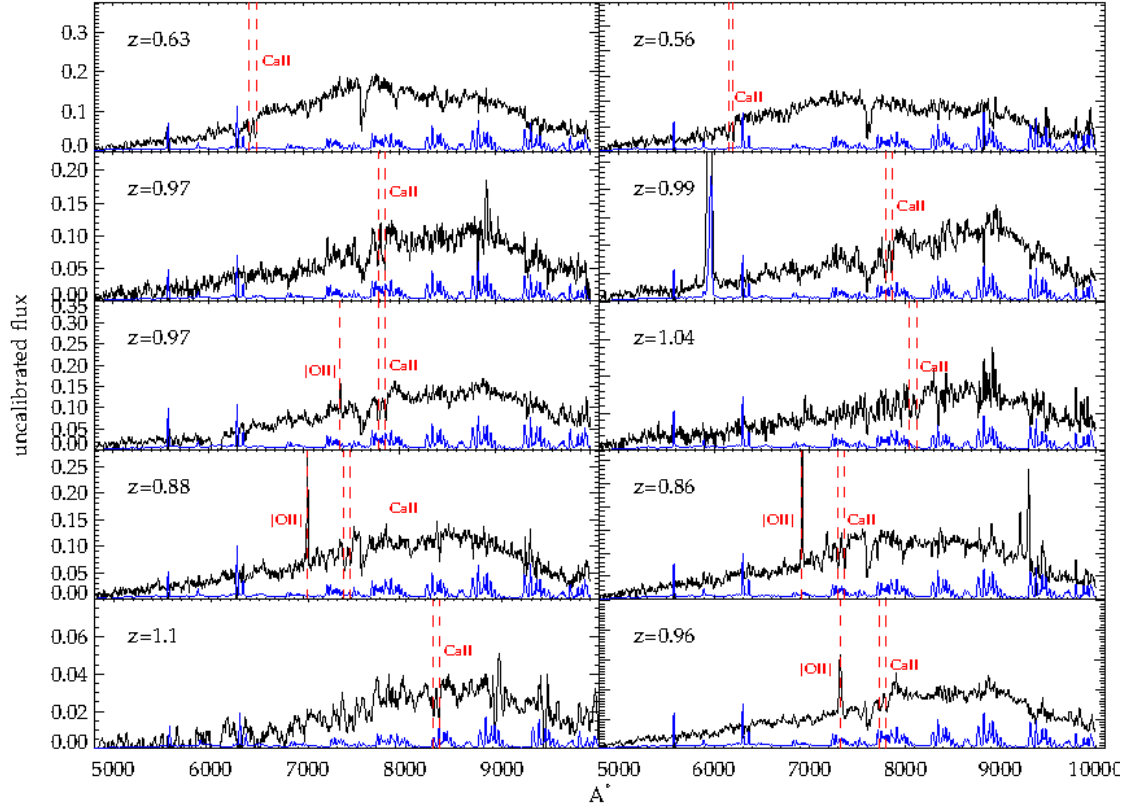
Figure 4.10: Reduced 1-D VLT LRGs spectra. The LRGs presented here, are the same objects that referred in the figures of §4.3. Emission/absorption lines as well as the sky spectrum for each object, are also shown.

sured redshifts of the same LRGs that were presented in the figures in the discussion of the reduction procedure (§4.3).

It should be note that ≈ 30 (58 out of 187) of our LRGs show emission features such as [OII] and in rarer cases, [OIII]. Such a trend might expected, due to the *Butcher-Oemler* effect. When galaxy populations from clusters have been studied at intermediate redshifts ($0.3 \lesssim z \lesssim 0.5$), Butcher & Oemler (1978) found that the fraction of the blue galaxies in distant clusters is larger compared to nearby clusters. Our results could be interpreted as an indication that $Em + Abs$ phenomena are taking place, supporting that these massive "post-starburst" galaxies are evolving with redshift (Roseboom et al., 2006). This result stressed even further the need to study the distant massive galaxies and track if the fraction of LRGs with [OII] emission increases with redshift.

During redshift determination, we adopt the flag scheme which almost mimics the one used for GAMA spectra in Chapter 1. Flag $q = 3$ and $q = 2$ are for $90 - 100\%$ and $75 - 90\%$ secure redshifts, respectively. We include two new flags, $q = 1$ and $q = 0$, where the former is given to galaxies where their spectra did not show any obvious feature, so we could not have a reliable redshift measurement. The $q = 0$ flag, describes cases where $ESOREX$ is not able to make an object detection across the slit. Both of these two lower values flags, will be helpful for any future observations. From a total of 280 placed slits, we measured redshifts for 187 galaxies, which means a total success rate of $\approx 70\%$. We show the spectroscopic redshift distribution of $q = 3$ and $q = 2$ LRGs in Fig. 4.11. Table 4.3 contains a summary of the redshift measurements for the VIMOS LRGs, which are categorized into the two colour cuts as in Chapter 2, for the $700 \deg^{-2}$ and the $240 \deg^{-2}$ LRG sample with Priority A and B, respectively (see Fig. 3.1). Six observed targets were labelled as SDSS STARS, out of which 3 have been flagged with reliable redshifts, two did not show any prominent feature ($q = 0$) and one has been confirmed to be star. The star spectrum has been flagged as q=0. Furthermore, two LRGs have been determined to be stars. So the stellar contamination in the spectroscopic observations is 1 per cent, even smaller compared to the 4.5 per cent as presented in §3.2.1 and §3.6.3. The low per cent of stellar contamination in the spectroscopic LRGs, does not have any significant effect on the clustering measurements, as will presented next. In Appendix A, we present the properties of all the LRGs in Stripe 82 with accurate measured spectroscopic redshifts ($q = 3$ and $q = 2$). For each object, it is also provided the redshift quality flag, the priority sample that belongs and the presence of emission line on its spectrum.

Our results confirm as we expected already from §3.2.1 and Fig. 3.10 that the Priority B sample, is sampling more distant LRGs compared to the bluer selection of Priority A. This can be seen in Fig. 4.12, where we present the redshift distribution of the two samples. The $240 \deg^{-2}$-Priority B LRG sample occupies the redshift range above $z \sim 0.75$, while the $700 \deg^{-2}$-Priority A LRGs cover also the same z-range, starting now from $z > 0.4$. We notice that compared to the original z-steps of the evolutionary tracks of Fig. 3.1, the measured spectroscopic redshifts place the LRGs to a lower redshift. The offset on the observed redshift values is ~ 0.2.
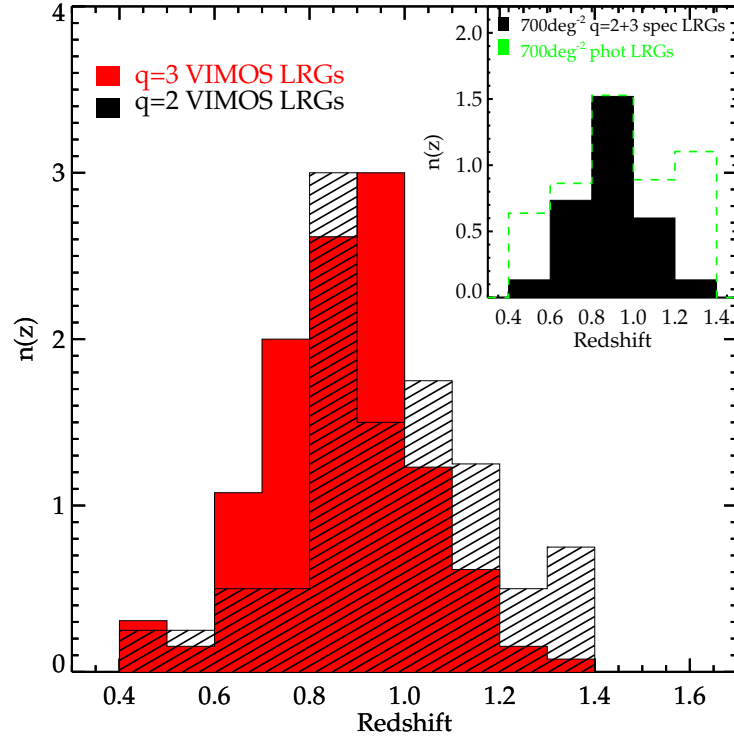
Figure 4.11: Spectroscopic redshift distribution of the VIMOS $700 \deg^{-2}$ LRGs in Stripe 82. From a total sample of 280 LRGs, 147 are flagged with $q = 3$ (90-100%), 40 with $q = 2$ (75-90%) and 93 with $q = 1/0$ were undefined. The inner panel, shows the *n(z)* of the $700 \deg^{-2}$ spectroscopic LRGs and the $700 \deg^{-2}$ photometric LRGs.

Table 4.3: Summary of VIMOS LRGs spectroscopic redshift measurements

Sample	Redshift Quality Flags			
	$q = 3$	$q = 2$	$q = 1$	$q = 0$
Priority A LRGs	108	16	44	7
($700 \ deg^{-2}$)				
Priority B LRGs	39	24	29	13
($240 \ deg^{-2}$)				
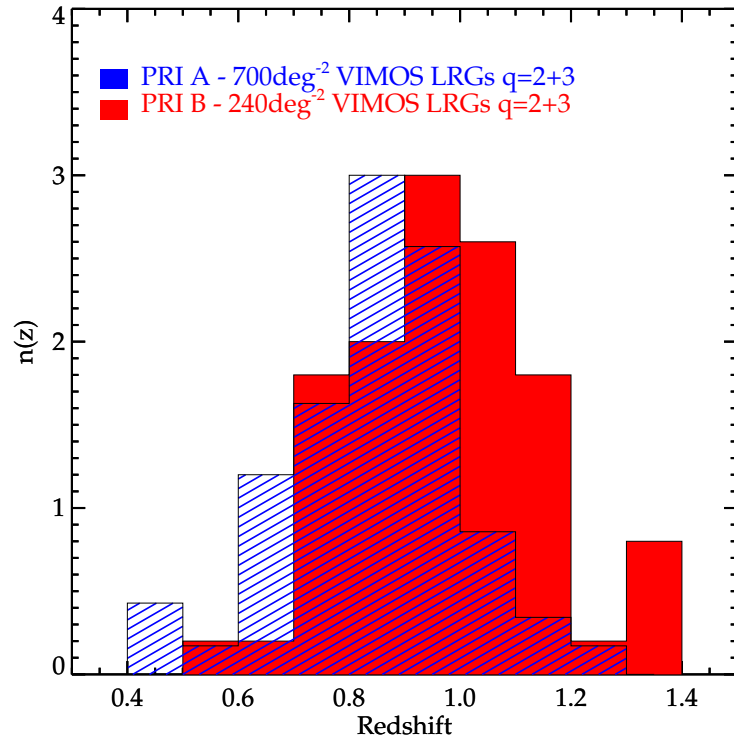
Figure 4.12: The redshift distribution of the $700 \deg^{-2}$ - Priority A and $240 \deg^{-2}$ - Priority B LRGs (objects with $q = 3 + 2$). The $240 \deg^{-2}$ LRGs show a higher redshift distribution, as expected from their redder selection.

From here after, we will refer to the results from the $700 \ \mathrm{deg}^{-2}$ LRGs sample in Stripe 82 of Chapter 2 (Nikoloudakis et al., 2013) as the photometric LRGs, since the Newman cross-correlation technique has been applied to derive the *n(z)*. The spectroscopic *n(z)* compared to photometric *n(z)* (inner panel in Fig. 4.11), is in good agreement, except at the tails of the distribution. This might be due the fact, that even though our observations made with the upgraded CCDs, we could still notice that the red end is affected by fringing effects and the sky subtraction is poor in some cases. Moreover, in more extreme cases, absorption by water vapour that occurs at ∼9300Å could also be responsible for the lack of redshift measurements in the highest z range. Nonetheless, the objects without an accurate redshift measurement (flags $q = 0, 1$) or even those that might have been misclassified, would be able to fill the empty z-ranges of Fig. 4.11. As our flagging criteria are very strict, we do not believe that the misclassified objects will contribute significantly to the measured spectroscopic *n(z)* shape. We will revisit the issue of uncovered z-range later on, when we will discuss the number density of the spectroscopic LRGs in §4.5.

A simple indicative test, to understand the completeness of the spectroscopic LRG sample compared to the whole population of the $700 \ \mathrm{deg}^{-2}$ LRG sample in Stripe 82, is via their number counts. In Fig. 4.13 we show the number counts of the $700 \ \mathrm{deg}^{-2}$ LRG photometric and spectroscopic samples in Stripe 82. Impressively, the spectroscopic LRGs show the same completeness almost up to faintest K limit. They are congruent with the number counts of the photometric $700 \ \mathrm{deg}^{-2}$ LRGs, confirming moreover that $\approx 30\%$ LRGs do not have spectroscopic measurements. Unfortunately, for the moment there is no other undertaken, or even incomplete, K-limited LRG survey in the literature that we could use for comparison with the Stripe 82 LRG number counts.

To sum up, from what has been learnt until now we are convinced that the spectroscopic observations which have been carried with VIMOS and the resulting *n(z)*, have mapped a representative fraction of the total $700 \ \mathrm{deg}^{-2}$ LRGs in Stripe 82. By exploiting the properties of the spectroscopic LRGS, we have the opportunity to extract even greater information for the evolution of the high-z LRGs in Stripe 82, by constraining further the position of these massive galaxies in redshift. Follow-up observations are
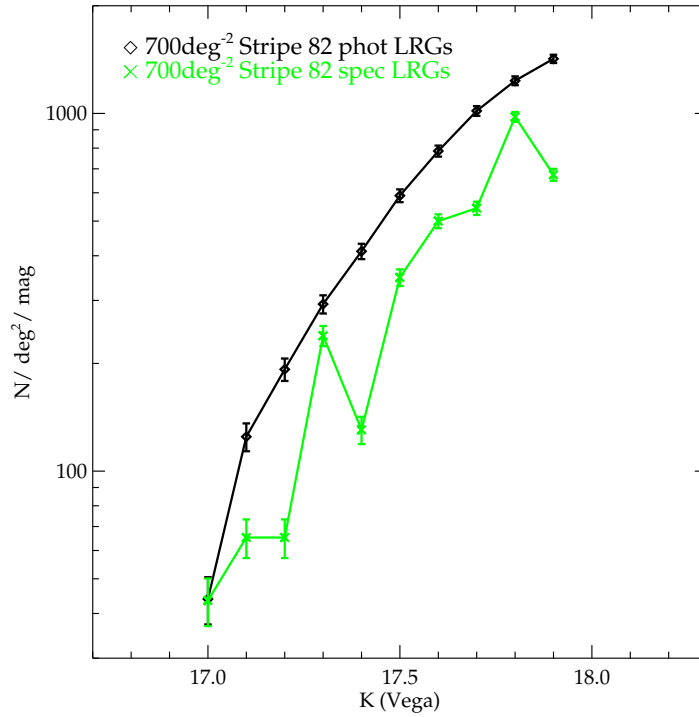
Figure 4.13: Differential K-band number counts for the $700\ \mathrm{deg}^{-2}$-Priority A photometric (black diamond) and spectroscopic (green star) LRGs in Stripe 82. Uncertainty in the galaxy count measurements is given by the Poisson 1σ errors.

clearly needed, as we need more data to check further their redshift distribution. However, on the assumption that the spectroscopic $n(z)$ of the Stripe 82 LRGs is correct, we next check the effect on our clustering analysis of Chapter 2.

4.5 Clustering Analysis

So far we have described how to analyze and accurately measure the redshifts of a representative spectroscopic sample of the $700\ \mathrm{deg}^{-2}$ LRG sample in Stripe 82. It is of great interest to repeat part of the clustering analysis of these LRGs, similar to what we have shown in Chapter 2 (§3.5), but now taking into account their spectroscopic redshift information. Spectroscopic incompleteness of the LRGs, does not prevent then from being valuable in defining their evolution up to present time.
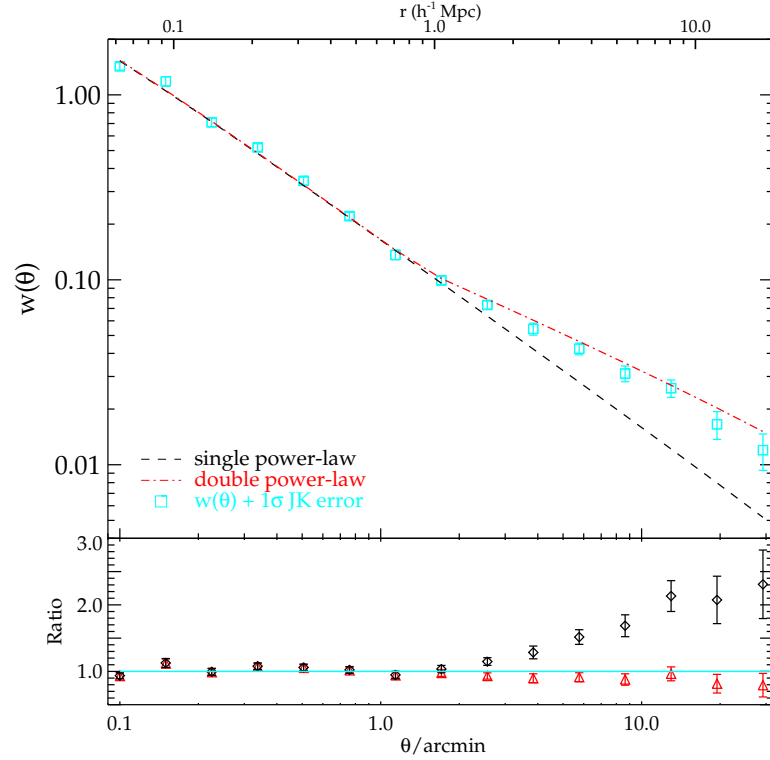
Figure 4.14: The best-fit single power law (diamond) and double power law (triangle), as have been established from the spectroscopic *n(z)* of the $700 \deg^{-2}$ LRGs, overplotted on their angular correlation function (square) with the 1σ Jackknife error. In the lower panel, we can see the fitting residuals.

4.5.1 $w(\theta)$ **and power-law fits**

Similar to the work presented in §3.5.2, we employ the same principle, that the angular correlation function can be described with power-laws. The first part of our analysis here, will be consisted by fitting power-laws to the systematics corrected $w(\theta)$ (see discussion in §3.6.3). The power-laws are fitted again in the range $0'.1 < \theta < 30'$ using χ^2-minimization. We first note that the 3-D clustering strengths of the two LRG samples are now lower than previously as a result of assuming the spectroscopic *n(z)*. For the single power-law, our best-fit r_0, γ pair is measured to be $r_0 = 6.02 \pm 0.05 \mathrm{h}^{-1}\mathrm{Mpc}$ and $\gamma = 2.01 \pm 0.01$, with a reduced minimum $\chi^2_{red} = 8.21$, compared to $r_0 = 7.54 \pm 0.16 \mathrm{h}^{-1}\mathrm{Mpc}$ and $\gamma = 2.01 \pm 0.01$ previously measured. The estimated best-fits $r_0 - \gamma$ values for the

double power-law at small scales are $r_{0,1} = 6.04 \pm 0.19 \mathrm{h}^{-1}\mathrm{Mpc}$ and $\gamma_1 = 2.01 \pm 0.02$, where at large scales are $r_{0,2} = 7.74 \pm 0.3 \mathrm{h}^{-1}\mathrm{Mpc}$ and $\gamma_2 = 1.62 \pm 0.04$ with a reduced minimum $\chi^2_{red} = 5.11$. The previously measured values from the photometric LRGs were $r_{0,1} = 7.63 \pm 0.27 \mathrm{h}^{-1}\mathrm{Mpc}$ and $\gamma_1 = 2.01 \pm 0.02$, while $r_{0,2} = 9.92 \pm 0.4 \mathrm{h}^{-1}\mathrm{Mpc}$ and $\gamma_2 = 1.64 \pm 0.04$ at small and large scales, respectively. In Fig. 4.14, we present the best-fit single and double power-laws of the spectroscopic $700 \ \mathrm{deg}^{-2}$ LRGs, as estimated from the updated spectroscopic *n(z)*. In Table 4.4, we summarize the results for the best-fits of the single and double power-laws of: the AAΩ LRGs of Sawangwit et al., the $700 \ \mathrm{deg}^{-2}$ photometric LRGs (Nikoloudakis et al., 2013) and the new results of the spectroscopic $700 \ \mathrm{deg}^{-2}$ LRGs.

The difference in the clustering strengths between the photometric and spectroscopic LRGs is caused the width of the spectroscopic *n(z)* (see Fig. 4.11 small panel) being narrower compared to the width of the photometric LRGs, hence the clustering of the spectroscopic LRGs is projected less in the 2-D. As expected, the slope in both cases (photometric and spectroscopic LRGs), remains almost the same . This behaviour is expected from Limber's equation, as the peak of the spectroscopic n(z) has not changed significantly compared to the photometric n(z) ($\bar{z}_{phot} = 1$ and $\bar{z}_{spec} = 0.9$), so the projection takes place at similar depth.

Table 4.4: Best fit parameters for the single and double power-law fits to the angular correlation function of the AAΩ LRGs, the Stripe 82 photometric 700 deg^{-2} LRGs and the spectroscopic 700 deg^{-2} LRGs (q=2+3).

Sample	$\bar{z}$	n_{g} $(h^3 Mpc^{-3})$	Single power-law			Double power-law			
			γ	$r_0 (h^{-1}\,\mathrm{Mpc})$	χ^2_{red}	$\gamma_{1,2}$	$r_{0,1,2}(h^{-1}\,\mathrm{Mpc})$	$r_b(h^{-1}\,\mathrm{Mpc})$	χ^2_{red}
AAΩ LRGs $(110 deg^{-2})$	0.68	2.7×10^{-4}	1.96 ± 0.01	7.56 ± 0.03	42.8	2.14 ± 0.01 1.81 ± 0.02	5.96 ± 0.03 7.84 ± 0.04	1.3	3.4
S82 phot LRGs $(700 deg^{-2})$	1.0	$3.20 \pm 0.16 \times 10^{-4}$	2.01 ± 0.01	7.54 ± 0.16	5.89	2.01 ± 0.02 1.64 ± 0.04	7.63 ± 0.27 9.92 ± 0.40	2.38	3.65
S82 spec LRGs $(700 deg^{-2})$	0.9	$5.88 \pm 2.74 \times 10^{-4}$	2.01 ± 0.01	6.02 ± 0.05	8.21	2.01 ± 0.02 1.62 ± 0.04	6.04 ± 0.19 7.74 ± 0.26	2.38	5.11

4.5.2 ΛCDM model fits

Additionally, to the power-law fits, we will try to fit the standard ΛCDM model to the $w(\theta)$ using the updated *n(z)* of the VIMOS LRGs. In Chapter 2, while performing similar fit for the photometric 700 $\deg^{-2}$ LRGs, we managed to achieve the best-fit at large scales only at 2-3σ level to the observed $w(\theta)$ (see Fig. 3.14). Here, by using the systematics corrected $w(\theta)$ combined with the spectroscopic *n(z)*, the best-fit linear bias parameter for the range $\sim 4' - 45'$ is estimated to be $b = 2.20 \pm 0.06$ with $\chi^2_{red} = 5.24$. In Fig. 4.15 we show the LRG $w(\theta)$ with the 1σ error and the best-fit ΛCDM model.

Once again, the upper limit of fitting range has been varied to avoid any influence from the non-linear regime. Thus, for the range $\sim 4' - 60'$ the best-fit bias is $b = 2.15 \pm 0.05$ with $\chi^2_{red} = 5.65$ and at $\sim 4' - 30'$ is $b = 2.24 \pm 0.06$ with $\chi^2_{red} = 4.94$. In contrast to what we have measured for the photometric LRGs in Chapter 2, the bias values for the spectroscopic case as presented here are smaller, falling in with previous studies. Once more though, in terms of the flat slope of $w(\theta)$ at large scales, the standard ΛCDM linear model is inconsistent with the data at $1 - 2\sigma$ level.

4.5.3 Halo model fits

By the same token, we will use the HOD formalism to fit the the observed angular correlation function and search for an alternative fit to the flat large-scale slope of the Stripe 82 LRGs. Adopting the 3-parameter (M_{min}, M_1, α) HOD model as in §3.5.4, we fit the systematics corrected $w(\theta)$ using the spectroscopic information for the Stripe 82 700 $\deg^{-2}$ LRGs. Due to the different inserted n(z) in the HOD model between this study and the one in Chapter 2, as well as the difference in the fitted $w(\theta)$, it is most likely that the output values of the parameters will vary. When we used the available photometric *n(z)* for the 700 $\deg^{-2}$ LRGs, the best-fit model parameters, while fitting using the full co-variance matrix over $0.25' < \theta < 60'$, which were: $M_{\min} = 2.19 \pm 0.21 \times 10^{13} h^{-1} M_{\odot}$, $M_1 = 21.9 \pm 2.1 \times 10^{13} h^{-1} M_{\odot}$, $\alpha = 2.25 \pm 0.05$, $n_g = 0.8 \pm 0.2 \times 10^{-4} h^3 Mpc^{-3}$, $M_{\rm eff} = 3.3 \pm 0.3 \times 10^{13} h^{-1} M_{\odot}$, $F_{\rm sat} = 3.17 \pm 0.08\%$, $b_{lin} = 2.81 \pm 0.10$ with $\chi^2_{\rm red} = 3.6$.

In Fig. 4.16 we show the best-fit HOD model for $w(\theta)$, compared to the data. The
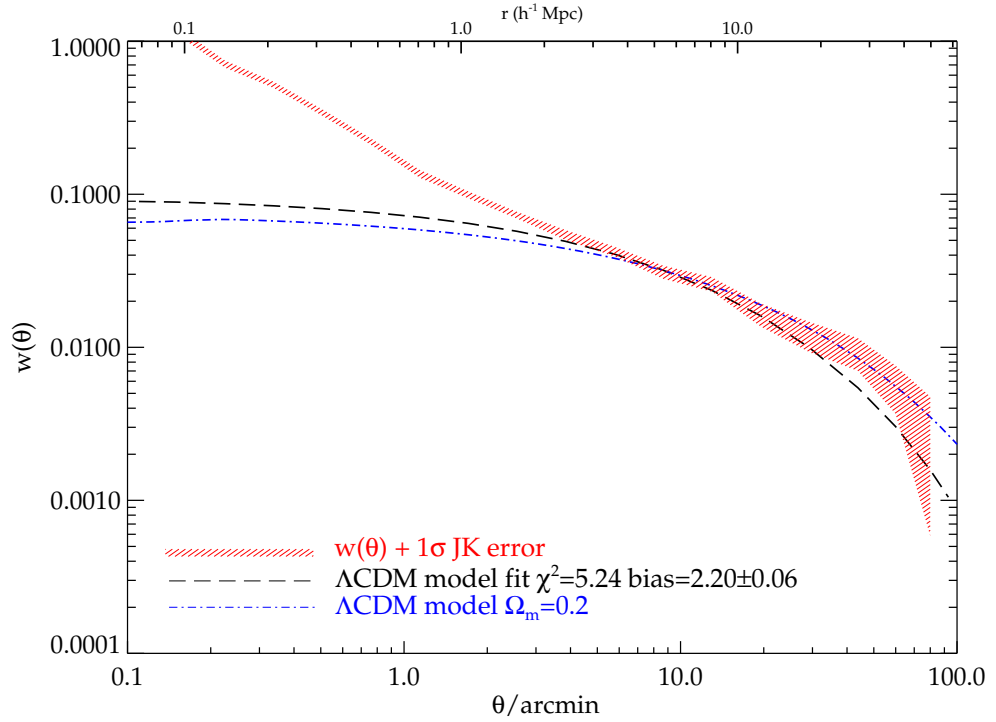
Figure 4.15: The best-fit spatially flat, ΛCDM model assuming $\Omega_m = 0.27$ compared to the observed $w(\theta)$ of the spectroscopic $700 \deg^{-2}$ LRGs in the linear regime. As with the photometric LRGs, the standard model cannot explain the large scale power excess in the angular correlation function of the Stripe 82 LRGs. The shaded area corresponds to $\pm 1\sigma$ jackknife error. Also shown is a spatially flat ΛCDM model with the same parameters as before except for a lower value of $\Omega_m = 0.2$ and an arbitrary normalisation. The $\Omega_m = 0.2$ model appears to give a better fit than the standard $\Omega_m = 0.27$ model.
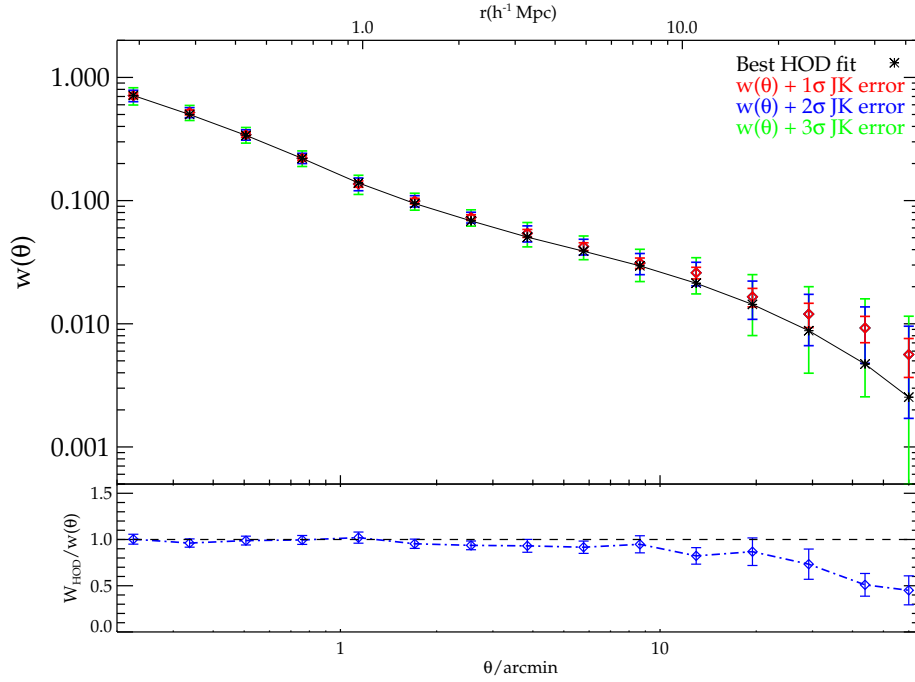
Figure 4.16: The measured $w(\theta)$ for the 700 $\deg^{-2}$ LRG sample with the best-fit HOD model (black star). The 1, 2 and 3σ Jackknife errors are shown in red, blue and green, respectively.

first thing we notice is that while at small scales the best-fit HOD is in good agreement with the $w(\theta)$ measurements, at large scales the model fits only at $1 - 2\sigma$. The best-fits have been improved to what we presented in Chapter 2, but yet the model is rejected at large scales. For the spectroscopic 700 $\deg^{-2}$ LRGs the best-fit HOD model parameters are: $M_{\min} = 0.72 \pm 0.08 \times 10^{13} h^{-1} M_{\odot}$, $M_1 = 10.2 \pm 1.1 \times 10^{13} h^{-1} M_{\odot}$, $\alpha = 1.72 \pm 0.03$, $n_{\rm g} = 3.8 \pm 1.8 \times 10^{-4} h^3 Mpc^{-3}$, $M_{\rm eff} = 2.0 \pm 0.18 \times 10^{13} h^{-1} M_{\odot}$, $F_{\rm sat} = 6.28 \pm 1.86\%$, $b_{lin} = 2.16 \pm 0.09$ with $\chi^2_{\rm red} = 3.4$

The new best-fit HOD model parameters now suggest that the minimum halo mass to contain a central galaxy needs to be only, $M_{\min} = 0.724 \pm 0.08 \times 10^{13} h^{-1} M_{\odot}$, which is three times smaller from the previous HOD model of the photometric LRGs in Stripe 82. The halo mass to contain one satellite galaxy has also dropped to $M_1 = 10.2 \pm 1.1 \times 10^{13} h^{-1} M_{\odot}$. Furthermore, the slope of the relation of the mean number of satellite galaxies and halo mass, α, decreased to 1.72 ± 0.03. Interestingly, the above results, are

more concordant with the HOD of the 2SLAQ and AAΩ LRGs of Sawangwit et al. which may also imply that the Stripe 82 LRGs have not experienced any evolution since $z \sim 1$. Moreover, the best-fit linear bias factor of the spectroscopic LRGs is comparable with the value derived from the best-fit standard model. Likewise, the galaxy number density from the best-fit halo model is consistent with that estimated from Eq. 3.14 (see Table 4.4).

4.5.4 Clustering Evolution

Besides the models presented already, in Fig. 4.17a,b we illustrate how the Stripe 82 clustering, assuming the spectroscopic *n(z)*, has evolved to the AAΩ LRG depth. To evolve the high-z LRGs clustering, we benefit the same clustering models as in §3.7.1, which comprise *comoving* and *virialised* evolution. However, the present findings are not so compatible with the results of §3.7.1, where we found that the clustering of the photometric $700 \deg^{-2}$ LRGs was poorly fitted by all models, although the best of these was the comoving clustering model. Instead, now we observe that the comoving model on large scales is not inconsistent, as well as, the virialised model. It is apparent from the fit residuals, that at small scales similar to Sawangwit et al. the virialised model gives a better fit to the slightly faster evolution needed to fit the small-scale correlation function amplitudes than a comoving model. At intermediate scales ($r > 1h^{-1}\mathrm{Mpc}$) it is unlikely for the galaxies to be virialised, hence we show this model only as a reference. These controversial results of the clustering models will be addressed further with the use of the integrated correlation function of the LRGs following next.

Nevertheless, if we use the integrated correlation function in a $20\,\mathrm{h}^{-1}\mathrm{Mpc}$ sphere, ξ_{20}, we can see from Fig. 4.18, that the spectroscopic LRGs now agree with stable clustering evolution, while Sawangwit et al. found the brighter LRG samples that agree the long-lived clustering model. From Fig. 4.18, we have that the spectroscopic $700 \deg^{-2}$ LRGs can simultaneously share two different clustering scenarios. The first one agrees with the stable clustering evolution of the bright LRG samples while the second stands with the no-evolution trend of the faint LRG samples. The first scenario is probably ruled out, as the spectroscopic $700 \deg^{-2}$ LRG sample n_g is much higher than the bright samples:
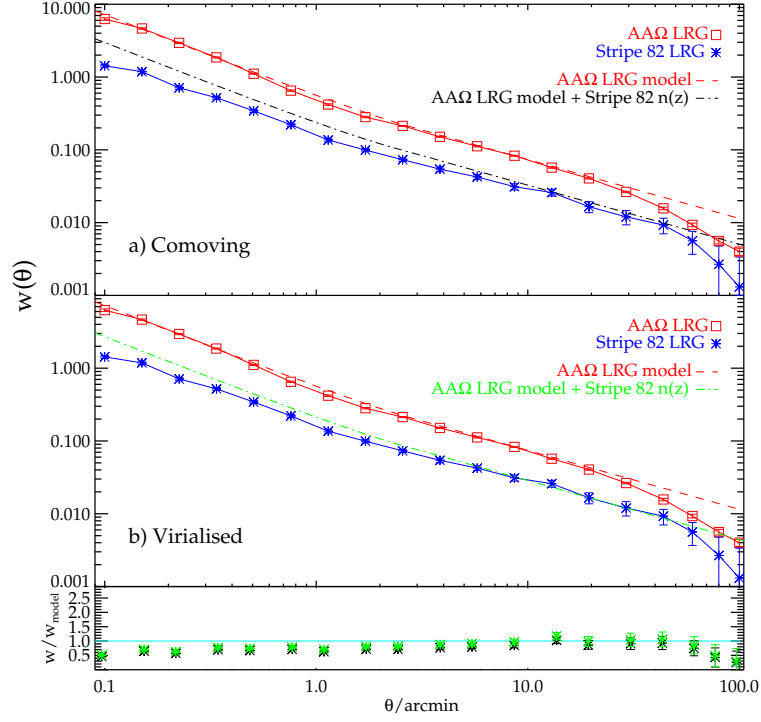
Figure 4.17: **a,b)** Using the best-fit double power-law $r_0 - \gamma$ values from Sawangwit et al. (2011) and utilising the estimated $700 \deg^{-2}$ Stripe 82 LRG spectroscopic *n(z)*, we evolve the Stripe 82 LRGs clustering under the assumption of comoving and virialised evolution clustering models (dashed-dot black and green line, respectively). The Stripe 82 LRG raw $w(\theta)$ is also shown (blue star line). The AAΩ LRG $w(\theta)$ measurements (red square) are also overplotted with their fitted comoving and a virialised evolution models (dashed red line). Virialised evolution fits better the Stripe 82 LRGs $w(\theta)$ at small and large scales compared to comoving evolution, as it can been seen from the residuals in the lower panel. The virialised model still overestimates the amplitude at $\theta < 2'$
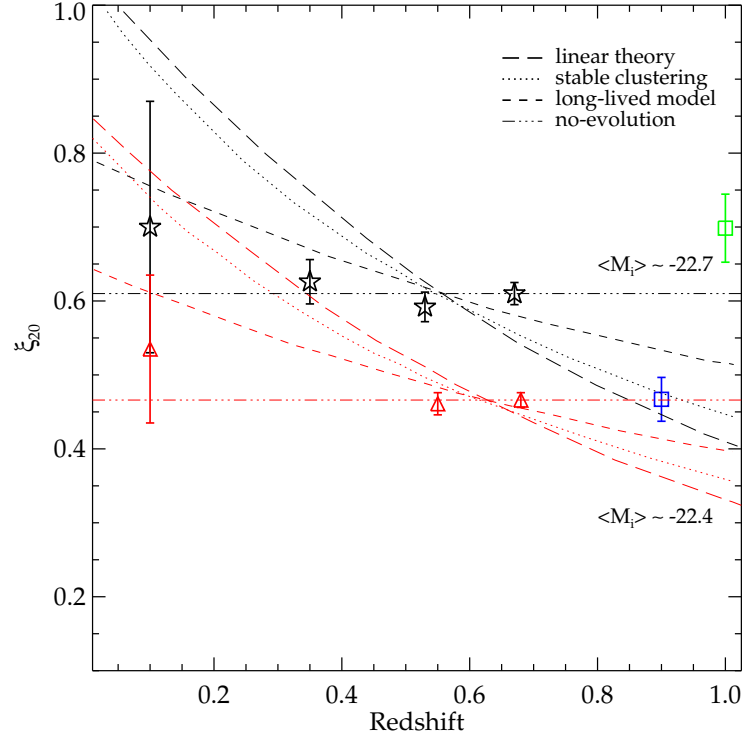
Figure 4.18: The LRG ξ_{20} measurements from Sawangwit et al. (2011), where stars represent the brighter samples (SDSS, 2SLAQ* and $AA\Omega^*$-LRG), and triangles the lower luminosity samples. The lowest redshift data are early-type galaxies from 2dFGRS (Norberg et al. 2002). The *i*-band absolute magnitude LRGs have been corrected using the dust map of Schlegel et al. (1998) and $K + e$ corrected to $z = 0$ using the Early-type galaxy templates from Bruzual & Charlot (2003). The photometric 700 deg^{-2} Stripe 82 LRGs ξ_{20} measurement is at $z = 1$ (green square), while the spectroscopic 700 deg^{-2} LRGs is at $z = 0.9$ (blue square).

SDSS, $2SLAQ^*$ and $AA\Omega^*$ LRGs, with $n_g = 5.88 \pm 2.74 \times 10^{-4}h^3\ Mpc^{-3}$ for the Stripe 82 LRGs and $n_g \sim 1 \times 10^{-4}h^3\ Mpc^{-3}$ for the bright LRGs.

The spectroscopic redshift distribution of the 700 deg^{-2} LRGs in Stripe 82 now give us a more physical explainable clue, due to the much narrower width in contrast with the photometric *n(z)*. The uncertainty in the number density of the spectroscopic LRGs $n_g = 5.88 \pm 2.74 \times 10^{-4}h^3Mpc^{-3}$ though, cannot place with confidence the spectroscopic 700 deg^{-2} LRGs in the area of the faint LRGs on Fig. 4.18. They can either occupy the long-lived (long-dashed line) in case where the $1 - 2\sigma$ uncertainty limit in their number

density is taken into consideration or the no-evolution model (dotted-dashed line) for the raw number density number. This leaves us with the conclusion, that the observed evolution of the LRGs clustering is very slow. These results are further supported with what has been seen in previous studies (White et al., 2007; Wake et al., 2008; Sawangwit et al., 2011).

Up to this point, the question that has arisen, is why there is such a difference between the photometric and spectroscopic *n(z)*. First, we need to explore more the effects of any errors that could have violated the redshift distribution resulting from cross-correlations. In Newman's work, there is a detailed discussion for the impact of random and systematic errors during the recovery of the true redshift distribution. Most of the systematic errors, such as : errors in the assumed cosmology, evolution in bias, errors in the autocorrelation measurements of the spectroscopic samples and field-to-field zero points variations, have already been named in Chapter 2 as we clarified that our measurements cannot be affected by those errors.

Random errors on the other hand, overall refer to: how the errors on the measurement of the redshift distribution probability, $\phi_p(z)$, scale with the selected r_{max} and how cosmic variance changes the error measurements. Since most of the galaxies have $\gamma \approx 1.6 - 1.9$, the errors scale very slowly with r_{max} as it has been shown from Eq.9b in Newman:

$$\sigma(\phi_p(z)) = \frac{3 - \gamma}{2\sqrt{\pi}H(\gamma)} \left(\Sigma_p \frac{dN_s}{dz} \Delta z \right)^{-1/2} \frac{d_A(z)\, dl/dz}{r_0^\gamma \, r_{max}^{2-\gamma}}, \tag{4.1}$$

where Σ_p is the mean surface density of objects in the photometric samples, the Stripe 82 LRGs in our case, and $\frac{dN_s}{dz}$ is the actual redshift distribution of the sample with the known redshift that used in the cross-correlations. Moreover, if one does not consider the small-separation pairs ($r_p < 1 - 2\mathrm{h}^{-1}\mathrm{Mpc}$) from the calculation of the integrated correlation functions, will have a 15% increase in the net errors. At least for our case, as we did not exclude the smallest scales, we can be assured that our measurements have the minimum possible uncertainty, but the error in the cross-correlations of the observational parameters could explain the broader photometric *n(z)*.

The $\phi_p(z)$ measurement, thus its errors, could be affected by the cosmic variance, which depends on how much the mean density of selected samples for cross-correlations
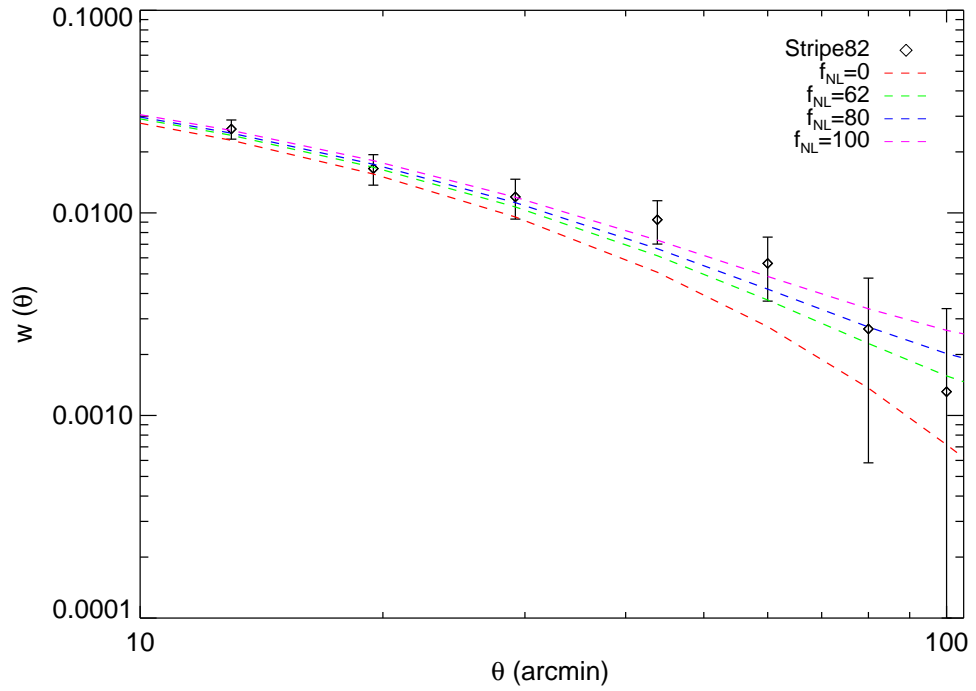
Figure 4.19: The Stripe-82 $z \approx 1$ LRG correlation function compared to a standard ΛCDM model ($f_{NL} = 0$) and models with increasing degrees of primordial non-Gaussianity ($f_{NL} = 62, 80, 100$).

are higher or lower than the Universal mean. The Monte Carlo test in the original work of Newman has explicitly proved that even for the DEEP2 footprint, the smallest field used in our calculations, the effect of cosmic variance is minimum. The author there, finally concludes to that if one wants to constrain quantitatively the nature of dark energy with future surveys i.e LSST and DES, everything can be tackled with the available information and the results will range well within estimated tolerances of the planned surveys.

Concisely, the most likely explanation for the broad photometric *n(z)* is due to cross-correlations errors, as the spectroscopic *n(z)* is more likely to be correct

4.5.5   Test for Non-Gaussianity

In Chapter 2, by introducing the primordial Non-Gaussianity via the f_{NL} factor for the scale dependent bias in the power spectrum of the dark matter halos, the measured $w(\theta)$ was more consistent with the non-Gaussian model of $f_{NL} = 90 \pm 30$.

With the available spectroscopic $n(z)$, we will deproject the $700 \deg^{-2}$ LRGs $w(\theta)$ to the non-Gaussian models as performed in Chapter 2. The large-scale cut-off $k_0 = 10^{-6}$, provided good fits for the other surveys in Chapter 2 (NVSS and $AA\Omega$), hence will be again adopted for our measurements. It's worth noting, that as in Chapter 2, we also applied different cut-off values, and found a non-monotonic behaviour for $w(\theta)$'s behaviour: for $k_0 = 10^{-4}$ the amplitude gets lower while for $k_0 = 10^{-3}$ rises again. Fig. 4.19 is illustrating the angular correlation function of the $700 \deg^{-2}$ LRGs, with various Non-Gaussian models, $f_{NL} = 62, 82, 100$ and the standard ΛCDM model for $f_{NL} = 0$. There is still evidence for non-Gaussianity at the $f_{NL} = 60 \pm 30$ ($\chi^2 = 6.7$) level assuming the spectroscopic $n(z)$.

4.6   Conclusions

In this chapter we have described the spectroscopic observations of the $700 \deg^{-2}$ LRGs in Stripe 82 that took place in Period 86, using VIMOS spectrograph on VLT. Presenting an outline of the reduction of the spectroscopic LRG data, we derived accurate spectroscopic redshifts for this LRG subsample. Introducing the available redshift distribution, we performed a clustering analysis to study the evolution of the distant $z \approx 1$ LRGs.

Applying the obligatory quality checks in the outputs of the VIMOS pipeline recipes, we confirmed that default parameters could reduce the raw data satisfactorily. The Priority-A / $700 \deg^{-2}$ LRGs are originally expected, based on evolutionary models of single burst and $\tau = 1Gyr$, to span the redshift range $0.4 < z < 1.4$. At least, this range was recovered by the cross-correlation method in Chapter 2. With completeness of $\approx 70\%$ for the secured measured spectroscopic redshifts, the spectroscopic $n(z)$ for the $700 \deg^{-2}$ LRGs is found to be narrower than the photometric sample of Chapter 2 with average redshift $z \sim 0.9$. The original assumptions, for the bluer/Priority-A and

redder/Priority-B LRG selection, implying a higher peak in the redshift distribution of the Priority-B / 240 $\deg^{-2}$ LRGs have clearly confirmed as presented in Fig. 4.12. The resulting spectroscopic *n(z)* of the Stripe 82 700 $\deg^{-2}$ LRGs though, did not completely cover the same z-range as the photometric 700 $\deg^{-2}$ LRGs in Chapter 2 . Possible explanations for the missing objects might be due to fringing and bad sky subtraction, or even because we did not accurately configure VIMOS for the desired observations. But the more likely conclusion in the *n(z)* width implied by the cross-correlation technique, with the cross-correlations errors to be responsible for the broad photometric *n(z)*.

Interestingly, spectroscopic measurements of $\approx 30\%$ LRGs have shown prominent emission features, supporting even more the scenario of increasing the number of the massive "post-starburst" galaxies with redshift. Notwithstanding that the spectroscopic data cover an area of $< 0.5\deg^2$, reaching the faintest K-band coverage limits on Stripe 82, this yields them as a quite representative sample for exploring the underlying physics of the high-z LRGs evolution.

Adopting the narrower spectroscopic *n(z)* of the 700 $\deg^{-2}$ LRGs, the best-fit power-laws gave smaller clustering strengths but similar slopes, compared to the values of the photometric 700 $\deg^{-2}$ LRGs of Chapter 2. The measured number density of the spectroscopic LRGs agreed more with the fainter SDSS, 2SLAQ and $AA\Omega$-LRGs. Predictions from HOD models indicated that the number density as well the bias of the spectroscopic 700 $\deg^{-2}$ LRGs is now closer to the low redshift LRG samples of Sawangwit et al. (2011), supporting a slow clustering evolution.

Evolving the Stripe 82 $z \sim 0.9$ LRG clustering to the $AA\Omega$-LRG $z \sim 0.68$ depth, the angular correlation function measurements in concordance are described, by a stable clustering model at small scales and a comoving clustering model at larger scales. The spectroscopic 700 $\deg^{-2}$ LRGs are more compatible with simple evolution models, but the uncertainty in their space density makes it non-trivial to constrain an evolutionary scenario. While the flat slope of $w(\theta)$ persists at large scales and is not in agreement with the ΛCDM linear model, the primordial Non-Gaussianity significance for the spectroscopic 700 $\deg^{-2}$ LRGs has now slightly reduced, at the level of $f_{NL} = 60 \pm 30$, compared to $f_{NL} = 90 \pm 30$ of the photometric 700 $\deg^{-2}$ LRGs, but still is rejected assuming the re-

cent Planck measurements with $f_{\mathrm{NL}}^{\mathrm{local}} = 2.7 \pm 5.8(1\sigma)$ (Planck Collaboration XXIV et al., 2013).

Chapter 5

Revealing the early Universe: counts and clustering of Distant Red Galaxies in UltraVISTA

5.1 Introduction

Selecting and studying large distant luminous galaxies provides deeper insights on the process of galaxy formation and evolution, while testing the existing cosmological models. Optical surveys via the U-dropout technique (Steidel et al., 1996), successfully have managed to map the high-redshift populations of $z \sim 3$ Lyman break galaxies (LBGs), with stellar masses of $\sim 10^{10} \mathrm{M}_\odot$ and star-formation rates of $10 - 100 \mathrm{M}_\odot \mathrm{yr}^{-1}$ (Steidel et al., 2003; Shapley et al., 2001; Reddy et al., 2005). However, the most massive galaxies at these redshifts tend to have little flux bellow the Balmer break and thus are undetected in optical surveys.

The simple NIR selection criterion $(J-K) > 1.3$ (Franx et al., 2003), samples a specific type of galaxy, the so-called distant red galaxies (DRGs), at $2 < z < 4$ (Franx et al., 2003; van Dokkum et al., 2003; Förster Schreiber et al., 2004; Reddy et al., 2005). As compared to LBG selection, the purely NIR DRG selection offers the advantage of having less selection bias due to evolution and/or dust. DRGs contain a significant fraction of evolved stars (Förster Schreiber et al., 2004; Papovich et al., 2006; Kriek et al., 2006a) and while many DRGs show high star-formation rates ($\geq 100 \mathrm{M}_\odot \mathrm{yr}^{-1}$) (van Dokkum

et al., 2004; Reddy et al., 2005), some of them evolve passively with little star-formation activity (Labbé et al., 2005; Papovich et al., 2006; Kriek et al., 2006a,b; Reddy et al., 2006) As expected from their intrinsic K brightness, DRGs are more massive ($M_* \gtrsim 10^{11} M_\odot$) and older ($\sim 1-3$ Gyr old) compared to the LBGs at the same distance (Förster Schreiber et al., 2004; Iwata et al., 2005; Labbé et al., 2005; Papovich et al., 2006; van Dokkum et al., 2006).

Reddy et al. (2005) found similar characteristics in terms of stellar mass, star-formation rate and metallicity between the NIR selected and the optically selected galaxy samples. The differences between the K-selected and the optical selected galaxies can be further revealed by measuring their clustering properties, as the galaxy distribution is determined by the dark matter halo distribution and can be associated with the halo mass. Several clustering DRGs studies have reported high clustering strength $r_0 = 10 - 15 h^{-1} \mathrm{Mpc}$ (Daddi et al., 2003; Grazian et al., 2006; Foucaud et al., 2007; Quadri et al., 2007, 2008; Kim et al., 2011), similar to the most luminous red galaxies in the local Universe. The strong clustering of the DRGs, is implying that these red galaxies are hosted in massive dark matter haloes $M = 10^{13} - 10^{14} M_\odot$

Measurements of DRG clustering, either have been made in at small fields with deep coverage i.e. in the ultradeep 4.5arcmin^2 Faint Infrared Extragalactic Survey (FIRES) Hubble Deep Field-South (HDF-S) field with $K_{Vega} < 24$ DRGs (Daddi et al., 2003) and in the Great Observatories Origin Deep Survey (GOODS) Chandra Deep Field-South (CDF-S) field with 125arcmin^2 and $K_{AB} < 23.5$ (Grazian et al., 2006), or at sufficiently large separations with shallower data i.e. in the UKIRT Infrared Deep Sky Survey (UKIDSS) Deep eXtragalactic Survey (DXS) SA22 with 3.3 deg^2 and $K_{Vega} < 19.7$ DRGs (Kim et al., 2011) and in UKIDSS Ultra Deep Survey (UDS) with ~ 0.65 deg^2 and $K_{Vega} < 21.8$ (Quadri et al., 2008).

In this chapter, we use the newly available deep photometric NIR imaging data from the UltraVISTA[1] survey and present a study of DRGs at $K_{s,AB} < 22.9$ over an area of 1.5

---

[1]Based on data products from observations made with ESO Telescopes at the La Silla Paranal Observatories under ESO programme ID 179.A-2005 and on data products produced by TERAPIX and the Cambridge Astronomy Survey Unit on behalf of the UltraVISTA consortium.
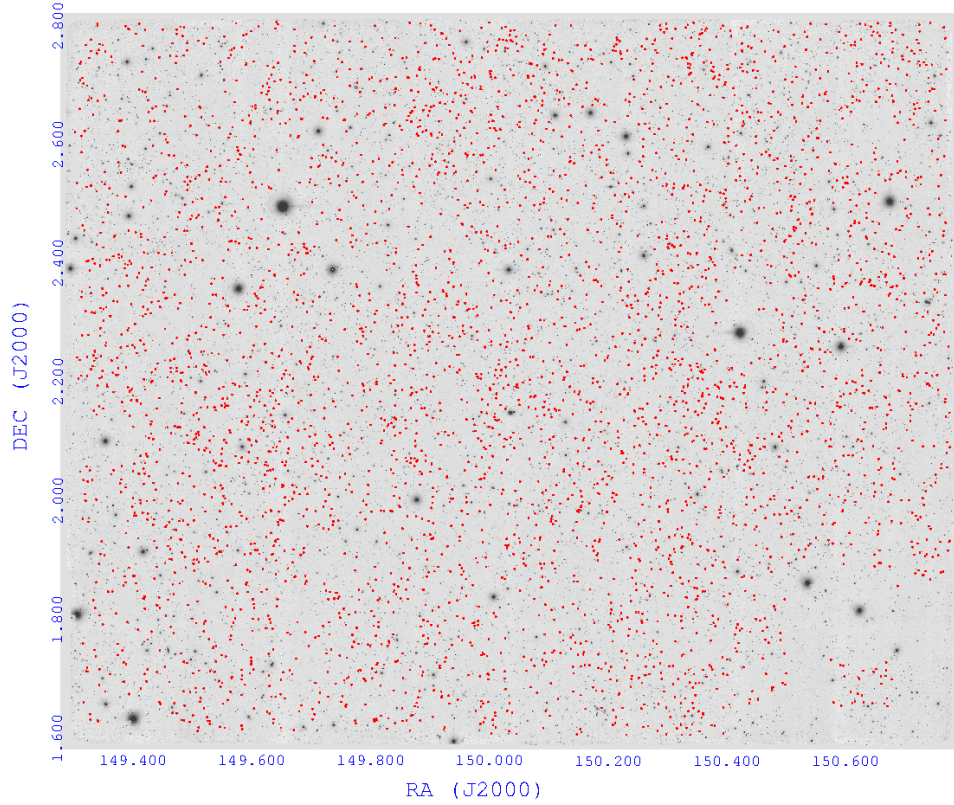
Figure 5.1: The K_s UltraVISTA mosaic. We see the distribution of the 4086 $K_s < 22.9$ DRGS over the total 1.5deg^2 masked field (red circles).

deg^2. With the available deep photometry, we want to study the properties of the DRGs based on their distribution and large scale clustering properties and further conclude on their origin and evolution. Throughout this chapter, we use a flat Λ-dominated cosmology with $\Omega_m = 0.27$, $H_0 = 100h \ \mathrm{kms}^{-1}\mathrm{Mpc}^{-1}$, h=0.7, $\sigma_8 = 0.8$ and magnitudes are given in the AB system unless otherwise noted.

5.2   Data

The UltraVISTA survey is covering an area of $1.5 \ \mathrm{deg}^2$ in four broad band near-infrared filters Y, J, H, K_s, centered on the Cosmological Evolution Survey (COSMOS) (Scoville et al., 2007). Up to date, the UltraVISTA survey is the largest deep near-infrared survey and can be compared with UKIDSS UDS (Almaini et al., 2007), the only relatively

large (not pencil-beam) survey. The UltraVISTA data have been taken with the VIRCAM instrument (Dalton et al., 2006; Emerson & Sutherland, 2010) on the VISTA telescope as part of the UltraVISTA programme. VIRCAM is the most efficient wide-field near-infrared camera due to its large mosaic (16 detectors).

In our analysis we use the UltraVISTA DR1 data release as fully presented by Mc-Cracken et al. (2012). where the 5σ AB stacked images reach depths of $Y = 24.7$, $J = 24.5$, $H = 24.0$ and $K_s = 23.8$ (2-arcsec aperture). Near-infrared shallower observations have been accumulated on the UltraVISTA field by the COSMOS team, as it is shown in Fig. 10 of McCracken et al., where the difference between $17 < Ks < 19$ BzK-selected stars in COSMOS and UltraVISTA as a function of RA and DEC is less than 0.1 mags for all cases. Within the the UltraVISTA DR1, except the source list catalogue from single image extraction, there are also available "dual-mode" catalogues where the K_s band image used for detection. By using the latter catalogues, we are ensured that no source matching errors will be inserted.

5.2.1   Selection of DRGs

DRGs are selected according to the well established criterion of (Franx et al., 2003), $(J - K) > 1.3$ from the UltraVISTA DR1 of McCracken et al. (2012). All K_s magnitudes quoted bellow are the MAG_AUTO from SExtractor software (Bertin & Arnouts, 1996) which have been adopted as total K_s-band magnitudes, while all colour measurements are obtained from the *aperture* magnitudes (fixed 2-arcsec). The DRG selection criterion demands a joint detection in the J and K_s bands and because UltraVISTA data are 95% complete at $J < 24.2$, this resulting a limit magnitude of $K_s < 22.9$ (which is about a magnitude brighter than the K_s-completeness limit). The completeness magnitudes have been computed as the magnitudes, at which, 95% of a simulated stellar population which has been randomly placed into the real field, can be fully recovered. McCracken et al. in their photometric catalogues, have flagged each object with inaccurate photometry, which we take into account when selecting our data in conjunction with the flags from the photometric redshift catalogue as we will discuss in §5.2.2.

Applying all the previously described approach, we select a sample of 4086 DRGs
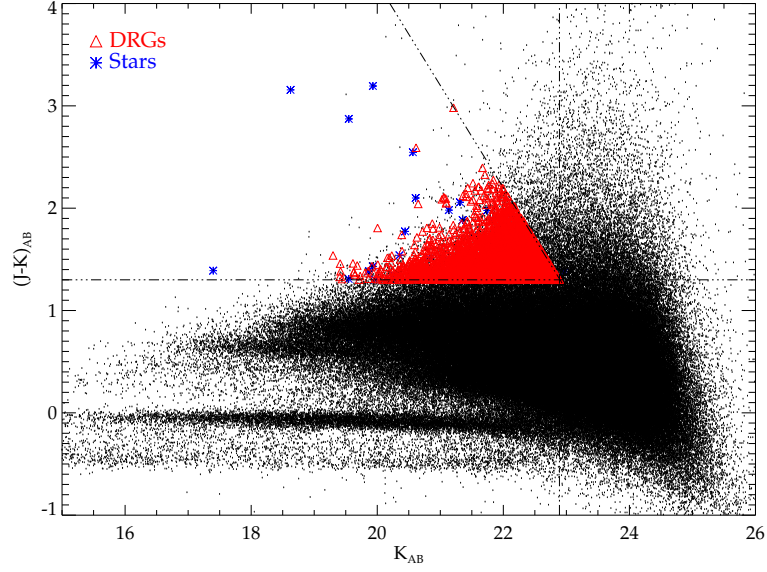
Figure 5.2: $J(-K)_{AB}$ against K_{AB} for sources in the UltraVISTA field. The K-selected objects are shown with the small points, while DRGs that meet the $(J - K) > 1.3$ criterion and have been flagged as galaxies (see text for further details), are represented with the triangles. Objects flagged as stars at the DRGs colour-space region are shown with asterisks. The lines indicate the selection criterion for the DRGs, where we highlight the magnitude limit at $K_s = 22.9$ in order the DRGs to have J detection with $J < 24.2$.

over the 1.5deg^2 masked area in the UltraVISTA field (Fig. 5.1). UltraVISTA survey, by being the deepest moderately large near-infrared survey to date, provides a unique opportunity to sample an large enough population of DRGs at adequate depths. Fig. 5.2 shows the $(J - K)$ colour versus the K_s-band magnitude of DRGs and the rest objects in UltraVISTA field. Except the star locus at $(J - K) = 0$, that is a boundary for the stellar population and galaxies, in the DRGs colour-space region there are also displayed objects which have been characterized as stars through the χ^2 template fitting procedure, during the photometric redshift estimation (see §5.2.2).

5.2.2 Photmetric redshift distribution of DRGs

The DRGs $(J - K) > 1.3$ colour selection criterion has been originally been designed to select DRGs that cover the interval $2 \lesssim z \lesssim 4$ (Franx et al., 2003), with a peak at $z \sim 3$ (Franx et al., 2003; Daddi et al., 2003). Nowadays, it has been widely established though,
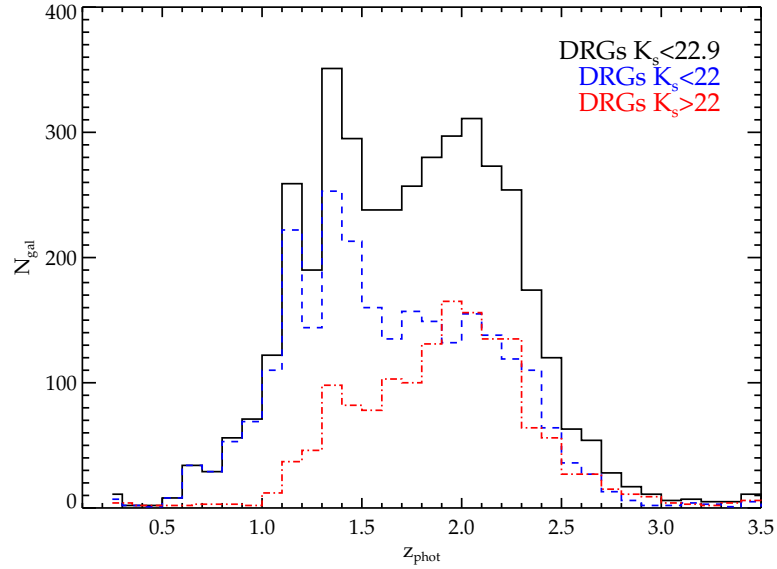
Figure 5.3: The photometric redshift distribution for the whole UltraVISTA DRGs sample (solid line). Furthermore, the photometric distribution for bright ($K_s < 22$ dashed$-$line) and faint ($K_s < 22$ dot-dashed$-$line) DRGs is indicating that there is a strong contamination from the brighter DRGs sample to the fainter, and vice versa.

that the DRGs *n(z)* can have a broad range from $z \sim 1$ up to $z \sim 3.5$ (Grazian et al., 2006; Conselice et al., 2007; Papovich et al., 2006; Lane et al., 2007; Quadri et al., 2007), with the fraction of the $z < 2$ DRGs to increase at brighter magnitudes. The observed different redshift range in each study arises from the different sample under examination in terms of depth and in terms of the available accompanying spectroscopic data that can either be used directly or to constrain the photometric redshifts.

Ilbert et al. (2013) estimated the photometric redshift distribution for all the UltraV-ISTA galaxies ($\approx 220,000$) at $K_s < 24$ with $0.2 < z < 4$ and performed a stellar mass function study for star-forming and quiescent galaxies. These authors used the available broad and intermediate band/narrow band data from the overlapping COSMOS field : u^*, B_j, V_j, r^+, i^+, $z+$, $IA484$, $IA527$, $IA624$, $IA679$, $IA738$, $IA767$, $IA427$, $IA464$, $IA505$, $IA574$, $IA709$, $IA827$, $NB711$, and $NB816$ (see Table 1. in Ilbert et al (2009)), as well as four bands at $3.6 - 8\mu$m from S-COSMOS and the GALEX NUV band, along

with the UltraVISTA NIR bands in order to derive the photometric redshifts using "Le Phare" (Arnouts et al., 2002; Ilbert et al., 2006). To test the accuracy of the photometric redshifts, they combine several spectroscopic samples, and after using 10.800 secured spectroscopic redshifts (see Fig. 1 in Ilbert et al. (2013)), their precision at $z < 1.5$ at $i^+ < 22.5$ was $\sigma_{\Delta z/(1+z)} = 0.008$, $\sim 3\%$ at $1.5 < z < 4.0$.

Ilbert et al. have assigned each objects with extra flags in addition to those from McCracken et al. catalogues, so when we matched the two catalogues, we excluded objects with flags others than galaxies and if they were masked areas. The resulting *n(z)* of the UltraVISTA DRGs is found to have a broad range from $0.5 < z < 3$ with $\bar{z} = 1.76$, as we can see in Fig. 5.3. Dividing our DRGs sample at $K_s > 22$ and $K_s < 22$, it is clear that there is a strong overlapping in their redshift ranges. Grazian et al. (2006) in the GOODS-MUSIC with DRGs at $K_s < 23.5$ observed the contribution from $K_s < 22$ DRGs in the range $1 \leq z \leq 2$, which are actually dusty starbursts and their red infrared colours are due to strong dust absorption (Papovich et al., 2006). Lane et al. (2007) using a brighter sample of DRGs $K = 22.5$ in the UKIDSS UDS, concluded for the most of their DRGs, which were also overlapped with the $R - K$ selection of extreme red objects (EROs), that shown to have SEDs of star-forming galaxies or AGNs at $z \leq 2$. Thus for the relative bright DRG samples and specially those selected in brighter limits than their completeness, their estimated photometric *n(z)* cannot be affected by photometric errors. Furthermore, a small variation in the $(J - K)$ colour cannot have a great effect on the *n(z)* (Conselice et al., 2007). All these, support even more that we have a very accurate photometric *n(z)* for our sample and allowing us to derive robust measurements of clustering properties and the redshift evolution of the UltraVISTA DRGs.

5.2.3   Number counts of DRGs

Fig. 5.4 shows the K-band differential number counts of the K-selected galaxies and DRGs in UltraVISTA field. The number density of K-selected galaxies and DRGs in the UltraVISTA field is derived using the number of objects per square degree and per
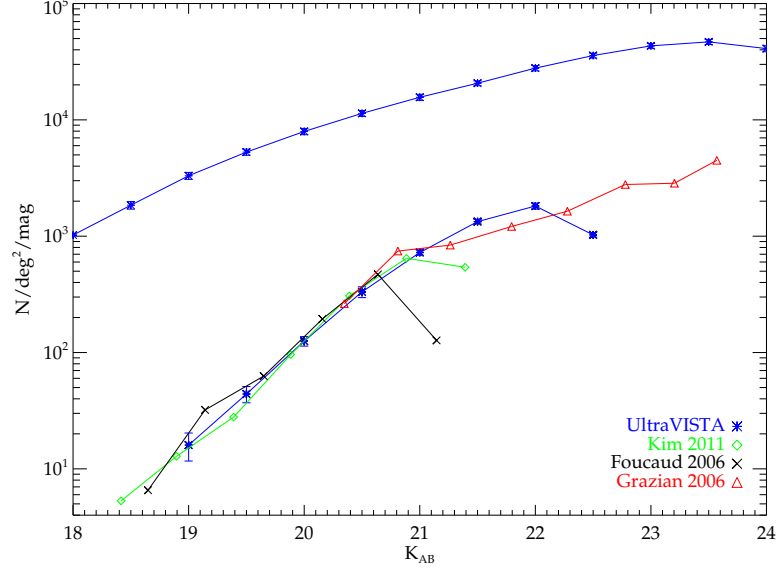
Figure 5.4: Number counts of all galaxies (upper lines) and DRGs. The counts of all galaxies are only K samples, while the DRGs are selected by $(J - K) > 1.3$ and $J < 24.2$ limit due completeness. For comparison we show all galaxies and DRGS in Foucaud et al. (2007) and Kim et al. (2011) from UKIDSS UDS and DXS fields with 0.65deg^2 and 3.3deg^2 area, respectively.

magnitude bin in the K_s-band following Avni & Bahcall (1980) :

$$n(K_s) = \frac{1}{\Delta K_s} \sum_{i=1}^{N_{obj}} \left[\sum_{j=1}^{N_{field}} Area_j^{max} \right]^{-1}, \qquad (5.1)$$

where in our case we have only one continuous field with 1.5deg^2 area and the counts have been computed in bins of $\Delta K_s = 0.5$ magnitude.

We compare our field galaxy number density with the results from the UKIDSS DXS field (Kim et al., 2011). The DRG number counts, in addition are compared with results from studies in the: UKIDSS DXS (Kim et al., 2011), UKIDSS UDS (Foucaud et al., 2007) and GOODS-South field (Grazian et al., 2006). From Fig. 5.4, we notice that the Ultra-VISTA DRG number counts span a range from $19 < K_s < 22.9$ and are in very good agreement with the DRG counts from the brighter samples of Kim et al. (2011) and Foucaud et al. (2007) and with the fainter sample of Grazian et al. (2006). We also can confirm the break feature in the slope at $K_s \sim 20.5$, but not so strongly as has been previously ob-

Table 5.1: K-band differential number counts of galaxies and DRGs in the UltraVISTA survey. The sample of all galaxies is selected only in the K-band, where the DRGs are further limited by $J < 24.2$ completeness. No correction is applied to the DRGs number counts, since they are selected at $K_s < 22.9$, a magnitude brighter than the K_s completeness.

	Galaxies		DRGs	
K bin	Raw	$[deg^{-2}(mag)^{-1}]$	Raw	$[deg^{-2}(mag)^{-1}]$
17.0	204	272		
17.5	426	568		
18.0	767	1022		
18.5	1385	1846		
19.0	2480	3306	12	16
19.5	3961	5281	33	44
20.0	5962	7949	94	125
20.5	8530	11373	249	332
21.0	11726	15634	543	724
21.5	15493	20657	1001	1334
22.0	20880	27840	1362	1816
22.5	26796	35728	770	1026
23.0	32455	43273		
23.5	35104	46805		

served in the wide range of the combined DRGs number counts of Foucaud et al. (2007). This behaviour, has already been noticed in the global K-band number counts (Gardner et al., 1993). The uncertainty in our number counts is estimated from the jacknife rms variance, where we divided the UltraVISTA field into 8 subfields. Table 5.1 lists the number counts of each sample in UltraVISTA field.

5.3 The clustering of DRGs

5.3.1 Angular Clustering

For the two-point angular correlation function measurements, we use the minimum variance estimator from Landy & Szalay (1993), according the same procedures as in Chapters 2 and 3. The measurement uncertainty of the angular correlation function has been estimated using field-to-field errors. Since our field covers a relative small area, we expect the integral constrain to have a significant effect on our clustering measurements, particularly at larger scales at which we are more interested in this work. So it is necessary to correct the observed $w_{obs}(\theta)$ and the real $w(\theta)$ as :

$$w_{obs}(\theta) = w(\theta) - IC, \tag{5.2}$$

where as we introduced in Chapter 2, the integral constraint (IC) can be numerically calculated from the equation of Roche & Eales (1999):

$$IC = \frac{\sum RR(\theta)w(\theta)}{\sum RR(\theta)}. \tag{5.3}$$

Previous DRG studies assumed a single power law with the usual fixed slope $\delta = 0.8$ for the $w(\theta)$ in Eq. 5.3, or even a double power law in case where larger scales were covered. But as underlined by Kim et al. (2011), using a single power law over a wide range cannot appropriately describe the data or in the case of using a double power law, a flatter slope can lead to uncertain integral constraint measurements. Following the same authors, we choose to describe the correlation function with a form of:

$$w_{obs}(\theta) = \alpha_1 \theta^{-\beta 1} + \alpha_2 \theta^{-\beta 2} - C, \tag{5.4}$$

where C is constant. This functional form, as shown by Kim et al. (2011), provided a good fit not only to the angular correlation function of the DRGs in UKIDSS DXS field, but also for the AAΩ LRGs of Sawangwit et al. (2011). To estimate the IC, we use an iterative process at which the functional form of $w(\theta)$ is fitted to the $w_{obs}(\theta)$ and then using Eq. 5.3 we calculate the IC. Then, the IC is applied to the $w_{obs}(\theta)$ and we refit the model and recalculate the IC until there is a convergence of the IC value (usually after very few
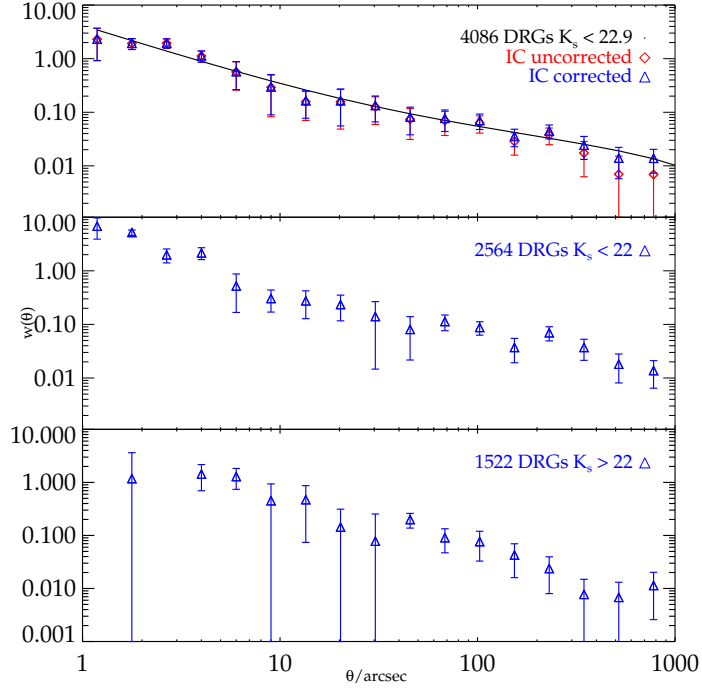
Figure 5.5: The angular correlation function of DRGs in UltraVISTA field.

iterations). In Fig. 5.5 we show the angular correlation function corrected for the integral constraint for the whole (top panel), $K_s < 22$ (middle panel) and $K_s > 22$ (bottom panel) DRGs at the UltraVISTA field. Furthermore, for the whole DRGs sample (top panel) we show the $w(\theta)$ points uncorrected for the integral constraint and the assumed fitted form for the $w(\theta)$ from Eq. 5.4. Due to our field size limitations and in order to avoid any systematics from IC correction, edge effects and sample variance, all our large scale clustering measurements presented next, are from galaxy separations up to $\sim 800''$.

5.3.2   Spatial Clustering

Our aim now is to derive the spatial correlation measurements of the UltraVISTA DRGs at large scales, since small scales have already been extensively studied in smaller fields. We will project the predicted spatial galaxy correlation function $\xi(r)$ to the angular correlation function through Limber's formula (Eq. 1.26), adopting the DRG photometric

redshift distribution presented in Fig. 5.3. As can be seen from Fig. 5.5, there is an up-turn at $\theta < 20''$, that will be used to separate small and large scales. The inflection at the angular correlation function arises from the signature of the one-halo and two-halo terms in the clustering signal, and only Quadri et al. (2008) and Kim et al. (2011) (with upturns at $\theta \sim 0.17$ and $\theta \sim 0.47$, respectively) used a double power-law to fit their measurements, while earlier studies used only a single power-law (Grazian et al., 2006; Foucaud et al., 2007; Quadri et al., 2007). Before we present the results for the large scale spatial clustering measurements of the UltraVISTA DRGS, we perform a comparison with results from the literature (for brighter and fainter DRGs) by applying similar colour cuts and discuss any differences in our findings.

Our comparisons start with the $2 < z < 3.5$ $K_{Vega} < 21$ sample of Quadri et al. (2007) in the Multiwavelength Survey by Yale-Chile (MUSYC) (over 300 arcmin^2). We have to notice, that despite the common depths in J and K bands for our DRGs sample and the MUSYC DRGs, the estimated photometric redshift distributions differ a lot. In the MUSYC DRGs the correlation functions have been fitted with single power-laws with fixed slopes: $\gamma = 1.6$ and $\gamma = 1.8$ and in two ranges : $0'' < \theta < 200''$ and $40'' < \theta < 200''$. Using $\gamma = 1.8$, as is the most common value, in the first fitting range the estimated correlation length of the UltraVISTA DRGs is $r_0 = 9.05 \pm 0.47 \mathrm{h}^{-1}\mathrm{Mpc}$, while in the $40'' < \theta < 200''$ range is $r_0 = 8.69 \pm 0.75 \mathrm{h}^{-1}\mathrm{Mpc}$. Our values are smaller for both cases compared to Quadri et al., where they measured: $r_0 = 12.0^{+0.9}_{-1.0}\mathrm{h}^{-1}\mathrm{Mpc}$ and $r_0 = 11.1^{+1.3}_{-1.4}\mathrm{h}^{-1}\mathrm{Mpc}$, respectively. The quoted errors of the clustering strengths from the MUSYC DRGs are Poisson errors and this reduces the uncertainty in r_0. Quadri et al. provide furthermore the estimated uncertainty from field-to-field variance for the r_0 measurement in the $40'' < \theta < 200''$ range. Their measured value in this case was $r_0 = 11.1^{+2.8}_{-4.2}\mathrm{h}^{-1}\mathrm{Mpc}$, thus now we are in agreement with their value. Quadri et al. (2008) in a later study with $2 < z < 3$ $K_{Vega} < 21$ DRGs in the UKIDSS UDS (over ~ 0.65 deg^2), used a large scale slope $\gamma = 1.47 \pm 0.14$ over the range $40'' < \theta < 500''$ and estimated $r_0 = 10.6 \pm 1.6 \mathrm{h}^{-1}\mathrm{Mpc}$ (with errors from bootstrap simulations). By adopting their slope and at the same fitting regime, our measured spatial correlation length is $r_0 = 9.14 \pm 0.93 \mathrm{h}^{-1}\mathrm{Mpc}$, which is consistent with their value.

Our next comparison will be with the brighter $1 < z < 3$ $K_{Vega} < 19.7$ DRGS in UKIDSS DXS of Kim et al. (2011) (over ~ 3.3 deg^2). These authors used a double power-law, separating small ($\theta < 0.48'$) and large ($0.48 < \theta < 19'$) scales. At small scales their fitted slope was $\gamma = 2.38 \pm 0.27$, while for large scales they adopted the slope from Quadri et al. (2008) ($\gamma = 1.47$). Their spatial clustering length measurements, for the whole DRG sample at small and large scales were $r_{0,small} = 4.66 \pm 0.20$h^{-1}Mpc and $r_{0,large} = 10.32 \pm 0.40$h^{-1}Mpc, respectively. In our case, the small scale clustering strength is $r_{0,small} = 3.02 \pm 0.36$h^{-1}Mpc, and $r_{0,large} = 8.63 \pm 0.81$h^{-1}Mpc at large scales. Our values are not consistent with the Kim et al. results, but this difference can be explained as the errors in their $w(\theta)$ measurements are Poisson and hence can decrease the error budget of r_0 as observed in the case of Quadri et al. (2007) when Poisson and field-to-field errors were used.

Moreover, the UKIDSS DXS DRGs of Kim et al. have been divided in two samples; one at $K_{Vega} < 18.8$ ($1 < z < 2$) and the second one at $K_{Vega} > 18.8$ ($2 < z < 3$). Applying the same values for the power-laws fit parameters, as in the case of the whole $K_{Vega} < 19.7$ DRGs sample, Kim et al. measured the clustering strengths at large scales to be: $r_{0,large} = 17.19 \pm 0.8$h^{-1}Mpc and $r_{0,large} = 9.52 \pm 0.7$h^{-1}Mpc for $K_{Vega} < 18.8$ and $K_{Vega} > 18.8$ DRGs, respectively. The UltraVISTA DRGs values are consistent with Kim et al. results and are : $r_0 = 17.1 \pm 1.6$h^{-1}Mpc and $r_0 = 8.90 \pm 0.80$h^{-1}Mpc, respectively.

A different study in the UKIDSS UDS was performed by Foucaud et al. (2007), but this time with a brighter DRGs sample at $K < 20.7$. The authors do not mention their fitting ranges, only the fixed value of the power-law slope,$\gamma = 2$, hence we will assume our large scale fitting range for this test. Foucaud et al. introduced the spectroscopic *n(z)* from Conselice et al. (2007), which have a similar $\bar{z} \sim 1$ with our data at the same K_s-limit. The measured value of the clustering strength for their sample estimated to be $r_0 = 11.0^{+3.7}_{-2.4}$h^{-1}Mpc, when in our case is $r_0 = 8.35 \pm 0.63$h^{-1}Mpc and is in agreement with the value from the $K < 20.7$ UKIDSS UDS DRGs.

Our last comparison is with $K < 23.5$ GOODS-MUSIC DRGs of Grazian et al. (2006) (135 arcmin^2). These authors performed a study for the whole, $K < 22$ ($1 < z < 2$) and $K > 22$ ($2 < z < 4$) DRG samples using a fixed slope at $1'' < \theta < 100''$. Thus, using

a fixed slope of $\gamma = 1.8$, the clustering strength for the whole, $K < 22$ and the $K > 22$ GOODS-MUSICS DRG samples was: $r_0 = 9.78^{+2.85}_{-3.24}\mathrm{h}^{-1}\mathrm{Mpc}$, $r_0 = 7.41^{+3.45}_{-4.84}\mathrm{h}^{-1}\mathrm{Mpc}$ and $r_0 = 13.4^{+2.99}_{-3.20}\mathrm{h}^{-1}\mathrm{Mpc}$, respectively. In our data, for the whole ($K < 22.9$), the $K < 22$ and the $K > 22$ UltraVISTA DRGs samples our clustering strengths values are $r_0 = 9.11 \pm 0.57\mathrm{h}^{-1}\mathrm{Mpc}$, $r_0 = 10.94 \pm 0.61\mathrm{h}^{-1}\mathrm{Mpc}$ and $r_0 = 9.14 \pm 1.02\mathrm{h}^{-1}\mathrm{Mpc}$, respectively. Since Grazian et al. were probing a fainter sample (~ 0.6 mag) than the UltraVISTA DRGs, we see that we are in agreement only as an upper limit in the r_0 uncertainties for the case of the $K > 22$ cut. Overall we conclude that the UltraVISTA DRGs clustering is consistent with previous clustering.

5.3.3 Clustering as a function of colour and magnitude

From our comparisons in the previous section, we saw that our DRG data can reproduce similar results from what has already been found in terms of comoving correlation lengths through the standard route of power-law measurements. Here, we will try to constrain the clustering evolution of the DRGs, by applying different $(J - K)$ colour and K magnitude limits. Our sample is sufficiently large enough to apply various limits with accurate statistics.

In Table 5.2, we summarize the results from colour and magnitude limits of the UltraVISTA DRGs. Our comoving correlation lengths have been estimated by applying fixed slope ($\gamma = 1.8$), so to be easily used as reference, in any other comparison. Furthermore, the measured r_0 and γ from power-law fits, for each DRGs selection are also presented. At the smaller scales, the clustering can be enhanced due to multiple galaxies within the same haloes, so we are focusing our measurements in the large scales only, using the $20'' < \theta < 800''$ range, as there we can probe better the clustering of the dark matter haloes that host the galaxies (Lee et al., 2006; Quadri et al., 2008).

In Fig. 5.6, we present the comoving correlation length as a function of the $(J - K)_{min}$ colour threshold (top panel) applying a fixed slope of $\gamma = 1.8$ and the freely fitted slopes. The measured slopes as a function of the same $(J - K)$ colour limits are displayed in the bottom panel. Due to our sample size and magnitude range, we can examine in more detail the clustering behaviour within the DRG sample. A stronger clustering
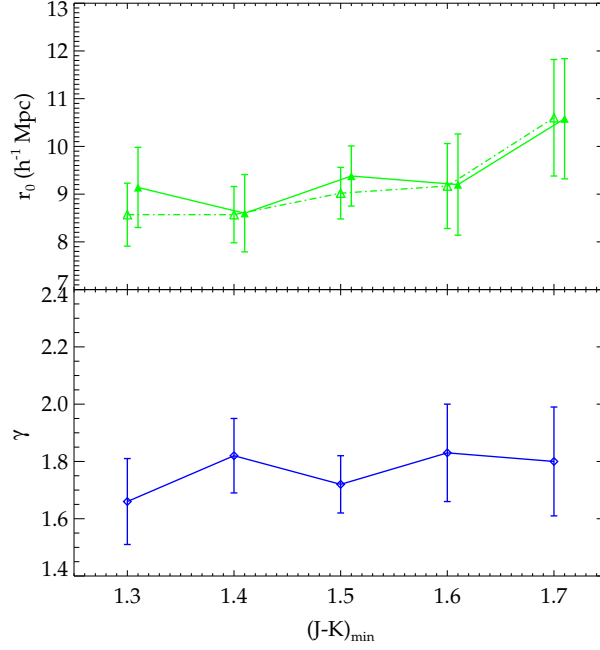
Figure 5.6: Top panel shows the comoving correlation length for UltraVISTA DRGs redder than the $(J - K)_{min}$ colour threshold with fixed slope ($\gamma = 1.8$, open triangle) and using the measured slope (filled triangle), as shown in the bottom panel. The fitting range of the power laws is $20'' < \theta < 800''$. The r_0 points estimated from fixed and measured slopes at the top panel have been shifted for display purposes.

for redder K-selected galaxies has been confirmed previously (i.e., Quadri et al., 2007; Daddi et al., 2003), but these studies did not include the DRG $(J - K)$ colour ranges as presented for first time in our study, since their DRG samples densities were quite small (264 and 24 DRGs, respectively), and this trend seems to be really weak within our samples. For the UltraVISTA DRGs we observe that there is a trend of increasing median redshift ($\bar{z}$) with colour limit (see Table 5.2). Moreover, by examining bluer samples, the same trends is observed, where for samples with $(J - K)_{min} = 1.2$, 1.1, 1.0 and 0.9 the estimated $\bar{z}$ values are : 1.65, 1.58, 1.48 and 1.41, respectively. This might be an indicator that the relationship between clustering strength and colour is due to redshift evolution, something that is in contrast with the findings of Quadri et al. (2007), where they observed only a small variation of ≈ 0.1 in $\bar{z}$ across their studied colour range of $1.0 < (J - K)_{min} < 2.4$. From the bottom panel of Fig. 5.6, the measured slopes do

Table 5.2: Clustering properties of colour and magnitude limited DRGs in UltraVISTA Survey

		Fitting range: $20'' < \theta < 800''$			
Selection	Ngal	$r_0(\gamma = 1.8)$	r_0	γ	$\bar{z}$
		$(h^{-1}Mpc)$			
$K < 22.9$	4086	8.57 ± 0.66	9.14 ± 0.84	1.66 ± 0.14	1.76
$K < 22.5$	3814	8.69 ± 0.66	9.32 ± 0.84	1.66 ± 0.14	1.74
$K < 22.0$	2564	9.82 ± 0.75	10.61 ± 1.08	1.69 ± 0.14	1.67
$K < 21.5$	1366	11.57 ± 0.87	11.50 ± 1.3	1.61 ± 0.12	1.46
$K < 21.0$	606	11.85 ± 1.15	13.65 ± 1.6	1.56 ± 1.17	1.46
$(J - K)_{min} = 1.3$	4086	8.57 ± 0.66	9.14 ± 0.84	1.66 ± 0.14	1.76
$(J - K)_{min} = 1.4$	2411	8.57 ± 0.59	8.60 ± 0.81	1.82 ± 0.13	1.86
$(J - K)_{min} = 1.5$	1413	9.02 ± 0.54	9.38 ± 0.63	1.72 ± 0.11	1.97
$(J - K)_{min} = 1.6$	823	9.17 ± 0.89	9.20 ± 1.06	1.83 ± 0.17	2.10
$(J - K)_{min} = 1.7$	462	10.6 ± 1.22	10.58 ± 1.26	1.80 ± 1.19	2.30

not show any large variation across the fitted colour range, implying that the form of clustering is not affected a lot by redshift.

Next, we want to explore the clustering strengths of magnitude limited DRGs. From the top panel of Fig. 5.7, we see the estimated clustering strengths of K_s-selected DRGs using fixed slopes ($\gamma = 1.8$) and also clustering strengths as estimated if we use freely fitted slopes. The measured slopes are shown in the bottom panel of Fig. 5.7, where we see that across the studied K_s range, the best-fitted estimated value is $\gamma = 1.65$, and this explains the larger differences between the measured r_0 from fixed and the freely fitted slopes of the brighter samples. Moreover, brighter samples show stronger clustering and the trend is monotonically decreasing towards fainter samples. Our results are consistent with previous studies where brighter samples appeared more clustered (Grazian et al., 2006; Foucaud et al., 2007; Kim et al., 2011), but do not agree with Quadri et al. (2007) where the relationship for K-selected samples between K and r_0 was not so strong. The trend between K and r_0 within the DRGs sample has not been found previously, and
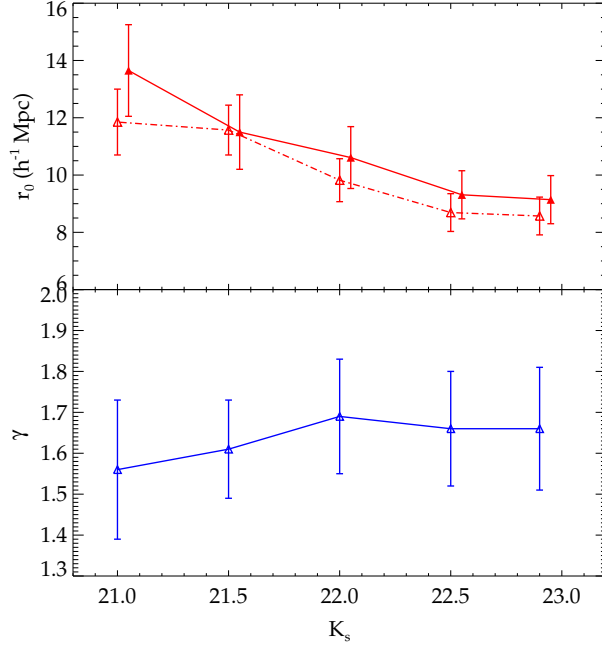
Figure 5.7: Top panel shows the comoving correlation length for K_s-limited UltraVISTA DRGs with fixed slope ($\gamma = 1.8$, open triangle) and using the measured slope (filled triangle), as shown in the bottom panel. The fitting range of the power laws is $20'' < \theta < 800''$. The r_0 points estimated from fixed and measured slopes at the top panel have been shifted for display purposes.

could further support luminosity segregation as noted by Foucaud et al. (2007)

5.3.4   Clustering evolution

Until now, we have explored the majority of the clustering characteristics of the unique UltraVISTA DRG sample. To interpret further our findings, it is of great interest to trace the clustering evolution of the luminous and massive DRGs, to their lower redshift descendants. In the ΛCDM model of structure formation, the galaxy distribution depends mainly on the dark matter halo distribution, hence by tracking the evolution of the galaxies host dark matter haloes, we can follow the evolution of galaxies with redshift. One method to compare different classes of objects, is as we have already presented for the high-z LRGs in Chapters 2 and 3, via the integrated correlation function ξ_{20}.

   To obtain the bias of the DRGs in the UltraVISTA field, we fit the ΛCDM model to
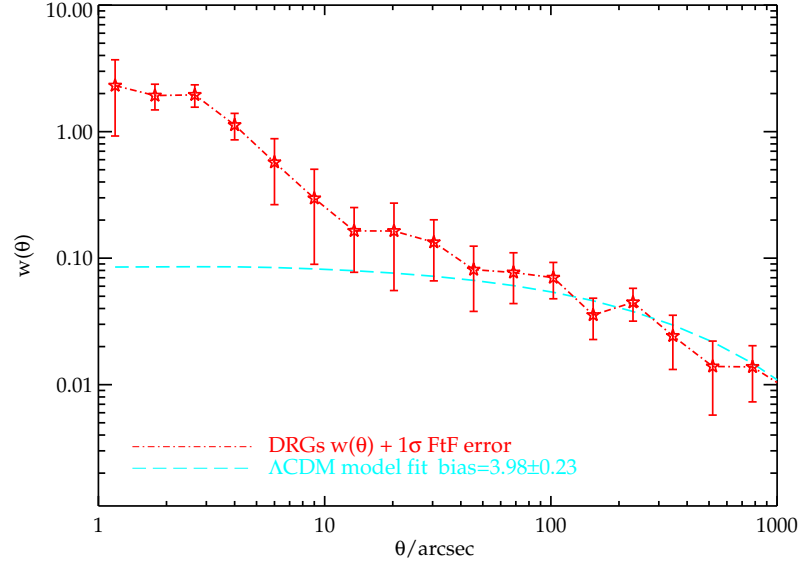
Figure 5.8: The measured angular correlation function of the UltraVISTA DRGs, fitted with the predicted standard model.

the measured angular correlation function. Fig. 5.8 shows the best fit ΛCDM model to the measured angular correlation function, and the estimated best linear bias factor is $b = 3.98 \pm 0.26$. We also note, that compared with the Stripe 82 LRGs, the DRG $w(\theta)$ measurements agree with the standard model, despite their flatter measured slope of $\gamma = 1.6 \pm 1.4$ compared to the rest K_s-limited samples (see Table 5.2), hence we have no evidence for primordial Non-Gaussianity in the UltraVISTA DRGs. Previous reported values, regarding the DRGs bias, were $b = 4.0^{+1.4}_{-0.8}$ from the $K < 20.7$ DRGs at $\bar{z} = 1.0$ of Foucaud et al. (2007) and $b = 5.0 \pm 0.4$ from the $K_{Vega} < 21$ $2 < z < 3.5$ DRGs in UKIDSS UDS of Quadri et al. (2008). The measured number density of the UltraVISTA DRGs is $n_g = 4.85 \pm 1.5 \times 10^{-4} h^3\ Mpc^{-3}$, and is consistent with number density of Quadri et al. (2008), $n_g = 6.5 \pm 3 \times 10^{-4} h^3\ Mpc^{-3}$.

The measured number density of the UltraVISTA DRGs, is comparable at 1.5σ with the number density of the AAΩ LRGs and the Stripe 82 spectroscopic LRGs, with $n_g = 2.7 \times 10^{-4} h^3\ Mpc^{-3}$ and $n_g = 5.88 \pm 2.74 \times 10^{-4} h^3\ Mpc^{-3}$, respectively. So, our approach for clustering evolution, will be according to what has presented already in Chapters 2
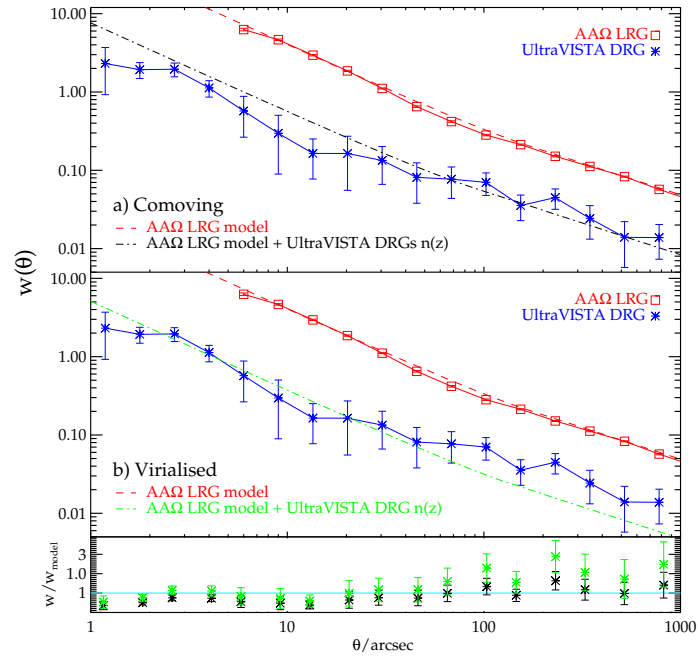
Figure 5.9: **a,b)** Using the best-fit double power-law $r_0 - \gamma$ values from the AAΩ LRGS and utilising the UltraVISTA DRG *n(z)*, we evolve DRGs clustering under the assumption of comoving and virialised evolution clustering models (dashed-dot black and green line, respectively). The UltraVISTA DRG raw $w(\theta)$ is also shown (blue star line). The AAΩ LRG $w(\theta)$ measurements (red square) are also overplotted with their fitted comoving and a virialised evolution models (dashed red line). Comoving evolution fits better the DRGs $w(\theta)$ at small and large scales compared to virialised evolution, as it can been seen from the residuals in the lower panel.
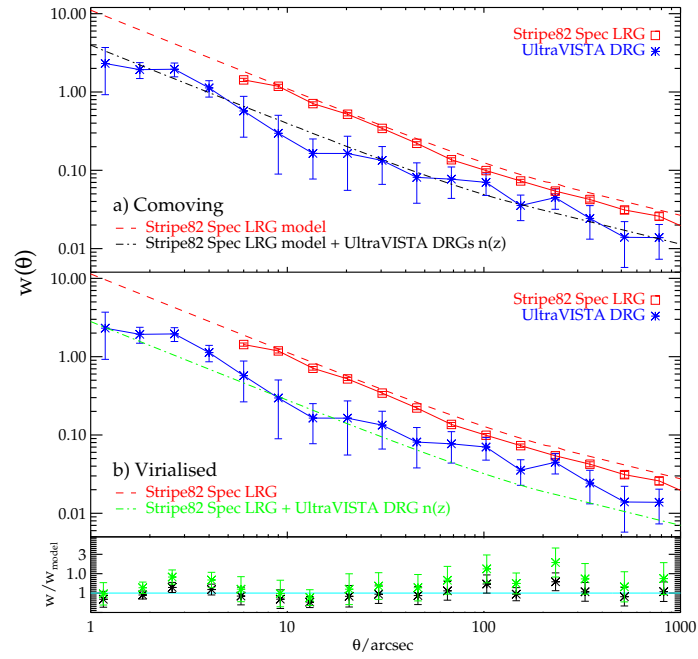
Figure 5.10: **a,b)**Using the best-fit double power-law $r_0 - \gamma$ values from the Stripe 82 spectroscopic LRGs sample and utilising the UltraVISTA DRG *n(z)*, we evolve DRGs clustering under the assumption of co-moving and virialised evolution clustering models (dashed-dot black and green line, respectively). The UltraVISTA DRG raw $w(\theta)$ is also shown (blue star line). The Stripe 82 $w(\theta)$ measurements (red square) are also overplotted with their fitted comoving and a virialised evolution models (dashed red line). Comoving evolution fits better the DRGs $w(\theta)$ at small and large scales compared to virialised evolution, as it can been seen from the residuals in the lower panel.

and 3, so similarly we will evolve the clustering of the DRGs to the lower-z LRGs. In Fig. 5.9 and Fig. 5.10, we present the evolved *comoving* and *virialised* models, using the best-fitted double power law parameters of the AAΩ and Stripe 82 LRGs, to the Ultra-VISTA DRGs depth. For both cases, we immediately notice, that the DRGs clustering is better described with the comoving model, that is consistent with DRGs preserving their comoving number density with redshift, without any other process involved (i.e. merging).

Nevertheless, if we use the integrated correlation function in a $20 \ \mathrm{h}^{-1}\mathrm{Mpc}$ sphere, ξ_{20}, we see from Fig. 5.11, that the the UltraVISTA DRGs ξ_{20} amplitude agrees with the no-evolution clustering model of the $3L_*$, while if we assume 1.5σ in the ξ_{20} then it is also described by the $2L_*$ LRGs and the Stripe 82 spectroscopic LRGs no-evolution model. Compared to the stable clustering or linear theory model, the long lived model agrees more with the data in every case. Since the estimated number density of the DRGs $n_g = 4.85 \pm 1.5 \times 10^{-4} h^3 \ Mpc^{-3}$, is much higher than the brighter LRGs samples, with $n_g = 1.1 - 1.2 \times 10^{-4} h^3 \ Mpc^{-3}$, the UltraVISTA DRGs cannot be described from the no-evolution clustering model of the $3L_*$ LRGs. The DRG clustering could be placed between the no-evolution and the long lived model of the fainter samples, even though the latter model is a very extreme case.

Grazian et al. (2006) also measured the amplitudes for the $\xi_{(}20)$ of their samples, using a simplified passive evolution and a merging model of Matarrese et al. (1997) and Moscardini et al. (1998). None of these two models, managed to give a satisfactory conclusion for their samples. For their low-z $K < 22$ DRGs sample, with $< M_i > -22.3$, $\xi_{20} \sim 0.415$ and with large error in ξ_{20}, we note that this DRGs could be the progenitors of the $2L_*$ and Stripe 82 LRGs, either if they evolved with the no-evolution or the long-lived clustering model. As we have seen so far with the ξ_{20} measurements, it is not straightforward to conclude on the DRGs descendants at lower redshfits and particularly, if there is an obvious connection with the LRGs samples studied in the previous Chapters.

Finally, we will try to study a larger variety of different classes of objects, by interpreting the evolution of bias with redshift using the object-conserving model of Fry
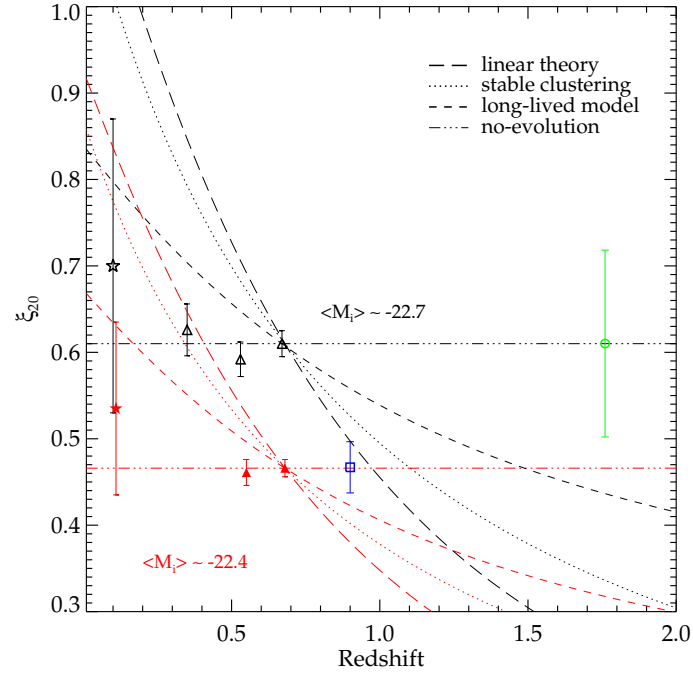
Figure 5.11: ξ_{20} measurements assuming different clustering models. The ξ_{20} measurements from Sawang-wit et al. (2011), where open symbols the brighter samples (SDSS, 2SLAQ* and $AA\Omega^*$-LRG), while the lower luminosity samples are shown with triangles. The lowest redshift data are early-type galaxies from 2dFGRS (Norberg et al. 2002) and the spectroscopic 700 deg^{-2} Stripe 82 LRGs is at $z = 0.9$ (blue square). The i-band absolute magnitude LRGs have been corrected using the dust map of Schlegel et al. (1998) and $K + e$ corrected to $z = 0$ using the Early-type galaxy templates from Bruzual & Charlot (2003). UltaVISTA DRGs are shown with the open green circle. Due to the higher number density of the DRGs compare to the brighter LRGs sample, the only possible clustering model that can be compared with the DRGs $\xi(20)$ amplitude at 1.5σ, is the no-evolution model of the $2L_*$ and the Stripe 82 LRGs.
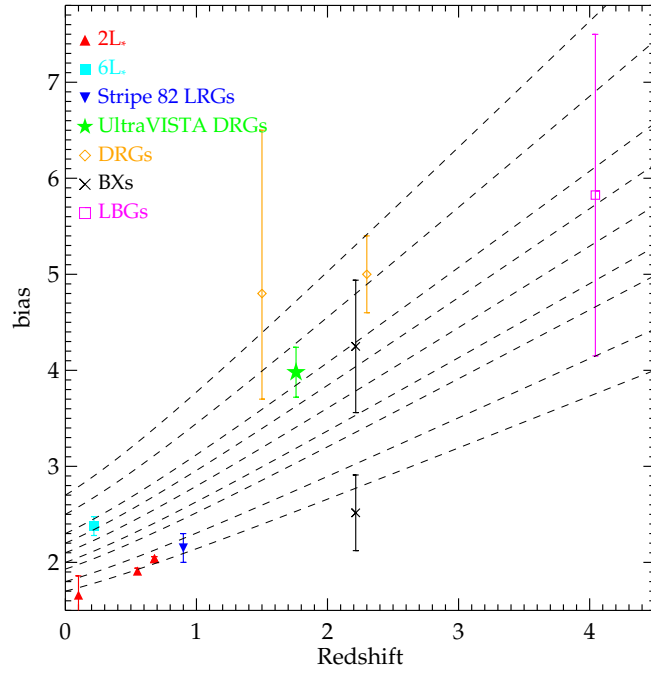
Figure 5.12: Tracks show the evolution of bias with redshift using the object-conserving model of Fry (1996). Triangles show the $2L_*$ LRGs of Sawangwit et al. (2011), square shows the $6L_*$ ellipticals from Zehavi et al. (2005c), upside-down triangle corresponds to the bias of the Stripe 82 spectroscopic LRGs, while star shows the bias of the UltraVISTA DRGs. Diamond at lower and higher redshift are from the DRGs of Grazian et al. (2006) and Quadri et al. (2008), respectively. Asterisks show the bias of the BXs galaxies from Adelberger et al. (2005a,b), while the diamond is for the LBGs of Allen et al. (2005).

(1996). In Fig. 5.12, we present the tracks of the linear bias evolution with redshift using Eq. 3.36, following Quadri et al. (2007). Our DRGs sample, seem to be evolved only to bright $6L_*$ local ellipticals of Zehavi et al. (2005c), whereas the $i_{Vega} < 24.5$ LBGs at $z \sim 4$ of Allen et al. (2005) and the BXs of Adelberger et al. (2005b), could be the progenitors of the UltraVISTA DRGs as well for the low-z DRGs of Grazian et al. (2006) and Quadri et al. (2008) DRGs. This connection between LBGs, DRGs and BXs has been predicted by simulations (Guo & White, 2009), while the fact that galaxies with high redshift will evolve into objects with high bias at $z \sim 0$, has already been underlined in other optically selected samples (Baugh et al., 1998; Ouchi et al., 2004; Adelberger et al., 2005b; Quadri et al., 2007). Quadri et al. (2007), for their $2 < z < 3.5$ DRGs with $b = 5.78 \pm 0.68$, could not strongly conclude on the DRGs bias evolution.

5.4   Discussion and conclusions

In this chapter we have presented the largest and deeper sample so far of Distant Red Galaxies (DRGs) from the NIR UltraVISTA survey. The field size and depth, enabled us to study a unique sample of 4086 DRGs, selected by the $(J - K) > 1.3$ criterion, from the UltraVISTA DR1 data release (McCracken et al., 2012) at $K_s < 22.9$ and $J < 24.2$. It has been well established, that the $(J - K) > 1.3$ criterion selects DRGs not only at $2 \lesssim z \lesssim 4$ (Franx et al., 2003; Daddi et al., 2003), but furthermore at $z < 2$ (Grazian et al., 2006; Papovich et al., 2006; Conselice et al., 2007; Lane et al., 2007).

The photometric redshift distribution of the UltraVISTA DRGs extends from $0.5 < z < 3$ with $\bar{z} = 1.76$. The measured precision of our photometric redshift when compared to spectroscopic data (Ilbert et al., 2013), leaves no doubt for the accuracy of these data and indicates that they can be safely used. Within our DRG sample, we observe a strong overlapping, if we split the samples at fainter and brighter DRGs at $K > 22$ and $K < 22$, respectively. Grazian et al. (2006) applied this rough selection in their DRG sample, to separate them in $1 < z < 2$ and $2 < z < 4$ samples, where the $z < 2$ counterparts increased at brighter magnitudes. For their lower-z DRGs at $K < 22$, with a similar *n(z)* like ours, they argued that DRGs there are dominated by dusty starbursts. As we see

from Table 5.2, the only way to isolate DRGs at higher-z, is by applying redder $(J - K)$ cut. UltraVISTA DRGs K_s number counts are in a very good agreement with all the other studies from fainter and brighter samples (Grazian et al., 2006; Foucaud et al., 2007; Kim et al., 2011). In addition, from the wide covered $18.5 < K_s < 22.9$ range of the UltraVISTA DRGs number counts, our data further support the break at $K_s = 20.5$, previously noticed by (Foucaud et al., 2007), which can be related with the global K-band number counts (Gardner et al., 1993).

The UltraVISTA DRGs comoving clustering strength, $r_0 = 9.14 \pm 0.84 \mathrm{h}^{-1}\mathrm{Mpc}$ for $\gamma = 1.66 \pm 0.14$, is in line with previous results, which have showed that DRGS are strongly clustered objects (Daddi et al., 2003; Grazian et al., 2006; Foucaud et al., 2007; Quadri et al., 2007, 2008; Kim et al., 2011). To ensure that our clustering measurements will not be affected from edge effects, or overestimated integral constraint corrections, we perform our measurements in the $20'' < \theta < 800''$ range. Furthermore, to correct for the integral constraint, we applied a functional form to describe the correlation, a recipe successfully introduced for the UKIDSS DXS DRGs by Kim et al. (2011). Our probed scales, in terms of measured angle and magnitude limit, are unique, since the largest field of $3.3 \mathrm{deg}^2$ from Kim et al. (2011) was limited to $K_{Vega} < 19.7$, whereas Quadri et al. (2008) with a similar depth to the UltraVISTA DRGs was limited to a field $\sim 2.3\times$ smaller than ours, measuring the correlation function up to $\theta < 500''$.

By adopting the magnitude limits of previously studied DRGs, we managed to reproduce almost comparable results for each sample that our DRGs have been compared with. In some cases, we were subject to the different redshift range that has been sampled and/or the uncertainty in the measurement of the angular correlation function. The latter factor, affects the clustering measurements, as where the errors in $w(\theta)$ measurements are being described by Poisson statistics, this unnaturally reduces the error budget of r_0. This has been demonstrated within Quadri et al. (2007) data, where with Poisson errors they measured, $r_0 = 11.1^{+1.3}_{-1.4}\mathrm{h}^{-1}\mathrm{Mpc}$ and with field-to-field variance that changed to $r_0 = 11.1^{+2.8}_{-4.2}\mathrm{h}^{-1}\mathrm{Mpc}$.

Studying the clustering of colour-limited and K_s limited DRGs samples, we see that the DRG's trend of increasing clustering with $(J - K)$ colour is not as strong as has

been confirmed previously for K-selected galaxies at bluer $(J - K)$ limits (Daddi et al., 2003; Quadri et al., 2007). This trend for local galaxies is arising from the higher stellar ages and higher metallicity, but could also affect the higher redshift galaxies (Förster Schreiber et al., 2004; van Dokkum et al., 2004; Shapley et al., 2004). For redder $(J - K)$ samples, we observed an increase in the median redshift, in contrast with the results over the studied colour-range of Quadri et al. (2007). In case of K_s-limited DRGs, there is a monotonically increasing clustering trend for brighter samples, as mentioned but not analytically shown in Grazian et al. (2006); Foucaud et al. (2007); Kim et al. (2011). Our results, that are not consistent with the K-selected galaxies of Quadri et al. (2007), could add more evidences for luminosity division as noted by Foucaud et al. (2007).

The UltraVISTA DRGs with an estimated bias, $b = 3.98 \pm 0.26$, do not show any departure from the predictions of standard model, with absence of primordial Non-Gaussianity. While evolving the clustering of the DRGs, to those obtained for low-z LRGs from AAΩ and Stipe 82, we find that the only model able fit the $w(\theta)$ measurements is no-evolution model, where means that DRGs conserve their comoving galaxy density. Quoting the clustering amplitude within $20\mathrm{h}^{-1}\mathrm{Mpc}$, a scale where linearity is expected to better than a few percent, we can compare the measurements between different populations. The DRG number density, $n_g = 4.85 \pm 1.5 \times 10^{-4} h^3\ Mpc^{-3}$, makes clear that the brighter $3L_*$ LRGs with much lower number densities cannot be descendants of our sample, while only with extreme upper limits $(1 - 2\sigma)$ in the ξ_{20}, UltraVISTA DRGs could be the progenitors of the fainter LRG samples. But this approach is not helpful in order to robustly describe the clustering of the DRGs. Finally, exploring the bias evolution of the DRGs assuming the simple object-conserving model of Fry (1996), where it came out that our DRGs as well as the higher-z DRGs of Quadri et al. (2008) could be the progenitors of $6L_*$ local ellipticals, while BXs and LBGs can be the progenitors of the UltraVISTA DRGs. This relationship between LBGs, BXs and DRGs has been predicted by N-body simulations Guo & White (2009). But in Quadri et al. (2007) study, when they evolved the halo mass of their K-selected samples, it has been shown that their descendants tend to occupy massive haloes with $10^{13} - 10^{14} M_\odot$, while DRGs could even occupy cluster-scale haloes with $\gtrsim 10^{14} M_\odot$, so the evolution picture of the DRGs is not clear yet.

Chapter 6

Conclusions

6.1 Summary of the main results

In this thesis, we used observations of the large-scale structure and statistical tools over a wide redshift range, with the aim of constraining the cosmological models and galaxy formation physics. In Chapter 1, we reviewed the theoretical framework, observational evidences and tools that can be used to test further towards the standard cosmological paradigm, ΛCDM.

In Chapter 2 we investigated the proposed XMS spectrograph, where with its ability to place 4000 MOS slits simultaneously over a 1^0 field , which can mark a new era in the history of multi-object wide-field spectroscopic galaxy surveys by mapping 1000deg^2 area. The aim of the XMS Cosmology Redshift Survey (CRS) is to measure the gravitational growth rate and BAO with ELGs and LRGs at $z \sim 0.5 - 0.7$ over a wide range of scales ($0.1\text{-}1000h^{-1}\text{Mpc}$), while the purpose of the Galaxy Evolution Survey (GES) is to enable robust studies into the Kpc to Mpc range of halo scales, for the halo mass function at $0.4 < z < 0.7$ groups of galaxies. Due to the large sky density at the desired depths, XMS Galaxy Evolution + Cosmology Redshift Survey (XGECRS), can serves XMS-GES and XMS-CRS science cases together.

We performed comparisons tests from forecasts based on the effective volume measurements (Feldman et al., 1994) between the XMS surveys and the future surveys: BOSS, WiggleZ and DESI. DESI ELG and LRG surveys effective volume are larger at all scales compared to the rest of the compared surveys. XMS-GES and XGECRS surveys, compared to DESI, will provide similar measurements at smaller scales. The effective volume of WiggleZ survey's measured to be $10\times$ smaller at all almost all scales compared to all XMS surveys. Despite $10\times$ larger area of BOSS, XMS GES and XGECRS surveys

will have only $\sim 1.5\times$ the BOSS error on the power spectrum measurements at large scales, while at small scales BOSS groups will have $20\times$ smaller membership of XMS GES groups. The advantage of using ELGs as LSS tracers for BAO and gravitational growth rate measurements is clear as the XMS ELG survey will have $3\times$ the effective volume of WiggleZ, whereas the XMS GES and XGECRS have competitive effective volumes with BOSS at large scales. Even more precise cosmological measurements we can obtain from future surveys such as EUCLID, with a total effective volume $V_{eff} = 19.7\mathrm{h}^{-3}\mathrm{Gpc}^3$ over $15000\mathrm{deg}^2$ and eBOSS LRG and ELG surveys over $7500\mathrm{deg}^2$, with $V_{eff} = 4.7\mathrm{h}^{-3}\mathrm{Gpc}^3$ and $V_{eff} = 2.4\mathrm{h}^{-3}\mathrm{Gpc}^3$.

Efficiency tests were made of XMS exposure times by observing $i < 22$ ELGs and $i < 21$ LRGs with 1.5h exposure with MOSCA spectrograph. These tests produced a satisfactory success rate of 66% and 58% for ELGs and LRGs, respectively. The observational accuracy of XMS tested using GAMA spectra, that artificially mimicked XMS conditions in the $5200 - 7200$Å passband, where the the success rate of this test was 88% in the range $0.4 \leq z \leq 0.8$.

In Chapter 3, we presented a unique sample $130,000$ LRGs in SDSS Stripe 82, selected from the SDSS DR7 $i + z$ and UKIDSS LAS K bands. Given that the massive candidates lack redshift information, we applied the cross-correlation method of Newman (2008), in order to recover the redshift distribution of the Stripe 82 LRGs. The resulting *n(z)* had an average of $z \sim 1$. Measuring the angular correlation function of the $700\ \mathrm{deg}^{-2}$ LRG sample we compared it with results from lower-z LRGs from Sawangwit et al. (2011). A decrease in the $w(\theta)$ amplitude with increasing redshift was observed, but more important, that the large scale clustering of the Stripe 82 LRGs was showing an unexpected power excess.

The number density of the $700\ \mathrm{deg}^{-2}$ LRGz, $n_g = 3.20 \pm 0.16 \times 10^{-4}\mathrm{h}^3\mathrm{Mpc}^{-3}$, matched the AA$\Omega$ LRGs density (roughly luminosity matched samples), thus we tried to evolve the Stripe 82 LRGs to the $z \sim 0.68$ depth of the AAΩ LRGs, using the *comoving* and *virialized* clustering models. Unfortunately, due to the flat slope at large scales, none of the models was able to fit the data. In addition, the ΛCDM model was only accepted at $2 - 3\sigma$ level, with a best-fit linear bias $b = 2.74 \pm 0.07$. Trying to explain further the large

scales flattening, using the HOD formalism in the framework of standard ΛCDM, we could not conclude on the Stripe 82 LRGs clustering as the power excess was affecting the two-halo term in the HOD fittings. From the HOD prescription, 95% of the Stripe 82 LRGs have been characterised as central galaxies in their host dark matter haloes of mass $\approx 10^{13} - 10^{14} h^{-1} M_\odot$, as expected for the LRGs.

Interpreting the clustering evolution at intermediates scales, the measured amplitude of the integrated correlation function of the Stripe 82 LRGs could not be matched with any model from the lower-z LRGs. At small scales, adopting the 'central-central mergers' model of Wake et al. (2008), the passive/stable clustering model has been rejected, as the massive LRGs needed to halve their number through merging, in order to match the observed number density at $z \sim 0.35$. The positive clustering signal at large scales was still detectable even after correcting for the known observable systematic effects (Ross et al., 2011). As an alternative route, we introduced the effect of primordial *non-Gaussianity* (Bartolo et al., 2004a) in the power spectrum of the LRGs. Non-Gaussian models of $f_{\rm NL} = 90 \pm 30$ were more consistent with the clustering amplitude at large scales, representing a 3σ detection comparable to the present upper limit from WMAP CMB measurements (Komatsu, 2010). Our results are rejected if we take into consideration the recent results from Planck with $f_{\rm NL}^{\rm local} = 2.7 \pm 5.8 (1\sigma)$ (Planck Collaboration XXIV et al., 2013), while results from (Planck Collaboration XVI et al., 2013b; Planck Collaboration XXIII et al., 2013) on measurements of low-l spectrum and wavelet coefficients with deviations from the standard model, indicate that further studies are necessary in order the measured $f_{\rm NL}^{\rm local}$ of Planck to be more robust.

In Chapter 4, we presented results from spectroscopic follow up observations with VIMOS spectrograph on VLT, for a sample of the $700 \deg^{-2}$ Stripe 82 LRGs of Chapter 3, over an area $< 0.5 \deg^2$. With secured spectroscopic redshifts for $\approx 70\%$ of the total 280 LRGs candidates, the recovered *n(z)* was narrower than the photometric *n(z)* of Chapter 2, with a slightly reduced average redshift $z \sim 0.9$. The spectroscopic *n(z)* support our assumptions, that a redder selection of the LRGs will sample more distant LRGs, About 30% of the LRGs with secured redshifts, showed emission lines (i.e. [OII], [OIII]), and it can be expected from the *Butcher-Oemler* effect, and even be a further evidence of $Em +$

Abs phenomena of "post-starburst " galaxies, as are evolving with redshift (Roseboom et al., 2006).

K-band number counts showed that the VIMOS LRGs had the same completeness as the photometric Stripe 82 LRGs. Performing a similar clustering analysis as in Chapter 3, we measured smaller clustering lengths due to the narrower width of the spectroscopic *n(z)*. The standard model when fitted to the observed $w(\theta)$, gave better fits with a reduced linear bias $b = 2.20 \pm 0.06$, but still was not consistent with the data at $1 - 2\sigma$ level due to the large-scale flat slope. To our surprise, despite the fact that the best-fit HOD model was in line with the data at $1 - 2\sigma$ level, the HOD outputs agreed more with the results of the lower-z LRGs, directing us again to the slow evolution scenario since $z \sim 1$. The evolved AAΩ LRGs virialized/stable clustering model matched better the spectroscopic LRGs at smaller scales, and the comoving/long-lived clustering model at larger scales.

The clustering of the spectroscopic LRGs had a more physical interpretation but still, due to the uncertainty in the number density, we could not place them with confidence in the ξ_{20} region of either the long-lived or the no-evolution clustering model of the faint LRGs. Definitely our findings were favouring that the observed evolution of the spectroscopic LRG was slow. The observed discrepancy between the width of the spectroscopic and photometric *n(z)* was more likely to have its origin in the cross-correlation errors of the observational systematics, as the spectroscopic *n(z)*, was more possible to represent the real distribution of the data. Finally, Non-Gaussianity was still detectable, but with a reduced significance of $f_{\mathrm{NL}} = 60 \pm 30$.

In Chapter 5, we presented the UltraVISTA survey, the largest deep near-infrared survey up to present, covering $1.5\mathrm{deg}^2$. We have selected 4086 DRGs via the $(J-K)_{AB} > 1.3$ colour criterion, at $J < 24.2$ and $K_s < 22.9$. With the available multi-photometric coverage, the photometric redshift distribution of the DRG sample, spanned a wide at $0.5 < z < 3$ with an average redshift $z \sim 1.76$. DRGs K_s number counts were in a very good agreement with all the previous studies and furthermore pointed out that we are sampling galaxies within the completeness limits of the survey.

The UltraVISTA DRGs were strongly clustered objects, when we compared our sam-

ple with other DRG samples, we were in agreement with almost every single case, unless if our sample was not selected as the compared sample, or if different statistics were applied in the other studies (e.g. Poisson errors in the $w(\theta)$ measurements). Separating our DRG sample in $(J - K)$-limited samples, we noticed that there was a small trend of increasing clustering strength with colour, but not as strong as observed for K-selected galaxies with bluer colours (Daddi et al., 2003; Quadri et al., 2008). On the other hand, we found that for increasing colour there was an increasing in the median redshift, in contrast with previous results. For K_s-limited UltraVISTA DRGs, a strong trend with increasing clustering with brighter samples was present, that could imply luminosity segregation (Foucaud et al., 2007).

The clustering of the highly biased UltraVISTA DRGS, was well predicted from the standard model, and when evolved to the lower-z Stripe 82 spectroscopic and AAΩ LRGs, was consistent in both cases only with the no-evolution clustering model. A strong conclusion could not be made from the amplitude of the ξ_{20} of the DRGs, as their large number density, could place them as progenitors of the fainter LRGs only at extreme cases. Finally, when investigating the bias evolution with redshift, under the assumption of the galaxy-conserving model of Fry (1996), the progenitors of the UltraVISTA DRGs could be LBG and BX galaxies, while the descendants of UltraVISTA DRGs could be only $6L_*$ local ellipticals, This picture was in contrast with the results of Quadri et al. (2008), where they predicted that DRGs should occupy cluster-scale haloes with $\gtrsim 10^{14} M_\odot$.

6.2 Future prospects

Galaxy surveys along with measurements of temperature fluctuations in the cosmic microwave background (CMB) have played a key role in the advances of modern cosmology over the last years. The standard cosmological flat ΛCDM model, has been supported by plethora of observations. On the other hand, observations also showed large deviations from the expectations of ΛCDM, suggesting that the standard model based solely on gravitational instability is lacking more complex physics.

More sophisticated design in the galaxy surveys are demanded, in order to minimise systematics and provide unbiased interpretations for models of hierarchical galaxy formation. This can be achieved with the existing and future ground- and spaced-based surveys: VST-ATLAS, Pan-STARRS, LSST, DES, EUCLID, extended ROentgen Survey with an Imaging Telescope Array (eROSITA; Predehl et al., 2010), and the 4-metre Multi-Object Spectroscopic Telescope (4MOST; de Jong, 2011). 4MOST, a multi-object spectrograph with 3000 fibres, will extensively map the southern sky, and could be a reliable replacement of XMS by having a variety of science drivers.

We need to use data in larger/deeper areas to test if Non-Gaussianity is still applied at higher redshift or if it arises from large scale gradients that amplify the 2-halo term clustering signal. VST-ATLAS and DES surveys, as they overlap with the VHS survey, can give us the chance to select high-z LRGs and extend further the galaxy clustering measurements at large scales. BOSS DR9 QSOs data (Pâris et al., 2012) can also be studied for primordial Non-Gaussianity as White et al. (2012) studied the clustering of BOSS QSOs only up to intermediate scales. It will be necessary to check larger scales and how much the results there are affected by systematics. Spectroscopic follow up observations, cannot cover the large samples of the high-z LRGs as it is time consuming, but they are important even for for a smaller fraction of data as can eliminate uncertainties.

If we adopt the HOD approach, as has been introduced only by Quadri et al. (2008); Tinker et al. (2010), we might be able to constrain the clustering of the massive DRGs and the properties of their host haloes. The existence of such massive objects at high redshift, as it was not predicted by earlier models of galaxy formation, demands further understanding and linking of the galaxy properties with their environment.

Appendix A

Properties of the Stripe 82 spectroscopic LRGs with secured redshift

The properties of all the LRGs in Stripe 82 with accurate measured spectroscopic redshifts ($q = 3$ and $q = 2$). For each object, it is also provided the redshift quality flag, the priority sample that belongs and the presence of emission line on its spectrum

Table A.1: SDSS Stripe 82 LRGs properties with accurate VLT/VIMOS spectroscopic redshifts. The redshift quality flag, the priority sample and the presence of emission line are also provided.

α (J2000)	δ (J2000)	Redshift	Flag/q	i_{AB}	z_{AB}	K_{Vega}	Priority	Emission
18.4695568	0.359054	0.340	3	21.81	21.27	17.9	A	Yes
19.6284161	0.274067	0.412	2	20.85	20.21	17.04	A	No
19.4099121	-0.116714	0.437	3	21.21	20.73	17.33	A	Yes
19.0481148	-0.104222	0.454	3	22.04	21.1	17.78	A	Yes
18.3718777	0.198882	0.487	3	20.8	20.32	17.03	A	Yes
20.2850304	-1.042851	0.497	3	21.77	21.12	17.83	A	Yes
19.4604225	0.178408	0.558	3	22.21	21.57	17.99	A	No
18.7224579	-0.468863	0.562	3	21.35	20.85	17.47	A	No
18.2182884	-0.06033	0.571	2	21.68	20.98	17.19	B	Yes
20.3563251	-0.91156	0.604	2	21.83	20.99	17.81	A	No
19.7030315	0.268033	0.606	3	21.59	21.0	17.69	A	No
19.5473366	0.180556	0.613	3	22.06	21.27	17.97	A	Yes
Continued on next page								

Table A.1 – continued from previous page

α (J2000)	δ (J2000)	Redshift	Flag/q	i_{AB}	z_{AB}	K_{Vega}	Priority	Emission
19.4371605	0.421928	0.614	3	21.67	21.36	17.8	A	No
19.1469078	0.406949	0.632	3	21.36	20.91	17.58	A	No
19.4258881	0.035308	0.635	3	21.05	20.52	17.57	A	Yes
19.2847385	-0.121557	0.636	3	21.77	21.13	17.96	A	No
16.3934174	-0.577591	0.636	3	21.94	21.37	17.79	A	No
18.9173126	0.048577	0.640	3	22.08	20.94	17.87	A	No
19.0187321	-0.066965	0.652	3	21.93	21.51	17.99	A	Yes
19.3107147	0.248947	0.675	2	21.75	21.14	17.83	A	Yes
18.9703979	-0.052477	0.678	3	20.92	20.33	17.14	A	Yes
19.4065323	0.413992	0.679	3	21.57	21.11	17.8	A	Yes
18.770586	-0.023354	0.683	3	21.66	21.1	17.9	A	No
20.4308987	-0.987153	0.683	3	21.17	20.35	17.36	A	Yes
20.3358421	-0.850926	0.692	3	22.31	21.27	17.73	B	No
18.3610535	0.414693	0.703	3	21.59	20.73	17.34	A	Yes
16.490509	-0.537666	0.705	3	22.17	21.42	17.48	B	No
19.6204205	-0.067892	0.710	3	21.35	20.71	17.31	A	No
19.4143066	-0.064197	0.712	3	21.37	20.76	17.3	A	No
19.8008289	-0.42858	0.712	3	21.71	20.8	17.8	A	Yes
19.4699459	-0.019679	0.714	3	21.66	21.03	17.75	A	No
19.5280342	-0.041205	0.716	3	21.86	21.25	17.98	A	No
19.8714123	0.268634	0.732	3	21.22	20.62	17.38	A	Yes
20.3790455	-0.92644	0.732	3	22.17	21.26	17.93	A	Yes
19.5905094	0.22672	0.742	3	21.93	21.14	17.96	A	Yes
19.1949635	0.172343	0.744	3	21.74	21.16	17.83	A	Yes
18.3973694	0.174302	0.748	3	21.38	20.83	17.23	A	Yes
20.3410549	-1.017331	0.751	3	22.08	21.22	17.77	B	Yes
19.7635326	0.187075	0.758	2	23.14	21.95	17.94	B	No

Table A.1 – continued from previous page

α (J2000)	δ (J2000)	Redshift	Flag/q	i_{AB}	z_{AB}	K_{Vega}	Priority	Emission
19.9537754	0.417635	0.760	3	21.54	20.73	17.59	A	No
19.9767284	0.187664	0.761	3	21.36	21.0	17.48	A	No
19.9681187	0.351407	0.766	3	21.69	20.96	17.56	A	No
19.9459801	0.344944	0.766	3	21.72	21.04	17.78	A	Yes
18.8964081	-0.037633	0.775	3	22.3	21.34	17.96	B	Yes
19.0955467	0.042046	0.780	3	22.23	21.9	17.94	B	Yes
19.101553	0.055901	0.780	3	22.42	21.6	17.93	B	Yes
19.2003212	0.086805	0.780	3	22.22	21.39	17.56	B	Yes
18.7706432	0.069835	0.780	3	21.76	21.05	17.63	A	No
21.5012417	1.223641	0.781	3	22.78	21.66	17.46	B	No
19.811121	0.349337	0.787	3	21.55	20.98	17.51	A	No
19.0964355	-0.026984	0.796	2	22.19	21.52	17.79	B	No
19.785574	0.195823	0.798	3	21.9	21.2	17.97	A	No
18.9508018	-0.131626	0.798	3	22.19	21.6	17.96	A	No
19.8831902	0.366758	0.805	3	21.83	21.04	17.84	A	No
18.6181488	0.206042	0.805	3	21.97	21.45	17.88	A	No
19.4138622	0.423616	0.806	2	22.15	21.31	17.88	A	No
18.703474	0.060968	0.806	3	21.56	21.29	17.81	A	Yes
18.965107	0.063923	0.807	3	21.73	21.18	17.81	A	No
19.6482277	0.211312	0.808	3	21.8	21.08	17.87	A	No
19.2433891	0.129794	0.810	3	21.62	21.25	17.46	A	Yes
18.6210537	0.201523	0.810	3	21.56	20.82	17.45	A	No
19.7427654	0.204769	0.814	2	21.55	21.12	17.69	A	No
19.0220623	0.05676	0.814	3	21.53	21.02	17.56	A	Yes
18.7776184	-0.079795	0.818	3	21.55	20.76	17.69	A	No
21.470377	1.2454081	0.820	2	22.15	21.71	17.9	B	No
19.6358147	0.195149	0.822	2	22.18	21.5	17.77	B	No

Continued on next page

Table A.1 – continued from previous page

α (J2000)	δ (J2000)	Redshift	Flag/q	i_{AB}	z_{AB}	K_{Vega}	Priority	Emission
19.5488281	-0.020798	0.822	2	22.34	21.24	17.91	B	No
18.9266586	0.060586	0.822	3	21.75	20.98	17.64	A	No
18.9257393	0.073218	0.823	3	22.14	21.51	17.81	B	No
19.4611282	-0.103509	0.833	3	21.75	21.3	17.73	A	Yes
19.5326347	-0.092793	0.843	2	21.34	20.6	17.54	A	No
19.4791603	0.338985	0.847	3	21.8	20.95	17.66	A	No
18.4407997	0.370861	0.849	3	21.43	20.38	17.46	A	No
19.7198486	0.209701	0.850	2	21.96	20.85	17.94	A	No
19.4068527	0.213056	0.850	3	21.71	20.98	17.72	A	No
18.807457	-0.031193	0.850	3	21.78	20.68	17.5	A	No
18.6266041	0.254131	0.851	3	21.74	20.93	17.63	A	No
19.0467758	0.242233	0.852	3	22.02	21.05	17.92	A	No
18.9506912	-0.08004	0.853	3	21.44	20.62	17.25	A	No
19.4452457	-0.040545	0.855	2	21.81	20.82	17.69	A	No
19.2438793	-0.113954	0.855	2	21.87	21.08	17.97	A	No
18.8852806	0.083258	0.855	3	21.39	20.57	17.46	A	No
20.4218845	-1.0378489	0.855	3	21.83	21.22	17.71	A	Yes
18.7956314	0.048656	0.864	3	21.85	21.38	17.81	A	Yes
18.8124714	-0.039909	0.865	3	21.77	20.85	17.72	A	No
19.9728622	0.196723	0.866	2	21.73	20.94	17.45	B	No
19.7536812	0.223301	0.870	3	21.6	20.78	17.62	A	No
19.1206474	0.103096	0.871	3	22.51	21.8	17.79	B	Yes
19.3665504	0.332729	0.873	3	22.3	21.5	17.93	B	Yes
19.083147	0.212887	0.873	3	22.0	21.41	17.93	A	Yes
20.2816181	-1.007916	0.888	3	22.2	21.02	17.59	B	No
19.6345139	0.030744	0.889	3	21.99	20.89	17.67	B	No
17.1849804	0.731956	0.891	3	22.46	21.43	17.79	B	No

Table A.1 – continued from previous page

α (J2000)	δ (J2000)	Redshift	Flag/q	i_{AB}	z_{AB}	K_{Vega}	Priority	Emission
19.2066402	0.063036	0.891	3	22.0	21.17	17.77	A	No
20.1318111	-0.586981	0.892	3	21.94	20.8	17.82	A	No
19.5627556	0.023135	0.892	3	21.69	20.79	17.7	A	No
19.6868324	-0.562067	0.895	2	21.62	20.58	17.74	A	No
19.0609512	0.218311	0.895	3	21.67	20.96	17.5	A	Yes
19.3583927	-0.02943	0.909	3	21.84	21.11	17.91	A	Yes
19.7935314	0.256958	0.910	3	22.24	21.14	17.73	B	No
19.7812862	0.193545	0.911	3	21.19	20.25	17.23	A	No
19.5993652	0.170788	0.917	2	22.63	21.88	17.96	B	No
19.7028522	0.232322	0.918	3	21.72	21.2	17.84	A	No
19.9293137	0.36293	0.919	3	22.18	21.42	17.78	B	No
19.9773064	-0.545121	0.922	3	21.18	20.57	17.25	A	No
16.2917767	-0.547099	0.928	3	22.5	21.55	17.6	B	No
19.2886887	-0.119713	0.932	3	21.71	20.94	17.8	A	No
19.3917618	0.265857	0.933	3	22.43	21.76	17.85	B	Yes
19.6134911	0.233262	0.933	2	21.85	21.05	17.99	A	No
18.6436024	0.190197	0.933	3	21.01	20.6	17.25	A	Yes
21.3912945	1.2464041	0.935	3	21.77	21.14	17.91	A	Yes
19.530035	0.038612	0.938	2	22.12	21.19	17.9	A	No
19.4528561	-0.074419	0.950	2	22.34	21.34	17.81	B	No
19.6134968	0.098166	0.952	3	22.68	21.59	17.99	B	No
19.8568897	0.382291	0.954	2	21.92	21.27	17.98	A	No
19.4007092	0.208038	0.954	3	21.92	20.93	17.45	B	No
19.4290142	0.278311	0.954	3	21.95	21.0	17.64	B	No
18.3603687	0.386345	0.954	3	22.18	21.61	17.68	B	Yes
18.3678417	0.258686	0.955	3	21.93	20.9	17.79	A	No
19.3564472	0.189158	0.958	3	21.85	21.04	17.74	A	No
Continued on next page								

Table A.1 – continued from previous page

α (J2000)	δ (J2000)	Redshift	Flag/q	i_{AB}	z_{AB}	K_{Vega}	Priority	Emission
19.397562	0.360649	0.959	3	21.93	21.03	17.97	A	No
20.4510956	-0.952701	0.964	3	21.3	20.57	17.28	A	Yes
19.7767849	0.221762	0.967	2	22.71	21.23	17.78	B	No
19.7455349	0.399798	0.973	3	22.04	21.15	17.85	A	No
19.7547226	0.390218	0.973	3	21.8	20.95	17.63	A	No
18.8094139	-0.03533	0.976	3	21.53	20.83	17.66	A	No
19.7919197	0.374996	0.977	3	22.26	21.26	17.97	A	No
16.6287766	-0.559111	0.977	3	21.79	21.0	17.88	A	No
16.4899521	-0.497117	0.977	3	21.6	20.91	17.56	A	No
19.7975693	0.342414	0.979	3	22.93	21.97	17.83	B	Yes
19.0863934	0.427994	0.980	3	22.09	21.03	17.8	A	No
16.6145248	-0.549421	0.980	3	22.16	21.28	17.88	A	No
16.5936108	-0.550798	0.980	3	21.56	20.9	17.65	A	No
18.7766151	0.021469	0.981	3	22.34	21.12	17.74	B	No
19.7808552	0.366232	0.983	3	21.72	20.82	17.86	A	No
18.871666	0.100813	0.983	3	21.55	20.94	17.55	A	No
19.0350723	0.221593	0.984	3	21.66	20.6	17.29	B	Yes
18.8040981	-0.064146	0.984	3	21.61	20.55	17.51	A	No
18.7796993	-0.057153	0.984	3	21.96	20.87	17.97	A	No
18.8581867	-0.047017	0.984	3	21.8	20.73	17.67	A	Yes
21.0526733	1.165592	0.985	3	21.19	20.17	17.32	A	Yes
19.4121113	0.354918	0.989	3	22.2	21.11	17.76	B	No
19.3915119	0.372614	0.993	3	21.88	21.25	17.94	A	Yes
19.0379066	-0.115163	1.011	2	22.65	21.73	17.95	B	No
19.1968231	-0.074235	1.014	3	21.74	21.06	17.93	A	Yes
19.3118305	-0.114921	1.017	3	21.64	20.68	17.81	A	Yes
19.9800606	0.356945	1.024	3	22.22	21.51	17.84	B	Yes

Continued on next page

Table A.1 – continued from previous page

α (J2000)	δ (J2000)	Redshift	Flag/q	i_{AB}	z_{AB}	K_{Vega}	Priority	Emission
18.9008713	0.056957	1.030	3	21.92	20.83	17.55	B	No
18.8663044	0.103916	1.035	3	21.92	21.01	17.9	A	No
19.0892124	-0.025449	1.043	2	22.89	21.76	17.8	B	No
19.0324936	0.127501	1.045	3	21.71	21.0	17.84	A	Yes
19.7874966	0.320677	1.047	3	21.15	20.2	17.34	A	No
19.7864952	0.328887	1.047	3	22.99	21.74	17.96	B	No
19.1099243	-0.043194	1.047	3	22.34	21.09	17.87	B	No
20.4721622	-0.906718	1.049	2	21.73	20.92	17.73	A	No
19.7488194	0.272378	1.051	3	22.02	21.12	17.76	A	No
19.2021637	0.126549	1.051	3	21.92	20.87	17.76	A	Yes
19.6223755	0.206581	1.053	3	21.88	20.78	17.44	B	No
19.7027397	0.254596	1.054	3	22.48	21.25	17.93	B	No
19.5398769	0.052616	1.054	3	22.0	20.79	17.85	A	No
19.3174267	0.192513	1.054	3	22.78	21.93	17.74	B	No
16.2974396	-0.442532	1.054	3	21.66	20.93	17.84	A	No
19.2878876	0.027248	1.057	2	22.49	21.84	17.7	B	No
19.4512463	-0.068939	1.068	2	23.1	21.83	17.95	B	No
19.5756264	0.095826	1.079	2	22.27	21.2	17.81	B	No
19.0880814	-0.116914	1.090	2	21.94	20.73	17.41	B	No
19.6446342	0.174344	1.108	2	22.6	21.73	17.64	B	No
19.7102184	0.384208	1.109	3	22.24	21.23	17.57	B	No
18.7422161	0.038365	1.118	3	22.47	21.29	17.55	B	No
18.7530174	-0.106268	1.123	3	21.35	20.78	17.09	A	No
19.0641727	-0.068061	1.136	3	22.09	20.99	17.62	B	No
19.0746899	-0.070653	1.138	3	21.86	21.12	17.83	A	Yes
16.2781296	0.325769	1.138	2	21.93	21.01	17.98	A	No
19.6975384	0.208385	1.153	3	22.29	21.24	17.46	B	No

Continued on next page

Table A.1 – continued from previous page

α (J2000)	δ (J2000)	Redshift	Flag/q	i_{AB}	z_{AB}	K_{Vega}	Priority	Emission
19.5258694	-0.045277	1.169	2	22.32	21.1	17.4	B	No
19.8669319	0.16838	1.175	2	23.36	21.73	17.74	B	No
18.9003468	0.10596	1.179	3	22.55	21.5	17.85	B	No
19.7464638	0.261089	1.187	2	22.17	20.96	17.36	B	No
19.5975227	0.196337	1.199	3	21.88	21.42	17.78	A	Yes
17.6361771	1.237698	1.269	3	22.14	21.07	17.99	A	Yes
18.6331844	0.202858	1.270	2	20.9	20.26	17.06	A	No
16.6336441	0.34763	1.283	2	22.42	21.93	17.57	B	No
18.6486092	0.252845	1.286	3	21.47	20.59	17.59	A	Yes
20.4547024	-0.101406	1.318	2	22.15	21.64	17.84	B	No
19.6112862	-0.128018	1.335	3	22.64	21.71	17.72	B	Yes
18.7074757	0.110936	1.34	2	22.61	21.92	17.84	B	No
19.9755802	0.224269	1.343	2	22.76	21.9	17.64	B	Yes

Appendix B

Vmmoscalib's parameters and outputs

Vmmoscalib's parameters

1. **Dispersion** : The expected spectral dispersion, 2.6Å/pixel (from CONFIGURATION TABLE).

2. **Peak Detection** : Initial peak detection threshold, 150 ADU (from CONFIGURATION TABLE). This threshold is used in the preliminary peak detection, where the reference lines candidates are selected from peaks having a maximum value above the background higher than this threshold

3. **Start/ End wavelength** : Wavelength interval where calibration is attempted. For MR grism the wavelength range is 3500-10000Å (from CONFIGURATION TABLE).

4. **Reference** : Reference wavelength for calibration, 7635.11Å (from CONFIGURATION TABLE). It is typically is chosen at the center of the extracted spectral range and is used in the determination of the inverse dispersion solution.

5. **Wdegree** : Degree of wavelength calibration polynomial, 4 (from CONFIGURATION TABLE). This value should be set to the lowest that would provide non-systematics residuals to the solution. As we will see later from the MOS DISPLAY RESIDUAL output, the default value of 4 is acceptable. A polynomial with the specified wdegree, is only used if the identified lines are at least twice as many the free parameters.

6. **Wradius** : Search radius when iterating pattern-matching with first-guess method, 4 pixel. The wavelengths from the input LINE CATALOG are transformed to CCD

181

pixel position using a first-guess model and a peak is searched within the defined search radius.

7. **Wreject** : Rejection threshold in dispersion relation fit, 0.7 pixel. Any reference line position displaying a residual greater than this threshold is excluded from the wavelength calibration polynomial fit iteration.

8. **Wmodemos** : Interpolation mode of wavelength solution, 1 (local). It improves the wavelength calibration by modeling the trend of the solution within each slit.

9. **Wcolumn** : Name of LINE CATALOG table.

10. **Cdegree** : Degree of spectral curvature polynomial, 2. For MR grism the default 2nd degree polynomial gives good results and the systematic residuals with oscillations of 0.2-0.3 pixels are acceptable (see Fig. 4.3)

11. **Cmode** : Interpolation mode of curvature solution applicable to MOS data, global. By setting cmode=1, we allow a global description of the spatial curvature to extract also those spectra whose edges cannot be traced due to confusion with nearby spectra.

12. **Slit Ident** : Attempt slit identification, true.

13. **Ddegree** : Degree of master flat field fitting polynomial along dispersion direction, ddegree=-1. The large scale trend is modeled by median filtering the spatial rectified spectra using a running smooth box with dimensions dradius and sradius.

14. **Dradius / Sradius** : Smooth box radius for flat field along dispersion direction and spatial direction, 10 and 10 pixels respectively.

Vmmoscalib recipe's most significant products, together with the configuration parameters that directly affect them are :

- MOS MASTER SCREEN FLAT, , is the normalised flat field image, derived dividing the master screen flat by its smoothed version. *ddegree, sradius, dradius, start/end wavelength.*

- MOS COMBINED SCREEN FLAT. , is the combined flat field image. It is the bias subtracted sum of all the input screen flat fields.

- MOS DISPLAY COEFFICIENT, is the table with the wavelength calibration polynomial coefficients. *wdegree, wmodemos.*

- MOS DISPLAY RESIDUAL. *start/end wavelength*

- MOS CURVATURE COEFFICIENT, , is the table with the coefficients of the spatial curvature fitting polynomials. *cdegree, cmode,*

- MOS CURVATURE TRACE, , is the table with the x CCD positions of the detected spectral edges at different y CCD positions. *cdegree, cmode.*

- MOS ARC SPECTRUM EXTRACTED, , is the rectified and wavelength calibrated arc lamp image. *start/end wavelength.*

- MOS SLIT LOCATION. , table with slit positions, both on the CCD and on the rectified image of MOS ARC SPECTRUM EXTRACTED image.

Appendix C

Vmmosscience's parameters and outputs

Vmmosscience's parameters

1. Sky Align : The polynomial order for sky lines adjustment, 0. The wavelength calibration is adjusted to the observed position of a set of sky lines, whose offsets from their expected positions are fitted by polynomials and then are added to the wavelength calibration polynomials. By setting *sky align=0*, we are just determining a median offset from the observed sky lines.

2. Wcolumn : Same as *vmmoscalib*.

3. Flat Field : True. The flat field correction is applied by dividing the bias subtracted from the input scientific images by the MOS MASTER SCREEN FLAT image.

4. Sky : Sky spectrum subtraction, local. We use the sky local method, in which the the sky trend is modeled for each column of pixels for each spectrum on the CCD. The advantage of this method arises as the signal is not resampled before the sky subtraction, reducing the problems related to small-scale interpolation.

5. Cosmics : Elimination of CR hits, true.

6. Stack Method : Average. Since we are run the vmmosscience on more that one input scientific image, we need to stack them. There is no need to align our input scientific images, as they are not dithered. By selecting the default parameter *stack method=average*, the image combination method stands simply from the average all the input scientific images.

7. Dispersion : Same as *vmmoscalib*.

8. **Start/ End wavelength** : Same as *vmmoscalib*.

9. **Reference** : Same as *vmmoscalib*.

10. **Slit Margin** : Number of spectrum edge pixels to exclude from object, 3 pixels. Most of our objects are positioned in the center of the slit spectra, so the default value of 3 pixel produces very accurate results.

11. **Ext Radius** : The maximum extraction radius for detected objects, 6 pixel. By using the default value, 6 pixel, together with the optimal extraction algorithm secures accurate extractions.

12. **Ext mode** : Extraction mode, Horne's optimal extraction.

Vmmosscience's most significant products, together with the configuration parameters that directly affect them are :

- MOS SCIENCE DISPLAY COEFFICIENT SKY, *sky align, start/end wavelength.*

- MOS SCIENCE ERROR FLUX REDUCED, *photometry.*

- MOS SCIENCE ERROR REDUCED, *dispersion, ext mode, start/end wavelength.*

- MOS SCIENCE SKY REDUCED, *dispersion, ext mode start/end wavelength.*

- MOS SCIENCE SKYLINES OFFSETS SLIT, *start/end wavelength.*

- MOS SCIENCE EXTRACTED, *dispersion, coscmics, flat field, sky align, start/end wavelength.*

- MOS SCIENCE REDUCED, *dispersion, ext mode, start/end wavelength.*

- MOS SCIENCE SKY, *sky, cosmics, start/end wavelength.*

- MOS SCIENCE SKY EXTRACTED, *dispersion, flat field, start/end wavelength.*

- MOS UNMAPPED SCIENCE, *sky,sky align, start/end wavelength.*

- OBJECT SCIENCE TABLE, *slit margin, ext radius*

Bibliography

Abazajian K. N., Adelman-McCarthy J. K., Agüeros M. A., Allam S. S., Allende Prieto C., An D., Anderson K. S. J., Anderson S. F. et al, 2009, ApJS, 182, 543

Abdalla F., Annis J., Bacon D., Bridle S., Castander F., Colless M., DePoy D., Diehl H. T. et al, 2012, ArXiv e-prints

Abdalla F. B., Banerji M., Lahav O., Rashkov V., 2011, MNRAS, 417, 1891

Abell G. O., 1959, Leaflet of the Astronomical Society of the Pacific, 8, 121

—, 1961, AJ, 66, 607

Adelberger K. L., Erb D. K., Steidel C. C., Reddy N. A., Pettini M., Shapley A. E., 2005a, ApJ, 620, L75

Adelberger K. L., Steidel C. C., Pettini M., Shapley A. E., Reddy N. A., Erb D. K., 2005b, ApJ, 619, 697

Albrecht A., Bernstein G., Cahn R., Freedman W. L., Hewitt J., Hu W., Huth J., Kamionkowski M. et al, 2006, ArXiv Astrophysics e-prints

Allen P. D., Moustakas L. A., Dalton G., MacDonald E., Blake C., Clewley L., Heymans C., Wegner G., 2005, MNRAS, 360, 1244

Almaini O., Foucaud S., Lane K., Conselice C. J., McLure R. J., Cirasuolo M., Dunlop J. S., Smail I., Simpson C., 2007, in Astronomical Society of the Pacific Conference Series, Vol. 379, Cosmic Frontiers, Metcalfe N., Shanks T., eds., p. 163

Anderson L., Aubourg E., Bailey S., Bizyaev D., Blanton M., Bolton A. S., Brinkmann J., Brownstein J. R. et al, 2012, MNRAS, 427, 3435

Arnouts S., Moscardini L., Vanzella E., Colombi S., Cristiani S., Fontana A., Giallongo E., Matarrese S. et al, 2002, MNRAS, 329, 355

Avni Y., Bahcall J. N., 1980, ApJ, 235, 694

Bartolo N., Komatsu E., Matarrese S., Riotto A., 2004a, Phys. Rep., 402, 103

—, 2004b, Phys. Rep., 402, 103

Baugh C. M., 2006, Reports on Progress in Physics, 69, 3101

Baugh C. M., Cole S., Frenk C. S., Lacey C. G., 1998, ApJ, 498, 504

Baum W. A., 1962, in IAU Symposium, Vol. 15, Problems of Extra-Galactic Research, McVittie G. C., ed., p. 390

Benítez N., Gaztañaga E., Miquel R., Castander F., Moles M., Crocce M., Fernández-Soto A., Fosalba P. et al, 2009, ApJ, 691, 241

Bennett C. L., Halpern M., Hinshaw G., Jarosik N., Kogut A., Limon M., Meyer S. S., Page L. et al, 2003, ApJS, 148, 1

Benoist C., Maurogordato S., da Costa L. N., Cappi A., Schaeffer R., 1996, ApJ, 472, 452

Berlind A. A., Weinberg D. H., 2002, ApJ, 575, 587

Bertin E., Arnouts S., 1996, A&AS, 117, 393

Bielby R., Hill M. D., Shanks T., Crighton N. H. M., Infante L., Bornancini C. G., Francke H., Héraudeau P. et al, 2013, MNRAS, 430, 425

Bielby R., Shanks T., Sawangwit U., Croom S. M., Ross N. P., Wake D. A., 2010, MNRAS, 403, 1261

Blake C., Collister A., Bridle S., Lahav O., 2007, MNRAS, 374, 1527

Blake C., Collister A., Lahav O., 2008, MNRAS, 385, 1257

Blake C., Glazebrook K., 2003, ApJ, 594, 665

Blake C., Jurek R. J., Brough S., Colless M., Couch W., Croom S., Davis T., Drinkwater M. J. et al, 2009, MNRAS, 395, 240

Blake C., Kazin E. A., Beutler F., Davis T. M., Parkinson D., Brough S., Colless M., Contreras C. et al, 2011, MNRAS, 418, 1707

Blake C., Wall J., 2002, MNRAS, 337, 993

Bond J. R., Efstathiou G., 1984, ApJ, 285, L45

—, 1987, MNRAS, 226, 655

Bond J. R., Efstathiou G., Tegmark M., 1997, MNRAS, 291, L33

Borch A., Meisenheimer K., Bell E. F., Rix H.-W., Wolf C., Dye S., Kleinheinrich M., Kovacs Z. et al, 2006, A&A, 453, 869

Bower R. G., Coles P., Frenk C. S., White S. D. M., 1993, ApJ, 405, 403

Bridle S. L., Lewis A. M., Weller J., Efstathiou G., 2003, MNRAS, 342, L72

Brown M. J. I., Dey A., Jannuzi B. T., Brand K., Benson A. J., Brodwin M., Croton D. J., Eisenhardt P. R., 2007, ApJ, 654, 858

Brown M. J. I., Webster R. L., Boyle B. J., 2000, MNRAS, 317, 782

Brown M. J. I., Zheng Z., White M., Dey A., Jannuzi B. T., Benson A. J., Brand K., Brodwin M. et al, 2008, ApJ, 682, 937

Bruzual G., Charlot S., 2003, MNRAS, 344, 1000

Budavári T., Connolly A. J., Szalay A. S., Szapudi I., Csabai I., Scranton R., Bahcall N. A., Brinkmann J. et al, 2003, ApJ, 595, 59

Bundy K., Ellis R. S., Conselice C. J., Taylor J. E., Cooper M. C., Willmer C. N. A., Weiner B. J., Coil A. L. et al, 2006, ApJ, 651, 120

Butcher H., Oemler Jr. A., 1978, ApJ, 219, 18

Cannon R., Drinkwater M., Edge A., Eisenstein D., Nichol R., Outram P., Pimbblet K., de
Propris R. et al, 2006, MNRAS, 372, 425

Carpenter E. F., 1938, ApJ, 88, 344

Carroll S. M., Press W. H., Turner E. L., 1992, ARA&A, 30, 499

Cimatti A., Daddi E., Renzini A., 2006, A&A, 453, L29

Coil A. L., Newman J. A., Cooper M. C., Davis M., Faber S. M., Koo D. C., Willmer
C. N. A., 2006, ApJ, 644, 671

Coil A. L., Newman J. A., Croton D., Cooper M. C., Davis M., Faber S. M., Gerke B. F.,
Koo D. C. et al, 2008, ApJ, 672, 153

Cole S., Percival W. J., Peacock J. A., Norberg P., Baugh C. M., Frenk C. S., Baldry I.,
Bland-Hawthorn J. et al, 2005, MNRAS, 362, 505

Coles P., 1993, MNRAS, 262, 1065

Colless M., Dalton G., Maddox S., Sutherland W., Norberg P., Cole S., Bland-Hawthorn
J., Bridges T. et al, 2001, MNRAS, 328, 1039

Colless M., Peterson B. A., Jackson C., Peacock J. A., Cole S., Norberg P., Baldry I. K.,
Baugh C. M. et al, 2003, ArXiv Astrophysics e-prints

Collister A., Lahav O., Blake C., Cannon R., Croom S., Drinkwater M., Edge A., Eisen-
stein D. et al, 2007, MNRAS, 375, 68

Conselice C. J., Newman J. A., Georgakakis A., Almaini O., Coil A. L., Cooper M. C.,
Eisenhardt P., Foucaud S. et al, 2007, ApJ, 660, L55

Content R., Barden S., Becerril S., Boehm A., Clark P., Costillo P., Dubbeldam C. M.,
Farrell T., Glazebrook K., Haynes R., Meisenheimer K., Miziarski S., Nikoloudakis N.,
Prada L. F., Rohloff R.-R., Shanks T., Sharples R. M., Wagner K., 2010, in Society of

Photo-Optical Instrumentation Engineers (SPIE) Conference Series, Vol. 7735, Society of Photo-Optical Instrumentation Engineers (SPIE) Conference Series

Conway E., Maddox S., Wild V., Peacock J. A., Hawkins E., Norberg P., Madgwick D. S., Baldry I. K. et al, 2005, MNRAS, 356, 456

Cooray A., Sheth R., 2002, Phys. Rep., 372, 1

Crocce M., Gaztañaga E., Cabré A., Carnero A., Sánchez E., 2011, MNRAS, 417, 2577

Croton D. J., Norberg P., Gaztañaga E., Baugh C. M., 2007, MNRAS, 379, 1562

da Costa L. N., Pellegrini P. S., Davis M., Meiksin A., Sargent W. L. W., Tonry J. L., 1991, ApJS, 75, 935

Daddi E., Cimatti A., Renzini A., Fontana A., Mignoli M., Pozzetti L., Tozzi P., Zamorani G., 2004, ApJ, 617, 746

Daddi E., Röttgering H. J. A., Labbé I., Rudnick G., Franx M., Moorwood A. F. M., Rix H. W., van der Werf P. P. et al, 2003, ApJ, 588, 50

Dalal N., Doré O., Huterer D., Shirokov A., 2008, Phys. Rev. D, 77, 123514

Dalton G. B., Caldwell M., Ward A. K., Whalley M. S., Woodhouse G., Edeson R. L., Clark P., Beard S. M., Gallie A. M., Todd S. P., Strachan J. M. D., Bezawada N. N., Sutherland W. J., Emerson J. P., 2006, in Society of Photo-Optical Instrumentation Engineers (SPIE) Conference Series, Vol. 6269, Society of Photo-Optical Instrumentation Engineers (SPIE) Conference Series

Davis M., Faber S. M., Newman J., Phillips A. C., Ellis R. S., Steidel C. C., Conselice C., Coil A. L., Finkbeiner D. P., Koo D. C., Guhathakurta P., Weiner B., Schiavon R., Willmer C., Kaiser N., Luppino G. A., Wirth G., Connolly A., Eisenhardt P., Cooper M., Gerke B., 2003, in Society of Photo-Optical Instrumentation Engineers (SPIE) Conference Series, Vol. 4834, Society of Photo-Optical Instrumentation Engineers (SPIE) Conference Series, Guhathakurta P., ed., pp. 161–172

Davis M., Geller M. J., 1976, ApJ, 208, 13

Davis M., Guhathakurta P., Konidaris N. P., Newman J. A., Ashby M. L. N., Biggs A. D., Barmby P., Bundy K. et al, 2007, ApJ, 660, L1

Davis M., Huchra J., Latham D. W., Tonry J., 1982, ApJ, 253, 423

Davis M., Meiksin A., Strauss M. A., da Costa L. N., Yahil A., 1988, ApJ, 333, L9

Davis M., Peebles P. J. E., 1983, ApJ, 267, 465

de Jong R., 2011, The Messenger, 145, 14

De Lucia G., Springel V., White S. D. M., Croton D., Kauffmann G., 2006, MNRAS, 366, 499

de Vaucouleurs G., 1958, AJ, 63, 253

Dekel A., Lahav O., 1999, ApJ, 520, 24

Dodelson S., 2003, Modern cosmology

Doughty N. A., Shane C. D., Wood F. B., 1974, Southern Stars, 25, 107

Dressler A., 1980, ApJ, 236, 351

Drinkwater M. J., Jurek R. J., Blake C., Woods D., Pimbblet K. A., Glazebrook K., Sharp R., Pracy M. B. et al, 2010, MNRAS, 401, 1429

Driver S. P., GAMA Team, Baldry I. K., Bamford S., Bland-Hawthorn J., Bridges T., Cameron E., Conselice C., Couch W. J., Croom S., Cross N. J. G., Driver S. P., Dunne L., Eales S., Edmondson E., Ellis S. C., Frenk C. S., Graham A. W., Jones H., Hill D., Hopkins A., van Kampen E., Kuijken K., Lahav O., Liske J., Loveday J., Nichol B., Norberg P., Oliver S., Parkinson H., Peacock J. A., Phillipps S., Popescu C. C., Prescott M., Proctor R., Sharp R., Staveley-Smith L., Sutherland W., Tuffs R. J., Warren S., 2009, in IAU Symposium, Vol. 254, IAU Symposium, Andersen J., Nordströara, m B., Bland-Hawthorn J., eds., pp. 469–474

Driver S. P., Hill D. T., Kelvin L. S., Robotham A. S. G., Liske J., Norberg P., Baldry I. K., Bamford S. P. et al, 2011, MNRAS, 413, 971

Dunkley J., Komatsu E., Nolta M. R., Spergel D. N., Larson D., Hinshaw G., Page L., Bennett C. L. et al, 2009, ApJS, 180, 306

Efstathiou G., Bond J. R., 1999, MNRAS, 304, 75

Efstathiou G., Kaiser N., Saunders W., Lawrence A., Rowan-Robinson M., Ellis R. S., Frenk C. S., 1990, MNRAS, 247, 10P

Eisenstein D. J., Annis J., Gunn J. E., Szalay A. S., Connolly A. J., Nichol R. C., Bahcall N. A., Bernardi M. et al, 2001, AJ, 122, 2267

Eisenstein D. J., Hogg D. W., Fukugita M., Nakamura O., Bernardi M., Finkbeiner D. P., Schlegel D. J., Brinkmann J. et al, 2003, ApJ, 585, 694

Eisenstein D. J., Hu W., Tegmark M., 1998, ApJ, 504, L57

Eisenstein D. J., Zehavi I., Hogg D. W., Scoccimarro R., Blanton M. R., Nichol R. C., Scranton R., Seo H.-J. et al, 2005, ApJ, 633, 560

Emerson J. P., Sutherland W. J., 2010, in Society of Photo-Optical Instrumentation Engineers (SPIE) Conference Series, Vol. 7733, Society of Photo-Optical Instrumentation Engineers (SPIE) Conference Series

Feldman H. A., Kaiser N., Peacock J. A., 1994, ApJ, 426, 23

Fioc M., Rocca-Volmerange B., 1997, A&A, 326, 950

Fisher K. B., Huchra J. P., Strauss M. A., Davis M., Yahil A., Schlegel D., 1995, ApJS, 100, 69

Flaugher B., 2005, International Journal of Modern Physics A, 20, 3121

Förster Schreiber N. M., van Dokkum P. G., Franx M., Labbé I., Rudnick G., Daddi E., Illingworth G. D., Kriek M. et al, 2004, ApJ, 616, 40

Foucaud S., Almaini O., Smail I., Conselice C. J., Lane K. P., Edge A. C., Simpson C., Dunlop J. S. et al, 2007, MNRAS, 376, L20

Franx M., Labbé I., Rudnick G., van Dokkum P. G., Daddi E., Förster Schreiber N. M., Moorwood A., Rix H.-W. et al, 2003, ApJ, 587, L79

Freedman W. L., Madore B. F., Gibson B. K., Ferrarese L., Kelson D. D., Sakai S., Mould J. R., Kennicutt Jr. R. C. et al, 2001, ApJ, 553, 47

Friedmann A., 1922, Zeitschrift fur Physik, 10, 377

Fritz A., Vipers Team, 2011, in Contributed talk at EAS Symposia 'S9 Galaxy Evolution: The Key for Galaxy Formation Theories' of the JENAM 2011 European Week of Astronomy and Space Science (EWASS), Saint-Petersburg, Russia, 4-8 July 2011. http://jenam2011.org/conf/. Edited by B. Rocca-Volmerange and A. Dosroshkevich, online at ftp://ftp.iap.fr/pub/from_users/rocca/incoming/JENAM2011_Session9/

Fry J. N., 1996, ApJ, 461, L65

Fukugita M., Ichikawa T., Gunn J. E., Doi M., Shimasaku K., Schneider D. P., 1996, AJ, 111, 1748

Gardner J. P., Cowie L. L., Wainscoat R. J., 1993, ApJ, 415, L9

Glazebrook K., Blake C., Couch W., Forbes D., Drinkwater M., Jurek R., Pimbblet K., Madore B. et al, 2007, ArXiv Astrophysics e-prints

Gonzalez-Perez V., Baugh C. M., Lacey C. G., Kim J.-W., 2011, MNRAS, 417, 517

Goto T., Yamauchi C., Fujita Y., Okamura S., Sekiguchi M., Smail I., Bernardi M., Gomez P. L., 2003, MNRAS, 346, 601

Grazian A., Fontana A., Moscardini L., Salimbeni S., Menci N., Giallongo E., de Santis C., Gallozzi S. et al, 2006, A&A, 453, 507

Groth E. J., Peebles P. J. E., 1977, ApJ, 217, 385

Guo H., Zehavi I., Zheng Z., 2012, ApJ, 756, 127

Guo Q., White S. D. M., 2009, MNRAS, 396, 39

Guth A. H., 1981, Phys. Rev. D, 23, 347

Guzzo L., Pierleoni M., Meneux B., Branchini E., Le Fèvre O., Marinoni C., Garilli B.,
    Blaizot J. et al, 2008, Nature, 451, 541

Guzzo L., Scodeggio M., Garilli B., Granett B. R., Abbas U., Adami C., Arnouts S., Bel J.
    et al, 2013, ArXiv e-prints

Guzzo L., Strauss M. A., Fisher K. B., Giovanelli R., Haynes M. P., 1997, ApJ, 489, 37

Hamilton A. J. S., 1988, ApJ, 331, L59

—, 1993, ApJ, 417, 19

Hinshaw G., Nolta M. R., Bennett C. L., Bean R., Doré O., Greason M. R., Halpern M.,
    Hill R. S. et al, 2007, ApJS, 170, 288

Ho S., Cuesta A., Seo H.-J., de Putter R., Ross A. J., White M., Padmanabhan N., Saito S.
    et al, 2012, ApJ, 761, 14

Hogg D. W., 1999, ArXiv Astrophysics e-prints

Holtzman J. A., 1989, ApJS, 71, 1

Horne K., 1986, PASP, 98, 609

Hu W., Dodelson S., 2002, ARA&A, 40, 171

Hu W., Sugiyama N., 1996, ApJ, 471, 542

Hubble E., 1929, Proceedings of the National Academy of Science, 15, 168

—, 1934, ApJ, 79, 8

—, 1936, ApJ, 84, 517

Ilbert O., Arnouts S., McCracken H. J., Bolzonella M., Bertin E., Le Fèvre O., Mellier Y.,
    Zamorani G. et al, 2006, A&A, 457, 841

Ilbert O., McCracken H. J., Le Fevre O., Capak P., Dunlop J., Karim A., Renzini M. A., Caputi K. et al, 2013, ArXiv e-prints

Ivezić Ž., Smith J. A., Miknaitis G., Lin H., Tucker D., Lupton R. H., Gunn J. E., Knapp G. R. et al, 2007, AJ, 134, 973

Iwata I., Inoue A. K., Burgarella D., 2005, A&A, 440, 881

Jackson J. C., 1972, MNRAS, 156, 1P

Jarosik N., Bennett C. L., Dunkley J., Gold B., Greason M. R., Halpern M., Hill R. S., Hinshaw G. et al, 2011, ApJS, 192, 14

Jing Y. P., Mo H. J., Boerner G., 1998, ApJ, 494, 1

Jungman G., Kamionkowski M., Kosowsky A., Spergel D. N., 1996, Phys. Rev. D, 54, 1332

Kaiser N., 1987, MNRAS, 227, 1

Kaiser N., Pan-STARRS Project Team, 2004, in Bulletin of the American Astronomical Society, Vol. 36, American Astronomical Society Meeting Abstracts #204, p. 828

Kim J.-W., Edge A. C., Wake D. A., Stott J. P., 2011, MNRAS, 410, 241

Knox L., Page L., 2000, Physical Review Letters, 85, 1366

Komatsu E., 2010, Classical and Quantum Gravity, 27, 124010

Komatsu E., Dunkley J., Nolta M. R., Bennett C. L., Gold B., Hinshaw G., Jarosik N., Larson D. et al, 2009, ApJS, 180, 330

Komatsu E., Smith K. M., Dunkley J., Bennett C. L., Gold B., Hinshaw G., Jarosik N., Larson D. et al, 2011, ApJS, 192, 18

Komatsu E., Spergel D. N., 2001, Phys. Rev. D, 63, 063002

Kravtsov A. V., Berlind A. A., Wechsler R. H., Klypin A. A., Gottlöber S., Allgood B., Primack J. R., 2004, ApJ, 609, 35

Kriek M., van Dokkum P. G., Franx M., Förster Schreiber N. M., Gawiser E., Illingworth
    G. D., Labbé I., Marchesini D. et al, 2006a, ApJ, 645, 44

Kriek M., van Dokkum P. G., Franx M., Quadri R., Gawiser E., Herrera D., Illingworth
    G. D., Labbé I. et al, 2006b, ApJ, 649, L71

Labbé I., Huang J., Franx M., Rudnick G., Barmby P., Daddi E., van Dokkum P. G., Fazio
    G. G. et al, 2005, ApJ, 624, L81

Lacey C., Cole S., 1993, MNRAS, 262, 627

Lahav O., Lilje P. B., Primack J. R., Rees M. J., 1991, MNRAS, 251, 128

Landy S. D., Szalay A. S., 1993, ApJ, 412, 64

Lane K. P., Almaini O., Foucaud S., Simpson C., Smail I., McLure R. J., Conselice C. J.,
    Cirasuolo M. et al, 2007, MNRAS, 379, L25

Laureijs R., Amiaux J., Arduini S., Auguères J. ., Brinchmann J., Cole R., Cropper M.,
    Dabin C. et al, 2011, ArXiv e-prints

Lawrence A., Warren S. J., Almaini O., Edge A. C., Hambly N. C., Jameson R. F., Lucas
    P., Casali M. et al, 2007, MNRAS, 379, 1599

Le Fèvre O., Guzzo L., Meneux B., Pollo A., Cappi A., Colombi S., Iovino A., Marinoni
    C. et al, 2005a, A&A, 439, 877

Le Fèvre O., Saisse M., Mancini D., Brau-Nogue S., Caputi O., Castinel L., D'Odorico S.,
    Garilli B., Kissler-Patig M., Lucuix C., Mancini G., Pauget A., Sciarretta G., Scodeggio
    M., Tresse L., Vettolani G., 2003, in Society of Photo-Optical Instrumentation Engi-
    neers (SPIE) Conference Series, Vol. 4841, Society of Photo-Optical Instrumentation
    Engineers (SPIE) Conference Series, Iye M., Moorwood A. F. M., eds., pp. 1670–1681

Le Fèvre O., Vettolani G., Garilli B., Tresse L., Bottini D., Le Brun V., Maccagni D., Picat
    J. P. et al, 2005b, A&A, 439, 845

Lee K.-S., Giavalisco M., Gnedin O. Y., Somerville R. S., Ferguson H. C., Dickinson M.,
    Ouchi M., 2006, ApJ, 642, 63

Lemaître G., 1927, Annales de la Societe Scietifique de Bruxelles, 47, 49

Levi M., Bebek C., Beers T., Blum R., Cahn R., Eisenstein D., Flaugher B., Honscheid K. et al, 2013, ArXiv e-prints

Lewis A., Challinor A., Lasenby A., 2000, ApJ, 538, 473

Lilly S. J., Le Fèvre O., Renzini A., Zamorani G., Scodeggio M., Contini T., Carollo C. M., Hasinger G. et al, 2007, ApJS, 172, 70

Limber D. N., 1953, ApJ, 117, 134

—, 1954, ApJ, 119, 655

Liske J., Lemon D. J., Driver S. P., Cross N. J. G., Couch W. J., 2003, MNRAS, 344, 307

Loh Y.-S., Strauss M. A., 2006, MNRAS, 366, 373

Loveday J., Maddox S. J., Efstathiou G., Peterson B. A., 1995, ApJ, 442, 457

Lupton R., Gunn J. E., Ivezić Z., Knapp G. R., Kent S., Yasuda N., 2001, in Astronomical Society of the Pacific Conference Series, Vol. 238, Astronomical Data Analysis Software and Systems X, Harnden Jr. F. R., Primini F. A., Payne H. E., eds., p. 269

Ma C.-P., Fry J. N., 2000, ApJ, 543, 503

Maddox S. J., Efstathiou G., Sutherland W. J., Loveday J., 1990, MNRAS, 243, 692

Madgwick D. S., Hawkins E., Lahav O., Maddox S., Norberg P., Peacock J. A., Baldry I. K., Baugh C. M. et al, 2003, MNRAS, 344, 847

Maldacena J., 2003, Journal of High Energy Physics, 5, 13

Masjedi M., Hogg D. W., Cool R. J., Eisenstein D. J., Blanton M. R., Zehavi I., Berlind A. A., Bell E. F. et al, 2006, ApJ, 644, 54

Masters D., Capak P., 2011, PASP, 123, 638

Matarrese S., Coles P., Lucchin F., Moscardini L., 1997, MNRAS, 286, 115

Matarrese S., Verde L., Jimenez R., 2000, ApJ, 541, 10

McCracken H. J., Milvang-Jensen B., Dunlop J., Franx M., Fynbo J. P. U., Le Fèvre O., Holt J., Caputi K. I. et al, 2012, A&A, 544, A156

McPherson A. M., Born A. J., Sutherland W. J., Emerson J. P., 2004, in Society of Photo-Optical Instrumentation Engineers (SPIE) Conference Series, Vol. 5489, Society of Photo-Optical Instrumentation Engineers (SPIE) Conference Series, Oschmann Jr. J. M., ed., pp. 638–649

Meiksin A., White M., Peacock J. A., 1999, MNRAS, 304, 851

Mo H., van den Bosch F. C., White S., 2010, Galaxy Formation and Evolution

Moore A. W., Connolly A. J., Genovese C., Gray A., Grone L., Kanidoris II N., Nichol R. C., Schneider J., Szalay A. S., Szapudi I., Wasserman L., 2001, in Mining the Sky, Banday A. J., Zaroubi S., Bartelmann M., eds., p. 71

Moscardini L., Coles P., Lucchin F., Matarrese S., 1998, MNRAS, 299, 95

Myers A. D., Brunner R. J., Nichol R. C., Richards G. T., Schneider D. P., Bahcall N. A., 2007, ApJ, 658, 85

Navarro J. F., Frenk C. S., White S. D. M., 1997, ApJ, 490, 493

Newman J. A., 2008, ApJ, 684, 88

Neyman J., Scott E. L., 1952, ApJ, 116, 144

Nikoloudakis N., Shanks T., Sawangwit U., 2013, MNRAS, 429, 2032

Norberg P., Baugh C. M., Gaztañaga E., Croton D. J., 2009, MNRAS, 396, 19

Norberg P., Baugh C. M., Hawkins E., Maddox S., Madgwick D., Lahav O., Cole S., Frenk C. S. et al, 2002, MNRAS, 332, 827

Norberg P., Baugh C. M., Hawkins E., Maddox S., Peacock J. A., Cole S., Frenk C. S., Bland-Hawthorn J. et al, 2001, MNRAS, 328, 64

Ouchi M., Shimasaku K., Okamura S., Furusawa H., Kashikawa N., Ota K., Doi M., Hamabe M. et al, 2004, ApJ, 611, 685

Padmanabhan N., Budavári T., Schlegel D. J., Bridges T., Brinkmann J., Cannon R., Connolly A. J., Croom S. M. et al, 2005, MNRAS, 359, 237

Padmanabhan N., Schlegel D. J., Seljak U., Makarov A., Bahcall N. A., Blanton M. R., Brinkmann J., Eisenstein D. J. et al, 2007, MNRAS, 378, 852

Papageorgiou A., Plionis M., Basilakos S., Ragone-Figueroa C., 2012, MNRAS, 422, 106

Papovich C., Moustakas L. A., Dickinson M., Le Floc'h E., Rieke G. H., Daddi E., Alexander D. M., Bauer F. et al, 2006, ApJ, 640, 92

Pâris I., Petitjean P., Aubourg É., Bailey S., Ross N. P., Myers A. D., Strauss M. A., Anderson S. F. et al, 2012, A&A, 548, A66

Park C., Vogeley M. S., Geller M. J., Huchra J. P., 1994, ApJ, 431, 569

Peacock J. A., Dodds S. J., 1994, MNRAS, 267, 1020

Peacock J. A., Smith R. E., 2000, MNRAS, 318, 1144

Peebles P. J. E., 1973, ApJ, 185, 413

—, 1980, The large-scale structure of the universe

Peebles P. J. E., Hauser M. G., 1974, ApJS, 28, 19

Peebles P. J. E., Yu J. T., 1970, ApJ, 162, 815

Percival W. J., Reid B. A., Eisenstein D. J., Bahcall N. A., Budavari T., Frieman J. A., Fukugita M., Gunn J. E. et al, 2010, MNRAS, 401, 2148

Percival W. J., Sutherland W., Peacock J. A., Baugh C. M., Bland-Hawthorn J., Bridges T., Cannon R., Cole S. et al, 2002, MNRAS, 337, 1068

Perlmutter S., Aldering G., Goldhaber G., Knop R. A., Nugent P., Castro P. G., Deustua S., Fabbro S. et al, 1999, ApJ, 517, 565

Phillipps S., Fong R., Fall R. S. E. S. M., MacGillivray H. T., 1978, MNRAS, 182, 673

Planck Collaboration, Ade P. A. R., Aghanim N., Armitage-Caplan C., Arnaud M., Ashdown M., Atrio-Barandela F., Aumont J. et al, 2013, ArXiv e-prints

Planck Collaboration XVI, Ade P. A. R., Aghanim N., Armitage-Caplan C., Arnaud M., Ashdown M., Atrio-Barandela F., Aumont J. et al, 2013a, ArXiv e-prints

—, 2013b, ArXiv e-prints

Planck Collaboration XXIII, Ade P. A. R., Aghanim N., Armitage-Caplan C., Arnaud M., Ashdown M., Atrio-Barandela F., Aumont J. et al, 2013, ArXiv e-prints

Planck Collaboration XXIV, Ade P. A. R., Aghanim N., Armitage-Caplan C., Arnaud M., Ashdown M., Atrio-Barandela F., Aumont J. et al, 2013, ArXiv e-prints

Postman M., Geller M. J., 1984, ApJ, 281, 95

Predehl P., Andritschke R., Böhringer H., Bornemann W., Bräuninger H., Brunner H., Brusa M., Burkert W., Burwitz V., Cappelluti N., Churazov E., Dennerl K., Eder J., Elbs J., Freyberg M., Friedrich P., Fürmetz M., Gaida R., Hälker O., Hartner G., Hasinger G., Hermann S., Huber H., Kendziorra E., von Kienlin A., Kink W., Kreykenbohm I., Lamer G., Lapchov I., Lehmann K., Meidinger N., Mican B., Mohr J., Mühlegger M., Müller S., Nandra K., Pavlinsky M., Pfeffermann E., Reiprich T., Robrade J., Rohé C., Santangelo A., Schächner G., Schanz T., Schmid C., Schmitt J., Schreib R., Schrey F., Schwope A., Steinmetz M., Strüder L., Sunyaev R., Tenzer C., Tiedemann L., Vongehr M., Wilms J., 2010, in Society of Photo-Optical Instrumentation Engineers (SPIE) Conference Series, Vol. 7732, Society of Photo-Optical Instrumentation Engineers (SPIE) Conference Series

Quadri R., van Dokkum P., Gawiser E., Franx M., Marchesini D., Lira P., Rudnick G., Herrera D. et al, 2007, ApJ, 654, 138

Quadri R. F., Williams R. J., Lee K.-S., Franx M., van Dokkum P., Brammer G. B., 2008, ApJ, 685, L1

Reddy N. A., Erb D. K., Steidel C. C., Shapley A. E., Adelberger K. L., Pettini M., 2005, ApJ, 633, 748

Reddy N. A., Steidel C. C., Fadda D., Yan L., Pettini M., Shapley A. E., Erb D. K., Adelberger K. L., 2006, ApJ, 644, 792

Richards G. T., Myers A. D., Gray A. G., Riegel R. N., Nichol R. C., Brunner R. J., Szalay A. S., Schneider D. P. et al, 2009, ApJS, 180, 67

Riess A. G., Filippenko A. V., Challis P., Clocchiatti A., Diercks A., Garnavich P. M., Gilliland R. L., Hogan C. J. et al, 1998, AJ, 116, 1009

Riess A. G., Macri L., Casertano S., Lampeitl H., Ferguson H. C., Filippenko A. V., Jha S. W., Li W. et al, 2011, ApJ, 730, 119

Riess A. G., Strolger L.-G., Tonry J., Casertano S., Ferguson H. C., Mobasher B., Challis P., Filippenko A. V. et al, 2004, ApJ, 607, 665

Robertson H. P., 1935, ApJ, 82, 284

Roche N., Eales S. A., 1999, MNRAS, 307, 703

Roseboom I. G., Pimbblet K. A., Drinkwater M. J., Cannon R. D., de Propris R., Edge A. C., Eisenstein D. J., Nichol R. C. et al, 2006, MNRAS, 373, 349

Ross A. J., Brunner R. J., Myers A. D., 2008a, ApJ, 682, 737

Ross A. J., Ho S., Cuesta A. J., Tojeiro R., Percival W. J., Wake D., Masters K. L., Nichol R. C. et al, 2011, MNRAS, 417, 1350

Ross A. J., Percival W. J., Brunner R. J., 2010, MNRAS, 407, 420

Ross N. P., da Ângela J., Shanks T., Wake D. A., Cannon R. D., Edge A. C., Nichol R. C., Outram P. J. et al, 2007, MNRAS, 381, 573

Ross N. P., Shanks T., Cannon R. D., Wake D. A., Sharp R. G., Croom S. M., Peacock J. A., 2008b, MNRAS, 387, 1323

Rubin V. C., 1954, Proceedings of the National Academy of Science, 40, 541

Salopek D. S., Bond J. R., 1990, Phys. Rev. D, 42, 3936

Saunders W., Frenk C., Rowan-Robinson M., Lawrence A., Efstathiou G., 1991, Nature, 349, 32

Saunders W., Rowan-Robinson M., Lawrence A., Efstathiou G., Kaiser N., Ellis R. S., Frenk C. S., 1990, MNRAS, 242, 318

Saunders W., Sutherland W. J., Maddox S. J., Keeble O., Oliver S. J., Rowan-Robinson M., McMahon R. G., Efstathiou G. P. et al, 2000, MNRAS, 317, 55

Sawangwit U., Shanks T., Abdalla F. B., Cannon R. D., Croom S. M., Edge A. C., Ross N. P., Wake D. A., 2011, MNRAS, 416, 3033

Sawangwit U., Shanks T., Croom S. M., Drinkwater M. J., Fine S., Parkinson D., Ross N. P., 2012, MNRAS, 420, 1916

Schechter P., 1976, ApJ, 203, 297

Schlegel D. J., Blanton M., Eisenstein D., Gillespie B., Gunn J., Harding P., McDonald P., Nichol R., Padmanabhan N., Percival W., Richards G., Rockosi C., Roe N., Ross N., Schneider D., Strauss M., Weinberg D., White M., 2007, in Bulletin of the American Astronomical Society, Vol. 39, American Astronomical Society Meeting Abstracts, p. 132.29

Schlegel D. J., Finkbeiner D. P., Davis M., 1998, ApJ, 500, 525

Schneider D. P., Richards G. T., Hall P. B., Strauss M. A., Anderson S. F., Boroson T. A., Ross N. P., Shen Y. et al, 2010, AJ, 139, 2360

Scoccimarro R., Sefusatti E., Zaldarriaga M., 2004, Phys. Rev. D, 69, 103513

Scoccimarro R., Sheth R. K., Hui L., Jain B., 2001, ApJ, 546, 20

Scoville N., Abraham R. G., Aussel H., Barnes J. E., Benson A., Blain A. W., Calzetti D., Comastri A. et al, 2007, ApJS, 172, 38

Scranton R., Johnston D., Dodelson S., Frieman J. A., Connolly A., Eisenstein D. J., Gunn J. E., Hui L. et al, 2002, ApJ, 579, 48

Seljak U., 2000, MNRAS, 318, 203

Seo H.-J., Eisenstein D. J., 2003, ApJ, 598, 720

Seo H.-J., Eisenstein D. J., Zehavi I., 2008, ApJ, 681, 998

Shanks T., Bean A. J., Ellis R. S., Fong R., Efstathiou G., Peterson B. A., 1983, ApJ, 274, 529

Shanks T., Boyle B. J., Croom S., Loaring N., Miller L., Smith R. J., 2000, in Astronomical Society of the Pacific Conference Series, Vol. 200, Clustering at High Redshift, Mazure A., Le Fèvre O., Le Brun V., eds., p. 57

Shanks T., Sutton D. H., Fong R., Metcalfe N., 1989, MNRAS, 237, 589

Shapley A. E., Erb D. K., Pettini M., Steidel C. C., Adelberger K. L., 2004, ApJ, 612, 108

Shapley A. E., Steidel C. C., Adelberger K. L., Dickinson M., Giavalisco M., Pettini M., 2001, ApJ, 562, 95

Shectman S. A., Landy S. D., Oemler A., Tucker D. L., Lin H., Kirshner R. P., Schechter P. L., 1996, ApJ, 470, 172

Sheth R. K., Lemson G., 1999, MNRAS, 304, 767

Sheth R. K., Mo H. J., Tormen G., 2001, MNRAS, 323, 1

Sheth R. K., Tormen G., 2002, MNRAS, 329, 61

Skibba R. A., Sheth R. K., 2009, MNRAS, 392, 1080

Slosar A., Hirata C., Seljak U., Ho S., Padmanabhan N., 2008, J. Cosmology Astropart. Phys., 8, 31

Smith J. A., Tucker D. L., Kent S., Richmond M. W., Fukugita M., Ichikawa T., Ichikawa S.-i., Jorgensen A. M. et al, 2002, AJ, 123, 2121

Smith R. E., Peacock J. A., Jenkins A., White S. D. M., Frenk C. S., Pearce F. R., Thomas P. A., Efstathiou G. et al, 2003, MNRAS, 341, 1311

Smoot G. F., Bennett C. L., Kogut A., Wright E. L., Aymon J., Boggess N. W., Cheng E. S., de Amici G. et al, 1992, ApJ, 396, L1

Spergel D. N., Bean R., Doré O., Nolta M. R., Bennett C. L., Dunkley J., Hinshaw G., Jarosik N. et al, 2007, ApJS, 170, 377

Spergel D. N., Verde L., Peiris H. V., Komatsu E., Nolta M. R., Bennett C. L., Halpern M., Hinshaw G. et al, 2003, ApJS, 148, 175

Steidel C. C., Adelberger K. L., Shapley A. E., Pettini M., Dickinson M., Giavalisco M., 2003, ApJ, 592, 728

Steidel C. C., Giavalisco M., Pettini M., Dickinson M., Adelberger K. L., 1996, ApJ, 462, L17

Strauss M. A., Huchra J. P., Davis M., Yahil A., Fisher K. B., Tonry J., 1992, ApJS, 83, 29

Sugiyama N., 1995, ApJS, 100, 281

Sunyaev R. A., Zeldovich Y. B., 1970, Ap&SS, 7, 3

Tanvir N. R., Ferguson H. C., Shanks T., 1999, MNRAS, 310, 175

Tegmark M., Blanton M. R., Strauss M. A., Hoyle F., Schlegel D., Scoccimarro R., Vogeley M. S., Weinberg D. H. et al, 2004a, ApJ, 606, 702

Tegmark M., Strauss M. A., Blanton M. R., Abazajian K., Dodelson S., Sandvik H., Wang X., Weinberg D. H. et al, 2004b, Phys. Rev. D, 69, 103501

Tinker J. L., Wechsler R. H., Zheng Z., 2010, ApJ, 709, 67

Tinker J. L., Weinberg D. H., Zheng Z., Zehavi I., 2005, ApJ, 631, 41

Totsuji H., Kihara T., 1969, PASJ, 21, 221

Tyson J. A., 2002, in Society of Photo-Optical Instrumentation Engineers (SPIE) Conference Series, Vol. 4836, Society of Photo-Optical Instrumentation Engineers (SPIE) Conference Series, Tyson J. A., Wolff S., eds., pp. 10–20

van Dokkum P. G., Förster Schreiber N. M., Franx M., Daddi E., Illingworth G. D., Labbé I., Moorwood A., Rix H.-W. et al, 2003, ApJ, 587, L83

van Dokkum P. G., Franx M., Förster Schreiber N. M., Illingworth G. D., Daddi E., Knudsen K. K., Labbé I., Moorwood A. et al, 2004, ApJ, 611, 703

van Dokkum P. G., Quadri R., Marchesini D., Rudnick G., Franx M., Gawiser E., Herrera D., Wuyts S. et al, 2006, ApJ, 638, L59

Verde L., Wang L., Heavens A. F., Kamionkowski M., 2000, MNRAS, 313, 141

Vivès S., Le Mignant D., Madec F., Jaquet M., Prieto E., Martin L., Le Fèvre O., Gunn J., Carr M., Smee S., Barkhouser R., Sugai H., Tamura N., 2012, in Society of Photo-Optical Instrumentation Engineers (SPIE) Conference Series, Vol. 8446, Society of Photo-Optical Instrumentation Engineers (SPIE) Conference Series

Wake D. A., Croom S. M., Sadler E. M., Johnston H. M., 2008, MNRAS, 391, 1674

Wake D. A., Nichol R. C., Eisenstein D. J., Loveday J., Edge A. C., Cannon R., Smail I., Schneider D. P. et al, 2006, MNRAS, 372, 537

Walker A. G., 1937, Proceedings of the London Mathematical Society, s2-42, 90

Warren S. J., Hambly N. C., Dye S., Almaini O., Cross N. J. G., Edge A. C., Foucaud S., Hewett P. C. et al, 2007, MNRAS, 375, 213

White M., Myers A. D., Ross N. P., Schlegel D. J., Hennawi J. F., Shen Y., McGreer I., Strauss M. A. et al, 2012, MNRAS, 424, 933

White M., Zheng Z., Brown M. J. I., Dey A., Jannuzi B. T., 2007, ApJ, 655, L69

White S. D. M., Frenk C. S., 1991, ApJ, 379, 52

White S. D. M., Rees M. J., 1978, MNRAS, 183, 341

Willmer C. N. A., da Costa L. N., Pellegrini P. S., 1998, AJ, 115, 869

Wood-Vasey W. M., Miknaitis G., Stubbs C. W., Jha S., Riess A. G., Garnavich P. M., Kirshner R. P., Aguilera C. et al, 2007, ApJ, 666, 694

Wright E. L., Eisenhardt P. R. M., Mainzer A. K., Ressler M. E., Cutri R. M., Jarrett T., Kirkpatrick J. D., Padgett D. et al, 2010, AJ, 140, 1868

Wu K. K. S., Lahav O., Rees M. J., 1999, Nature, 397, 225

Xia J.-Q., Baccigalupi C., Matarrese S., Verde L., Viel M., 2011, J. Cosmology Astropart. Phys., 8, 33

Xia J.-Q., Bonaldi A., Baccigalupi C., De Zotti G., Matarrese S., Verde L., Viel M., 2010a, J. Cosmology Astropart. Phys., 8, 13

Xia J.-Q., Viel M., Baccigalupi C., De Zotti G., Matarrese S., Verde L., 2010b, ApJ, 717, L17

Yadav J., Bharadwaj S., Pandey B., Seshadri T. R., 2005, MNRAS, 364, 601

York D. G., Adelman J., Anderson Jr. J. E., Anderson S. F., Annis J., Bahcall N. A., Bakken J. A., Barkhouser R. et al, 2000, AJ, 120, 1579

Yu J. T., Peebles P. J. E., 1969, ApJ, 158, 103

Zehavi I., Blanton M. R., Frieman J. A., Weinberg D. H., Mo H. J., Strauss M. A., Anderson S. F., Annis J. et al, 2002, ApJ, 571, 172

Zehavi I., Eisenstein D. J., Nichol R. C., Blanton M. R., Hogg D. W., Brinkmann J., Loveday J., Meiksin A. et al, 2005a, ApJ, 621, 22

Zehavi I., Zheng Z., Weinberg D. H., Frieman J. A., Berlind A. A., Blanton M. R., Scoccimarro R., Sheth R. K. et al, 2005b, ApJ, 630, 1

—, 2005c, ApJ, 630, 1

Zheng Z., Zehavi I., Eisenstein D. J., Weinberg D. H., Jing Y. P., 2009, ApJ, 707, 554

Zwicky F., 1952, PASP, 64, 247

Zwicky F., Herzog E., Wild P., 1968, Catalogue of galaxies and of clusters of galaxies